

**Novel spintronic device concepts based on
spin-gapless semiconductors and half-metallic
magnets**

Dissertation

zur Erlangung des Doktorgrades der Naturwissenschaften
(Dr. rer. nat.)

der

Naturwissenschaftlichen Fakultät II
Chemie, Physik und Mathematik

der Martin-Luther-Universität
Halle-Wittenberg

vorgelegt von

Herrn

THORSTEN UDO AULL

geb. am 24.08.1994 in Fulda

Erstgutachterin: Prof. Dr. Ingrid Mertig
Zweitgutachter: Prof. Dr. Steffen Trimper
Drittgutachter: Prof. Dr. Biplab Sanyal

Datum der Abgabe: 17. Februar 2022
Datum der öffentlichen Verteidigung: 21. Juli 2022
Vorsitzender der Promotionskommission: Prof. Dr. Kay Saalwächter

Abstract

Magnetic tunnel junctions (MTJs) based on Fe, Co, CoFeB and half-metallic Heusler compounds were extensively studied for magnetic logic and memory applications. Despite their very high tunnel magnetoresistance (TMR) ratios, such devices do not exhibit current rectification, i.e., a diode effect. Recently, current rectification was achieved in a new MTJ concept based on a spin-gapless semiconductor (SGS) and a half-metallic magnet (HMM). In this cumulative thesis, we report on novel spintronic device concepts based on the unique spin-dependent transport properties of HMMs and SGSs. First, by employing density functional theory (DFT) we screen the family of quaternary Heusler alloys for SGSs and HMMs with similar lattice constants, large spin-gaps below and above their Fermi energy, and Curie temperatures above room temperature for spintronic applications. Next, by using DFT combined with non-equilibrium Green's functions, we computationally design two different MTJs based on HMMs and SGSs within the family of quaternary Heusler compounds as electrode materials separated by different numbers of MgO layers and investigate their transport properties and TMR ratio. We demonstrate that the MTJs under consideration present current rectification with relatively high on/off ratios, an inverse TMR effect and we show that the breakdown voltage is limited by the energy gap of the SGS and HMM materials. Then, we propose a new SGS–HMM junction which is to some extent similar to conventional metal-semiconductor junctions (Schottky-barrier diodes), the so-called Ohmic spin diode (OSD). This device acts as a diode with linear current-voltage characteristics, zero threshold voltage, and infinite on/off ratio at zero temperature. Finally, we design four different OSDs based on HMM and SGS quaternary Heusler compounds with high Curie temperatures for room temperature application.

Kurzzusammenfassung

Magnetische Tunnelkontakte (MTJs) aus Fe, Co, CoFeB und halb-metallischen Heusler-Legierungen zur Anwendung in magnetischer Logik und Speichermedien wurden bereits intensiv untersucht. Ungeachtet der hohen magnetischen Tunnelwiderstände (TMRs) weisen diese Bauelemente keine Diodenkennlinie auf. Diese Eigenschaft wurde kürzlich in einem neuen Konzept einer Tunnelodiode, in welcher ein Halbleiter ohne Spin-Anregungslücke (SGS) und ein halbmetallischer Magnet (HMM) verwendet werden, gezeigt. In dieser kumulativen Arbeit werden die Konzepte neuartiger, spintronischer Bauelemente untersucht, welche auf den einzigartigen, spin-abhängigen Eigenschaften von HMMs und SGSs basieren. Zuerst durchsuchen wir, mit Hilfe von Dichtefunktionaltheorie (DFT), die Familie der quaternären Heusler-Legierungen nach HMMs und SGSs, welche ähnliche Gitterkonstanten, große Energielücken über und unterhalb der Fermienergie und Curietemperaturen über Raumtemperatur aufweisen. Hieraus konstruieren wir, unter Verwendung von DFT und nicht-Gleichgewichts-Green-Funktionen, zwei unterschiedliche MTJs bestehend aus einem HMM und einem SGS, welche durch verschiedene Schichtdicken von MgO getrennt werden und untersuchen deren Transporteigenschaften sowie den TMR Effekt. Wir zeigen, dass diese MTJs eine Diodenkennlinie mit relativ hohem Ein-/Ausschaltstromverhältnis besitzen, einen inversen-TMR Effekt aufweisen und die Durchbruchspannung von dem Betrag der Energielücke der SGSs und HMMs abhängt. Danach stellen wir ein neues HMM–SGS Bauelement vor, welches ähnlich zu Metall-Halbleiter-Dioden (Schottky-Dioden) ist: die sogenannte Ohmsche Spindiode (OSD). Zum Schluss konstruieren wir vier OSDs aus HMMs und SGSs aus der Familie der quaternären Heusler-Legierungen mit hohen Curietemperaturen für Raumtemperatur-Anwendungen.

Contents

| | |
|---|------------|
| List of Figures | III |
| List of abbreviations | IV |
| 1 Introduction | 1 |
| 2 Electronic structure | 5 |
| 2.1 Many-body problem | 5 |
| 2.2 Density functional theory | 7 |
| 2.2.1 Hohenberg-Kohn theorem | 8 |
| 2.2.2 Kohn-Sham scheme | 10 |
| 2.2.3 Exchange-correlation energy functional | 12 |
| 2.3 Extension to spin-polarized systems | 14 |
| 2.4 Basis sets | 16 |
| 2.4.1 Linear combination of atomic orbitals | 16 |
| 2.4.2 Slater type orbitals | 17 |
| 2.4.3 Gaussian type orbitals | 17 |
| 2.5 Pseudopotentials | 18 |
| 3 Electronic transport | 21 |
| 3.1 Landauer-Büttiker formalism | 22 |
| 3.2 Non-equilibrium Green's function method | 25 |
| 3.2.1 Hamiltonian, overlap matrix, and Green's function of the system | 25 |
| 3.2.2 Response to an incoming wave | 29 |
| 3.2.3 Charge density operator | 30 |
| 3.2.4 Current and transmission | 35 |
| 4 Half-metallic magnets and spin-gapless semiconductors | 37 |
| 4.1 Heusler alloys | 38 |
| 4.1.1 Quaternary Heuslers | 39 |
| 4.1.2 Half-metallic magnetism in Heusler compounds | 39 |
| 4.1.3 Spin-gapless semiconducting behavior in Heusler compounds | 40 |
| 4.2 Two-dimensional materials | 41 |
| 4.2.1 Half-metallic ferromagnetism in two-dimensional materials | 42 |
| 4.2.2 Spin-gapless semiconducting behavior in two-dimensional materials | 42 |
| 5 Overview of spintronic devices | 43 |
| 5.1 Giant magnetoresistance and tunnel magnetoresistance effect | 44 |
| 5.2 Spin diodes | 45 |
| 5.2.1 Spin-torque diode | 46 |
| 5.2.2 Magnetic tunnel diode | 47 |
| 5.2.3 Resonant magnetic tunnel diode | 48 |
| 5.2.4 Reconfigurable magnetic tunnel diode | 49 |
| 5.2.5 Ohmic spin diode | 50 |
| 5.3 Spin transistors | 51 |
| 5.3.1 Datta-Das transistor | 51 |

| | | |
|----------|--|------------|
| 5.3.2 | Spin field-effect transistor | 52 |
| 5.3.3 | Spin-valve and magnetic tunnel transistor | 53 |
| 5.3.4 | Reconfigurable magnetic tunnel transistor | 54 |
| 6 | Results and Discussion | 57 |
| 6.1 | Screening for spin-gapless semiconductors and half-metallic magnets within the family of quaternary Heusler compounds | 58 |
| 6.2 | Magnetic tunnel junctions based on spin-gapless semiconductors and half-metallic magnets for magnetic memory and logic applications. | 72 |
| 6.3 | Half-metal–spin-gapless semiconductor junctions (Ohmic spin diodes) | 88 |
| 6.4 | Design of Ohmic spin diodes based on quaternary Heusler compounds | 103 |
| 7 | Summary and Outlook | 111 |
| | List of publications | 113 |
| | Bibliography | 114 |

List of Figures

| | | |
|------|--|-----|
| 1.1 | Evolution in the world’s technological installed capacity to store information over two decades | 1 |
| 1.2 | Representation of an early magnetic core memory | 2 |
| 1.3 | Schematic structure of a MTJ and comparison of the evolution of the GMR and the TMR effect over 35 years | 3 |
| 3.1 | Schematic drawing of an incoming and two outgoing, one reflected and one transmitted wave through a mesoscopic system | 21 |
| 3.2 | Schematic drawing of a two-terminal device composed of two semi-infinite electrodes and a central region | 26 |
| 3.3 | Schematic drawing of the integration contours for the retarded and advanced Green’s function | 33 |
| 4.1 | Schematic drawing of the DOS of a half-metallic magnet, a type-I spin-gapless semiconductor, and a type-II spin-gapless semiconductor | 37 |
| 4.2 | Structure adapted by half, full, and quaternary Heusler alloys | 38 |
| 4.3 | Top and side view of the trigonal prismatic and octahedral structure of two-dimensional transition-metal dichalcogenides | 41 |
| 5.1 | Two-current model for parallel and anti-parallel orientation of the magnetization of the electrodes of a magnetic tunnel junction | 44 |
| 5.2 | Schematic drawing of the spin-torque diode effect | 46 |
| 5.3 | Schematic band diagram of a magnetic tunnel diode and corresponding $I - V$ curve | 47 |
| 5.4 | Schematic drawing of the resonant spin tunnel diode and corresponding differential conductance as a function of the applied bias voltage | 48 |
| 5.5 | Schematic drawing of a reconfigurable magnetic tunnel diode together with the corresponding current-voltage characteristics | 49 |
| 5.6 | Schematic drawing of an Ohmic spin diode in parallel and anti-parallel orientation of the magnetization of the electrodes and the corresponding $I - V$ curves | 50 |
| 5.7 | Schematic representation of the Datta-Das transistor | 51 |
| 5.8 | Schematic drawing of a spinFET | 52 |
| 5.9 | Schematic drawing of the operation principle of a spin-valve and magnetic tunnel transistor | 53 |
| 5.10 | Schematic picture of a reconfigurable magnetic tunnel transistor together with its band diagram. | 55 |
| 6.1 | Comparison of the lattice parameters for type-II SGSs and for HMMs as well as type-I SGSs within the family of quaternary Heusler compounds and their Curie temperatures | 58 |
| 6.2 | Schematic representation of the MTJ based on a HMM and a SGS together with the dependency of the TMR effect on the bias voltage. | 72 |
| 6.3 | Schematic representation of the Ohmic spin diode for parallel oriented electrode magnetization and schematic DOS of the HMM and SGS material together with the corresponding $I - V$ characteristics | 88 |
| 6.4 | Calculated $I - V$ curves of four suggested OSDs based on quaternary Heusler compounds | 103 |

List of abbreviations

| | |
|-------------|---|
| AE | all-electron |
| CMOS | complementary metal-oxide-semiconductor |
| DFT | density functional theory |
| DOS | density of states |
| FET | field-effect transistor |
| GF | Green's function |
| GGA | generalized gradient approximation |
| GMR | giant magnetoresistance |
| GTO | Gaussian-type orbital |
| HMM | half-metallic magnet |
| LCAO | linear combination of atomic orbitals |
| LDA | local density approximation |
| MRAM | magnetic random access memory |
| MTD | magnetic tunnel diode |
| MTJ | magnetic tunnel junction |
| MTT | magnetic tunnel transistor |
| NEGF | non-equilibrium Green's functions |
| OSD | Ohmic spin diode |
| PBE | Perdew-Burke-Ernzerhof |
| PP | pseudopotential |
| SCF | self-consistent field |
| SGS | spin-gapless semiconductor |
| STO | Slater-type orbital |
| TMR | tunnel magnetoresistance |
| USPP | ultrasoft pseudopotential |

1 Introduction

In 1965, Moore found out that the number of transistors in dense integrated circuits is doubled every 24 months [1] and similarly there is an exponential increase in the ability to store digital data (see Fig. 1.1). In 2011, Hilbert and Lopez studied the evolution in the world's storage capacity where they took all different types of devices known in the whole world into account [2]. In Fig. 1.1, we see that there is not only an exponential increase in the storage capacity but also there is, especially in the last decade under study, a transformation from an analog form like books, newsprints, films, and videotapes to digital devices like CDs, DVDs, and hard disk drives. And this digital form of storage devices has evolved extremely quickly which is attributed to the invention of spintronics.

In conventional electronics, electrons are used in two particular ways to store information. Either the charge of electrons is used in the form of the number of electrons that are stored in a capacitor, or one monitors currents, so one counts how many electrons are passing through a specific wire per unit of time. A different approach is to use the spin of the electrons and the directly associated magnetic moment of a material. The ability to store information by using magnetism, especially through the magnetization direction of materials, is already known since the middle of the 1950s when a very simple concept of a magnetic storage device, the so-called magnetic core memory (see Fig. 1.2), was introduced. Since the 2000s this concept arouses great interest.

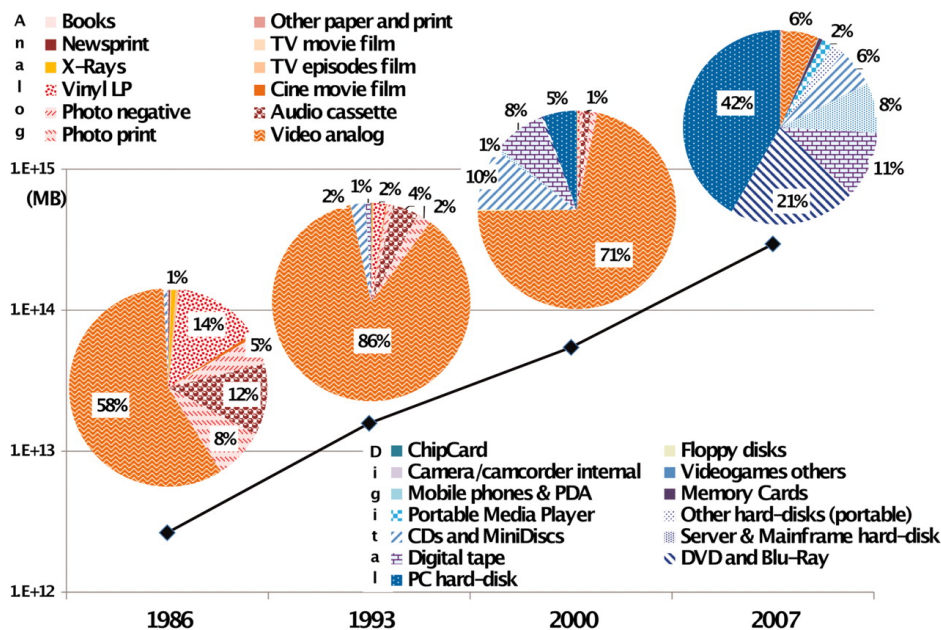


Figure 1.1: Evolution in the world's technological installed capacity to store information from 1986 to 2007. From M. Hilbert and S. Lopez Science **332**, 60 (2011); The World's Technological Capacity to Store, Communicate, and Compute Information, Ref. [2]. Reprinted with permission from AAAS.

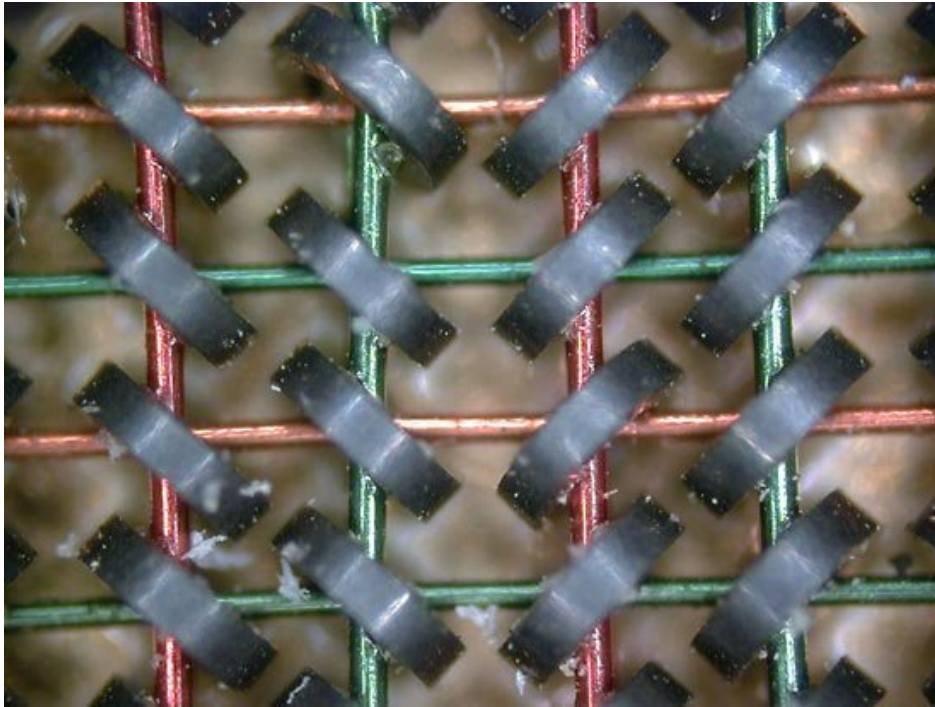


Figure 1.2: Representation of an early magnetic core memory. The grey rings consist of a soft magnetic material and the information is stored in the magnetization of these rings. They can be magnetized either clockwise or counterclockwise around the circumference by driving a current through the green or pink copper wires, respectively. Reprinted from H.J. Sommer III, Professor of Mechanical Engineering, Penn State University, Magnetic-core memory, accessed 15.02.2022; Ref. [3].

One major problem of the magnetic core memory was that it could not be scaled because shrinking copper wires would require large currents to change the magnetization (cf. Fig. 1.2). The main concepts inside the magnetic core memory are still used for fabricating storage devices using magnetism. At the end of the 1980s, Grünberg [4] and Fert [5] laid the foundation of spintronics with the discovery of the giant magnetoresistance (GMR) effect. This effect made it possible to fabricate very sensitive detectors for magnetic fields and thus increase the storage capacity of hard disk drives by a factor of more than 1000. Nowadays, the GMR structures in reading heads in hard disk drives are replaced by magnetic tunnel junctions (MTJs) (for the schematic structure of a MTJ and the associated equivalent resistor circuit diagram see Fig. 1.3(a)). The tunnel magnetoresistance (TMR) effect states that the resistance of magnetic layers separated by an insulator depends on the relative orientation of the magnetization of the magnetic layers to each other. It is already known since 1975 [6] but exceeded the GMR effect just in the 1990s (cf. Fig. 1.3(b)).

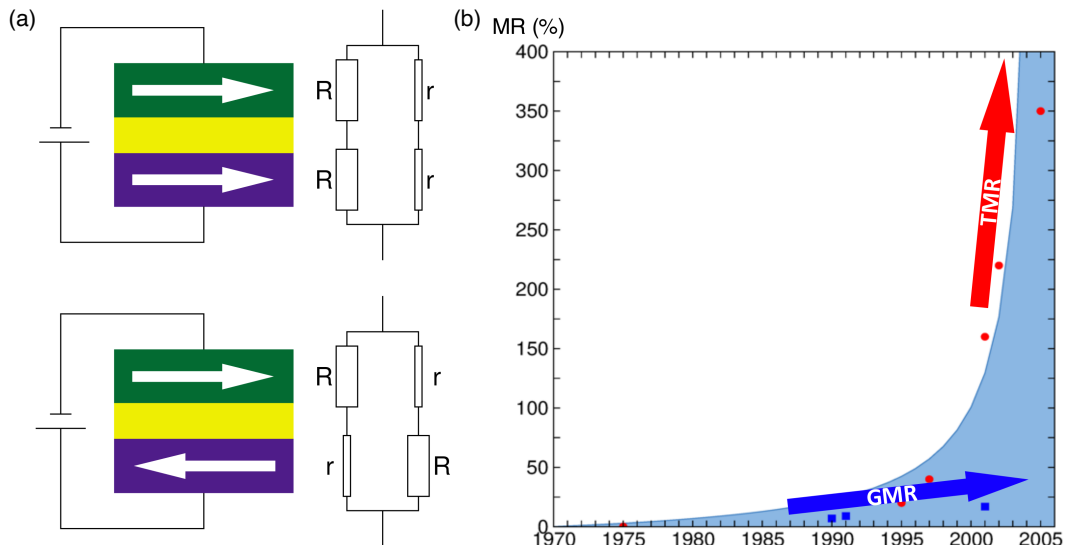


Figure 1.3: (a) Schematic structure of a MTJ in parallel (upper part) and anti-parallel (lower part) orientation of the magnetization of the electrodes together with the corresponding equivalent resistor circuit diagram. (b) Comparison of the evolution of the GMR and TMR effect over 35 years. In the 1990s the TMR effect exceeded the GMR effect.

The breakthrough of the TMR effect was in 2004 where Parkin *et al.* [7] realized a TMR effect of 200 % at room temperature by using MgO as a tunnel barrier. In spintronics development, MTJs played a crucial role since they are promising for many applications ranging from non-volatile memory devices, such as STT-MRAM and SOT-MRAM, to read-head sensors as mentioned above and from non-volatile logic concepts [8–10] to new computing architectures like logic-in-memory computing. Using half-metallic magnets (HMMs) as electrode materials led to the discovery of extremely large TMR effects due to the 100 % spin-polarization of the current. Replacing one of the electrodes in a MTJ with a spin-gapless semiconductor (SGS) gives rise to additional functionalities, i.e., an inverse TMR and diode effect as well as reconfigurability of the tunnel junction [11] making such devices extremely important for spintronic applications.

Based on this motivation, the major goals of the present thesis are:

1. Search for electrode materials that possess either spin-gapless or half-metallic properties with high Curie temperatures making them suitable for room temperature applications.
2. The computational design of MTJs based on HMM and SGS Heusler compounds and investigating their current-voltage characteristics and TMR ratio for magnetic memory and logic applications.
3. Proposing a new diode concept based on SGSs and HMMs analogous to the Schottky-

barrier diode (metal-semiconductor diode), the so-called Ohmic spin diode (OSD).

4. Designing OSDs based on quaternary Heusler alloys employing first-principle calculations.

Therefore, the following four chapters will lay the theoretical foundation for the results, which are presented in the cumulative part of the thesis. First, we provide the theoretical basis for the calculations. We introduce the many-body problem and the fundamentals of density functional theory, which allows us to investigate the electronic structure of materials very efficiently and reliably compared to experiments. Furthermore, we describe the method of choice to calculate electronic properties, which is based on linear combinations of atomic orbitals as basis-set combined with pseudopotentials. In the third part, we discuss electronic transport. There, we describe the Landauer-Büttiker formalism and derive the non-equilibrium Green's function method which is a common approach to calculate the charge densities and current in nanoscale devices. Afterwards, we expound the half-metallic and spin-gapless semiconducting properties of two material classes which arouse substantial interest for spintronic device application, i.e. Heusler alloys and two-dimensional materials. Then, in Chapter 5, we present an overview of spintronic devices. We outline the basic phenomenon of spintronics, the GMR and TMR effect, and elucidate the operation principle of a few selected spintronic diodes and transistors. In the final part, we chose four publications, each addressing one of the goals as stated above, to present our obtained results. Finally, we conclude the thesis with a summary and a brief outlook.

2 Electronic structure

To characterize the devices under study, which are introduced in the results part (Chapter 6), we need to solve the many-body problem. Therefore, in this chapter, we will briefly present the many-body problem and the Born-Oppenheimer approximation. Afterwards, we will explain the fundamentals of density functional theory (DFT), the most common approach to solve the many-body problem. We elucidate its theoretical background, the Hohenberg-Kohn theorem, and the Kohn-Sham scheme. Then, we introduce the so-called Jacob's ladder and present the most used approximations of the exchange and correlation functional in material science. Subsequently, we demonstrate how the method can be used for spin-polarized systems, and finally, we present a basis-set approach solving the Kohn-Sham equations as well as the pseudopotential method.

2.1 Many-body problem

The fundamental problem in solid-state physics starts with the interaction of N electrons at position \mathbf{r} with M nuclei at site \mathbf{R} . In quantum mechanics, this interaction can be described by the Hamiltonian

$$\begin{aligned} \hat{H} = & - \sum_i \frac{\hbar^2}{2m_e} \nabla_i^2 - \sum_I \frac{\hbar^2}{2M_I} \nabla_I^2 + \frac{1}{8\pi\epsilon_0} \sum_{i \neq j} \frac{e^2}{|\mathbf{r}_i - \mathbf{r}_j|} \\ & + \frac{e^2}{4\pi\epsilon_0} \sum_{I,i} \frac{Z_I}{|\mathbf{r}_i - \mathbf{R}_I|} + \frac{e^2}{8\pi\epsilon_0} \sum_{I \neq J} \frac{Z_I Z_J}{|\mathbf{R}_I - \mathbf{R}_J|}. \end{aligned} \quad (2.1)$$

Here the lowercase subscripts mark the electrons with mass m_e and charge e while the uppercase subscripts denote the nuclei with mass M and charge Ze .

To simplify equations, we will adopt atomic units throughout this thesis ($e = m_e = \hbar = 4\pi\epsilon_0 = 1$). The first term in Eq. (2.1) represents the kinetic energy operator of the electrons

$$\hat{T}_e = -\frac{1}{2} \sum_i^N \nabla_i^2, \quad (2.2)$$

while the second term defines the kinetic energy operator of the nuclei

$$\hat{T}_n = -\frac{1}{2} \sum_I^M \frac{1}{M_I} \nabla_I^2. \quad (2.3)$$

The third is the electron-electron interaction operator

$$\hat{U}_{ee} = \frac{1}{2} \sum_{i \neq j}^N u(\mathbf{r}_i, \mathbf{r}_j) = \frac{1}{2} \sum_{i \neq j}^N \frac{1}{|\mathbf{r}_i - \mathbf{r}_j|}. \quad (2.4)$$

The fourth term, which is known as the potential operator, represents the interaction between the electrons and the nuclei

$$\hat{V}_{en} = \sum_{i,I}^{N,M} v(\mathbf{r}_i, \mathbf{R}_I) = \sum_{i,I}^{N,M} \frac{Z_I}{|\mathbf{r}_i - \mathbf{R}_I|}, \quad (2.5)$$

and the last term is the so-called nuclei-nuclei interaction operator

$$\hat{U}_{nn} = \frac{1}{2} \sum_{I \neq J}^M \frac{Z_I Z_J}{|\mathbf{R}_I - \mathbf{R}_J|}. \quad (2.6)$$

Since the Hamiltonian (Eq. (2.1)) is time-independent, the time-dependent wavefunction can be rewritten by the product of a time-dependent phase modulation factor (e^{-iEt}) and the time-independent part of the wavefunction. Hereby, we end up with the stationary Schrödinger equation

$$\hat{H}\Psi = E\Psi, \quad (2.7)$$

where E denotes the energy. Unfortunately, determining the ground state of the system by solving the corresponding Schrödinger equation is numerically impossible. However, as the electron mass is rather small compared to the mass of the nuclei ($M \sim 10^3 \cdot m_e$), the characteristic nuclei kinetic energy (Eq. (2.3)) is orders of magnitude smaller than the one of the electrons. Thus, a common assumption is that the electrons move adiabatically with the nuclei leading to the Born-Oppenheimer approximation [12]. There we assume that the electrons just respond to a stationary potential and hence a product ansatz for the total wavefunction allows us to split the Hamiltonian (Eq. (2.1)) into an electronic Hamiltonian

$$\hat{H}_{el} = \hat{T}_e + \hat{U}_{ee} + \hat{V}_{ext}, \quad (2.8)$$

and a Hamiltonian for the nuclei

$$\hat{H}_n = \hat{T}_n + \hat{U}_{nn}. \quad (2.9)$$

Despite the simplification from the Born-Oppenheimer approximation, these two equations are still too difficult to solve for an appropriate number of electrons and nuclei. Usually, for the electronic structure, the electronic Hamiltonian is further simplified while the equation for the nuclei is neglected. Before jumping now to the methods of how one can solve the Schrödinger equation for the electronic system, it is necessary to understand how to calculate the fundamental properties in electronic structure theory, i.e., the ground-state energy and the electron density. The first quantity, the total energy, is defined as the expectation value

of the Hamiltonian

$$E = \frac{\langle \Psi | \hat{H}_{el} | \Psi \rangle}{\langle \Psi | \Psi \rangle}. \quad (2.10)$$

Thus, by definition, the ground-state wavefunction Ψ_0 of a system is related to the lowest energy. Consequently, for the ground state, the variation of the energy functional has to be stationary and as a result, we end up with the ground-state Schrödinger equation

$$\frac{\delta E[\Psi_0]}{\delta \Psi_0^*} = \frac{H_{el} \Psi_0}{\langle \Psi_0 | \Psi_0 \rangle} - \frac{\langle \Psi_0 | \hat{H}_{el} | \Psi_0 \rangle \Psi_0}{\langle \Psi_0 | \Psi_0 \rangle^2} = 0 \Leftrightarrow H_{el} \Psi_0 = E_0 \Psi_0. \quad (2.11)$$

In the same way, one can define the electron density $n(\mathbf{r})$ as the expectation value of the electron density operator

$$\hat{n} = \sum_i^N \delta(\mathbf{r} - \mathbf{r}_i), \quad (2.12)$$

and thus the electron density reads

$$n(\mathbf{r}) = \frac{\langle \Psi | \hat{n} | \Psi \rangle}{\langle \Psi | \Psi \rangle} = N \frac{\int d^3r_2 \dots d^3r_N |\Psi(\mathbf{r}, \mathbf{r}_2, \dots, \mathbf{r}_N)|^2}{\int d^3r_1 d^3r_2 \dots d^3r_N |\Psi(\mathbf{r}_1, \mathbf{r}_2, \dots, \mathbf{r}_N)|^2}. \quad (2.13)$$

2.2 Density functional theory

The goal of DFT is determining the ground state energy E_0 and the electron densities $n(\mathbf{r})$ for a large number of interacting electrons, which is the fundamental problem of modern solid-state physics. For that, let us first explain briefly why determining the ground state by solving the equation $\hat{H}_{el} \Psi = E \Psi$ is unfeasible. One reason is that the computational cost to solve this equation scales exponentially with the number of electrons. Another reason is that the many-body wavefunction contains more information than necessary. To clarify this, we would like to present the example of Ref. [13]. The oxygen atom has 8 electrons and thus, even when we neglect the spin, the wavefunction of the oxygen atom depends on 24 coordinates; 3 spatial coordinates per electron. To solve this problem we need either a basis set or the discretization of space. If we now consider a rather small grid with 10 points per coordinate, we need 10^{24} numbers to represent the wavefunction. As usual, these numbers are stored as floating points, with 64 bits (= 8 byte) each. Thus, to store this wavefunction would require $8 \cdot 10^{12}$ TB of storage capacity. Fortunately, Thomas and Fermi suggested in the late 1920s to consider the electron density as the central variable instead of the many-particle wavefunction and thus regard the energy as a functional of the free-electron charge-density [14–16]. The authors describe the electrons as a classical liquid and their kinetic energy is approximated

using a functional of the density. Due to particular shortcomings, it is impossible to describe the properties of molecules and solids qualitatively within this method. Thus, Dirac improved the theory in 1930 by adding a term for the exchange energy [17], which was neglected in the Thomas-Fermi model. However, nearly forty years later, Hohenberg and Kohn introduced a powerful theorem based on the idea to describe the many-particle problem in terms of the one-electron charge-density [18].

Please note that there are many other theories for solving the many-particle problem like the Hartree-Fock [19, 20] approximation, coupled clusters [20], many-body perturbation theory [21–24], in particular the Bethe-Salpeter equation [25], and the GW approximation [26], and full configuration interaction [20], but DFT is the most efficient for solids.

2.2.1 Hohenberg-Kohn theorem

Modern DFT is based on two Hohenberg-Kohn theorems [19, 27–29]. The first one states that for a given ground-state electron density n_0 , the external potential \hat{V}_{ext} is a unique functional of this electron density apart from an additive constant and hence two mappings A and B between the external potential, ground-state wavefunction Ψ_0 and ground-state electron density are bijective

$$\{\hat{V}_{ext}\} \xleftrightarrow{A} \{\Psi_0\} \xleftrightarrow{B} \{n_0\}. \quad (2.14)$$

This means that there is a one-to-one correspondence between the external potential and the ground-state electron density. Since the Hamiltonian and the wavefunctions provide full knowledge of the ground-state density, we can now write the expectation value of any observable \hat{O} as a functional of the ground-state density

$$O_0 = O[n_0] = \langle \Psi_0[n_0] | \hat{O} | \Psi_0[n_0] \rangle. \quad (2.15)$$

This relation holds especially for the energy functional.

The second Hohenberg-Kohn theorem states that for any external potential or number of particles one can define a universal functional of the electron density $F[n]$. This means, in particular, that for a certain external potential \hat{V} an energy functional of the electron density $E[n]$ can be defined and the ground-state electron density is the electron density that minimizes this functional. A proof of both theorems can be found in Refs. [30], [31], and [27]. In general, the energy functional can be defined as follows:

$$E[n(\mathbf{r})] = \int d^3r V_{ext}(\mathbf{r})n(\mathbf{r}) + F[n(\mathbf{r})] = \int d^3r V_{ext}(\mathbf{r})n(\mathbf{r}) + \langle \Psi | \hat{T}_e + \hat{U}_{ee} | \Psi \rangle \quad (2.16)$$

It is worth noting that for the ground-state density this functional equals the ground-state

energy of the system, which leads us to

$$E[n_0(\mathbf{r})] = \min_{n(\mathbf{r})} E[n(\mathbf{r})] \leq E[n(\mathbf{r})]. \quad (2.17)$$

Unfortunately, the proof of this theorem by Hohenberg and Kohn is restricted to electron densities $n(\mathbf{r})$ that are the ground-state electron densities $n_0(\mathbf{r})$ of H_{el} with a certain potential. However, as many reasonable densities do not fulfill this requirement, different formulations for the Hohenberg-Kohn functional were developed by Levy [32–34] and Lieb [34–36]. In general, they split the minimization procedure into two parts. As a first step we minimize the energy over the set of wavefunctions with a fixed density $n(\mathbf{r})$

$$E_{LL}[n(\mathbf{r})] = \int d^3r V_{ext}(\mathbf{r})n(\mathbf{r}) + \min_{\Psi \rightarrow n(\mathbf{r})} \langle \Psi | \hat{T}_e + \hat{U}_{ee} | \Psi \rangle. \quad (2.18)$$

By this procedure, we arrive at the lowest energy for a given density and thus the ground-state density can be observed by minimizing this energy functional

$$E_0 = \min_{\{n\}} E_{LL}[n(\mathbf{r})]. \quad (2.19)$$

In a second step, we use the Lagrange multiplier μ to ensure particle number conservation

$$\delta E = \delta \left\{ F[n(\mathbf{r})] \int d^3r V_{ext}(\mathbf{r})n(\mathbf{r}) - \mu \left(\int d^3r n(\mathbf{r}) - N \right) \right\} = 0. \quad (2.20)$$

Taking the functional derivative of Eq. (2.20) with respect to the density leads to the Euler-Lagrange equation

$$\frac{\delta F[n(\mathbf{r})]}{\delta n} + V_{ext}(\mathbf{r}) - \mu = 0. \quad (2.21)$$

Thus, using the formalism of Levy and Lieb we can calculate the ground-state energy for any density received from a wavefunction Ψ for N -electrons. Since all reasonable densities are N -representable [19, 37], the Levy-Lieb formulation provides a general rule for the calculation of the ground-state energy using the electron density. Consequently, with the Hohenberg-Kohn theorems, we ensured that the electron density is sufficient to calculate all characteristics of a system and we arrived at an equation for the ground-state energy of a many-electron system involving only functionals or derivatives of functionals of the electron density. However, up to now only the functional dependency of the external potential, usually the potential of the nuclei, is given. Accordingly, a subsequent approach was proposed by Kohn and Sham [38] which is presented in the next section.

2.2.2 Kohn-Sham scheme

Kohn and Sham paved the way for the success of DFT by presenting an approach that is partially based on a single Slater determinant. The fundamental idea is to map the original many-electron problem onto an auxiliary system of non-interacting particles moving in an effective potential V_{eff} [38]. Therefore, we have to consider the following hypothesis: it exists a fictitious system of non-interacting particles whose ground-state density is equal to the ground-state electron density of the original system. For such an auxiliary system with N electrons, the ground-state wavefunction can be expressed as a Slater determinant of non-interacting single-particle orbitals

$$\Psi(\mathbf{x}_1, \mathbf{x}_2, \dots, \mathbf{x}_N) = \frac{1}{\sqrt{N!}} \begin{vmatrix} \varphi_1(\mathbf{x}_1) & \varphi_2(\mathbf{x}_1) & \dots & \varphi_N(\mathbf{x}_1) \\ \varphi_1(\mathbf{x}_2) & \varphi_2(\mathbf{x}_2) & \dots & \varphi_N(\mathbf{x}_2) \\ \vdots & \vdots & \ddots & \vdots \\ \varphi_1(\mathbf{x}_N) & \varphi_2(\mathbf{x}_N) & \dots & \varphi_N(\mathbf{x}_N) \end{vmatrix}, \quad (2.22)$$

where the orbital wavefunctions φ_i satisfy the Schrödinger equation

$$\left[-\frac{1}{2} \nabla^2 + V_{eff}[n](\mathbf{r}) \right] \varphi_i(\mathbf{r}) = \epsilon_i \varphi_i(\mathbf{r}). \quad (2.23)$$

Thus, the energy functional reads

$$E_S[n] = T_S[n] + \int d^3r V_{eff}(\mathbf{r})n(\mathbf{r}). \quad (2.24)$$

According to Eq. (2.21), the variation of Eq. (2.24) results in

$$\frac{\delta T_S[n]}{\delta n(\mathbf{r})} + V_{eff}[n](\mathbf{r}) - \mu_S = 0. \quad (2.25)$$

Here T_S denotes the non-interacting kinetic energy term and μ_S the Lagrange multiplier. Now the essential element is rearranging the terms in the energy functional of Hohenberg and Kohn (Eq. (2.16)) in the way that we obtain the equation above.

$$\begin{aligned} E[n] &= T[n] + U_{ee}[n] + \int d^3r V_{ext}(\mathbf{r})n(\mathbf{r}) \\ &= T_S[n] + (T[n] - T_S[n]) + E_H[n] + (U_{ee}[n] - E_H[n]) + \int d^3r V_{ext}(\mathbf{r})n(\mathbf{r}) \\ &= T_S[n] + E_H[n] + E_{xc}[n] + \int d^3r V_{ext}(\mathbf{r})n(\mathbf{r}). \end{aligned} \quad (2.26)$$

In this equation, $E_H[n]$ constitutes the classical Coulomb interaction, as well as their self-interaction. It is also known as the Hartree energy

$$E_H[n] = \frac{1}{2} \int \int d^3r d^3r' \frac{n(\mathbf{r})n(\mathbf{r}')}{|\mathbf{r} - \mathbf{r}'|}. \quad (2.27)$$

$E_{xc}[n]$ represents the exchange-correlation energy functional

$$E_{xc}[n] = T[n] - T_S[n] + U_{ee}[n] - E_H[n]. \quad (2.28)$$

It is worth noting that the rearrangement in Eq. (2.26) is only valid when the ground-state density of the interacting many-particle system can be mapped onto the ground-state density of the auxiliary system of non-interacting particles. Under the rearrangement, the Euler-Lagrange equation (2.21) becomes

$$\frac{\delta T_S[n]}{\delta n(\mathbf{r})} + V_{ext}(\mathbf{r}) + V_H[n](\mathbf{r}) + V_{xc}[n](\mathbf{r}) - \mu = 0 \quad (2.29)$$

and thus it turns out that the equations (2.25) and (2.29) are equivalent when

$$\begin{aligned} V_{eff}[n](\mathbf{r}) &= V_{ext}(\mathbf{r}) + V_H[n](\mathbf{r}) + V_{xc}[n](\mathbf{r}) - (\mu - \mu_S) \\ &= V_{ext}(\mathbf{r}) + V_H[n](\mathbf{r}) + V_{xc}[n](\mathbf{r}). \end{aligned} \quad (2.30)$$

Here the difference between the Lagrange multipliers μ and μ_S was embedded in the exchange-correlation term $V_{xc}(\mathbf{r})$. In this way, the variation of the energy functional (Eq. (2.26)) with respect to the density of the fictitious system leads directly to the well-known Kohn-Sham equations

$$\left[-\frac{1}{2}\nabla^2 + V_{ext}(\mathbf{r}) + V_H[n](\mathbf{r}) + V_{xc}[n](\mathbf{r}) \right] \varphi_i(\mathbf{r}) = \epsilon_i \varphi_i(\mathbf{r}). \quad (2.31)$$

The potential V_H indicates a Hartree-like repulsion

$$V_H[n](\mathbf{r}) = \int d^3r' \frac{n(\mathbf{r}')}{|\mathbf{r} - \mathbf{r}'|}, \quad (2.32)$$

while the exchange-correlation potential $V_{xc}[n](\mathbf{r})$ is defined as the functional derivative of the related energy counterpart

$$V_{xc}[n](\mathbf{r}) = \frac{\delta E_{xc}[n]}{\delta n(\mathbf{r})}. \quad (2.33)$$

Finally, in the representation of the non-interacting single-electron wavefunctions φ_i , the electronic density becomes

$$n(\mathbf{r}) = \sum_{\alpha}^{occ.} |\varphi_{\alpha}(\mathbf{r})|^2. \quad (2.34)$$

Basically, within the Born-Oppenheimer approximation, Kohn and Sham found an exact solution for the many-particles problem that no longer contains wavefunctions of the interacting many-electron system. The ground-state electron density can now be calculated using single-electron wavefunctions that fulfill a Schrödinger-like equation, but with an unknown exchange-correlation potential which prevents us from solving Eq. (2.31). Thus, in modern DFT the main challenge is finding suitable approximations for the potential $V_{xc}[n](\mathbf{r})$ [39, 40].

2.2.3 Exchange-correlation energy functional

As a first step, the exchange-correlation energy functional in Kohn-Sham DFT is split into an exchange (E_x) term and a correlation part (E_c) as

$$E_{xc}[n] = E_x[n] + E_c[n] = \int d^3r n(\mathbf{r}) [\varepsilon_x(n(\mathbf{r})) + \varepsilon_c(n(\mathbf{r}))]. \quad (2.35)$$

Throughout this section, ε_{α} denotes the energy density of the system. Furthermore, the two functionals, E_x and E_c , can be defined as follows [41]

$$E_x[n] = \langle \Phi_S[n] | \hat{U}_{ee} | \Phi_S[n] \rangle - \frac{1}{2} \int \int d^3r d^3r' \frac{n(\mathbf{r})n(\mathbf{r}')}{|\mathbf{r} - \mathbf{r}'|} \quad (2.36)$$

and

$$E_c[n] = \langle \Psi[n] | \hat{T} + \hat{V}_{ext} + \hat{U}_{ee} | \Psi[n] \rangle - \langle \Phi_S[n] | \hat{T} + \hat{V}_{ext} + \hat{U}_{ee} | \Phi_S[n] \rangle. \quad (2.37)$$

$|\Phi_S[n]\rangle$ represents the Kohn-Sham wavefunction while $|\Psi[n]\rangle$ stands for the ground-state wavefunction of the real interacting system with density $n(\mathbf{r})$. Nevertheless, an exact mathematical expression of these energy functionals, which describe the many-particle interactions, is unknown. In principle, an explicit form could be constructed by solving all possible systems, but this attempt is obviously unfeasible. Thus, to calculate the ground-state energy of the interacting system, approximations are necessary. Due to this, over the last decades, several exchange and correlation functionals were developed [42–45]. However, the major difficulty in designing new functionals is that the addition of more parameters which make the functional more flexible or satisfy more constraints does not guarantee an improvement in describing the interactions across chemical environments. Thus, a systematical improve-

ment of the exchange-correlation energy functional is impossible. To characterize functionals, Perdew presented a hierarchy called "Jacob's ladder" [46] which starts at the bottom with the Hartree approximation, where only the classical electron interaction is taken into account and other remaining exchange and correlation energies are neglected. Every rung thereafter represents an additional ingredient to the functional and in the end the ladder results in the divine functional. The first two rungs of this ladder represent the two most common parametrizations in modern DFT, which are the local density approximation (LDA) and the generalized gradient approximation (GGA). Historically, the most important approximation is LDA which was first suggested by Kohn and Sham [38], where the exchange-correlation functional reads

$$E_{xc}^{LDA} = \int d^3r n(\mathbf{r}) \varepsilon_{xc}^{uniform}(|n(\mathbf{r})|). \quad (2.38)$$

Here $\varepsilon_{xc}^{uniform}$ stands for the exchange-correlation energy of a uniform electron liquid per volume [28].

Additionally, GGAs include the gradient of the density and are of the general form

$$E_{xc}^{GGA} = \int d^3r f(n_\sigma(\mathbf{r}), \nabla n_\sigma(\mathbf{r})). \quad (2.39)$$

It turns out that, in comparison with LDAs, GGAs tend to improve the results for ionization energies, total energies, and geometrical energy differences. Obviously, GGA considers inhomogeneities in the density more than LDA can. A drawback of both, LDA and GGA, is the systematic underestimation of band gaps in insulators and semiconductors [47]. Advanced approaches, such as LDA+U [48], self-interaction correction (SIC) [37, 49], and the application of semi-local exchange-correlation potentials [50] as well as self-energy corrections (GW) [51] lead to accurate band gap widths compared to the experiments. In defiance of the success of LDA and GGA, the challenge in finding new improvements in exchange-correlation functionals goes on. So, with the inclusion of the Laplacian and similar quantities, the so-called meta-GGA, the step on the third rung was already made. The fourth rung was reached with a different approach, i.e., applying terms with a dependency on the occupied Kohn-Sham orbitals. This can be done in different manners, e.g. by mixing a fraction of the exact exchange to other functionals, leading to the so-called hybrid functionals [52]. Among all functionals, the one introduced by Perdew, Burke, and Ernzerhof (PBE) [53] stands out since it is the most popular functional in material science and used for all calculations within this thesis. This is caused by many reasons, e.g. hybrid functionals, which offer the most accurate description for the exchange and correlation energy, are computationally rather demanding calculations since they require the calculation of the exact exchange. PBE, in fact, is computationally very efficient and provides, besides other properties, reasonable results for

the lattice constants and energies. In this approximation, the exchange part reads [53]

$$E_x^{PBE}[n(\mathbf{r})] = - \int d^3r n(\mathbf{r}) \frac{3k_F}{4\pi} F_x(s) \quad (2.40)$$

with

$$F_x(s) = 1 + k - \frac{k}{(1 - \mu s^2/k)} \quad (2.41)$$

where k and μ are constants, i.e. $k = 0.804$ and $\mu = 0.21951$. s names a dimensionless gradient and is defined as

$$s = \frac{|\nabla n(\mathbf{r})|}{2k_F n(\mathbf{r})}. \quad (2.42)$$

The correlation part is given by [53]

$$E_c^{PBE}[n(\mathbf{r})] = \int d^3r n(\mathbf{r}) \left[\varepsilon_c^{uniform} + H(r_S, \zeta, t) \right]. \quad (2.43)$$

r_s denotes the local Seiz radius ($n(\mathbf{r}) = 3/(4\pi r_s) = k_F^3/3\pi^2$), $\zeta = (n_\uparrow(\mathbf{r}) - n_\downarrow(\mathbf{r}))/n(\mathbf{r})$ the spin polarization, and $t = |\nabla n(\mathbf{r})|/(2\phi(\zeta)k_s n(\mathbf{r}))$ another dimensionless density gradient. Furthermore, $k_s = \sqrt{4k_F/(\pi a_0)}$ marks the Thomas-Fermi screening wave number and $\phi(\zeta) = [(1 + \zeta)^{\frac{2}{3}} + (1 - \zeta)^{\frac{2}{3}}]/2$ is a spin-scaling factor. With this, $H(r_S, \zeta, t)$ reads

$$H(r_S, \zeta, t) = \frac{\gamma \phi^3(\zeta)}{a_0} \ln \left[1 + \frac{\beta t^2}{\gamma} \cdot \frac{1 + At^2}{1 + At^2 + A^2 t^4} \right] \quad (2.44)$$

with

$$A = \frac{\beta}{\gamma} \left[\exp \left\{ -\frac{\varepsilon_c^{uniform} a_0}{\gamma \phi^3(\zeta)} \right\} - 1 \right]^{-1} \quad (2.45)$$

and the constants $\beta \approx 0.066725$ and $\gamma = (1 - \ln 2)/\pi^2 \approx 0.031091$.

Nevertheless, since all known exchange-correlation functionals are just approximations, one has to compare, in the end, the calculated results with experimental data.

2.3 Extension to spin-polarized systems

So far, we discussed the formulation of DFT for non-magnetic (non-spin-polarized) systems. Due to the fact that the spin polarization leads to a magnetization density $\mathbf{m}(\mathbf{r})$ and the magnetization $\mathbf{m}[n(\mathbf{r})]$ is a functional of the ground-state electron density $n(\mathbf{r})$, in principle, application of DFT to magnetic systems is possible.

This extension of DFT to the spin polarized case was done by von Barth and Hedin in 1972 [54]. The authors defined the energy functional in terms of the spin density matrix $\rho_{\alpha\beta}(\mathbf{r})$ which is given by

$$\rho_{\alpha\beta}(\mathbf{r}) = n(\mathbf{r})\delta_{\alpha\beta} + (\mathbf{m}(\mathbf{r}) \cdot \boldsymbol{\sigma})_{\alpha\beta}, \quad (2.46)$$

where $\delta_{\alpha\beta}$ denotes the Kronecker delta and $\boldsymbol{\sigma} = (\sigma_x, \sigma_y, \sigma_z)$ are the Pauli matrices.

To describe the vector field $\mathbf{m}(\mathbf{r})$ in the notation of DFT, we have to generalize the concept of the Kohn-Sham orbitals. In the non-polarized case, the orbitals are scalar functions while for the description of a general magnetization density with single-particle wavefunctions, we have to use a representation with two-component spinors

$$\Psi_i(\mathbf{r}) = \begin{bmatrix} \varphi_{i\alpha}(\mathbf{r}) \\ \varphi_{i\beta}(\mathbf{r}) \end{bmatrix}, \quad (2.47)$$

where $\varphi_{i\alpha}$ and $\varphi_{i\beta}$ indicate the two spin projections. Using these two-component spinors, the spin density matrix can be written as

$$\rho(\mathbf{r}) = \sum_i^{occ.} \begin{bmatrix} \varphi_{i\alpha}(\mathbf{r}) \\ \varphi_{i\beta}(\mathbf{r}) \end{bmatrix} \begin{bmatrix} \varphi_{i\alpha}(\mathbf{r}) & \varphi_{i\beta}(\mathbf{r}) \end{bmatrix}^* = \sum_i^{occ.} \begin{bmatrix} \varphi_{i\alpha}(\mathbf{r})\varphi_{i\alpha}^*(\mathbf{r}) & \varphi_{i\alpha}(\mathbf{r})\varphi_{i\beta}^*(\mathbf{r}) \\ \varphi_{i\beta}(\mathbf{r})\varphi_{i\alpha}^*(\mathbf{r}) & \varphi_{i\beta}(\mathbf{r})\varphi_{i\beta}^*(\mathbf{r}) \end{bmatrix}. \quad (2.48)$$

For collinear ferromagnets, the non-diagonal elements of this spin density matrix become zero.

In addition, using spinors, the magnetization density $\mathbf{m}(\mathbf{r})$ and electron density $n(\mathbf{r})$ can be expressed as

$$\mathbf{m}(\mathbf{r}) = \mu_B \sum_i^{occ.} \Psi_i^\dagger(\mathbf{r}) \boldsymbol{\sigma} \Psi_i(\mathbf{r}) \quad (2.49)$$

and

$$n(\mathbf{r}) = \sum_i^{occ.} \Psi_i^\dagger(\mathbf{r}) \mathbf{I} \Psi_i(\mathbf{r}), \quad (2.50)$$

where μ_B stands for the Bohr magneton and \mathbf{I} represents the unit matrix. As described in Ref. [54], with the spin density matrix, all ground-state properties of a magnetic system can be determined. Especially, the total energy is a unique functional of that spin density matrix and reaches its minimum for the ground-state value. Thus, as a first step, we have to calculate the total energy as a functional of the spin density matrix and afterwards apply the variation principle to find the minimum. For the spin-polarized case, the energy functional

is defined as

$$E[\rho] = T[\rho] + \frac{1}{2} \int d^3r d^3r' \frac{n(\mathbf{r})n'(\mathbf{r}')}{|\mathbf{r} - \mathbf{r}'|} + \sum_{\alpha,\beta} \int d^3r V_{\alpha\beta}^{ext}(\mathbf{r})\rho_{\alpha\beta}(\mathbf{r}) + E_{xc}[\rho]. \quad (2.51)$$

Accordingly, the single-particle Kohn-Sham equations can be written in the same way as in the non-polarized case

$$\sum_{\beta} \left[\delta_{\alpha\beta} \frac{1}{2} \nabla^2 + V_{\alpha\beta}^{eff}(\mathbf{r}) \right] \varphi_{i\beta}(\mathbf{r}) = \delta_{\alpha\beta} \epsilon_i \varphi_{i\beta}(\mathbf{r}). \quad (2.52)$$

Here the effective potential matrix elements $V_{\alpha\beta}^{eff}$ are defined as

$$V_{\alpha\beta}^{eff} = V_{\alpha\beta}^{ext}(\mathbf{r}) + \delta_{\alpha\beta} \int d^3r' \frac{n(\mathbf{r}')}{|\mathbf{r} - \mathbf{r}'|} + V_{\alpha\beta}^{xc}(\mathbf{r}), \quad (2.53)$$

where the exchange-correlation potential matrix elements read

$$V_{\alpha\beta}^{xc}(\mathbf{r}) = \frac{\delta E_{xc}[\rho]}{\delta \rho_{\alpha\beta}(\mathbf{r})}. \quad (2.54)$$

2.4 Basis sets

2.4.1 Linear combination of atomic orbitals

One way to solve the Kohn-Sham equations (Eq. (2.31) or (2.52)) is based on finding a proper basis set for the expansion of the wavefunction. Finkelstein and Horowitz proposed in 1928 a linear combination of atomic orbitals (LCAO) to describe the molecular orbital of the H_2^+ ion [55]. This method was further developed by Lennard-Jones who analyzed the bonding in diatomic molecules of the first main row of the periodic table with this technique [56]. More than 20 years later Roothaan introduced a generalized form of the LCAO approach for spin-polarized many-particle systems where the many-electron wavefunction was expressed as a linear combination of a set of unknown basis-functions [57]. Hence, in general, the wavefunction for every system can be written as

$$\Psi(\mathbf{r}) = \sum_i c_i \chi_i(\mathbf{r}). \quad (2.55)$$

Here the c_i 's are expansion coefficients that need to be determined by the self-consistent field (SCF) method and $\{\chi_i\}$ forms a complete set of functions. Basically, this expansion is infinite, but in practice, it is truncated after some steps.

2.4.2 Slater type orbitals

Slater-type orbitals (STOs) have been one of the first forms of basis functions and read [20, 58]

$$\chi(r) = \frac{(2\zeta/a_0)^{n+1/2}}{(2n)!} r^{n-1} e^{-\zeta r/a_0} Y_{lm}(\theta, \varphi). \quad (2.56)$$

Here Y_{lm} are the real spherical harmonics, ζ is the so-called orbital exponent which is related to the effective charge of the nucleus, r is the distance of the electron from the nucleus, and n , m , and l denote the quantum numbers.

Anyway, the exponential function in STOs is of hydrogen-like character and thus this description is the most natural for atomic structure calculations. However, the usage of STOs drastically increases the computation time since $K^4/8$ two-electron integrals have to be calculated within the SCF procedure. Thus, different descriptions for the atomic orbitals were developed which are presented in the next sections.

2.4.3 Gaussian type orbitals

In 1950, the usage of Gaussian-type orbitals (GTOs) was introduced by Boys, where one cartesian Gaussian orbital centered on atom μ reads [20, 59]

$$\chi(r) = N x_{\mu}^i y_{\mu}^k z_{\mu}^l \text{ with } N = \left(\frac{2\alpha}{\pi}\right)^{\frac{3}{4}} \left[\frac{(8\alpha)^{i+k+l} i! k! l!}{(2i)! (2k)! (2l)!}\right], \quad (2.57)$$

where α is a positive orbital exponent, and i , k , and l are non-negative integers. It is worth noting that such Cartesian GTOs have no quantum number n . Thus, every real orbital ($1s, 2s, \dots$) needs to be described by a linear combination of several GTOs with different orbital exponents.

As an alternative to the Cartesian representation, a spherical representation of the Gaussians is also possible

$$\chi(r) = N r_{\mu}^{n-1} e^{-\alpha r_{\mu}^2} \frac{1}{\sqrt{2}} (Y_l^{m*}(\theta, \varphi) \pm Y_l^m(\theta, \varphi)). \quad (2.58)$$

Here Y_l^m stands for the complex spherical harmonics.

Please note, in comparison to STOs, for small values of r , GTOs give poor representations of these atomic orbitals. Thus, a linear combination of multiple functions is very important. As a consequence, many more integrals are concerned in the calculations with GTOs than in the related STO calculations, but nevertheless, the calculation of these integrals takes less computation time. This is a consequence of the fact that the result of the product of two three-dimensional Gaussian functions is another Gaussian function around a shifted

center. As a result, the three- and four-center two-electron integrals are reduced to two-center integrals.

2.5 Pseudopotentials

Usually, multi-particle systems possess a large number of atoms or electrons and thus calculations of their electronic properties take up a lot of time. In consequence, sometimes a separation of the electrons into core- and valence-electrons on every atom is reasonable [60]. The total energy is then calculated as the sum of the core- and valence-electron energies.

A more sophisticated method is the so-called pseudopotential (PP) approach. Initially, the concept of PPs was developed to simplify electronic structure calculations by eliminating the inert core electrons within a frozen-core approximation [61, 62] and account only for the valence electrons. Usually, the structure and properties of the considered system are then sufficiently described by the valence electrons. The gist of the PP approach is to substitute the strong core potential, including all valence-core interactions, with a PP whose ground state wavefunction Ψ^{PS} reproduces the all-electron (AE) wavefunction Ψ^{AE} at and beyond a particular core radius r_C [19]. Following the derivation for the orthogonalized plane wave method (OPW) [63], the valence AE wavefunction Ψ_v^{AE} is augmented with core wavefunctions Ψ_c^{AE} to obtain finally the pseudo-wavefunction, which reads in Dirac notation

$$|\Psi_{v,i}^{PS}\rangle = |\Psi_{v,i}^{AE}\rangle + \sum_c B_{cv,i} |\Psi_{c,i}^{AE}\rangle. \quad (2.59)$$

The composite index $i = \{E, l, m\}$ represents the dependence on the energy E and the angular momentum (l, m) . Assuming orthonormality, Eq. (2.59) can be written as [64]

$$|\Psi_{v,i}^{PS}\rangle = |\Psi_{v,i}^{AE}\rangle + \sum_c |\Psi_{c,i}^{AE}\rangle \langle \Psi_{c,i}^{AE} | \Psi_{v,i}^{PS} \rangle. \quad (2.60)$$

Inserting this equation into the Schrödinger equation $\hat{H} |\Psi^{AE}\rangle = E |\Psi^{AE}\rangle$ leads to the result that the pseudo-wavefunction is an eigenstate of the Hamiltonian

$$[\hat{T} + V_c^{PS}] |\Psi_i^{PS}\rangle = E^{PS} |\Psi_i^{PS}\rangle. \quad (2.61)$$

Thus, the pseudopotential V_v^{PS} can be calculated by inverting Eq. (2.61)

$$V_v^{PS} = V(\mathbf{r}) \sum_c (E_v - E_c) |\Psi_c^{AE}\rangle \langle \Psi_c^{AE}|, \quad (2.62)$$

where $V(\mathbf{r})$ denotes the Coulomb potential.

Phillips and Kleinman introduced the PP method for the calculation of wavefunctions [65]

which brings along some consequences. In particular, V_{ps} is a non-local, energy-dependent potential. As evident from the index i , depending on the angular momentum, the projector term acts differently on each state. Nevertheless, according to Kleinman and Bylander [66], one can convert the non-local pseudopotential into a semi-local form

$$V^{PS} = V(\mathbf{r}) + \sum_l V_l^{PS} \hat{P}_l, \quad (2.63)$$

where \hat{P}_l is an angular momentum projection operator. Since the sum over all l converges fast with increasing l , the sum can be aborted at a specific $l = l_{max}$. Most often, $l_{max} \leq 3$ is sufficient to ensure convergence. Typically, l_{max} is increased by 1 and the potential $V(\mathbf{r})$ covers the $l = 0$ part. In addition, the projector term in Eq. (2.63) is repulsive and short-ranged and thus damps the dominating Coulomb repulsion near the core and annihilates the nodes of Ψ^{AE} resulting in smoother wavefunctions Ψ^{PS} close to the nucleus.

During the last decades, several approaches have been presented to optimize the pseudopotential V^{PS} with respect to physical plausibility and application (see Refs. [64, 67, 68], and references therein). For that reason, the pseudo-wavefunction has to fulfill additional requirements. First of all, although $\Psi^{AE} \neq \Psi^{PS}$, the electron density inside the core radius r_C needs to be conserved [61, 69] and thus the following requirements have to be fulfilled

$$\int_0^{r_C} dr r^2 |\Psi^{AE}|^2 = \int_0^{r_C} dr r^2 |\Psi^{PS}|^2. \quad (2.64)$$

Additionally, Ψ^{PS} should reproduce the scattering properties of Ψ^{AE} over a wide energy range. For that, the logarithmic derivatives have to coincide at r_C to ensure that

$$\frac{1}{\Psi_v^{PS}(r_C)} \left. \frac{d\Psi_v^{PS}(r)}{dr} \right|_{r=r_C} = \frac{1}{\Psi_v^{AE}(r_C)} \left. \frac{d\Psi_v^{AE}(r)}{dr} \right|_{r=r_C}. \quad (2.65)$$

Subsequently, by fulfilling Eq. (2.65), a good transferability of the PP is accomplished at a few energy points per angular momentum channel, comprising the range of occupied states [67, 70].

Further progress in this field was done by Vanderbilt by introducing the so-called ultrasoft pseudopotential (USPP) [70]. In this scheme the normalization condition (Eq. (2.64)) is relaxed, leading to smoother pseudo-wavefunctions Ψ^{PS} inside the core radius r_C . Hence, this approach leads to a reduction of atomic orbitals $\chi_i(\mathbf{r})$ which form the total wavefunction in the expansion (2.55). This is realized by augmenting the square modulus of the pseudo-wavefunctions using additional contributions Q_{ij} to recapture the original electric charge

densities. Therefore, the generalized norm-conserving condition within this scheme reads

$$\langle \Psi_i^{AE} | \Psi_j^{AE} \rangle = \langle \Psi_i^{PS} | \Psi_j^{PS} \rangle + Q_{ij}. \quad (2.66)$$

Now, the only remaining constraint for the USPPs is given by the matching condition at r_C (Eq. (2.65)). In general, USPPs tend to be less transferable than normal PPs and one needs to consider more reference energies in Eq. (2.65) [70]. However, in return, the narrowed basis-set allows for expensive calculations.

As a consequence, combining norm-conserving USPPs with numerical basis sets allows one to deal with large systems and predict their ground-state properties efficiently. In contrary to Slater- and Gaussian-type orbitals, numerical basis sets are treated only up to certain cutoff radii [71]. Thus, the matrices are sparse and small in size leading to a speedup of the calculations. The resulting numerical orbital, also known as pseudo-atomic orbital, is an eigenfunction of the atomic pseudo-Hamiltonian in a spherical box [71, 72]. Within the "split-valence" method [73], the basis set is constructed in a way that one (single- ζ), two (double- ζ), and more orbitals per quantum channel l are taken into account. Please note that the choice of the cut-off radii for the basis set as well as the core radii for the pseudopotential depend on the considered system.

3 Electronic transport

The calculation of a current through a nanoscale device is a very challenging problem. The size of such systems is comparable to the Fermi wavelength of the conduction electrons and thus the effective-mass approximation [74] is not valid anymore [75]. Due to the scattering of the electrons by only a few atoms, one has to consider on the one hand the electronic structure of the system and on the other hand the electrons' arrangement. DFT-based methods yield reasonable results for periodic systems and molecules but fail somehow when an external bias is applied or when one looks at open systems and hence a more sophisticated description is necessary.

Up to now, to describe electronic transport in terms of *ab initio* methods, three conceptually different schemes are available, i.e., the Kubo-Greenwood equation [76, 77], the Boltzmann transport theory [78, 79], and the Landauer-type approach [80–82].

In Kubo theory, the conductivity is calculated quantum mechanically using the current-current correlation function of the ground-state. Within this method, the transport coefficient is given in the linear response regime and the strength of scattering inside the system is not restricted. However, beyond linear response, this formalism is no longer valid [76]. The Boltzmann approach is based on the incoherent scattering of the conduction electrons at defects. The mean free path of the electrons is short compared to the characteristic size of the system. Within this approach, all phase information is lost. In the Landauer-type approaches, the nanoscopic conductor is treated as a quantum-mechanical scatterer for electrons that are incoming from one lead and moving out at another. This approach can be extended for open systems by combining the Keldiysh method [83] with the Landauer-Büttiker formalism [80]. For that, one has to impose certain boundary conditions. Nowadays, this combination is usually called the non-equilibrium Green's functions (NEGF) method.

In this chapter, we will cover only the last transport formalism. For this purpose, we will first establish the Landauer formula and afterwards introduce the NEGF method.

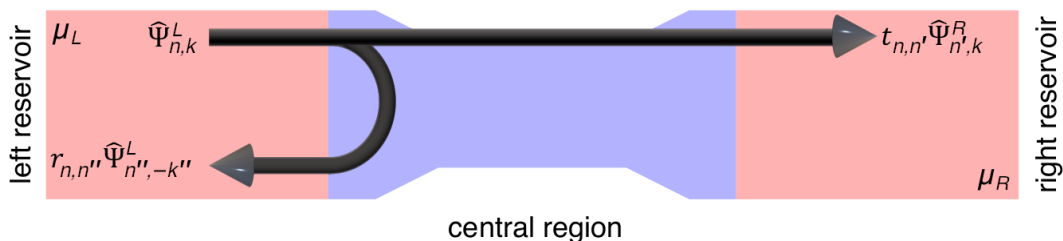


Figure 3.1: Schematic drawing of an incoming wave $\Psi_{n,k}^L$ and two outgoing, one reflected wave $\Psi_{n'',-k''}^L$ and one transmitted wave $\Psi_{n',k'}^R$ through a mesoscopic system. The sample consists of two leads with different chemical potentials (μ_L and μ_R) and a central region.

3.1 Landauer-Büttiker formalism

With the Landauer formalism, we can describe systems where a sample of length L is sandwiched between two electron reservoirs (see Fig. 3.1) and, to be valid, this length L has to be much smaller than the electron relaxation length l_r ($L \ll l_r$) [84]. Hence, here we consider elastic scattering within the central region. In addition, we assume that inside the reservoirs, the electrons can move reflectionless, and the number of modes contributing to the current is given by

$$M = \sum_n \theta(E - \epsilon_n), \quad (3.1)$$

where

$$\epsilon_n = E(n, k = 0), \quad (3.2)$$

and θ is the Heaviside step function.

The system can be thermalized at a specific temperature and chemical potential of each contact. Accordingly, electrons entering the system from a reservoir are described by the Fermi-Dirac distribution $f(E)$ of the specific contact.

Due to the elastic scattering, an incoming wave from the left reservoir at a certain energy E gives rise to a superposition with reflected and transmitted states at the same energy

$$\Psi_{n,k_n}^L = \sum_{n'} t_{n,n'}(E) \Psi_{n',k_{n'}}^R - \sum_{n''} r_{n,n''}(E) \Psi_{n'',-k_{n''}}^L, \quad (3.3)$$

where $t_{n,n'}$ denotes the transmission coefficient between the state n with wave-vector k_n of the incoming electron and the transmitted state n' with wave-vector $k_{n'}$ of a transmitted electron at energy E while $r_{n,n''}$ is the reflection coefficient between the original state n, k_n and the reflected state $n'', k_{n''}$ at the same energy.

Hence, we can calculate the transmitted current density at a given energy E and state n, k as

$$j_{n,k_n}^t(E) = \sum_{n'} \|t_{n,n'}(E)\|^2 j_{n',k_{n'}}(E). \quad (3.4)$$

Here $j_{n',k'}$ is the current density of the state n' in the right reservoir.

A moving uniform electron gas with N electrons per unit length carries a current $I = Nv$, where v denotes its velocity. Thus, the current in a certain mode m per unit length is determined by the group velocity which is defined as the derivative of the dispersion relation

of band m

$$j_{m,k_m} = v_{k_m}(E_m)f(E_m) = \frac{1}{2\pi} \frac{\partial E_m}{\partial k} f(E_m). \quad (3.5)$$

Here $f(E_m)$ is for the Fermi-Dirac distribution

$$f(E_m) = \frac{1}{1 + e^{\frac{E_m - E_F}{k_B T}}}, \quad (3.6)$$

where T denotes the temperature, E_F the Fermi level, and k_B the Boltzmann constant.

With this, the total current flowing from the left to the right contact is given by

$$\begin{aligned} I_{L \rightarrow R}^t &= \int dk \sum_n j_{n,k_n}(E) = \int dk \sum_{n,n'} \|t_{n,n'}(E)\|^2 j_{n',k_{n'}}(E) \\ &= \frac{1}{2\pi} \int dk \sum_{n,n'} \|t_{n,n'}(E)\|^2 \frac{\partial E_{n'}}{\partial k} f(E_{n'} - \mu_L). \end{aligned} \quad (3.7)$$

μ_L marks the chemical potential of the left reservoir.

To convert the integration over k into an integration over the energy we make use of the density of states (DOS) $D(E)$ which reads for one-dimensional systems $D(E) = \left(\frac{\partial E}{\partial k}\right)^{-1}$. Hereby, the current becomes

$$\begin{aligned} I_{L \rightarrow R}^t &= \frac{1}{2\pi} \int_{-\infty}^{\infty} dE D(E) \frac{\partial E}{\partial k} f(E - \mu_L) \sum_{n,n'} \|t_{n,n'}(E)\|^2 \\ &= \frac{1}{2\pi} \int_{-\infty}^{\infty} dE \left(\frac{\partial E}{\partial k}\right)^{-1} \frac{\partial E}{\partial k} f(E - \mu_L) \sum_{n,n'} \|t_{n,n'}(E)\|^2 \\ &= \frac{1}{2\pi} \int_{-\infty}^{\infty} dE f(E - \mu_L) \sum_{n,n'} \|t_{n,n'}(E)\|^2 \\ &= \frac{1}{2\pi} \int_{-\infty}^{\infty} dE f(E - \mu_L) \sum_n T_n(E), \end{aligned} \quad (3.8)$$

where $T_n(E)$ denotes the transmission per conduction channel n , and the Fermi-Dirac distribution $f(E - \mu_L)$ implies that electrons are injected from the left lead up to the chemical potential μ_L into the right-moving modes.

Analogous, the current from the right to the left lead reads

$$I_{R \rightarrow L}^t = \frac{1}{2\pi} \int_{-\infty}^{\infty} dE f(E - \mu_R) \sum_{n',n} \|t_{n',n}(E)\|^2 = \frac{1}{2\pi} \int_{-\infty}^{\infty} dE f(E - \mu_R) \sum_{n'} T_{n'}(E). \quad (3.9)$$

Accordingly, here $T_{n'}(E)$ represents the transmission probability of mode n' of the right reservoir. Due to time inversion symmetry, the transmission coefficient from the left to the

right lead $t_{n,n'}$ must be equal to the one from the right to the left contact $t_{n',n}$. For that reason, the following relation for the total transmission probabilities from the left to the right reservoir holds:

$$\sum_n T_n(E) = \sum_{n,n'} \|t_{n,n'}(E)\|^2 = \sum_{n',n} \|t_{n',n}(E)\|^2 = \sum_{n'} T_{n'}(E). \quad (3.10)$$

Finally, the total current is calculated as the difference between the current from the left to the right contact and the current from the right to the left contact. Thus, using Eqs. (3.8) and (3.9) the current is given by

$$I = I_{L \rightarrow R}^t - I_{R \rightarrow L}^t = \frac{1}{2\pi} \int_{-\infty}^{\infty} dE \left[\sum_n T_n(E) \right] [f(E - \mu_L) - f(E - \mu_R)]. \quad (3.11)$$

Neglecting temperature, the Fermi-Dirac distribution becomes a step function. Furthermore, we can identify the difference of the chemical potentials as the applied voltage $V = \mu_L - \mu_R$ and thus we obtain the following formula for the conductance

$$G = \frac{1}{2\pi} \sum_n T_n(V). \quad (3.12)$$

This last equation is known as the two-terminal Landauer formula [85]. The prefactor, however, is only half of the conductance quantum $G_0 = 1/\pi$. This is due to the fact that for spin-degenerate systems, the transmission for the spin-up and spin-down channel is equal so that a factor of two appears.

The formalism above was extended by Büttiker to calculate the current in multi-terminal devices [80, 82]. To account for multiple terminals, one has to sum up the current of all terminals and thus the current in lead p reads

$$I_p = \frac{1}{2\pi} \sum_{q,n} T_{q \leftarrow p,n}(E) \mu_p - T_{p \leftarrow q,n}(E) \mu_q. \quad (3.13)$$

With $V_i = \mu_i$ we obtain

$$I_p = \sum_q G_{qp} V_p - G_{pq} V_q, \quad (3.14)$$

where

$$G_{qp} = \frac{1}{2\pi} \sum_n T_{q \leftarrow p,n}. \quad (3.15)$$

Since the current has to be zero when all potentials are equal, the conductance from lead p to q has to be equal to that from q to p ($G_{qp} = G_{pq}$) and thus the current can be calculated as

$$I_p = \sum_q G_{qp}(V_p - V_q). \quad (3.16)$$

The formalism discussed above left out the calculation of the transmission matrix T_n for each particular channel n and the dependence of the transmission matrix on the applied bias voltage. One solution for that is the combination of the Kohn-Sham single-particle description with the NEGF approach.

3.2 Non-equilibrium Green's function method

The NEGF approach became the state-of-the-art method for the calculation of current and charge densities in nanoscale conductors, both, molecular and semiconducting, under an applied bias [86, 87]. The aim of the following sections is to introduce the one particle Green's functions in a compact form together with the derivation of the expressions for the charge density and the current.

3.2.1 Hamiltonian, overlap matrix, and Green's function of the system

We now consider a system that consists of three parts, particularly of two semi-infinite leads (left and right) and the central region (see Fig. 3.2). Since we do not take interactions between the left and right electrodes into account, the central region must be sufficiently large and includes parts of the electrodes with bulk properties and the entire scattering region [88]. Providing that the system is translational invariant in the plane perpendicular to the transport direction, the Hamiltonian for the perpendicular elements of any \mathbf{k} point reads

$$\hat{\mathbf{H}}_{\mathbf{k}} = \begin{bmatrix} \hat{H}_{L,\mathbf{k}} & \hat{V}_{LC,\mathbf{k}} & 0 \\ \hat{V}_{LC,\mathbf{k}}^\dagger & \hat{H}_{C,\mathbf{k}} & \hat{V}_{RC,\mathbf{k}}^\dagger \\ 0 & \hat{V}_{RC,\mathbf{k}} & \hat{H}_{R,\mathbf{k}} \end{bmatrix}. \quad (3.17)$$

For simplicity, in the following, we derive the transport equations for one-dimensional systems where $\mathbf{k} = k_x$. For higher dimensions, one has to consider that only the perpendicular part of \mathbf{k} contributes to transport. $\hat{H}_{L,\mathbf{k}}$ and $\hat{H}_{R,\mathbf{k}}$ denote the Hamiltonian of the semi-infinite left and right lead, respectively, while $\hat{H}_{C,\mathbf{k}}$ is the Hamiltonian of the central region. $\hat{V}_{LC,\mathbf{k}}$ ($\hat{V}_{RC,\mathbf{k}}$) describes the interaction between the left (right) electrode and the central region. Now, we split the electrodes into planes of unit cells and suppose that each plane interacts only with the neighboring plane as depicted in Fig. 3.2. This results in the following Hamiltonians

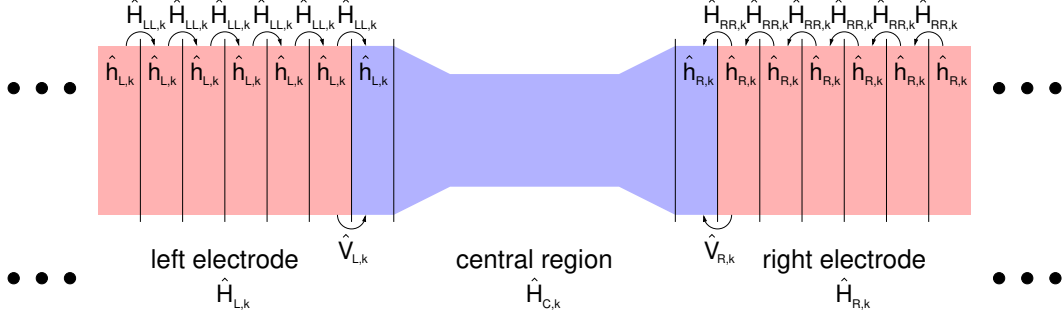


Figure 3.2: Schematic drawing of a two-terminal device composed of two semi-infinite electrodes and a central region. The central region must be sufficiently large and includes parts of electrodes by which the left and right leads could be treated as bulk material.

for the left and right lead

$$\hat{H}_{L,k} = \begin{bmatrix} \ddots & \ddots & & 0 \\ \ddots & \hat{h}_{L,k} & \hat{H}_{LL,k} & \\ & \hat{H}_{LL,k}^\dagger & \hat{h}_{L,k} & \hat{H}_{LL,k} \\ 0 & & \hat{H}_{LL,k}^\dagger & \hat{h}_{L,k} \end{bmatrix} \quad \text{and} \quad \hat{H}_{R,k} = \begin{bmatrix} \hat{h}_{R,k} & \hat{H}_{RR,k}^\dagger & & 0 \\ \hat{H}_{RR,k} & \hat{h}_{R,k} & \hat{H}_{RR,k}^\dagger & \\ & \hat{H}_{RR,k} & \hat{h}_{R,k} & \ddots \\ 0 & & \ddots & \ddots \end{bmatrix}. \quad (3.18)$$

$$\begin{bmatrix} \hat{H}_{L,k} & \hat{V}_{LC,k} & 0 \\ \hat{V}_{LC,k}^\dagger & \hat{H}_{C,k} & \hat{V}_{RC,k}^\dagger \\ 0 & \hat{V}_{RC,k} & \hat{H}_{R,k} \end{bmatrix} \begin{pmatrix} |\Psi_{L,k}\rangle \\ |\Psi_{C,k}\rangle \\ |\Psi_{R,k}\rangle \end{pmatrix} = E_k \begin{pmatrix} |\Psi_{L,k}\rangle \\ |\Psi_{C,k}\rangle \\ |\Psi_{R,k}\rangle \end{pmatrix}. \quad (3.19)$$

From the first and third row of Eq. (3.19), we obtain the following relations between the wavefunctions of the electrodes and the central region

$$\hat{H}_{L,k} |\Psi_{L,k}\rangle + \hat{V}_{LC,k} |\Psi_{C,k}\rangle = E_k |\Psi_{L,k}\rangle \implies |\Psi_{L,k}\rangle = (z - \hat{H}_{L,k})^{-1} \hat{V}_{LC,k} |\Psi_{C,k}\rangle, \quad (3.20)$$

$$\hat{V}_{RC,k} |\Psi_{C,k}\rangle + \hat{H}_{R,k} |\Psi_{R,k}\rangle = E_k |\Psi_{R,k}\rangle \implies |\Psi_{R,k}\rangle = (z - \hat{H}_{R,k})^{-1} \hat{V}_{RC,k} |\Psi_{C,k}\rangle, \quad (3.21)$$

where

$$z = E_k \pm i\eta. \quad (3.22)$$

At this point, we would like to introduce the Green's function (GF) method which can be

used to solve partial differential equations like the Schrödinger equation [89]

$$\hat{H} |\Psi\rangle = E |\Psi\rangle, \quad (3.23)$$

where \hat{H} denotes the Hamilton operator.

The corresponding GF is defined as the solution of the equation

$$(z - \hat{H})\hat{G}(E) = I, \quad z = E \pm i\eta. \quad (3.24)$$

Here I stands for the identity matrix.

Depending on the positive or negative sign, we receive different side limits, which are usually referred to as advanced ($-$) and retarded ($+$) GF. Accordingly, by using the unperturbed GF of the left and right contact, Eqs. (3.20) and (3.21) can be rewritten as

$$|\Psi_{L,\mathbf{k}}\rangle = \hat{g}_{L,\mathbf{k}} \hat{V}_{LC,\mathbf{k}} |\Psi_{C,\mathbf{k}}\rangle, \quad (3.25)$$

and

$$|\Psi_{R,\mathbf{k}}\rangle = \hat{g}_{R,\mathbf{k}} \hat{V}_{RC,\mathbf{k}} |\Psi_{C,\mathbf{k}}\rangle, \quad (3.26)$$

where

$$\hat{g}_{L/R,\mathbf{k}} = (z - \hat{H}_{L/R,\mathbf{k}})^{-1} \quad (3.27)$$

are the GFs of the unperturbed semi-infinite contacts.

In the so-called spectral representation, the advanced (\hat{G}^-) and retarded (\hat{G}^+) GF can be expressed in terms of the wavefunctions as follows

$$\hat{G}_{\mathbf{k}}^{\pm}(E) = \sum_n \frac{|\Psi_{n,\mathbf{k}}\rangle \langle \Psi_{n,\mathbf{k}}|}{E - E_n \pm i\eta} f(E_{n,\mathbf{k}} - E_F), \quad (3.28)$$

where $f(E_{n,\mathbf{k}} - E_F)$ denotes the Fermi-Dirac distribution.

From this equation, one can easily identify the following relation between the advanced and retarded GF

$$\left(\hat{G}_{\mathbf{k}}^+\right)^\dagger = \hat{G}_{\mathbf{k}}^-. \quad (3.29)$$

So far, we have considered the basis set $|\Psi\rangle$ to be orthogonal. If this is not the case, the overlap $\hat{S} = \langle \Psi | \Psi \rangle$ has to be taken into account. The overlap matrix of the considered system

then reads

$$\hat{\mathbf{S}}_{\mathbf{k}} = \begin{bmatrix} \hat{S}_{L,\mathbf{k}} & \hat{S}_{LC,\mathbf{k}} & 0 \\ \hat{S}_{LC,\mathbf{k}}^\dagger & \hat{S}_{C,\mathbf{k}} & \hat{S}_{RC,\mathbf{k}}^\dagger \\ 0 & \hat{S}_{RC,\mathbf{k}} & \hat{S}_{R,\mathbf{k}} \end{bmatrix} \quad (3.30)$$

with

$$\begin{aligned} \hat{S}_{i,\mathbf{k}} &= \langle \Psi_{i,\mathbf{k}} | \Psi_{i,\mathbf{k}} \rangle, \quad i = \{L, C, R\} \\ \hat{S}_{LC,\mathbf{k}} &= \langle \Psi_{L,\mathbf{k}} | \Psi_{C,\mathbf{k}} \rangle \\ \hat{S}_{RC,\mathbf{k}} &= \langle \Psi_{R,\mathbf{k}} | \Psi_{C,\mathbf{k}} \rangle. \end{aligned} \quad (3.31)$$

Consequently, the GF can be calculated from the equation

$$(zS - \hat{H})\hat{G}(E) = I. \quad (3.32)$$

Assuming that the GF of the considered device is given by

$$\hat{\mathbf{G}}_{\mathbf{k}} = \begin{bmatrix} \hat{G}_{L,\mathbf{k}} & \hat{G}_{LC,\mathbf{k}} & \hat{G}_{LR,\mathbf{k}} \\ \hat{G}_{CL,\mathbf{k}} & \hat{G}_{C,\mathbf{k}} & \hat{G}_{CR,\mathbf{k}} \\ \hat{G}_{RL,\mathbf{k}} & \hat{G}_{RC,\mathbf{k}} & \hat{G}_{R,\mathbf{k}} \end{bmatrix}, \quad (3.33)$$

where we utilized the relation $(\hat{G}_{ij,\mathbf{k}})^\dagger = \hat{G}_{ji,\mathbf{k}}$, we get from Eq. (3.32)

$$\begin{bmatrix} z\hat{S}_{L,\mathbf{k}} - \hat{H}_{L,\mathbf{k}} & z\hat{S}_{LC,\mathbf{k}} - \hat{V}_{LC,\mathbf{k}} & 0 \\ z\hat{S}_{LC,\mathbf{k}}^\dagger - \hat{V}_{LC,\mathbf{k}}^\dagger & z\hat{S}_{C,\mathbf{k}} - \hat{H}_{C,\mathbf{k}} & z\hat{S}_{RC,\mathbf{k}}^\dagger - \hat{V}_{RC,\mathbf{k}}^\dagger \\ 0 & z\hat{S}_{RC,\mathbf{k}} - \hat{V}_{RC,\mathbf{k}} & z\hat{S}_{R,\mathbf{k}} - \hat{H}_{R,\mathbf{k}} \end{bmatrix} \cdot \begin{bmatrix} \hat{G}_{L,\mathbf{k}} & \hat{G}_{LC,\mathbf{k}} & \hat{G}_{LR,\mathbf{k}} \\ \hat{G}_{CL,\mathbf{k}} & \hat{G}_{C,\mathbf{k}} & \hat{G}_{CR,\mathbf{k}} \\ \hat{G}_{RL,\mathbf{k}} & \hat{G}_{RC,\mathbf{k}} & \hat{G}_{R,\mathbf{k}} \end{bmatrix} = \begin{bmatrix} I & 0 & 0 \\ 0 & I & 0 \\ 0 & 0 & I \end{bmatrix}. \quad (3.34)$$

Considering now the three equations obtained from the second column of $\hat{\mathbf{G}}_{\mathbf{k}}$

$$(z\hat{S}_{L,\mathbf{k}} - \hat{H}_{L,\mathbf{k}})\hat{G}_{LC,\mathbf{k}} + (z\hat{S}_{LC,\mathbf{k}} - \hat{V}_{LC,\mathbf{k}})\hat{G}_{C,\mathbf{k}} = 0 \quad (3.35)$$

$$(z\hat{S}_{LC,\mathbf{k}}^\dagger - \hat{V}_{LC,\mathbf{k}}^\dagger)\hat{G}_{LC,\mathbf{k}} + (z\hat{S}_{C,\mathbf{k}} - \hat{H}_{C,\mathbf{k}})\hat{G}_{C,\mathbf{k}} + (z\hat{S}_{RC,\mathbf{k}}^\dagger - \hat{V}_{RC,\mathbf{k}}^\dagger)\hat{G}_{RC,\mathbf{k}} = I \quad (3.36)$$

$$(z\hat{S}_{RC,\mathbf{k}} - \hat{V}_{RC,\mathbf{k}})\hat{G}_{C,\mathbf{k}} + (z\hat{S}_{R,\mathbf{k}} - \hat{H}_{R,\mathbf{k}})\hat{G}_{RC,\mathbf{k}} = 0, \quad (3.37)$$

we obtain from Eqs. (3.35) and (3.37)

$$\hat{G}_{LC,\mathbf{k}} = -\hat{g}_{L,\mathbf{k}} (z\hat{S}_{LC,\mathbf{k}} - \hat{V}_{LC,\mathbf{k}}) \hat{G}_{C,\mathbf{k}} \quad (3.38)$$

$$\hat{G}_{RC,\mathbf{k}} = -\hat{g}_{R,\mathbf{k}} (z\hat{S}_{RC,\mathbf{k}} - \hat{V}_{RC,\mathbf{k}}) \hat{G}_{C,\mathbf{k}}. \quad (3.39)$$

Inserting these equations into Eq. (3.36) leads to

$$\begin{aligned}
 & - \left(z\hat{S}_{LC,\mathbf{k}}^\dagger - \hat{V}_{LC,\mathbf{k}}^\dagger \right) \hat{g}_{L,\mathbf{k}} \left(z\hat{S}_{LC,\mathbf{k}} - \hat{V}_{LC,\mathbf{k}} \right) \hat{G}_{C,\mathbf{k}} + \left(z\hat{S}_{C,\mathbf{k}} - \hat{H}_{C,\mathbf{k}} \right) \hat{G}_{C,\mathbf{k}} \\
 & - \left(z\hat{S}_{RC,\mathbf{k}}^\dagger - \hat{V}_{RC,\mathbf{k}}^\dagger \right) \hat{g}_{R,\mathbf{k}} \left(z\hat{S}_{RC,\mathbf{k}} - \hat{V}_{RC,\mathbf{k}} \right) \hat{G}_{C,\mathbf{k}} = I.
 \end{aligned} \tag{3.40}$$

Thus, the GF of the central region $\hat{G}_{C,\mathbf{k}}$ reads

$$\hat{G}_{C,\mathbf{k}}(E) = \left[z\hat{S}_{C,\mathbf{k}} - \hat{H}_{C,\mathbf{k}} - \hat{\Sigma}_{L,\mathbf{k}}(E) - \hat{\Sigma}_{R,\mathbf{k}}(E) \right]^{-1}, \tag{3.41}$$

with

$$\hat{\Sigma}_{L,\mathbf{k}}(E) = \left(z\hat{S}_{LC,\mathbf{k}}^\dagger - \hat{V}_{LC,\mathbf{k}}^\dagger \right) \hat{g}_{L,\mathbf{k}}(E) \left(z\hat{S}_{LC,\mathbf{k}} - \hat{V}_{LC,\mathbf{k}} \right) \tag{3.42}$$

$$\hat{\Sigma}_{R,\mathbf{k}}(E) = \left(z\hat{S}_{RC,\mathbf{k}}^\dagger - \hat{V}_{RC,\mathbf{k}}^\dagger \right) \hat{g}_{R,\mathbf{k}}(E) \left(z\hat{S}_{RC,\mathbf{k}} - \hat{V}_{RC,\mathbf{k}} \right) \tag{3.43}$$

which are the so-called self-energies of the left and right lead, respectively.

So far, we discussed the ground-state properties of the system and thus, in the following, we will discuss what happens when we apply a bias voltage to the considered system.

3.2.2 Response to an incoming wave

In the non-equilibrium case, the reservoirs possess different chemical potentials and therefore will inject electrons. Subsequently, these electrons will occupy states n corresponding to incoming waves $|\Psi_{n\mathbf{k}}\rangle$. The response of our system $|\Phi_{n\mathbf{k}}\rangle$ can be calculated with the equation [89]

$$\hat{H}_{\mathbf{k}} (|\Psi_{n\mathbf{k}}\rangle + |\Phi_{n\mathbf{k}}\rangle) = E_{\mathbf{k}} (|\Psi_{n\mathbf{k}}\rangle + |\Phi_{n\mathbf{k}}\rangle). \tag{3.44}$$

If the electrons are injected from the left contact, the incoming wave and response are given by

$$|\Psi_{n\mathbf{k}}\rangle = \begin{pmatrix} |\Psi_{L,n\mathbf{k}}\rangle \\ 0 \\ 0 \end{pmatrix}, \text{ and } |\Phi_{n\mathbf{k}}\rangle = \begin{pmatrix} |\Phi_{L,n\mathbf{k}}\rangle \\ |\Phi_{C,n\mathbf{k}}\rangle \\ |\Phi_{R,n\mathbf{k}}\rangle \end{pmatrix} \tag{3.45}$$

Therefore, applying Eqs. (3.17) and (3.44), the response from the central region reads

$$\begin{aligned}
 -(\hat{H}_k - E_k) |\Psi_{nk}\rangle &= (\hat{H}_k - E_k) |\Phi_{nk}\rangle \\
 |\Phi_{nk}\rangle &= -\mathbf{G}_k \begin{pmatrix} E_k - \hat{H}_{L,k} \\ -\hat{V}_{L,k}^\dagger \\ 0 \end{pmatrix} |\Psi_{L,nk}\rangle = \hat{\mathbf{G}}_k \begin{pmatrix} 0 \\ \hat{V}_{L,k}^\dagger \\ 0 \end{pmatrix} |\Psi_{L,nk}\rangle \\
 \Rightarrow |\Phi_{CL,nk}\rangle &:= \hat{G}_{C,k} \hat{V}_{L,k}^\dagger |\Psi_{L,nk}\rangle
 \end{aligned} \tag{3.46}$$

Here we assumed that $|\Psi_{L,nk}\rangle$ is a solution of the Schrödinger equation for the left reservoir ($\hat{H}_{L,k} |\Psi_{L,nk}\rangle = E_k |\Psi_{L,nk}\rangle$).

In the same way, for an incoming wave from the right lead, the response on state m can be defined as

$$|\Phi_{CR,mk}\rangle := \hat{G}_{C,k} \hat{V}_{R,k}^\dagger |\Psi_{R,mk}\rangle. \tag{3.47}$$

It is worth noting that the scattering states (Eqs. (3.46) and (3.47)), using all feasible incoming waves from every electrode, provide a complete set of solutions of the Schrödinger equation, except for the localized states in the central region [90]. Furthermore, here the only part of the wave that travels across the central part is the incoming wave ($|\Psi_{C,k}\rangle = |\Phi_{CL,nk}\rangle$). As a consequence, by applying Eq. (3.26), we can express the wavefunction in the right lead $|\Psi_{R,k}\rangle$ in terms of the incoming wave from the left contact $|\Psi_{L,nk}\rangle$

$$|\Psi_{R,k}\rangle = \hat{g}_{R,k} \hat{V}_{R,k} |\Psi_{C,k}\rangle = \hat{g}_{R,k} \hat{V}_{R,k} \hat{G}_{C,k} \hat{V}_{L,k}^\dagger |\Psi_{L,nk}\rangle. \tag{3.48}$$

To calculate the wavefunction in the left reservoir containing the incoming wave $|\Psi_{L,nk}\rangle$, we obtain a slightly more complicated formula

$$|\Psi_{L,k}\rangle = \left(1 + \hat{g}_{L,k} \hat{V}_{L,k} \hat{G}_{C,k} \hat{V}_{L,k}^\dagger\right) |\Psi_{L,nk}\rangle. \tag{3.49}$$

Knowing the wavefunctions for the incoming waves in the different reservoirs allows us to satisfy the different solutions depending on the electron reservoirs which fill the contacts.

For the non-equilibrium case, two quantities are of peculiar interest: the charge density and the current. Therefore, we start with the charge density operator in the next section.

3.2.3 Charge density operator

In a self-consistent DFT cycle for the non-equilibrium system, the fundamental goal is the determination of the charge density for the device region. This can be done by using the

wave functions in the central region given by incoming waves of the left and right electrodes

$$\hat{n} = \hat{n}_R + \hat{n}_L, \quad (3.50)$$

where

$$\hat{n}_L = \sum_{n,\mathbf{k}} |\Phi_{CL,n\mathbf{k}}\rangle \langle \Phi_{CL,n\mathbf{k}}| f(E_{n\mathbf{k}} - \mu_L), \quad (3.51)$$

and

$$\hat{n}_R = \sum_{m,\mathbf{k}} |\Phi_{CR,m\mathbf{k}}\rangle \langle \Phi_{CR,m\mathbf{k}}| f(E_{m\mathbf{k}} - \mu_R). \quad (3.52)$$

By applying Eq. (3.46), we can rewrite the above equation as follows

$$\begin{aligned} \hat{n}_L &= \sum_{n,\mathbf{k}} \hat{G}_{C,\mathbf{k}} \hat{V}_{L,\mathbf{k}}^\dagger [|\Psi_{L,n\mathbf{k}}\rangle \langle \Psi_{L,n\mathbf{k}}|] \hat{V}_{L,\mathbf{k}} \hat{G}_{C,\mathbf{k}}^\dagger f(E_{n\mathbf{k}} - \mu_L) \\ &= \sum_{n,\mathbf{k}} \int_{-\infty}^{\infty} dE f(E - \mu_L) \hat{G}_{C,\mathbf{k}} \hat{V}_{L,\mathbf{k}}^\dagger [|\Psi_{L,n\mathbf{k}}\rangle \langle \Psi_{L,n\mathbf{k}}| \delta(E - E_{n\mathbf{k}})] \hat{V}_{L,\mathbf{k}} \hat{G}_{C,\mathbf{k}}^\dagger \\ &= \frac{i}{2\pi} \sum_{\mathbf{k}} \int_{-\infty}^{\infty} dE f(E - \mu_L) \hat{G}_{C,\mathbf{k}} \hat{V}_{L,\mathbf{k}}^\dagger [\hat{g}_{L,\mathbf{k}} - \hat{g}_{L,\mathbf{k}}^\dagger] \hat{V}_{L,\mathbf{k}} \hat{G}_{C,\mathbf{k}}^\dagger. \end{aligned} \quad (3.53)$$

Here the last step is based on the Dirac identity [91]

$$\lim_{\eta \rightarrow 0^+} \frac{1}{x \pm i\eta} = \mp i\pi \delta(x) + \mathcal{P} \left(\frac{1}{x} \right), \quad (3.54)$$

and $\hat{g}_{L,\mathbf{k}}$ represents the spectral representation of the retarded GF of the left contact, which reads

$$\hat{g}_{L,\mathbf{k}} = \hat{g}_{L,\mathbf{k}}^+ = \sum_n \frac{|\Psi_{L,n\mathbf{k}}\rangle \langle \Psi_{L,n\mathbf{k}}|}{E - E_n + i\eta} \quad (3.55)$$

and it holds

$$\hat{g}_{L,\mathbf{k}}^+ - \left(\hat{g}_{L,\mathbf{k}}^+ \right)^\dagger = \hat{g}_{L,\mathbf{k}}^+ - \hat{g}_{L,\mathbf{k}}^-. \quad (3.56)$$

At this point, we would like to introduce a new quantity to characterize the interaction between the left lead and the device region, the so-called broadening matrix

$$\hat{\Gamma}_{L,\mathbf{k}} = i \hat{V}_{L,\mathbf{k}}^\dagger [\hat{g}_{L,\mathbf{k}} - \hat{g}_{L,\mathbf{k}}^\dagger] \hat{V}_{L,\mathbf{k}} = i [\hat{\Sigma}_{L,\mathbf{k}} - \hat{\Sigma}_{L,\mathbf{k}}^\dagger], \quad (3.57)$$

where $\hat{\Sigma}_{L,\mathbf{k}}$ represents the self-energy of the left contact (cf. Eq. (3.42)).

Repeating the steps above for the right lead results in the non-equilibrium charge density operator

$$\hat{n} = \frac{1}{2\pi} \sum_{\mathbf{k}} \int_{-\infty}^{\infty} dE \left[\hat{G}_{C,\mathbf{k}} \hat{\Gamma}_{L,\mathbf{k}} \hat{G}_{C,\mathbf{k}}^{\dagger} f(E - \mu_L) + \hat{G}_{C,\mathbf{k}} \hat{\Gamma}_{R,\mathbf{k}} \hat{G}_{C,\mathbf{k}}^{\dagger} f(E - \mu_R) \right] \quad (3.58)$$

Formally, we can divide the charge density operator into an equilibrium and a non-equilibrium part

$$\begin{aligned} \hat{n} &= \hat{D}_L + \hat{\Delta}_{RL} \\ &= \frac{1}{2\pi} \sum_{\mathbf{k}} \int_{-\infty}^{\infty} dE \hat{G}_{C,\mathbf{k}} \left[\hat{\Gamma}_{L,\mathbf{k}} + \hat{\Gamma}_{R,\mathbf{k}} \right] \hat{G}_{C,\mathbf{k}}^{\dagger} f(E - \mu_L) \\ &\quad + \frac{1}{2\pi} \sum_{\mathbf{k}} \int_{-\infty}^{\infty} dE \hat{G}_{C,\mathbf{k}} \hat{\Gamma}_{R,\mathbf{k}} \hat{G}_{C,\mathbf{k}}^{\dagger} (f(E - \mu_R) - f(E - \mu_L)) \end{aligned} \quad (3.59)$$

which is equivalent to

$$\begin{aligned} \hat{n} &= \hat{D}_R + \hat{\Delta}_{LR} \\ &= \frac{1}{2\pi} \sum_{\mathbf{k}} \int_{-\infty}^{\infty} dE \hat{G}_{C,\mathbf{k}} \left[\hat{\Gamma}_{L,\mathbf{k}} + \hat{\Gamma}_{R,\mathbf{k}} \right] \hat{G}_{C,\mathbf{k}}^{\dagger} f(E - \mu_R) \\ &\quad + \frac{1}{2\pi} \sum_{\mathbf{k}} \int_{-\infty}^{\infty} dE \hat{G}_{C,\mathbf{k}} \hat{\Gamma}_{L,\mathbf{k}} \hat{G}_{C,\mathbf{k}}^{\dagger} (f(E - \mu_R) - f(E - \mu_L)). \end{aligned} \quad (3.60)$$

The equilibrium part of the charge density operator

In the equilibrium case, combining the density of the left and right reservoir is feasible [88]. Demanding that the states of the leads are not coupled via the device region, we can rewrite the product $\hat{G}_{C,\mathbf{k}} \left[\hat{\Gamma}_{L,\mathbf{k}} + \hat{\Gamma}_{R,\mathbf{k}} \right] \hat{G}_{C,\mathbf{k}}^{\dagger}$ as

$$\begin{aligned} \hat{G}_{C,\mathbf{k}} \left[\hat{\Gamma}_{L,\mathbf{k}} + \hat{\Gamma}_{R,\mathbf{k}} \right] \hat{G}_{C,\mathbf{k}}^{\dagger} &= i \hat{G}_{C,\mathbf{k}} \left[\left(\hat{\Sigma}_{L,\mathbf{k}} + \hat{\Sigma}_{R,\mathbf{k}} \right) - \left(\hat{\Sigma}_{L,\mathbf{k}} + \hat{\Sigma}_{R,\mathbf{k}} \right)^{\dagger} \right] \hat{G}_{C,\mathbf{k}}^{\dagger} \\ &= -i \hat{G}_{C,\mathbf{k}} \left[\left(\hat{G}_{C,\mathbf{k}}^{\dagger} \right)^{-1} - \left(\hat{G}_{C,\mathbf{k}} \right)^{-1} \right] \hat{G}_{C,\mathbf{k}}^{\dagger} \\ &= -i \left(\hat{G}_{C,\mathbf{k}} - \hat{G}_{C,\mathbf{k}}^{\dagger} \right) = -2 \text{Im} \left[\hat{G}_{C,\mathbf{k}} \right]. \end{aligned} \quad (3.61)$$

With this, the equilibrium part of the charge density operator reads [88]

$$\begin{aligned} \hat{D}_L &= \frac{1}{\pi} \sum_{\mathbf{k}} \int_{-\infty}^{\infty} dE \text{Im} \left[\hat{G}_{C,\mathbf{k}} \right] f(E - \mu_L) \\ &= \frac{1}{\pi} \sum_{\mathbf{k}} \text{Im} \left[\int_{-\infty}^{\infty} dE \hat{G}_{C,\mathbf{k}} f(E - \mu_L) \right]. \end{aligned} \quad (3.62)$$

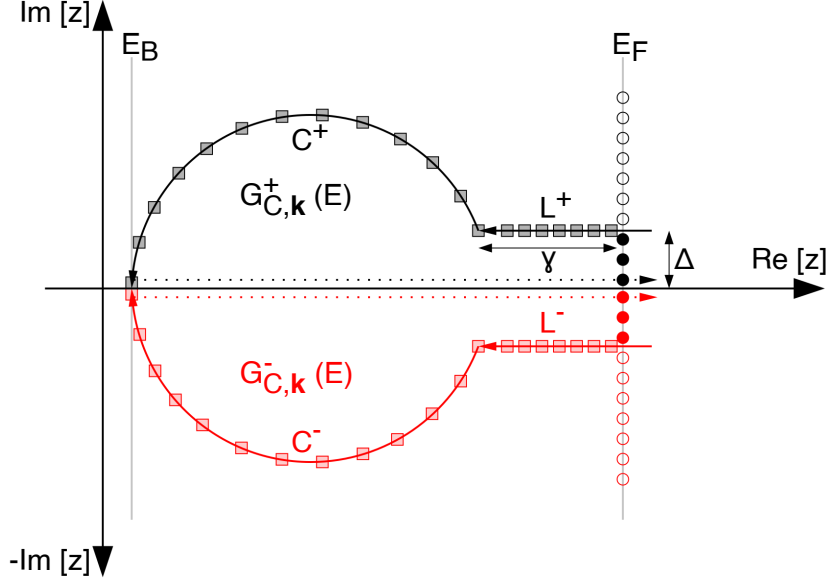


Figure 3.3: Schematic drawing of the integration contours L^+ ($[\infty + i\Delta; E_F - \gamma + i\Delta]$), C^+ , and $[E_B + i\eta; \infty + i\eta]$ (L^- ($[\infty - i\Delta; E_F - \gamma - i\Delta]$), C^- , and $[E_B - i\eta; \infty - i\eta]$) of the retarded (black) (advanced (red)) Green's function enclosing the Fermi poles (black and red dots, respectively) together with typical points for the Gaussian quadrature on the contour (black and red squares). E_F and E_B denote the Fermi level and the bottom of the valence band, respectively.

Please note that for a non-collinear magnetic system the definition of the density as the imaginary part of the retarded Green's function is not valid. This is based on the fact that the imaginary part of each complex number is a real quantity but for a non-collinear system the elements in the spin density matrix can be complex.

For the retarded GF $\hat{G}^+(E)$, the poles are all lying on the real axis, and apart from that, the function is analytic. Thus, it is practical to do the integral over the complex contour for the Green's functions. According to the residue theorem for the complex contour beginning with segment L^+ , followed by C^+ , and proceeding along the real axis from $E_B + i\eta$ to $\infty + i\eta$ (see Fig. 3.3), it holds

$$\oint dz \hat{G}(z) f(z - \mu_L) = 2\pi i k_B T \sum_{z_n} \hat{G}(z_n). \quad (3.63)$$

Here T denotes the temperature, and the Matsubara poles of the Fermi-Dirac distribution are located at $z_n = i(2n + 1)\pi k_B T$, $n = 1, 2, 3, \dots$ [92].

With the residues of the Fermi-Dirac distribution, $-k_B T$, we obtain for the retarded and

advanced GF

$$\int dE \hat{G}_{C,k}^+(E) f(E - \mu) = - \int_{C^++L^+} dz^+ \hat{G}^+(z^+) f(z^+ - \mu) - 2\pi i k_B T \sum_{z_n^+} \hat{G}^+(z_n^+) \quad (3.64)$$

and

$$\int dE \hat{G}_{C,k}^-(E) f(E - \mu) = - \int_{C^-+L^-} dz^- \hat{G}^-(z^-) f(z^- - \mu) + 2\pi i k_B T \sum_{z_n^-} \hat{G}^-(z_n^-). \quad (3.65)$$

Now, for a given temperature, the contour integral can be calculated numerically in the complex plane. Thus, the integration can be performed by Gaussian quadrature with a minimal number of points (see Fig. 3.3). Since the main variation on L stems from the Fermi-Dirac distribution, $f(z - \mu)$ should be used as a weight function (see Ref. [93] for a detailed description of this method).

The non-equilibrium part of the charge density operator

Since the scattering states break time-reversal symmetry due to their boundary conditions, $\hat{\Delta}_{RL}$ and $\hat{\Delta}_{LR}$, are non-analytical quantities. In fact, the imaginary part of these quantities is directly related to the local current [94]. To obtain the values of $\hat{\Delta}_{RL}$ and $\hat{\Delta}_{LR}$, these quantities must be evaluated on a fine energy point grid and for a finite level broadening $i\eta$. Due to numerical errors mainly arising from the real-axis integrals, the results for Eqs. (3.59) and (3.60) are not equivalent. Hence, it is reasonable to use a weighted sum of both integrals for the calculation of the charge density operator [88]

$$\hat{n} = w \left(\hat{D}_L + \hat{\Delta}_{RL} \right) + (1 - w) \left(\hat{D}_R + \hat{\Delta}_{LR} \right), \quad (3.66)$$

with

$$w = \frac{\left(\hat{\Delta}_{LR} \right)^2}{\left(\hat{\Delta}_{LR} \right)^2 + \left(\hat{\Delta}_{RL} \right)^2}. \quad (3.67)$$

The choice of the weighting factor w can be justified by the following argument: Let us assume that a stochastic variable $\tilde{\Delta}_{LR}$ with its mean value Δ_{LR} is the result of the numerical integration, and the variance is proportional to the square of the overall size of the numerical integral, i.e., $\text{Var}(\tilde{\Delta}_{LR}) \propto (\Delta_{LR})^2$. Now, the numerical calculation with weighted integrals as Eq. (3.66) becomes a stochastic variable \tilde{n} with variance $\text{Var}(\tilde{n}) \propto w^2 (\Delta_{RL})^2 - (1-w)^2 (\Delta_{LR})^2$. The weighting w which minimizes this variance is the one given in Eq. (3.67).

Please note that for spin-polarized calculations, the weight has to be calculated for every spin channel separately.

3.2.4 Current and transmission

Different chemical potentials in the leads give rise to a flow of electrons. Thus, we can define the probability current as the time derivative of the charge density in the central region [89]

$$j = \frac{\partial n(\mathbf{r})}{\partial t} = \sum_{i\mathbf{k}} \frac{\partial(\langle \Psi_{\mathbf{k}} | i | \Psi_{\mathbf{k}} \rangle)}{\partial t}. \quad (3.68)$$

Considering the time-dependent Schrödinger equation $i \frac{\partial |\Psi_{\mathbf{k}}\rangle}{\partial t} = \hat{H}_{\mathbf{k}} |\Psi_{\mathbf{k}}\rangle$ and splitting the probability current j into one part containing the incoming electrons from the left lead into the central region and a second part for the incoming electrons of the right contact leads to

$$j = j_L + j_R, \quad (3.69)$$

where

$$j_{L/R} = i \sum_{\mathbf{k}} \left(\langle \Psi_{L/R,\mathbf{k}} | \hat{V}_{L/R,\mathbf{k}} | \Psi_{C,\mathbf{k}} \rangle - \langle \Psi_{C,\mathbf{k}} | \hat{V}_{L/R,\mathbf{k}}^\dagger | \Psi_{L/R,\mathbf{k}} \rangle \right). \quad (3.70)$$

A more detailed derivation of the probability current can be found in Ref. [89].

Now, the charge current i at a certain energy point E can be treated as the current which transfers one electron with charge $-e$ with the same probability as the probability current. Hence, the electric current from the left to the right contact $i^R(E)$ can be expressed by applying Eqs. (3.26) and (3.48)

$$\begin{aligned} i_R(E) &= -i \sum_{\mathbf{k}} \left(\langle \Psi_{R,\mathbf{k}} | \hat{V}_{R,\mathbf{k}} | \Psi_{C,\mathbf{k}} \rangle - \langle \Psi_{C,\mathbf{k}} | \hat{V}_{R,\mathbf{k}}^\dagger | \Psi_{R,\mathbf{k}} \rangle \right) \\ &= -i \sum_{\mathbf{k}} \left(\langle \Psi_{C,\mathbf{k}} | \hat{V}_{R,\mathbf{k}}^\dagger (\hat{g}_{R,\mathbf{k}} - \hat{g}_{R,\mathbf{k}}^\dagger) \hat{V}_{R,\mathbf{k}} | \Psi_{C,\mathbf{k}} \rangle \right) = - \sum_{\mathbf{k}} \langle \Psi_{C,\mathbf{k}} | \hat{\Gamma}_{R,\mathbf{k}} | \Psi_{C,\mathbf{k}} \rangle \\ &= - \sum_{n\mathbf{k}} \langle \Psi_{L,n\mathbf{k}} | \hat{V}_{L,\mathbf{k}} \hat{G}_{C,\mathbf{k}}^\dagger \hat{\Gamma}_{R,\mathbf{k}} \hat{G}_{C,\mathbf{k}} \hat{V}_{L,\mathbf{k}}^\dagger | \Psi_{L,n\mathbf{k}} \rangle. \end{aligned} \quad (3.71)$$

As a result, the total current flowing from the left lead to the right reads

$$\begin{aligned} I_R &= \sum_{\mathbf{k}} \int_{-\infty}^{\infty} dE f_L(E) \sum_n \delta(E - E_n) \langle \Psi_{L,n\mathbf{k}} | \hat{V}_{L,\mathbf{k}} \hat{G}_{C,\mathbf{k}}^\dagger \hat{\Gamma}_{R,\mathbf{k}} \hat{G}_{C,\mathbf{k}} \hat{V}_{L,\mathbf{k}}^\dagger | \Psi_{L,n\mathbf{k}} \rangle \\ &= \sum_{\mathbf{k}} \int_{-\infty}^{\infty} dE f_L(E) \sum_{n,m} \delta(E - E_n) \langle \Psi_{R,n\mathbf{k}} | \hat{V}_{L,\mathbf{k}} | \Psi_{m,\mathbf{k}} \rangle \langle \Psi_{m,\mathbf{k}} | \hat{G}_{C,\mathbf{k}}^\dagger \hat{\Gamma}_{R,\mathbf{k}} \hat{G}_{C,\mathbf{k}} \hat{V}_{L,\mathbf{k}}^\dagger | \Psi_{R,n\mathbf{k}} \rangle \\ &= \sum_{m,\mathbf{k}} \int_{-\infty}^{\infty} dE f_L(E) \langle \Psi_{m,\mathbf{k}} | \hat{G}_{C,\mathbf{k}}^\dagger \hat{\Gamma}_{R,\mathbf{k}} \hat{G}_{C,\mathbf{k}} \hat{V}_{L,\mathbf{k}}^\dagger \left(\sum_n \delta(E - E_n) | \Psi_{L,n\mathbf{k}} \rangle \langle \Psi_{L,n\mathbf{k}} | \right) \hat{V}_{L,\mathbf{k}} | \Psi_{m,\mathbf{k}} \rangle \\ &= \frac{1}{2\pi} \sum_{\mathbf{k}} \int_{-\infty}^{\infty} f_L(E) \sum_m \langle \Psi_{m,\mathbf{k}} | \hat{G}_{C,\mathbf{k}}^\dagger \hat{\Gamma}_{R,\mathbf{k}} \hat{G}_{C,\mathbf{k}} \hat{V}_{L,\mathbf{k}}^\dagger | \Psi_{m,\mathbf{k}} \rangle \end{aligned}$$

$$= \frac{1}{2\pi} \sum_{\mathbf{k}} \int_{-\infty}^{\infty} dE \operatorname{Tr} \left[\hat{G}_{C,\mathbf{k}}^\dagger \hat{\Gamma}_{R,\mathbf{k}} \hat{G}_{C,\mathbf{k}} \hat{\Gamma}_{L,\mathbf{k}} \right] f_L(E), \quad (3.72)$$

where $f_L(E) = f(E - \mu_L)$ represents the Fermi-Dirac distribution of the left lead.

Thus, the total current of the device is given by [80, 95]

$$\begin{aligned} I &= I_L - I_R \\ &= \frac{1}{2\pi} \sum_{\mathbf{k}} \int_{-\infty}^{\infty} dE \operatorname{Tr} \left[\hat{G}_{C,\mathbf{k}}^\dagger \hat{\Gamma}_{R,\mathbf{k}} \hat{G}_{C,\mathbf{k}} \hat{\Gamma}_{L,\mathbf{k}} \right] (f(E - \mu_L) - f(E - \mu_R)). \end{aligned} \quad (3.73)$$

This is exactly the Landauer equation for the current (Eq. (3.11)) with the \mathbf{k} -resolved transmission

$$T_{\mathbf{k}}(E) = \operatorname{Tr} \left[\hat{G}_{C,\mathbf{k}}^\dagger(E) \hat{\Gamma}_{R,\mathbf{k}}(E) \hat{G}_{C,\mathbf{k}}(E) \hat{\Gamma}_{L,\mathbf{k}}(E) \right]. \quad (3.74)$$

Spin transport

The transmission in Eq. (3.74) in matrix representation for any energy point E reads

$$T(E) = \operatorname{Tr} \left[\left(\hat{\Gamma}_L(E) \hat{G}_C(E) \right)^\dagger \hat{\Gamma}_R(E) \hat{G}_C(E) \right]. \quad (3.75)$$

Here we neglected the index \mathbf{k} for simplicity.

We cover now a system where the spins in both leads are aligned in z -direction while the central region possesses an arbitrary spin polarization. In that case, the GF of the central region \hat{G}_C can be represented as a full matrix while the matrices $\hat{\Gamma}_L$ and $\hat{\Gamma}_R$ are diagonal matrices of the form

$$\hat{\Gamma}_{L/R} = \begin{bmatrix} \hat{\Gamma}_{L/R}^\uparrow & 0 \\ 0 & \hat{\Gamma}_{L/R}^\downarrow \end{bmatrix}, \text{ and } \hat{G}_C = \begin{bmatrix} \hat{G}_C^{\uparrow\uparrow} & \hat{G}_C^{\uparrow\downarrow} \\ \hat{G}_C^{\downarrow\uparrow} & \hat{G}_C^{\downarrow\downarrow} \end{bmatrix}. \quad (3.76)$$

Accordingly, we obtain four independent transmission probabilities to characterize the transport of one electron flowing from one electrode with spin $\pm z$ to another with spin polarization $\pm z$. Thus, the total transmission is given by a sum of these transmission probabilities

$$T(E) = T^{\uparrow\uparrow}(E) + T^{\uparrow\downarrow}(E) + T^{\downarrow\uparrow}(E) + T^{\downarrow\downarrow}(E). \quad (3.77)$$

Consequently, the spin-resolved transmission reads

$$T^{\sigma\sigma'}(E) = \operatorname{Tr} \left[\left(\hat{\Gamma}_L^\sigma(E) \hat{G}_C^{\sigma\sigma'}(E) \right)^\dagger \hat{\Gamma}_R^{\sigma'}(E) \hat{G}_C^{\sigma\sigma'}(E) \right]. \quad (3.78)$$

The terms with mixed spins, $T^{\uparrow\downarrow}$ and $T^{\downarrow\uparrow}$, represent the so-called adiabatic spin-flip transmissions. Hence, they attain the value 0 when the spins in the central region are also aligned along the z -axis.

4 Half-metallic magnets and spin-gapless semiconductors

Since we have elucidated our theoretical methods in the previous chapters, we will now focus on two material classes with unique electronic transport properties, particularly the half-metallic magnets (HMMs) which were predicted by de Groot *et al.* in 1983 [96], and the spin-gapless semiconductors (SGSs) which were proposed in 2008 by Wang [97]. Both classes attracted great research interest for spintronic application in the last decade [11, 98–101]. The HMMs possess an energy gap between the valence- and conduction-band in one spin channel and continuous bands for electrons with the other spin polarization. Thus, for one spin polarization, the electrons are semiconducting, while for the other, the electrons keep their metallic character. As a consequence, the conduction electrons at the Fermi energy (E_F) are 100% spin-polarized [96].

On the other hand, the SGSs lie on the border between magnetic semiconductors and HMMs. For type-I SGSs, the minority-spin bands behave like in HMMs while the majority-spin bands behave differently. The conduction- and valence-band edges touch at the Fermi level, and thus there appears a zero-width gap as presented in Fig. 4.1 (b).

In contrast, type-II SGSs have a unique electronic band structure. In this materials appears a finite gap below and above E_F for different spin-channels while the valence- and conduction-band edges of different spin-channels touch at the Fermi level. A schematic representation of the DOS of HMMs and SGSs (type I and type II) is given in Fig. 4.1.

Both properties, half-metallicity as well as spin-gapless behavior, have been identified in the family of two-dimensional materials as well as in Heusler compounds. In this chapter, we will focus on both material classes while we start with Heusler compounds and subsequently discuss the two-dimensional systems.

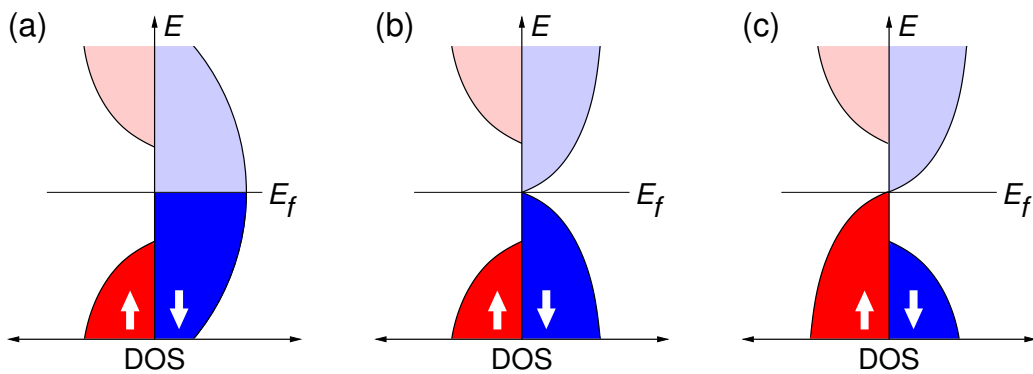


Figure 4.1: Schematic drawing of the DOS of (a) a half-metallic magnet, (b) a type-I spin-gapless semiconductor, and (c) a type-II spin-gapless semiconductor.

4.1 Heusler alloys

The discovery of Heusler compounds dates back to the beginning of the 20th century when Heusler revealed that the addition of *sp* elements to Cu-Mn alloys makes such materials ferromagnetic even though these alloys do not contain any ferromagnetic element [102]. Originally, Heusler compounds have been defined as ternary intermetallic compounds. At the stoichiometric composition, the family is subdivided into full Heuslers (X_2YZ) and semi-Heusler compounds (XYZ) which crystallize in $L2_1$ and $C1_b$ structures, respectively. Thus, one unit cell is composed of four interpenetrating fcc sublattices where atoms are located at the positions $(0, 0, 0)$ and $(1/2, 1/2, 1/2)$ for the X element, $(1/4, 1/4, 1/4)$ for the Y atom and $(3/4, 3/4, 3/4)$ for the Z element (see Fig. 4.2). In semi-Heusler compounds, the site $(1/2, 1/2, 1/2)$ is vacant. The $L2_1$ structure forms when the nuclear charge of the X element is less than the one of Y in the same period while $C1_b$ forms under the opposite conditions [103]. It is worth noting that the $C1_b$ structure can be created out of the $L2_1$ by interchanging 50% of the X atoms with Y elements. Accordingly, this structure is no longer centrosymmetric. In most of the today known Heusler compounds, Mn enters as Y element while it is also possible that Mn occupies the X positions although only a few of these systems were studied experimentally [104–107]. Fundamentally, the Heusler structure is formed from the ordered coupling of two binary B2 compounds, i.e. XY and XZ, where both compounds may crystallize in CsCl type structure, e.g., CoMn and CoAl result in Co_2MnAl . Thus, the ability of materials to crystallize in the B2 structure indicates the possibility to form new

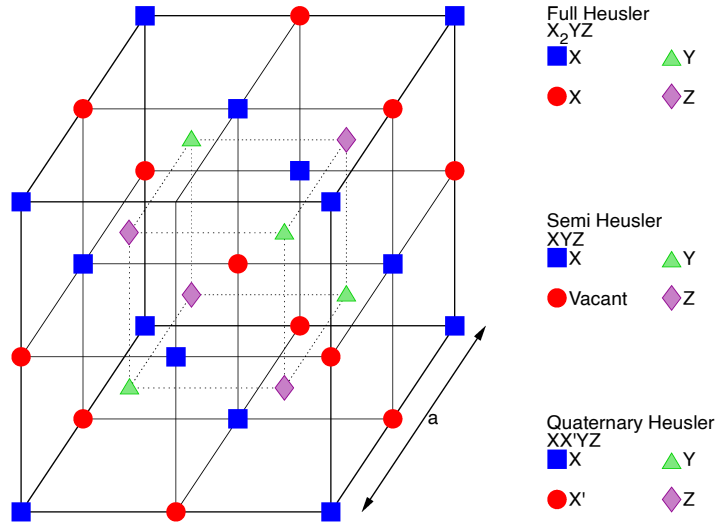


Figure 4.2: Structure adapted by half, full, and quaternary Heusler alloys. The lattice consists of four interpenetrating fcc lattices where in the case of semi-Heusler alloys (XYZ), one sublattice is vacant.

Heusler compounds. Furthermore, it is also possible to leave one of the four sublattices unoccupied, so that such materials crystallize in the $C1_b$ structure. In the literature, the latter compounds are often denoted as semi- or half-Heusler compounds, while the compounds in the $L2_1$ structure are labeled full-Heusler alloys. Extensive experimental studies revealed that in stoichiometric composition the majority of Heusler compounds orders ferromagnetically. Through the observation of the shape memory effect in the compound Ni_2MnGa [108] and the discovery of half-metallic magnetism in $NiMnSb$ [96], Heusler alloys aroused tremendous theoretical and experimental interest within the last decades. Heusler compounds possess interesting magnetic properties. Within the same family, one can study a series of interesting magnetic phenomena like antiferromagnetism, helimagnetism, Pauli paramagnetism, itinerant and localized magnetism, or heavy-fermionic behavior [109–114], but within this thesis, we stick to half-metallic magnetism and spin-gapless semiconductors. These two properties were also identified within the family of quaternary Heusler compounds.

4.1.1 Quaternary Heuslers

In addition to usual full- and inverse-Heusler compounds, a special class with 1:1:1:1 stoichiometry crystallizing in the so-called Y-type structure arouse significant interest in the last decade [115]. These quaternary Heusler alloys possess the chemical formula $(XX')YZ$ while the X , X' , and Y elements are transition-metals and Z is an *sp* element. Here the X element is only located at the position $(0, 0, 0)$ while the X' atom occupies the position $(1/2, 1/2, 1/2)$ (see Fig. 4.2). Moreover, the valence of the X' element is lower than the valence of the X atoms while the valence of the Y atom is lower than the valence of both, X and X' . In literature, the parentheses are usually omitted for reasons of simplicity and thus these materials are denoted as $XX'YZ$. The family of ordered quaternary Heusler compounds is also often named LiMgPdSn-type Heuslers, which are also known as LiMgPdSb-type Heusler alloys.

4.1.2 Half-metallic magnetism in Heusler compounds

The characteristics of half-metallic magnetism were first introduced by de Groot *et al.* based on band structure calculations of the semi-Heusler compounds $NiMnSb$ and $PtMnSb$ [96]. In such materials, one of the spin channels is metallic, whereas the other spin subbands show a gap at the Fermi level (see Fig. 4.1(a)). Moreover, Ishida *et al.* found that also the full-Heusler compounds Co_2MnZ ($Z=Si, Ge$) exhibit half-metallic behavior [116, 117]. Since then, several other systems have been predicted to possess half-metallicity. Among these materials are the binary magnetic oxides, e.g. CrO_2 and Fe_3O_4 , diluted magnetic semiconductors ($Ga_{1-x}Mn_xAs$), zinc-blende compounds ($MnAs$ and $CrAs$) [118–120], and colossal magnetoresistance materials (Sr_2FeMoO_6 and $La_{0.7}Sr_{0.3}MnO_3$) [121]. In half-Heusler compounds, the half-metallic magnetism is accompanied to their special $C1_b$ structure and

as a consequence, to the symmetry of such systems. Since the position $(1/2, 1/2, 1/2)$ is unoccupied in the $C1_b$ structure, the symmetry of those systems is reduced to tetrahedral. Thus, the half-metallic gap originates from the strong hybridization of the d -states between the higher and lower valent transition metal elements [122]. Please note here that the half-metallic behavior of semi-Heusler compounds is very sensitive to the crystal structure and symmetry. The cubic point symmetry at the Mn sites in X_2MnZ Heusler compounds causes a symmetry of Mn-3d- t_{2g} states which differs from the symmetry of the Sb- p -states. For this reason, these states do not hybridize, and thus no gap is opened in the minority spin channel. In full-Heusler compounds, the appearance of half-metallic magnetism is a subtle issue and the explanation for this is quite complicated. More details about this can be found in Ref. [123]. It was demonstrated that all half-metallic full Heuslers follow the Slater-Pauling rule $M_t = Z_t - 24$ and thus the total magnetic moment M_t scales linear with the number of valance electrons Z_t [123]. For inverse Heusler compounds it was discovered that they follow the rule $M_t = Z_t - 18$ when $X = \text{Sc, Ti}$ or in some cases V [124]. In 2013, an *ab-initio* study focusing on the magnetic and electronic properties of Heusler compounds in LiMgPdSn-type structure revealed that many of these materials exhibit half-metallic character [125]. For these compounds, a Slater-Pauling behavior was also demonstrated. In all cases where $X' = \text{V}$, $Y = \text{Ti}$, and $Z = \text{Al or Si}$, the t_{1u} states are unoccupied and are located high in energy resulting in the Slater-Pauling rule $M_t = Z_t - 18$. When $Z = \text{As}$, the s and p orbitals are located deeper in energy and therefore the minority spin d orbitals are also deeper in energy resulting in an occupation of the t_{1u} states. Thus, for all $XVTiAs$ the rule $M_t = Z_t - 24$ rule is applicable. For all the other X , X' , and Y combinations, the Slater-Pauling behavior is the same as for the full Heuslers [125].

4.1.3 Spin-gapless semiconducting behavior in Heusler compounds

The first proposed spin-gapless semiconductor has been Co-doped PbPdO_2 in 2008 [97]. Since then, many different classes of materials ranging from two to three dimensions have been identified to exhibit SGS characteristics while a few of them could be confirmed by experiments. Moreover, nowadays, graphene nanoribbons altered by CH_2 radical groups [126], HgCr_2Se_4 under a pressure of 9 GPa [127] and boron nitride nanoribbons with vacancies [128] are known to possess spin-gapless characteristics. *Ab-initio* calculations revealed that several Heusler compounds exhibit either type-I or type-II SGS behavior. The first Heusler alloy whose type-I SGS properties were experimentally demonstrated was Mn_2CoAl [106]. In addition, this Heusler compound possesses high electron and hole mobility and a Curie temperature of 720 K [106] making it suitable for spintronic applications at room temperature. In 2013, two extended *ab-initio* studies focused on the electronic and magnetic properties of quaternary Heuslers and many have been identified to be SGSs [125, 129]. In 2019 Gao *et*

al. accomplished a high-throughput screening of SGSs in ordered quaternary Heuslers where they focused on the mechanical and dynamical stability and identified 70 stable SGSs. Furthermore, based on the spin characteristics of the bands near the Fermi energy, they showed that four types of SGSs can be realized [130].

4.2 Two-dimensional materials

Two-dimensional materials which possess ferromagnetic properties are of great potential for device applications. In the past few years, especially two-dimensional transition-metal dichalcogenides arouse great interest since they possess unique optical, mechanical, electronic, and magnetic properties and are thus very interesting for a wide range of device applications. Transition-metal dichalcogenides consist of hexagonal ordered metal atoms sandwiched between two layers of chalcogen atoms. The structure of this material class is presented in Fig. 4.3 and within this family, devices ranging from vertical field-effect transistors to vertical tunnel diodes have already been experimentally realized [131–136].

Especially, two-dimensional lateral heterojunctions opened up a new research field in material science and device applications [137]. The two-dimensional morphology makes the devices very sensitive to external control and the atomic thickness enables them to become extremely compact in size.

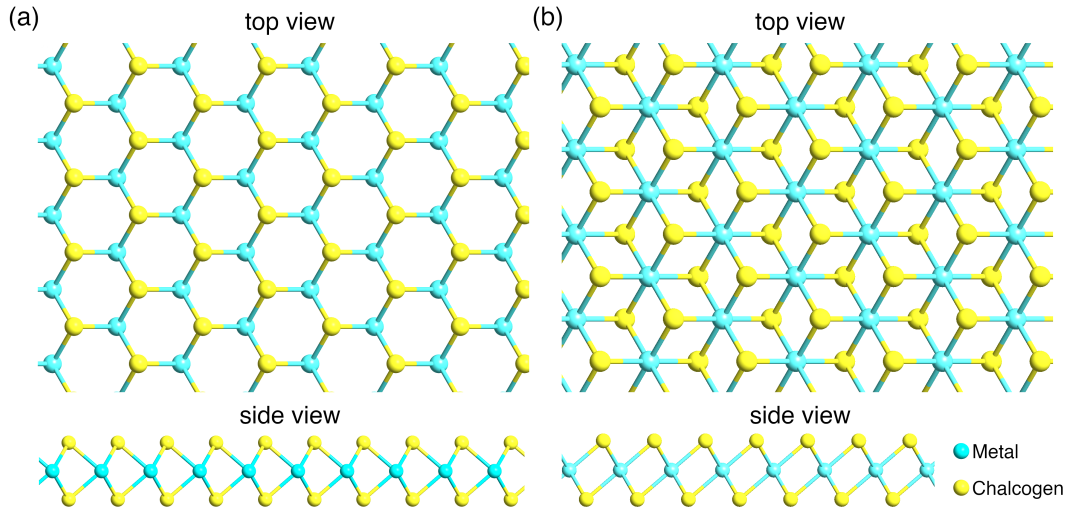


Figure 4.3: (a) Top and side view of the trigonal prismatic structure (2H phase) of two-dimensional transition-metal dichalcogenides. (b) The same as (a) for the octahedral structure (1T phase).

4.2.1 Half-metallic ferromagnetism in two-dimensional materials

In 2017, Huang *et al.* [138] discovered that one monolayer CrI_3 is an Ising ferromagnet, in particular a magnetic semiconductor which was the first experimental characterization of two-dimensional magnetism. Later, Bonilla *et al.* [139] observed ferromagnetism with large magnetic moments in two-dimensional VSe_2 on van der Waals substrates, particularly highly oriented pyrolytic graphite and MoS_2 . One monolayer Iron or Cobalt on top of two-dimensional MoS_2 (X/MoS_2 , $\text{X} = \text{Fe}, \text{Co}$) is predicted to possess robust half-metallic and thus also ferromagnetic properties with 100% spin polarization [140, 141]. On this basis of the Heisenberg spin Hamiltonian model, the calculated Curie temperature of this system is 465 K [141] making this system favorable for room temperature applications. In addition, a protective layer of h-BN does not have a negative influence on the electronic structure of Fe/MoS_2 . Thus, due to the room-temperature ferromagnetism and half-metallicity together with the excellent stability, two-dimensional Fe/MoS_2 seems to be a promising material for spintronic device applications. Among these materials, several monolayers of easily exfoliable di-halides CoI_2 , CrI_2 , FeBr_2 and FeCl_2 [142, 143], as well as tri-halides MX_3 ($\text{M} = \text{Mn}, \text{Ni}, \text{V}$ and $\text{X} = \text{Br}, \text{I}, \text{F}, \text{Cl}$) [144], and layered ternary CrSiTe_3 [145] of the telluride material class have been suggested to exhibit half-metallic magnetism.

4.2.2 Spin-gapless semiconducting behavior in two-dimensional materials

Among the family of two-dimensional transition-metal dichalcogenides, V-based compounds such as VS_2 , VSe_2 , and VTe_2 have gained particular interest in material science due to their intrinsic magnetism. Such compounds crystallize in two different phases: the 2H and 1T structure while the 2H phase is energetically more favorable [146]. In the 2H phase, the geometry of the metal atoms is trigonal prismatic (see Fig. 4.3 (a)), whereas in the 1T phase, one of the chalcogen layers is shifted with respect to the metal layer, which results in an octahedral geometry around the metal atoms (see Fig. 4.3 (b)). In fact, theoretically, in V-based compounds, both, the 2H and 1T phase, have been predicted to exhibit ferromagnetism [147], but experimentally it has only been verified in the 1T phase of VSe_2 [139] and VS_2 [148]. For VS_2 , it has been theoretically predicted that the 2H phase is energetically more stable and possesses a spin-gapless ground state [146, 149] while the 1T phase of VSe_2 does not present a spin-gapless behavior and is thus a normal ferromagnetic material. Nevertheless, depending on the growth conditions multiple two-dimensional transition-metal dichalcogenides are known to adopt either 2H or 1T structure in the one-monolayer limit [150]. Consequently, VS_2 crystallized in the 2H phase seems to be the most promising material for spintronic application within the family of transition-metal dichalcogenides. In addition to the aforementioned materials, also transition-metal di-halides MX_2 ($\text{M} = \text{Ni}, \text{Sc}, \text{Y}$ and $\text{X} = \text{Br}, \text{Cl}, \text{I}$) are predicted to possess spin-gapless semiconducting behavior [142, 143].

5 Overview of spintronic devices

Over more than four decades, chipmakers were able to scale down complementary metal-oxide-semiconductor (CMOS) field-effect transistors which allowed Moore's law [1] to stay on track. According to this law, the number of transistors in dense integrated circuits doubles every two years, which improves the performance in most of the circuits. Unfortunately, in pursuance of the International Roadmap for Devices and Systems (IRDS), scaling will reach the intrinsic physical limit in the near future [151].

Nowadays, integrated circuits are inextricable parts of microcontrollers and computer processors. The current computing technology is based on the von Neumann architecture [152], which consists of four separate elements, i.e. the central processing unit (CPU), the memory unit, the bus system, and the input/output devices. The bus system is shared between all elements leading to the so-called memory bottleneck [153]. Since the clock speed of the CPU exceeds the data transfer rate, the CPU is continually forced to wait for data from the memory. On top of that, it was demonstrated that for many computing tasks, most of the energy and time is needed for the data transfer between the memory and the CPU, rather than the information processing itself [154]. Moreover, the CPU and memory speed has increased much faster than the data transfer rate leading to an increase in the severity of the bottleneck with every new CPU generation.

To mitigate the memory bottleneck, in modern computer processors, high-speed memory, the so-called cache, is located close to the CPU, storing only the most frequently accessed data and instructions. This cache is made up of static random access memory (SRAM), which consists of six CMOS transistors and is therefore volatile. In addition to the volatility, SRAM elements are quite large, and thus, occupy a lot of space. As a result, the storage capacity of the cache is very small. Hence, replacing the SRAM elements with a non-volatile memory technology is an active research field in industry and academia. Currently, magnetic random access memory (MRAM) [155] is the most promising contender to replace SRAM. The MRAM technology combines relatively high access speeds with non-volatility, low power consumption, and unlimited endurance.

Additionally, the memory bottleneck motivated researchers to develop new or alternative computing architectures. For that reason, the research field of spintronics has attracted a lot of attention as it aims to improve the device performance in terms of memory and processing capability, and very low power consumption. As a result, many new spintronic devices have been proposed [156], ranging from beyond-CMOS devices [157] like BiSFETs [158] or spin-transfer-torque domain wall (STT/DW) devices [159] to racetrack memory [160] with skyrmions as information carriers [161] to replace conventional memory elements. Therefore, we focus here on the fundamentals of a few selected diode and transistor concepts. In the following, we will introduce the basic phenomena, which are favored for spintronics to replace conventional electronics in integrated circuits, i.e. the GMR and TMR effect, and then, we concentrate on five selected spin diodes. Afterwards, we introduce five spin transistors.

5.1 Giant magnetoresistance and tunnel magnetoresistance effect

Grünberg and Fert studied the electrical resistance in Fe/Cr multi-layer films and superlattices, respectively [4, 5]. The giant magnetoresistance (GMR) effect was carried out by the two groups independently on slightly different samples. They found that increasing the thickness of the non-magnetic Cr layers weakened the anti-parallel alignment of the magnetization of the Fe layers and led to a significant change of the electrical resistance when applying an external magnetic field. This effect can be attributed to the spin-dependent scattering of electrons in the Fe layers since aligning the magnetic orientation of the Fe layers to parallel allows electrons with a specific spin to flow through the sample, and thus, reduces the electrical resistance. Hence, the GMR effect can be evaluated by the following equation

$$\text{GMR} := \frac{\Delta R}{R} = \frac{R_{\uparrow\downarrow} - R_{\uparrow\uparrow}}{R_{\uparrow\uparrow}}. \quad (5.1)$$

After the discovery of the GMR effect, the interaction between magnetism and transport phenomena attracted great attraction and inspired the development of technical applications, i.e., magnetic recording heads in hard disk drives were successfully fabricated utilizing the GMR principle. Although, for some systems, large GMR values have been obtained at low temperatures, the ratios at room temperature were fairly small [162].

A different effect where also the resistance of the junction depends on the orientation of the magnetization of the electrodes emerges in tunnel junction formed by an insulating layer sandwiched between two magnetic layers and connected to two current-voltage probes. The two magnetic layers are therefore magnetically decoupled, and thus, their mutual orientation

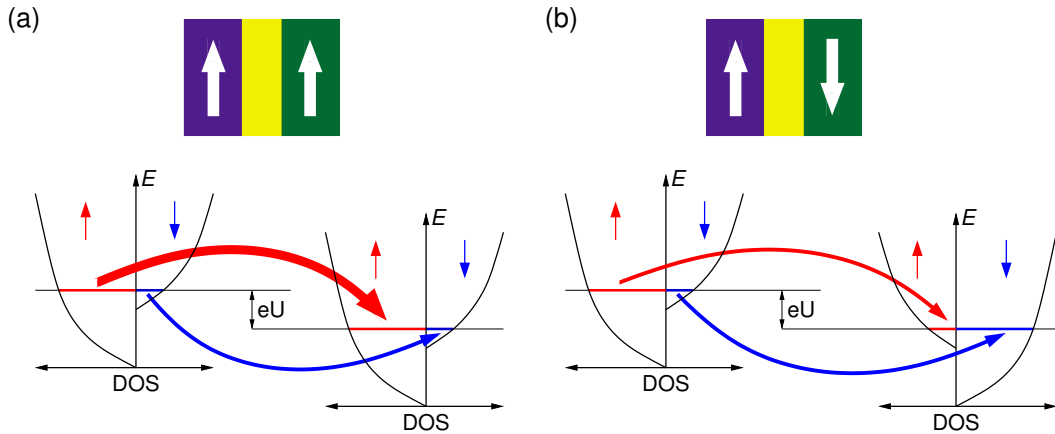


Figure 5.1: Two-current model for (a) parallel and (b) anti-parallel orientation of the magnetization of the electrodes of a magnetic tunnel junction. The thickness of the arrows is proportional to the amount of electrons which are able to tunnel through the barrier.

can be manipulated by applying an external magnetic field. If the tunnel barrier is thin enough, electrons are able to tunnel from one electrode to the other. Usually, the parallel alignment of the magnetization directions is the high-current state and the anti-parallel belongs to the low-current state (see Fig. 5.1). The efficiency of the electronic device is defined by the TMR ratio which is, according to Jullière's model [6], for zero bias given by

$$\text{TMR} := \frac{G_{\uparrow\uparrow} - G_{\uparrow\downarrow}}{G_{\uparrow\downarrow}}, \quad (5.2)$$

where $G_{\uparrow\uparrow}$ and $G_{\uparrow\downarrow}$ denote the conductance in the anti-parallel and parallel orientation of the magnetization directions of the electrodes, respectively. With a bias voltage V , Eq. (5.2) becomes

$$\text{TMR} = \frac{I_{\uparrow\uparrow} - I_{\uparrow\downarrow}}{I_{\uparrow\downarrow}}, \quad (5.3)$$

where $I_{\uparrow\uparrow}$ ($I_{\uparrow\downarrow}$) is the electrical flux through the magnetic tunnel junction (MTJ) for parallel (anti-parallel) orientation of the magnetization of the leads.

Although the TMR effect was already known since 1975 [6], remarkable results at room temperature have been measured first by Miyazaki *et al.* in 1994 [163] and Moodera *et al.* in 1995 [164]. In 2001, Mathon and Umerski [165] and Butler *et al.* [166] predicted large TMR effects of several thousand percent for iron electrodes separated by MgO. Within the same year, Bowen *et al.* demonstrated significant TMR values in epitaxial Fe/MgO/FeCo(001) tunnel junctions on GaAs(001) [167]. The breakthrough of the TMR effect was in 2004 when Parkin *et al.* [7] and Yuasa *et al.* [168] were able to fabricate Fe/MgO/Fe junctions which reached a TMR value of more than 200% at room temperature. Since then, MTJs have replaced GMR devices. Besides this, the TMR effect aroused great interest for spintronic device applications and is the basis of new non-volatile storage concepts like magnetic random access memory (MRAM) [169], mLogic [170], and all-spin logic devices [171].

Moreover, it was proposed that in asymmetric junctions, the amount of $I_{\uparrow\downarrow}$ exceeds $I_{\uparrow\uparrow}$ independent of the applied bias voltage, and thus, leads to a negative TMR value [172, 173].

5.2 Spin diodes

Currently, there is an enormous interest in the development of spintronic devices in which utilizing the spin of electrons, other than just the charges, is preferred to obtain new functionalities which go beyond the possible ones of conventional electronic devices. Spintronic diodes are revolutionary candidates, which have repercussions on several technological applications ranging from neural networks to the Internet of Things [174] due to the ability to combine rectification and memory in a single device. For instance, spin-torque diodes are promising

devices to emulate neurons in neuromorphic computing systems [175, 176]. In the following, we briefly overview the concept of five selected spintronic diodes. First, the spin-orbit torque diode and thereafter the magnetic tunnel diode, the resonant magnetic tunnel diode, the reconfigurable magnetic tunnel diode and finally, the Ohmic spin diode.

5.2.1 Spin-torque diode

In 2005, Tulapurkar *et al.* [177] discovered the spin-torque diode effect in MTJs. The authors designed a tunnel device that was able to convert a spin-polarized microwave current into a rectified voltage due to the simultaneous actions of a spin-transfer torque and the tunneling magnetoresistance (see Fig. 5.2 for a schematic illustration of the spin-torque diode effect). From then on, the interest in spin-torque diodes increased for two main reasons: (i) due to the complementary metal-oxide-semiconductor (CMOS) compatibility, i.e. these diodes can be fabricated with the same materials which are used for spin-transfer-torque MRAMs, and (ii) due to their size, i.e. actually they are the smallest known rectifiers. The performance of such spintronic diodes can be characterized by many different quantities such as output resistance, noise equivalent power (NEP), conversion efficiency, or sensitivity. The conversion efficiency is defined as the ratio between the dc delivered power and the input microwave power, and the sensitivity describes the amount of the rectified output from the input microwave power.

Recently, the spin-torque diode was also tipped to operate as a neuron in neuronal networks [175, 176].

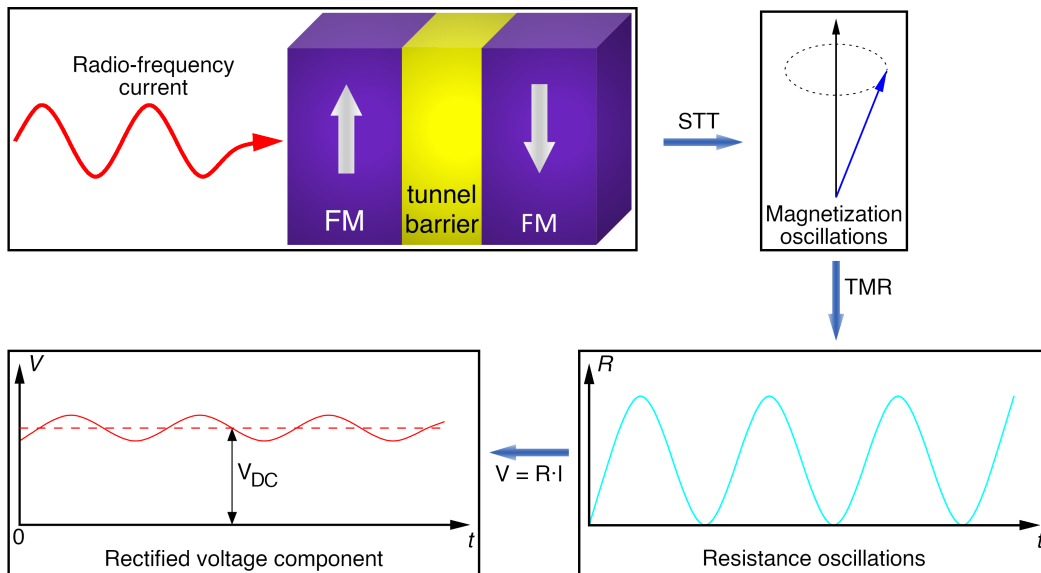


Figure 5.2: Schematic drawing of the spin-torque diode effect.

5.2.2 Magnetic tunnel diode

Due to their capability to achieve high-frequency operations, magnetic tunnel diodes (MTDs) (ferro-magnet–insulator–ferromagnet diodes), also known as spin tunnel diodes, are potential candidates for high-speed diode applications. Similar to conventional metal-insulator-metal (MIM) diodes, good performance requires high asymmetry, large response, and strong non-linearity together with low resistance [178]. These figures of merit are mainly affected by the difference in the work functions of the electrodes ($\phi_1 - \phi_2$) and the height of the tunnel barrier. On the one hand, a high asymmetry requires a high tunnel barrier together with a large work function difference of the electrodes, but on the other hand, a high tunnel barrier reduces the on-current. Consequently, a trade-off between these parameters is necessary. If a forward bias voltage is applied to a MTD, the effective thickness of the insulating layer is reduced, leading to an exponential increase of the tunneling current. Depending on the relative orientation of the magnetization of the electrodes, the MTD is situated either in a high-current or low-current state (see Fig. 5.3 for a schematic drawing of the operation principle of a MTD and the corresponding current-voltage characteristics). Therefore, MTDs are possible devices to combine rectification with memory.

However, symmetric MTDs ($\phi_1 = \phi_2$) are not applicable for logic application since their current-voltage characteristics are symmetric with $I(V) = -I(-V)$, leading to a loss of the rectification properties. Another approach to solving the issue of symmetric $I - V$ curves is to fabricate MTDs with two different insulating materials, which was introduced by de Buttet *et al.* [179] in 2006. Due to the different work functions of the insulators, in one bias direction, the effective barrier thickness and height decreases, while in the opposite bias direction, these quantities stay unchanged, leading to asymmetric current-voltage characteristics. One shortcoming of this approach is that the TMR value of these tunnel diodes with composite insulating layers lies between the achieved values for the single insulators, and thus, is not optimal [179]. Moreover, the asymmetry of the $I - V$ curve depends strongly on the thickness

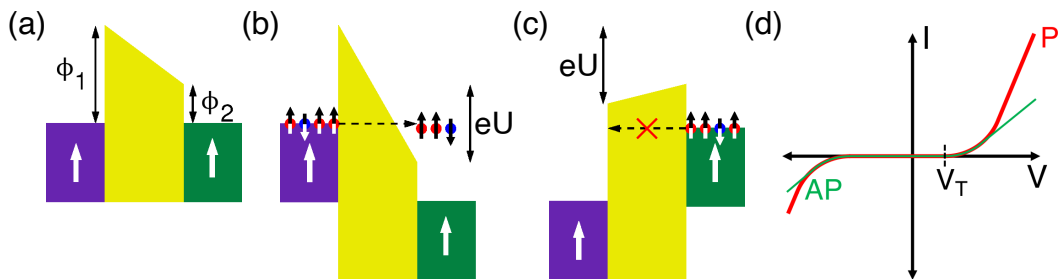


Figure 5.3: Schematic band diagram of a magnetic tunnel diode with parallel aligned magnetization of the electrodes (a) in equilibrium, (b) for and applied forward and (c) reverse bias voltage. (d) illustrates the $I - V$ curve for parallel (P) and anti-parallel (AP) orientation of the magnetization of the electrodes.

of both insulating materials [179].

Nevertheless, to ensure that the dominant transport mechanism is tunneling, the thickness of the insulating layer is designed below 4 nm [180], and hence there occur challenges related to the fabrication process of the very thin insulating layer.

5.2.3 Resonant magnetic tunnel diode

Resonant MTDs are of particular interest for magnetic memory technologies since the current MRAM cross-point memory architecture requires either a diode or a CMOS transistor (selection device) connected in series with the memory cell to block disturbing signal paths within the array of lines (sneak paths) [182, 183]. Nevertheless, the fabrication of MTJs together with CMOS transistors is challenging and hampers such a concept. To avoid the implementation of additional semiconductor components, Chshiev *et al.* [184] introduced a resonant MTD concept, which is based on an asymmetric double-barrier structure, and its asymmetric properties can be varied via an external magnetic field. Double tunnel junctions consist of two tunnel barriers of different transparency for the electrons, two ferromagnetic electrodes, and a non-magnetic contact (see Fig. 5.5(a)). The two tunnel barriers are anticipated to possess highly asymmetric conduction for different biases, and thus, act as a diode or current rectifier [184]. In the case of spin-independent conductivity, i.e., vanishing magnetoresistance, such a current rectification in double tunnel junctions was already identified [185], while effects of resonant transmission have been identified in the symmetric double tunnel junction Fe/MgO/Fe/MgO/Fe [186] although with a rather weak current rectification. Strong diode effects with a high current rectification ratio were demonstrated by Iovan *et al.* in 2006 in asymmetric metal/oxide double tunnel junctions [187].

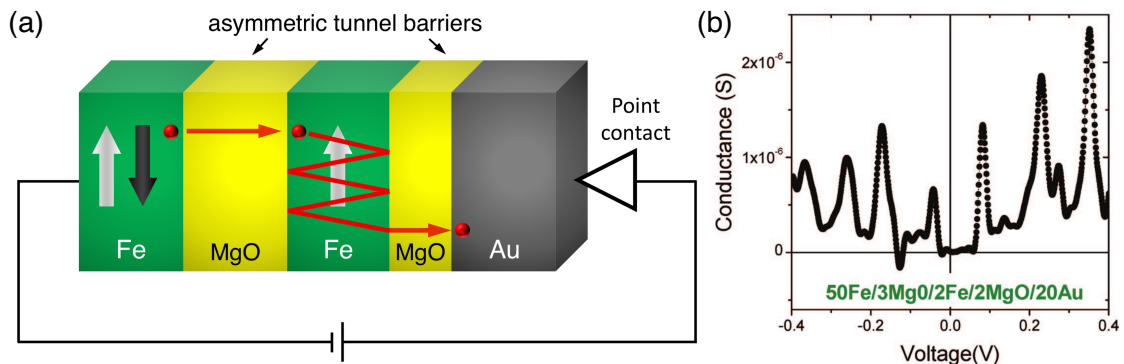


Figure 5.4: (a) Schematic drawing of the resonant spin tunnel diode and (b) the differential conductance (dI/dV) as a function of the applied bias voltage (V) in the quantum transport regime. The numbers in the lower part of the figure quote the thickness of the individual layers in nanometers. From A. Iovan *et al.* Spin Diode Based on Fe/MgO Double Tunnel Junction *Nano Lett.* **8**, 805 (2008); Ref. [181]. Reproduced with permission from the American Chemical Society (ACS).

Large resonant magnetic tunnel magnetoresistance values combined with a high current rectification ratio were observed in magnetic double tunnel junctions [181], making these kinds of devices an efficient hybrid of a diode and a spin switch. The different thickness of the insulating layers causes an asymmetry in the transparency of the two tunneling barriers, which sandwich the ferromagnetic layer in the middle. This middle layer separated from the outer electrodes is designed to be as thick as the electron Fermi wavelength in the material, resulting in a level spacing. However, the experimental results of Iovan *et al.* [181] point out that, depending on the applied bias voltage, the conductance through the tunnel junction presents multiple peaks (see Fig. 5.5 (b)). This behavior can be attributed to the transmission of electrons through discrete quantum well states but limits the voltage range to ± 0.06 V, in which the reported asymmetric Fe/MgO/Fe/MgO/Au junction possesses a diode-like behavior [181].

5.2.4 Reconfigurable magnetic tunnel diode

In 2019, Şaşıoğlu *et al.* [11] introduced a new concept of a reconfigurable magnetic tunnel diode (MTD) and magnetic tunnel transistor (MTT), and a patent application for both kinds of devices has been filed [188]. Recently, the proposed concept of the reconfigurable MTD was experimentally demonstrated using Heusler compounds as spin-gapless and half-metallic electrode materials [189]. Both devices, the reconfigurable MTD as well as the MTT which is discussed in the next section, can overcome the limits of conventional hot-electron devices and provide some additional functionalities like nonvolatility and reconfigurability. The tunnel diode is a two-terminal device that consists of a thin insulating layer (I) sandwiched between a spin-gapless semiconductor (SGS) electrode and a half-metallic magnet (HMM) electrode (see Fig. 5.5). Electrical current can flow through the reconfigurable MTD either in one or the other direction, depending on the relative magnetization orientation of the electrodes. Also, the rectification properties of this diode depend on the relative orientation of

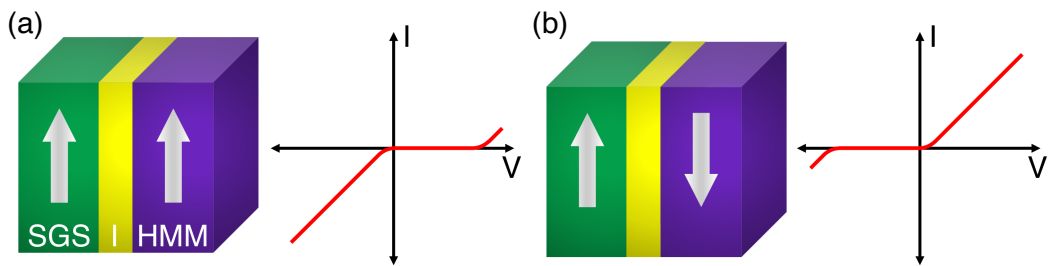


Figure 5.5: (a) Schematic drawing of a reconfigurable magnetic tunnel diode for parallel orientation of the magnetization directions of the electrodes together with the corresponding current-voltage ($I-V$) characteristics. The white arrows indicate the magnetization direction of the electrodes. (b) The same as (a) for anti-parallel orientation of the magnetization directions of the electrodes.

the magnetization of the SGS and HMM. If the electrode magnetization is parallel aligned, the tunneling current is allowed to pass only in one direction. In the opposite direction, the current is blocked completely (see Fig. 5.6 (a)). Thus, the reconfigurable MTD acts like a normal diode. When the magnetization direction of one electrode is reversed, so that we end up with an anti-parallel setup, the rectification properties of the HMM-I-SGS junction are also reversed (cf. Fig. 5.6 (b)). Due to this fact, such diodes can be configured dynamically by a current-induced spin-transfer torque or by applying an external magnetic field.

5.2.5 Ohmic spin diode

In the previous section, we introduced the reconfigurable MTD. The Ohmic spin diode (OSD) is an extension of this concept, i.e., in analogy to metal-semiconductor devices (Schottky-barrier diodes), this HMM-SGS junctions act as a diode. Under any finite forward bias, the two electrode materials form an Ohmic contact leading to linear current-voltage characteristics, while under reverse bias, the current is blocked due to the spin-dependent filtering of the electrons. Since conventional diodes possess a junction barrier, a threshold (or turn-on) voltage V_T must be supplied to turn the diode on. Such threshold voltages give rise to power dissipation ($P = V_T \cdot I$) in the form of heat, and thus, it is an undesirable feature. Due to the linear scaling of P with V_T , the power dissipation increases with increasing values of the threshold voltage. Contrary to conventional $p - n$ diodes, OSDs do not require any form of doping and exhibit no turn-on voltage. Other advantages of the OSD compared to conventional semiconductor diodes are the low resistance and the much higher current drive capability. Further details about the operation principle and features of the OSD are presented in Section 6.3.

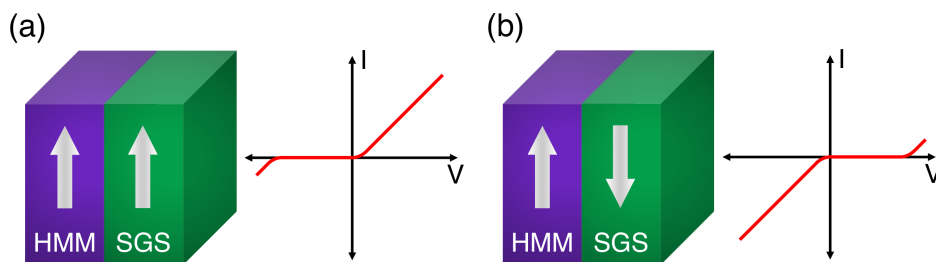


Figure 5.6: (a) Schematic drawing of an Ohmic spin diode in parallel orientation of the magnetization directions of the electrodes together with the corresponding current-voltage characteristics. (b) The same as (a) for anti-parallel orientation of the magnetization directions of the electrodes. The white arrows display the magnetization direction of each electrode.

5.3 Spin transistors

As mentioned in the introductory part of this chapter, conventional CMOS transistors had unprecedented success with scaling their dimension, but downscaling will reach the fundamental physical limits in the near future [151, 190]. Thus, in the following, we present five selected beyond-CMOS device concepts. First, we focus on the Datta-Das transistor and afterwards the spinFET, the spin-valve transistor, the magnetic tunnel transistor, and finally, we elucidate the basic idea behind the reconfigurable magnetic tunnel transistor.

5.3.1 Datta-Das transistor

In 1990, Datta and Das [191] proposed a new principle for an electronic device similar to optical devices by making use of the similarities between the polarization of a photon and the spin of an electron. The inspiration for this came from an optical device that consisted of an analyzer and a polarizer positioned at 90° to each other. Thus, in the initial configuration, the transmission of light is minimal. However, the polarizer and analyzer in the optical device were sandwiched between an electro-optical material that, by applying an external bias voltage, allowed to rotate the polarization of the photons when they propagate. When the

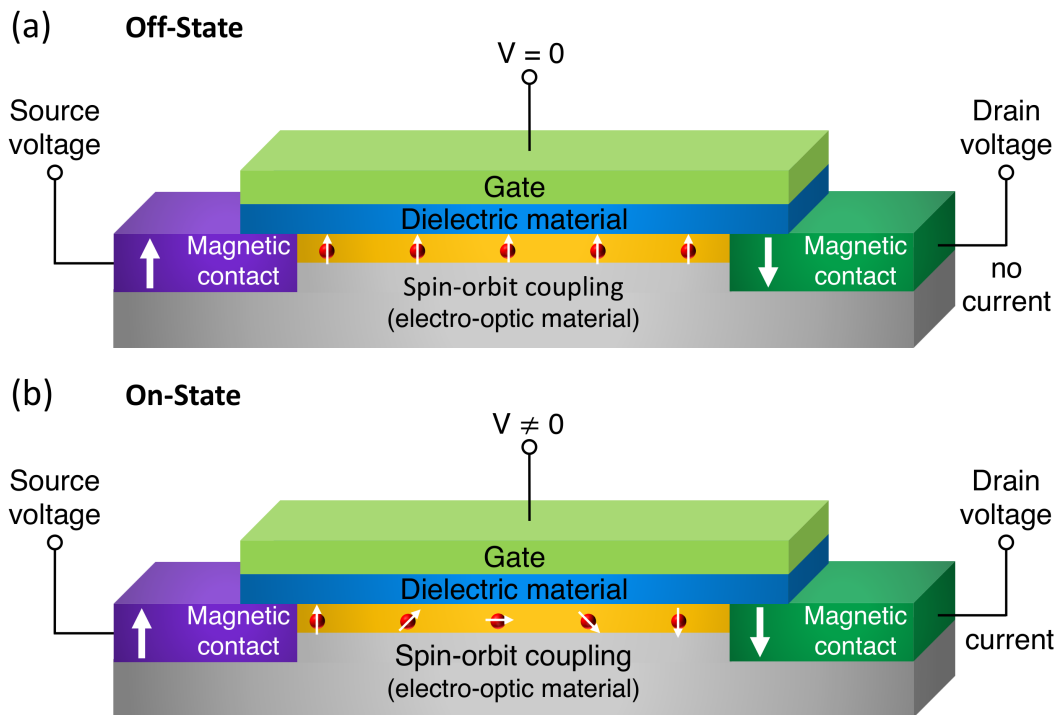


Figure 5.7: Schematic representation of the (a) off-state and (b) on-state of a Datta-Das transistor. The arrows display the magnetization direction of the source and drain material as well as the spin direction of the conduction electrons.

polarization was rotated by 90° , the transmission reached the maximum. Datta and Das proposed to use a device similar to a commercial field-effect transistor (FET) but with magnetic contacts. The electrons injected from the source possess spins aligned to the magnetization direction, similar to a polarizer that allows only photons with a specific polarization to pass (see Fig. 5.7). Similarly, the drain acts as an analyzer and transmits only electrons with an appropriately aligned spin. Thus, if the source injects majority-spin electrons and the drain detects minority-spin electrons, the transmission should be minimal (see Fig. 5.7 (a)). If the spin of the injected electrons is rotated when they traverse the channel connecting source and drain, the transmission reaches its maximum as in the optical case (see Fig. 5.7 (b)). Nevertheless, please note here a remarkable difference. To block photons, we need an analyzer and polarizer at 90° , while in the case of electrons, they need to be at 180° [192]. This is based on a fundamental difference: due to the spin of a photon ($s = 1$), the state of this particle is invariant under a rotation of 360° whereas an electron ($s = 1/2$) returns to its initial state under a rotation of 720° . The challenge in the principle of the Datta-Das transistor is to control the rotation of the spin of the traversing electrons. One possibility is an external magnetic field in the x -direction, which would result in a rotation of the spins in the yz -plane. Another way is the application of an electric field, providing that the channel presents spin-orbit interaction. Koo *et al.* suggested one version of the device in 2009 [193] and a different variant in 2015 [194]. This device is a so-called spin transistor since the gate voltage changes the resistance from a high value (off-state) to a low one (on-state), just as in a conventional CMOS transistor. Despite enormous attempts, up to now, the Datta-Das transistor has not been experimentally realized.

5.3.2 Spin field-effect transistor

Spin field-effect transistors (spinFETs) [195] combine conventional metal-oxide-semiconductor field-effect transistors (MOSFET) with switchable magnetic elements. The source and drain electrodes consist of ferromagnetic materials, and additionally, a MTJ is positioned over the

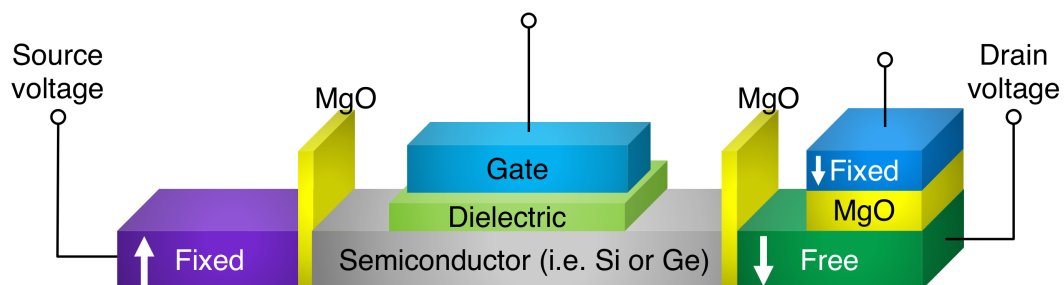


Figure 5.8: Schematic drawing of a spinFET. The white arrows indicate the magnetization direction of each ferromagnetic material.

drain to detect the relative magnetization direction of the drain contact via the TMR effect (see Fig. 5.8 for a schematic representation of the structure of a spinFET). In contrast to a conventional field-effect transistor, the resistance of the spinFET depends on the relative orientation of the magnetization directions of the source and drain electrodes. When they are oriented anti-parallel, the resistance of the channel is high, while in the case of a parallel orientation, the resistance is low. Additionally to the current that flows through the channel, the magnetization direction of the drain electrode can be switched by a current, which can be controlled by the applied voltage to the MTJ on top of the drain electrode.

Based on the half-metallic ferromagnetic Heusler compound $\text{Co}_2\text{FeAl}_{0.5}\text{Si}_{0.5}$, a spin-transfer-torque-switching MOSFET (STS-MOSFET) [196] was experimentally realized, offering transistor functions with CMOS compatibility and non-volatile memory together with high endurance and fast write times [197, 198].

5.3.3 Spin-valve and magnetic tunnel transistor

Another spintronic transistor is composed of two electrodes spaced by a very thin layer consisting of either alternating ferromagnetic and non-magnetic metallic materials, and thus, creating a spin-valve transistor [199], or an insulator, creating a magnetic tunnel transistor (MTT) [200] (see Fig. 5.9).

Spin-valve transistors were the first device in which semiconductors and ferromagnets have been closely integrated, and the properties of both materials are essential for controlling the current through the device [201]. The two magnetic layers in the spin-valve base act as an analyzer and polarizer of electron spins in the way that the relative orientation of the mag-

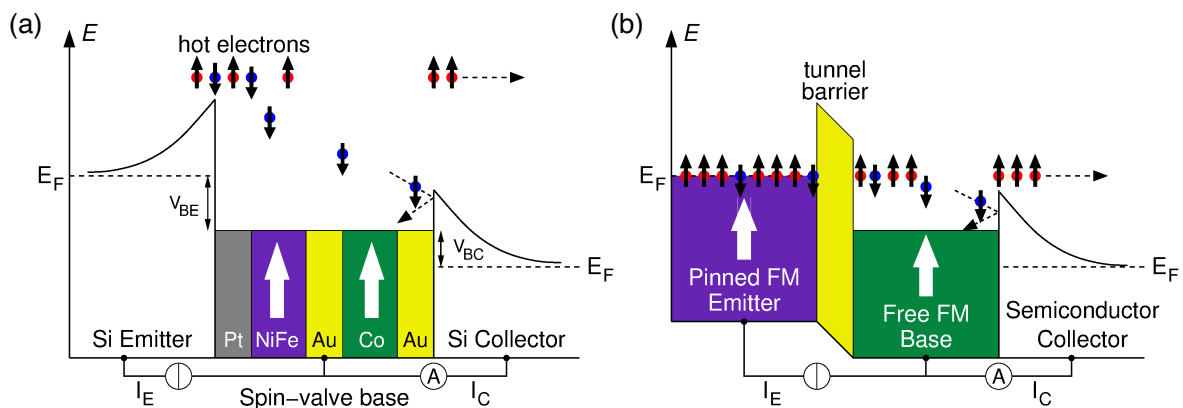


Figure 5.9: (a) Schematic drawing of the operation principle of a spin-valve transistor. (b) The same as (a) for the magnetic tunnel transistor. The white arrows represent the magnetization direction of the ferromagnetic materials while the black arrows display the spin of the conduction electrons.

netization direction of the two magnetic layers strongly affects the transmission through the base. Thus, the collector current depends on the magnetic order of the base. At the interface between the base and the semiconductors, energy barriers (Schottky barriers) arise [202]. These barriers inhibit electrons at the Fermi energy from flowing through the transistor. As a consequence, the operation principle of the spin-valve transistor relies on the spin-dependent transport of hot (non-equilibrium) electrons. When these hot electrons enter the base, they are involved in elastic as well as inelastic scattering processes which change their momentum distribution and energy. The scattering rate in the spin-valve structure can be controlled via an external magnetic field which changes the relative alignment of the magnetization directions of the ferromagnetic layers in the base electrode. Moreover, electrons can only enter the collector if they have retained enough energy to overcome the energy barrier and if their momentum matches with one of the available states in the semiconductor (see Fig. 5.9 (a)).

The principle of a MTT is somewhat similar. This device consists of a ferromagnetic emitter electrode, an insulator/metal base, and a semiconductor collector layer [200, 203, 204]. When a bias voltage is applied to the ferromagnetic emitter, spin-polarized electrons are injected into the base electrode through the tunnel barrier. The energy of the injected electrons can be varied by changing the bias voltage across the insulator. As in the spin-valve transistor, elastic and inelastic scattering processes in the base layer lead to a change of the momentum and/or a loss of energy, and only the electrons which maintain enough energy to surmount the energy barrier at the interface to the collector can be transmitted into available states in the semiconductor electrode (see 5.9 (b) for a schematic representation of the operation principle of a MTT). Since most of the scattering depends on the spin of the electrons, the collector current depends on the orientation of the magnetization of the base layer with respect to the one of the emitter material, and thus, can be controlled via an external magnetic field, as in the case of the spin-valve transistor.

5.3.4 Reconfigurable magnetic tunnel transistor

The reconfigurable magnetic tunnel diode, which was presented in the spin diode section (Section 5.2), lays the foundation for the three-terminal reconfigurable magnetic tunnel transistor (MTT). This type of transistor can be thought of as two back-to-back MTDs and is composed of a HMM-I-SGS-I-HMM structure which forms the emitter, base, and collector (see 5.10 (a)). The transistor allows electrons to flow in both directions, similar to a normal field-effect transistor, and can be switched from off to on by applying a bias voltage to the base electrode. Regardless of any reasonable applied positive bias voltage to the collector electrode, the transistor is in the off-state when no bias voltage is applied across the emitter-base insulator (see 5.10 (c)). In the off-state, the base-collector leakage current is suppressed up to a certain positive collector voltage ($V_{CB} > 0$) since electrons are not able to tunnel

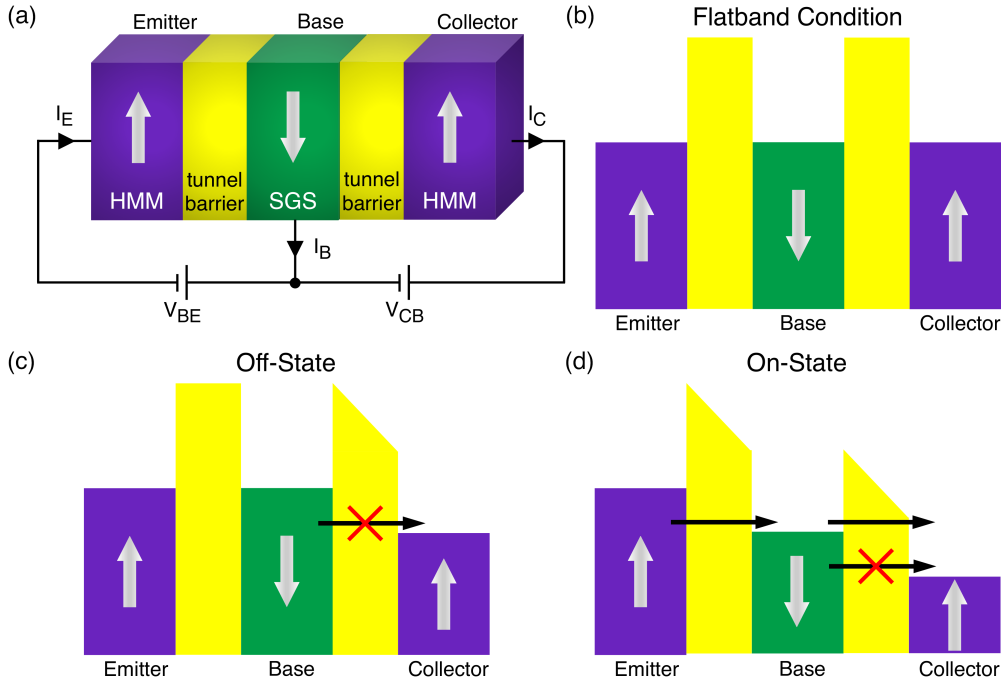


Figure 5.10: (a) Schematic picture of a reconfigurable magnetic tunnel transistor. (b) Its band diagram under flatband condition, (c) in the off- and (d) the on-state. The arrows represent the orientation of the magnetization direction of each electrode.

from the SGS base to the HMM collector due to the lack of states around the Fermi level in the half-metallic material. This can be easily understood on the basis of the schematic DOS picture of the SGS and the HMM, which we provided in Chapter 4 (Fig. 4.1). The maximum collector voltage at which the leakage current is completely blocked is determined by the energy difference between the Fermi energy and the majority-spin valence band, which usually amounts to less than 1 eV [205]. When one applies a finite positive bias voltage to the base electrode, as well as a finite bias to the collector electrode ($V_{BE} > 0$), hot electrons with high kinetic energy are transmitted from the emitter to the base through the tunneling barrier between both electrodes. These injected hot electrons will travel through the base region while some of them keep their high energy and, accordingly, are able to reach the half-metallic collector (see 5.10 (d)). Some other electrons might thermalize in the base electrode resulting in a base current I_B . Thus, the emitter current I_E is defined as the sum of the base and collector currents $I_E = I_B + I_C$. As a result, by applying a bias voltage to the base electrode, we are able to control the state of the reconfigurable MTT. An important feature of this transistor is that electrons can be transmitted in both directions like in conventional CMOS transistors which does not hold for hot-electron tunnel transistors in consequence of the thick base-collector tunnel barrier [206–208].

Due to the fact that the tunnel current exponentially increases with decreasing height

and thickness of the tunnel barrier, the insulating layer of the reconfigurable MTD and MTT should be as small as possible, resulting in an increase in the device performance. The current-voltage characteristics of the transistor are comparable to those of conventional unipolar hot-electron transistors, except for two strong distinctions: (i) the reconfigurable MTT does not exhibit a base-collector leakage current up to a specific base-collector bias voltage, and (ii) it allows for dual-mode operation. The latter implies that by applying a negative bias voltage between base and collector ($V_{CB} < 0$), the transistor operates in reverse-current mode since the electronic properties of the base and collector material allow also for reverse tunneling. Apart from these two properties, the reconfigurable MTT allows for reconfiguration by reversing the magnetization direction of electrodes for the desired application.

6 Results and Discussion

Within the previous chapters, we elucidated the theoretical background for our computational design of spintronic devices based on spin-gapless semiconductors (SGSs) and half-metallic magnets (HMMs). We introduced our methods and described the unique electronic and magnetic properties of SGSs and HMMs for the discussion of the transport properties. In the following sections, we will present four publications and bring them into the context of the present thesis.

Screening for spin-gapless semiconductor and half-metallic magnet within the family of quaternary Heusler compounds. Within the family of quaternary Heusler compounds, it is possible to identify HMMs as well as SGSs with similar lattice constants and atomic composition. This is an important requirement to enable the coherent growth of one material on top of others. Thus, in the first publication [TA1], we search for SGSs and HMM within the family of quaternary Heusler compounds with sizable energy gaps below and above the Fermi level and high Curie temperatures for new spintronic devices.

Magnetic tunnel junctions based on spin-gapless semiconductors and half-metallic magnets for magnetic memory and logic applications. The second goal of this thesis was to investigate the current-voltage ($I - V$) characteristics and tunnel magnetoresistance (TMR) effect of magnetic tunnel junction (MTJ) for magnetic memory and logic applications. Thus, in the second paper [TA2], by employing first-principles DFT and NEGF calculations, we investigate the $I - V$ characteristics of MTJs based on SGSs and HMMs as electrode material and demonstrate that such devices allow the electrical current to pass either in one or the opposite direction, depending on the relative orientation of the magnetization of the electrodes, which leads to an inverse TMR effect.

Half-metal–spin-gapless semiconductor junctions (Ohmic spin diodes). In the third publication [TA3], we present a new spintronic device concept called Ohmic spin diode (OSD), which is somewhat similar to conventional metal-semiconductor diodes (Schottky-barrier diodes). The devices consist of one half-metallic and one type-II SGS electrode and do not possess a junction barrier. Due to the unique electronic structure of these materials, such diodes show linear current-voltage ($I - V$) characteristics under forward bias while the current is blocked under reverse bias. By employing the NEGF method combined with DFT, we provide a proof-of-principle using two-dimensional, spin-gapless semiconducting VS_2 and half-metallic Fe/MoS_2 .

Design of Ohmic spin diodes based on quaternary Heusler compounds. In the fourth paper [TA4], we design, by employing first-principles calculations, different OSDs based on

ordered quaternary Heusler compounds with high curie temperatures and demonstrate that all of these devices possess linear $I - V$ curves together with zero threshold voltages.

6.1 Screening for spin-gapless semiconductors and half-metallic magnets within the family of quaternary Heusler compounds

SGSs are the key components of the magnetic tunnel junctions showing current rectification, as we discussed in the previous chapter. In the following paper, "Ab initio design of quaternary Heusler compounds for reconfigurable magnetic tunnel diodes and transistors" [TA1], we screen the family of ordered quaternary Heusler alloys $XX'YZ$ showing SGS and HMM characteristics. These materials possess similar lattice constants together with sizable energy gaps below and above the Fermi level and high Curie temperatures for spintronic device application. In total, we identify 9 HMMs, 5 type-I SGSs, and 11 type-II SGSs (see Fig. 6.1 (a)). In particular, we discuss the tunability of the position of the conduction-band minimum and the valance band maximum for the type-II materials arising from a substitution of different Z atoms. We also calculate the exchange parameters and use them in a multi-sublattice mean-field approximation to estimate the Curie temperature for all 25 compounds. We show that the T_C values follow a semi-empirical relation $T_C \propto \sum_i |m_i|$, and thus the Curie temperature increases with increasing sublattice magnetic moments (see Fig. 6.1 (b)).

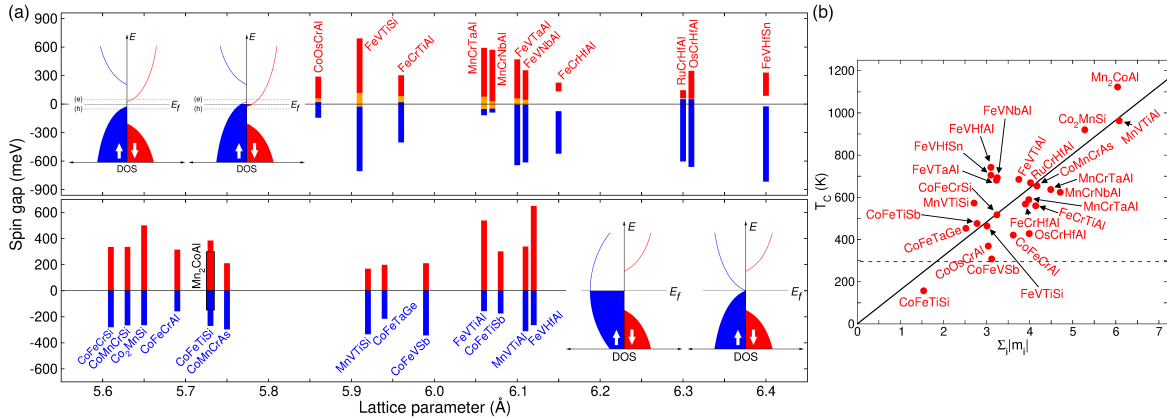


Figure 6.1: (a) Comparison between the lattice parameters of type-II SGSs and type-I SGSs as well as HMMs. The red and blue bars indicate the size of the gap in the majority and minority spin channel around the Fermi energy E_F , respectively. The orange or white bars represent the value of the overlap or the spin gap, respectively. The Fermi level is set to 0 meV. (b) The dependence of the calculated Curie temperatures on the sum of the absolute values of the sublattice magnetic moments. The dashed black line indicates the room temperature while the solid black line displays a linear fit. Adapted (figure) with permission from (T. Aull *et al.* Phys. Rev. Mater. **3**, 124415 (2019); *Ab initio* design of quaternary Heusler compounds for reconfigurable magnetic tunnel diodes and transistors, Ref. [TA1]). Copyright (2019) by the American Physical Society (APS).

The following publication: Reprinted (whole article) with permission from (T. Aull *et al.* Physical Review Materials **3**, 124415 (2019); *Ab initio* design of quaternary Heusler compounds for reconfigurable magnetic tunnel diodes and transistors, Ref. [TA1]). Copyright (2019) by the American Physical Society (APS).

***Ab initio* design of quaternary Heusler compounds for reconfigurable magnetic tunnel diodes and transistors**T. Aull ^{1,*}, E. Şaşıoğlu ¹, I. V. Maznichenko,¹ S. Ostanin,¹ A. Ernst,^{2,3} I. Mertig,^{1,2} and I. Galanakis ⁴¹*Institute of Physics, Martin Luther University Halle-Wittenberg, D-06120 Halle (Saale), Germany*²*Max Planck Institute of Microstructure Physics, Weinberg 2, D-06120 Halle (Saale), Germany*³*Institute for Theoretical Physics, Johannes Kepler University Linz, Altenberger Straße 69, A-4040 Linz, Austria*⁴*Department of Materials Science, School of Natural Sciences, University of Patras, GR-26504 Patra, Greece*

(Received 20 August 2019; revised manuscript received 6 November 2019; published 30 December 2019)

Reconfigurable magnetic tunnel diodes and transistors are a new concept in spintronics. The realization of such a device requires the use of materials with unique spin-dependent electronic properties such as half-metallic magnets (HMMs) and spin-gapless semiconductors (SGSs). Quaternary Heusler compounds offer a unique platform to design within the same family of compounds HMMs and SGSs with similar lattice constants to make coherent growth of the consecutive spacers of the device possible. Employing state-of-the-art first-principles calculations, we scan the quaternary Heusler compounds and identify suitable candidates for these spintronic devices combining the desirable properties: (i) HMMs with sizable energy gap or SGSs with spin gaps both below and above the Fermi level, (ii) high Curie temperature, (iii) convex hull energy distance less than 0.20 eV, and (iv) negative formation energies. Our results pave the way for the experimental realization of the proposed magnetic tunnel diodes and transistors.

DOI: [10.1103/PhysRevMaterials.3.124415](https://doi.org/10.1103/PhysRevMaterials.3.124415)**I. INTRODUCTION**

The growing interest in nanotechnology in the last decades laid the foundation of research in new materials with novel properties. In particular, the prediction of new magnetic nanomaterials for the realization of spintronic devices has become extremely important [1]. There are two ways to incorporate spin in electronic devices: either doping semiconductors with magnetic ions like Mn, Cr, or Fe in diluted magnetic semiconductors [2] or the growth of nanoscale magnetic materials like Heusler compounds [3]. The development of computational materials science triggered all these developments in spintronics. In particular, computational materials science paved the way for high-throughput screenings, which permitted efficient simulations of materials in order to predict magnetic, optical, and electronic characteristics, etc., of new materials. Furthermore, the simulations allowed researchers to investigate new metastable structures of known alloys where the electronic features change completely concerning the properties of the known stable structures.

Among the various materials under study for spintronics and magnetoelectronics, magnetic Heusler compounds have a significant importance due to their wide variety and their high Curie temperatures, and thus several studies covering their fundamental properties and their applications have been carried out [4]. Among the magnetic Heusler compounds, several have been identified as half-metallic magnets [5–9]. Also, even more peculiar properties have been suggested in literature like spin-gapless semiconducting or spin-filtering

properties, which lead to new functionalities [10]. Modern deposition techniques made fabrication of these exotic materials possible. A recent example is (CrV)TiAl, a quaternary Heusler compound which was predicted in Ref. [11] to be a fully compensated ferrimagnetic semiconductor, and then it was grown successfully and its unique magnetic properties have been confirmed [12]. Thus, there is merit in the study of this family of alloys and compounds.

A special class of materials, mentioned above, receiving substantial interest is the so-called gapless semiconductors, in which conduction- and valence-band edges touch at the Fermi level [13]. In such materials, the mobility of charge carriers is essentially much higher than in normal semiconductors, making them promising materials for nanoelectronic applications. The first gapless semiconductors that have been studied were Hg-based IV-VI compounds, especially HgCdTe, HgCdSe, and HgZnSe. But it turned out that all these alloys are toxic and oxidize easily [13]. Later, Kurzman *et al.* proposed PbPdO₂ as a gapless semiconductor [14] and its zero gap width was demonstrated experimentally [15]. Nowadays, one of the most studied gapless semiconductor is graphene [16]. In 2008 Wang proposed that doping PbPdO₂ with Co atoms would result in a new class of materials: the so-called spin-gapless semiconductors (SGSs) (see Refs. [17,18]). The spin-gapless semiconductors lie on the border between half-metallic magnets (HMMs) [19] and magnetic semiconductors. A schematic density of states (DOS) of a HMM and a SGS (type I and type II) is shown in Fig. 1. The spin-up (majority-spin) band in HMMs crosses the Fermi level like in a normal magnetic metal, but, in contrast to metals, in the spin-down (minority-spin) band a gap appears and the Fermi level lies in between the gap like in normal semiconductors. For type-I

*thorsten.aull@physik.uni-halle.de

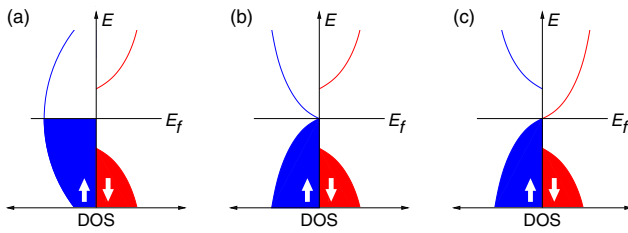


FIG. 1. Schematic representation of the density of states (a) for a half-metallic magnet (b) for a type-I spin-gapless semiconductor, and (c) for a type-II spin-gapless semiconductor.

SGSs, the minority-spin band looks like in HMMs but the difference is in the majority-spin band. The valence- and conduction-band edges are touching at the Fermi energy so that there appears a zero-width gap. On the other hand, type-II SGSs possess a unique electronic band structure that there is a finite gap just above and below the Fermi energy E_F for different spin channels, i.e., conduction- and valence-band edges of the different spin channels touch. Ferromagnetism is also possible in SGSs since the two spin band structures are different. One important advantage of type-I SGSs is that no energy is required for the excitation of the electrons from the valence to the conduction band and excited electrons or holes can be 100% spin polarized. It is worth noting that for type-II SGSs the spin-gapless semiconducting properties are not protected by any symmetry and can only appear if a free parameter, e.g., pressure, is tuned to a specific value.

Since the first proposal of spin-gapless semiconducting properties in Co-doped PbPdO_2 , different classes of materials ranging from three to two dimensions have been predicted to possess SGS characteristics and a few of them have been confirmed experimentally. Among them, graphene nanoribbons altered by CH_2 radical groups [20], in which magnetism originates from the unsaturated carbon states, show spin-gapless characteristics. HgCr_2Se_4 has a phase transition under a pressure of 9 GPa from the ferromagnetic semiconductor to the SGS state [21]. The boron nitride nanoribbons with vacancies present SGS properties [22]. *Ab initio* calculations from different groups have shown that several Heusler compounds present either type-I or type-II SGS properties. Mn_2CoAl was the first Heusler compound, the type-I SGS characteristics of which were experimentally demonstrated by Ouardi *et al.* [23]. Furthermore, Mn_2CoAl possesses a high Curie temperature of 720 K [23] and high electron and hole mobility. The search for SGSs has been extended recently to the family of ordered quaternary Heusler compounds which are usually named as LiMgPdSn -type Heuslers (also known as LiMgPdSb -type Heusler compounds) [24,25]. They have the chemical formula $(XX')YZ$ with transition-metal atoms X , X' , and Y , where the valence of X' is lower than the valence of X atoms and the valence of the Y element is lower than the valence of both X and X' . For reasons of simplicity usually in literature the parentheses are omitted and they are denoted as $XX'YZ$. In 2013, two extended *ab initio* studies have appeared focusing on their electronic and magnetic properties and several have been found to be SGSs [24,25]. Very recently, Gao *et al.* performed a systematic screening of the SGSs in ordered quaternary Heusler alloys focusing on the mechanical and

dynamical stability and identified 70 stable SGSs demonstrating that four types of SGSs can be realized based on the spin characteristics of the bands around the Fermi level [26].

II. MOTIVATION AND AIM

Spintronics and magnetoelectronics are two rapidly emerging fields in current nanoelectronics. HMMs have been considered as ideal electrode materials in magnetic tunnel junctions for spin-transfer torque magnetic memory applications due to their 100% spin polarization of the conduction electrons at the Fermi level, which leads to a very high tunnel magnetoresistance (TMR) effect. Half-metallic Heusler compounds have been used by several experimental groups to fabricate magnetic tunnel junctions due to their very high Curie temperatures and lattice parameter matching with the conventional tunnel barrier MgO . High TMR effects have been experimentally demonstrated in tunnel junctions made of Co-based Heusler compounds [27–29].

Although magnetic tunnel junctions made of half metals show large TMR effects making them very suitable for memory applications, they do not present any rectification (or diode effect) for logic operations. Logic-in-memory computing is an emerging field that promises to solve the bandwidth bottleneck issues in today's microprocessors. In semiconductor nanoelectronic devices, despite intensive efforts, the combination of nonvolatility and reconfigurability on the diode (transistor) level has not yet been achieved. Recently this became possible by utilizing the unique spin-dependent transport properties of SGSs and thus a new spintronic device concept has been proposed in Ref. [30], which combines reconfigurability and nonvolatility on the diode and transistor level. Furthermore, the proposed transistor overcomes the limitations of conventional hot electron quantum tunnel devices such as base-collector leakage currents in tunnel transistors [31], which might lead to high power dissipation.

The principles of the proposed reconfigurable magnetic tunnel diode (MTD) and transistor (MTT) have been extensively discussed in a very recent article (see Ref. [32]) and thus here we will present only a short overview of the proposed devices. The structure of the proposed reconfigurable MTD and its current-voltage (I - V) characteristics are schematically shown in Fig. 2. The MTD consists of a type-II SGS electrode and a HMM electrode separated by a thin insulating tunnel barrier and the rectification properties of the MTD are determined by the relative orientation of the magnetization directions of the electrodes. Using a type-I SGS instead of the HMM is also possible. When the magnetization directions of the electrodes are parallel to each other [see Fig. 2(a)] then the tunneling current is only allowed in one direction; in the reverse direction the tunneling current is blocked. Thus, the tunnel junction behaves like a rectifier, i.e., a diode. When the magnetization direction of one of the electrodes is reversed, then the rectification properties of the diode are also reversed as shown in Fig. 2(b). Hence, the MTD can be configured dynamically by current-induced spin-transfer torque or by an external magnetic field.

The first theoretical study on SGSs with type-II band structure within the Heusler family has been reported by two of the present authors in Ref. [24]. MTTs are an extension

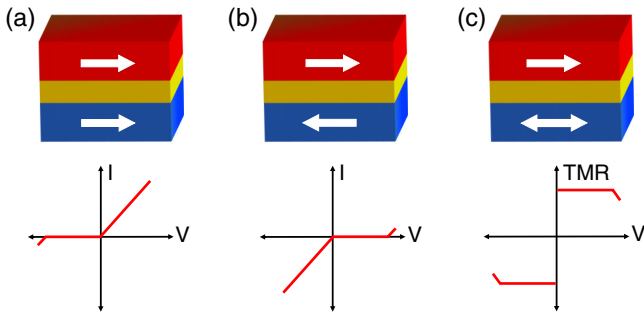


FIG. 2. Schematic representation of the reconfigurable magnetic tunnel diode for (a) parallel and (b) antiparallel orientations of the magnetization directions of the electrodes and corresponding current-voltage (I - V) characteristics. (c) Bias voltage dependence of the TMR effect in a magnetic tunnel diode. With arrows we show the magnetization direction of the electrodes.

of the concept of MTDs where two back-to-back MTDs are used to build a three-terminal device as described in Ref. [32]. The value of the gap in one spin channel for the HMMs and type-I SGSs as well as the gaps in different spin channels of type-II SGSs play a decisive role in determining the I - V characteristics of the MTD as discussed in Ref. [32]. Suitable SGSs and HMMs should have similar lattice constants so that the coherent growth of the device is possible. They should have high Curie temperatures, T_C , in order to be operational at room temperature. HMMs should possess large minority-spin gaps and SGSs should possess sizable gaps both below and above the Fermi level (for this reason, type-III and type-IV SGSs described in Ref. [26] are not suitable for such devices). And finally, in addition to negative formation energies, they should have a reasonably small convex hull energy distance so that their growth as metastable phases in the form of thin films could be feasible.

The aim of the present paper is to screen Heusler-based electrode materials with T_C values above room temperature for realization of the new device concept. Especially for type-II SGSs, to the best of our knowledge, up to now neither theoretical nor experimental work has been reported addressing the finite-temperature properties contrary to type-I SGSs [23,33]. To this end, we focus on the HMMs and SGSs (type I and type II) in ordered quaternary Heusler structure $XX'YZ$. In total, we identify 25 materials with sizable band gaps around the Fermi level which are either HMM or SGS and which fulfill the conditions mentioned above. In particular, for the SGS type-II materials, the tunability of the relative position of the valence-band maximum (VBM) and the conduction-band minimum (CBM) with substitution of different Z atoms is discussed. To study finite-temperature properties, we map the multisublattice complex itinerant electron problem onto the classical Heisenberg model with exchange parameters calculated using the Liechtenstein formalism [34]. We find that in agreement with previous studies due to the presence of a spin gap in both HMMs and SGSs the exchange interactions decay quickly with distance, and hence magnetism of these materials can be described considering only nearest- and next-nearest-neighbor intersublattice and intrasublattice exchange interactions. For all SGSs and most of the HMMs,

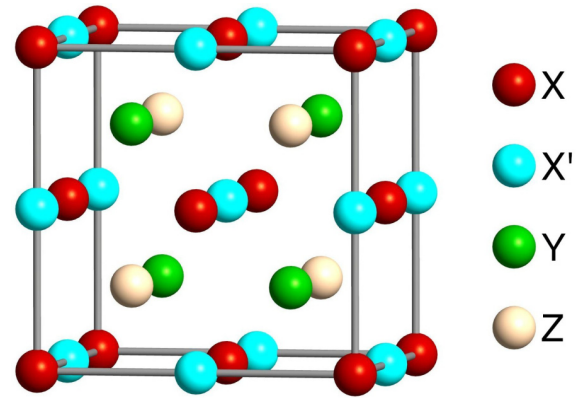


FIG. 3. Crystal structure of the quaternary Heusler alloys $XX'YZ$. X is located at Wyckoff position $4a(0, 0, 0)$, Y is located at $4c(\frac{1}{4}, \frac{1}{4}, \frac{1}{4})$, X' is located at $4b(\frac{1}{2}, \frac{1}{2}, \frac{1}{2})$, and Z is located at $4d(\frac{3}{4}, \frac{3}{4}, \frac{3}{4})$.

the estimated Curie temperatures are above room temperature, making them suitable candidates as electrode materials for reconfigurable device applications. Furthermore, we show that the T_C values obey a semiempirical relation $T_C \sim \sum_i |m_i|$, i.e., T_C increases with increasing sublattice magnetic moments. The rest of the paper is organized as follows. In Sec. III we describe the computational method while in Sec. IV our results are presented and discussed. Finally, we summarize and present our conclusions in Sec. V.

III. COMPUTATIONAL METHOD

For all calculations, we consider Heusler compounds with the chemical formula $XX'YZ$. As mentioned above X , X' , and Y are transition-metal atoms with descending valence and Z is a metalloid. Ordered quaternary Heusler compounds adopt the so-called LiMgPdSn-type cubic structure with space group $F\bar{4}3m$ (space group 216) (see Fig. 3), where the X atoms occupy Wyckoff position $4a(0, 0, 0)$, $X'4b(\frac{1}{2}, \frac{1}{2}, \frac{1}{2})$, $Y4c(\frac{1}{4}, \frac{1}{4}, \frac{1}{4})$, and $Z4d(\frac{3}{4}, \frac{3}{4}, \frac{3}{4})$ [35,36]. We should note that the X and X' atoms at $4a$ and $4b$ sites form a cubic lattice. The same is true for the Y and Z atoms sitting at the $4c$ and $4d$ sites. Overall the structure can be considered as fcc with four atoms as the basis along the long diagonal of the cube shown in Fig. 3 with the sequence X - Y - X' - Z . Note that this occupation scheme of the elements is energetically the most favorable with respect to any exchange of the atoms at the various sites [26]. The density functional theory (DFT) calculations were performed using the QuantumATK package [37], version O-2018.06, together with the norm-conserving PSEUDODOJO pseudopotentials [38]. We should note here that a recent study on SGSs using the GW approximation for the electronic self-energy to account for many-body exchange-correlation effects has shown that the effect of employing GW is small in the case of SGSs and the usual density functional theory gives a fair description of the electronic properties of these materials [39]. In the case of HMMs, the changes in the electronic structure by using GW should be even smaller due to their metallic character. For electronic structure calculations, we

used a linear combination of atomic orbitals (LCAO) method within the Perdew-Burke-Ernzerhof parametrization of the generalized gradient approximation functional [40] utilizing a $15 \times 15 \times 15$ Monkhorst-Pack grid [41] and a density mesh cutoff of 120 hartree. The total energy and forces have been converged at least to 10^{-4} eV and 0.01 eV/Å, respectively. Since we are only discussing magnetic materials, all calculations were performed taking spin polarization into account with collinear aligned spins. We used the calculated equilibrium lattice constant for each material. Note that all considered materials are mechanically as well as dynamically stable [26].

To study finite-temperature properties we map the complex multisublattice itinerant electron problem onto a classical effective Heisenberg Hamiltonian

$$H_{\text{eff}} = - \sum_{i,j} \sum_{\mu,\nu} J_{ij}^{\mu\nu} \mathbf{S}_i^\mu \cdot \mathbf{S}_j^\nu, \quad (1)$$

where μ and ν denote different sublattices, i and j indicate atomic positions, and \mathbf{S}_i^μ is the unit vector of the i site in the μ sublattice. The Heisenberg exchange parameters $J_{ij}^{\mu\nu}$ are calculated by employing the Liechtenstein formalism [34] within a self-consistent Green's-function method based on the multiple scattering theory within the density functional theory [42]. The crystalline structure information for the studied compounds obtained with the LCAO was used as input for electronic structure calculations by the Green's-function approach. According to our tests, both methods provide a very similar electronic structure for the systems under study. To estimate the Curie temperature T_C we use the mean-field approximation for a multisublattice system [43–45], which is given by

$$T_C = \frac{2}{3k_B} J_L^{\mu\nu}, \quad (2)$$

where $J_L^{\mu\nu}$ is the largest eigenvalue of $J_0^{\mu\nu} = \sum_j J_{0j}^{\mu\nu}$.

IV. RESULTS AND DISCUSSION

We subdivide this section into three parts. First, we overview the ground-state electronic and magnetic properties of the SGSs (type I and type II) and HMMs based on Heusler compounds. In the second part, we analyze the tuning of type-II SGSs. In the third and final part, we discuss the exchange interactions, magnon dispersion, and Curie temperatures.

A. Ground-state electronic and magnetic properties

The first step in our paper was to identify the Heusler compounds of potential interest. Then in the second step, we examined their electronic properties and we identified them as HMM or SGS. To carry out the first step we searched for type-I and type-II SGSs in the dataset of Gao *et al.* [26] and calculated their electronic structure to identify candidates with large spin gaps. After selecting suitable materials we checked all of them in the Open Quantum Materials Database [46]. Here we were interested in two energy quantities. The first one is the formation energy, E_{form} . This energy is the difference between the total energy of the $XX'YZ$ compound

in the Heusler structure presented in Fig. 3 and the sum of the energies of the isolated atoms of the chemical elements. This energy value should be negative in order to be able to grow the material in the Heusler structure. But this condition is not enough. The compound may prefer at this stoichiometry to grow in another structure or to separate in other phases (e.g., XY and $X'Z$ binary compounds). For each stoichiometry, the phases with the minimum energy define the so-called convex hull. We decided to choose as our search filter a distance from the convex hull, ΔE_{con} , less than 0.2 eV per atom because we think growing the compound in the Heusler structure as a metastable phase in the form of a thin film is possible since half-metallic CrAs in zinc-blende structure (space group $F\bar{4}3m$) with a hull distance of nearly 0.3 eV/at. (see Supplemental Material of Ref. [50]) was stabilized on GaAs(001) by using molecular-beam epitaxy [51–54]. Then for all the compounds which we identified to be of potential interest, we calculated the equilibrium lattice constant by minimizing the total energy and calculated the electronic structure. We have used the graphs presenting the total DOS versus the energy to identify HMM and SGS compounds (the DOS figures for all studied compounds are presented in the Supplemental Material [55]). In Table I, we present the final 25 quaternary Heusler compounds (only CoCoMnSi is really a usual full-Heusler compound Co_2MnSi), which we found to have negative E_{form} , ΔE_{con} less than 0.2 eV per atom, and band structure compatible with a HMM or a SGS (type I or type II). Among the 25 studied compounds, only CoFeVsb and CoMnCrAs have small absolute values of E_{form} , close to zero, which may affect their stability. All other compounds present a E_{form} absolute value quite high with CoFeTiSi being the most stable with a E_{form} value of -0.675 eV per atom as it can be seen in Table I. With respect to the convex hull energy distances, the values in Table I are very encouraging. Especially almost all type-II SGS studied compounds present ΔE_{con} less than 0.1 eV per atom, making them very promising to be grown in the form of thin films. Finally, we briefly comment on the equilibrium lattice constants a_0 presented also in Table I. The calculated values are between 5.6 and 6.4 Å and there are a lot of HMM (type-I SGS) and type-II SGS combinations where the lattice parameters a_0 match. For example, the HMM MnVTiSi and type-II SGS FeVTiSi have lattice constants which differ less than 0.01 Å.

The HMM or SGS character of the materials under study (see Fig. 1 for a schematic representation of the density of states) is compatible with the behavior of the total spin-magnetic moment. First, we focus on the HMM materials. For the ordered quaternary Heusler compounds, it is well known from Ref. [24] that the total spin magnetic moment in the unit cell m_{total} (in units of μ_B) versus the total number of valence electrons in the unit cell Z_T follows a Slater-Pauling rule:

$$m_{\text{total}} = Z_T - 18 \text{ or } Z_T - 24. \quad (3)$$

This rule means that there are exactly 9 or 12 occupied minority-spin bands, respectively. As demonstrated in Table I, where we present also the total number of valence electrons Z_T , all $XX'YZ$ compounds where X' is V or Cr fulfill the first variant of the rule while the rest of the compounds fulfill the second variant. In the first case there are 19, 20, or 21 valence electrons per unit cell while in the second case the number

TABLE I. Optimized lattice constants a_0 , sublattice and total magnetic moments, sum of the absolute values of the atomic spin magnetic moments $\sum_i |m_i|$, valence electron number Z_T , formation energy (E_{form}), convex hull distance energy (ΔE_{con}), and calculated and experimental Curie temperatures for 25 HMMs and SGSs. The ΔE_{con} and E_{form} values are taken from the Open Quantum Materials Database [46].

| Compound | a_0 (Å) | m_X (μ_B) | $m_{X'}$ (μ_B) | m_Y (μ_B) | m_{total} (μ_B) | $\sum_i m_i $ (μ_B) | Z_T | E_{form} (eV/at.) | ΔE_{con} (eV/at.) | $T_C^{(\text{MFA})}$ (K) | $T_C^{(\text{exp})}$ (K) |
|---------------------------------------|--------------|----------------------|-------------------------|----------------------|-----------------------------------|-------------------------------|-------|-------------------------------|-------------------------------------|-----------------------------|-----------------------------|
| Half-metallic magnets | | | | | | | | | | | |
| MnVTiAl | 6.11 | -2.54 | 2.60 | 0.91 | 1.00 | 6.08 | 19 | -0.172 | 0.188 | 963 | |
| MnVTiSi | 5.92 | -0.35 | 2.10 | 0.26 | 2.00 | 2.71 | 20 | -0.391 | 0.177 | 573 | |
| FeVTiAl | 6.06 | -0.78 | 2.42 | 0.45 | 2.00 | 3.75 | 20 | -0.247 | 0.117 | 685 | |
| FeVHfAl | 6.12 | -0.53 | 2.32 | 0.23 | 2.00 | 3.10 | 20 | -0.169 | 0.177 | 742 | |
| CoMnCrAs | 5.75 | 1.11 | -0.53 | 2.48 | 3.00 | 4.17 | 27 | -0.071 | 0.092 | 654 | |
| CoFeTiSi | 5.73 | 0.61 | 0.67 | -0.20 | 1.00 | 1.54 | 25 | -0.675 | 0.025 | 157 | |
| CoFeVSb | 5.99 | 1.08 | 1.20 | 0.78 | 3.00 | 3.12 | 27 | -0.016 | 0.198 | 308 | |
| CoFeCrSi | 5.61 | 1.04 | 0.22 | 1.86 | 3.00 | 3.24 | 27 | -0.293 | 0.075 | 517 | 790 [47] |
| CoCoMnSi | 5.65 | 1.06 | 1.06 | 3.03 | 5.00 | 5.28 | 29 | -0.449 | 0.000 | 920 | 985 [48] |
| Spin-gapless semiconductors (type I) | | | | | | | | | | | |
| MnCoMnAl | 5.73 | -2.01 | 0.99 | 3.03 | 2.00 | 6.04 | 26 | -0.271 | 0.035 | 1123 | 720 [23] |
| CoMnCrSi | 5.63 | 0.92 | -0.96 | 2.07 | 2.00 | 3.98 | 26 | -0.334 | 0.065 | 589 | |
| CoFeTiSb | 6.08 | 1.06 | 1.33 | -0.33 | 2.00 | 2.78 | 26 | -0.325 | 0.190 | 476 | |
| CoFeTaGe | 5.94 | 1.07 | 1.14 | -0.26 | 2.00 | 2.52 | 26 | -0.248 | 0.127 | 453 | |
| CoFeCrAl | 5.69 | 0.97 | -0.71 | 1.84 | 2.00 | 3.62 | 26 | -0.199 | 0.108 | 421 | 456 [49] |
| Spin-gapless semiconductors (type II) | | | | | | | | | | | |
| MnCrNbAl | 6.07 | 1.36 | 2.49 | -0.74 | 3.00 | 4.71 | 21 | -0.181 | 0.033 | 624 | |
| MnCrTaAl | 6.06 | 1.30 | 2.44 | -0.63 | 3.00 | 4.49 | 21 | -0.208 | 0.030 | 637 | |
| FeVTiSi | 5.91 | 0.57 | 2.33 | 0.10 | 3.00 | 3.01 | 21 | -0.452 | 0.173 | 464 | |
| FeVHfSn | 6.40 | 0.30 | 2.63 | 0.12 | 3.00 | 3.10 | 21 | -0.148 | 0.139 | 705 | |
| FeVNbAl | 6.11 | 0.81 | 2.32 | -0.11 | 3.00 | 3.25 | 21 | -0.189 | 0.126 | 693 | |
| FeVTaAl | 6.10 | 0.79 | 2.32 | -0.11 | 3.00 | 3.23 | 21 | -0.213 | 0.096 | 681 | |
| FeCrTiAl | 5.96 | 0.48 | 3.08 | -0.44 | 3.00 | 4.14 | 21 | -0.310 | 0.036 | 560 | |
| FeCrHfAl | 6.15 | 0.27 | 3.18 | -0.31 | 3.00 | 3.90 | 21 | -0.236 | 0.060 | 568 | |
| RuCrHfAl | 6.30 | 0.07 | 3.44 | -0.32 | 3.00 | 4.02 | 21 | -0.458 | 0.064 | 669 | |
| OsCrHfAl | 6.31 | 0.12 | 3.37 | -0.33 | 3.00 | 3.99 | 21 | -0.392 | 0.064 | 428 | |
| CoOsCrAl | 5.86 | 0.86 | -0.39 | 1.66 | 2.00 | 3.04 | 26 | -0.248 | 0.062 | 369 | |

of valence electrons in the unit cell is 25, 26, or 27. This behavior is clearly explained in Ref. [24]. When X' is V or Cr in the minority-spin band structure the triple degenerate at the Γ -point t_{1u} states are high in energy and are unoccupied and thus there are in total nine occupied minority-spin states and the gap in the minority-spin band structure is formed between the occupied t_{2g} and the unoccupied t_{1u} states. When X' is a heavier atom then the t_{1u} states are located lower in energy, being fully occupied, and the gap in the minority-spin band structure is formed between these states and the empty double degenerate at the Γ -point e_u states. Note that both the e_u and t_{1u} states obey the octahedral symmetry and not the tetrahedral symmetry of the lattice and thus are localized at the $4a$ and $4b$ sites occupied by the X and X' atoms.

In order to have a SGS material, the latter should have exactly 21 or 26 valence electrons per unit cell and thus a total spin magnetic moment of $3 \mu_B$ or $2 \mu_B$, respectively (note that in the case of 21 valence electrons the majority-spin (minority-spin) bands are now the spin-down (spin-up) bands and the Slater-Pauling rule is $m_{\text{total}} = 24 - Z_T$, resulting in a positive value of the total spin magnetic moment). The origin of these two numbers, 21 and 26, has been extensively discussed in Ref. [24] and a schematic representation is given

in Fig. 2 of this reference. To have a SGS the Fermi level should fall within gaps in both spin directions. In the case of 26 valence electron compounds, the situation is as in the usual HMM. In the minority-spin band structure, there are exactly 12 occupied bands. In the majority-spin band structure also the two e_u states are occupied which are separated by a gap from the unoccupied antibonding e_g and t_{2g} states. In the case of the compounds with 21 valence electrons, the majority-spin band structure is similar to the minority-spin band structure of the HMM with exactly 12 occupied bands. In the minority-spin band structure, the t_{1u} states are now empty, there are exactly nine occupied minority-spin bands, and there is a gap between the t_{1u} states and the bonding t_{2g} states which are just below them in energy. We remark in Table I that all five type-I SGS materials have 26 valence electrons, while all type-II SGSs with the exception of CoOsCrAl have 21 valence electrons.

We should also briefly discuss the spin magnetic moments in these compounds presented in Table I. The total spin magnetic moments are quite high for all studied compounds, being 2 or $3 \mu_B$. Only CoCoMnSi has a total spin magnetic moment of $5 \mu_B$ and the HMM MnVTiAl and CoFeTiSi of $1 \mu_B$. These large values of the total spin magnetic moment stem from the

large atomic spin magnetic moments of the transition-metal atoms. Depending on the X , X' , and Y chemical elements, the atomic spin magnetic moments at the various sites are ferromagnetically or antiferromagnetically coupled, resulting in ferrimagnetic compounds in most cases. As we stated above the X and X' atoms sit at the $4a$ and $4b$ sites, which are the corners of a cube, being next-nearest (second) neighbors. The Y and Z atoms sit at the $4c$ and $4d$ sites at the center of these cubes, being nearest (first) neighbors with the X and X' atoms. The Z atoms are metalloids (also known as sp elements) carrying negligible atomic spin magnetic moments; for this reason, we do not show them in Table I. Thus, the Y atom plays a crucial role, being the intermediary atom between X and X' . The late transition-metal atoms (Fe, Co,...) tend to have parallel spin magnetic moments when they are nearest neighbors, while the early transition-metal atoms (Mn, Cr,...) have the tendency to have antiparallel spin magnetic moments. We discuss the behavior of orientation of the atomic spin magnetic moments more in detail in the next section.

The most important quantity for the compounds under study is the width of the several gaps. First, we will start our discussion from the HMM and type-I SGS materials. In both cases as shown in Fig. 1 there is a gap in the minority-spin band structure and the Fermi level E_F falls within this gap, splitting it into two parts, one below and one above E_F . In the majority-spin band structure, E_F either intersects the bands (HMM case) or falls exactly within the zero-energy gap (type-I SGS). In the lower panel of Fig. 5, we present for all HMMs and type-I SGSs the calculated spin-minority energy gaps, coloring with blue the part below E_F and with red the part of the gap which is above E_F . The materials are ordered with ascending equilibrium lattice constant. For applications, we need materials with large energy gaps and with E_F close to the center of the gap (comparable gaps below and above E_F) in order to minimize the effect of defects which usually induce states at the edges of the bands. We remark that all compounds possess gaps which are quite large (exceeding 0.4 eV) and in some cases like FeVHfAl they are close to 1 eV. Also for all compounds under study both parts of the minority-spin gap below (blue color) and above (red color) E_F are sizable and thus are promising for the applications like magnetic tunnel diodes and transistors.

A more subtle case is the type-II SGS. Now we have a gap in both majority- and minority-spin band structures. In the ideal case, the maximum of the majority-spin valence band touches the minimum of the minority-spin conduction band as shown in Fig. 1. In reality for all compounds under study, this ideal case does not occur. First, as shown in the left panel of Fig. 4 there can be a finite gap between the maximum of the majority-spin valence band and the minimum of the minority-spin conduction band. This is the case for the type-II SGS materials with the larger lattice constants: FeCrHfAl, RuCrHfAl, OsCrHfAl, and FeHfSn. In the upper panel of Fig. 5 we display the results for these compounds. The white space separating the blue and red regions is the gap between the majority-spin VBM and the minority-spin CBM. This is sizable in the case of FeCrHfAl and FeVHfSn, and almost vanishing for RuCrHfAl and OsCrHfAl. The blue bars mark the part of the gap which is located exclusively in the minority-spin band structure as shown in the left panel of

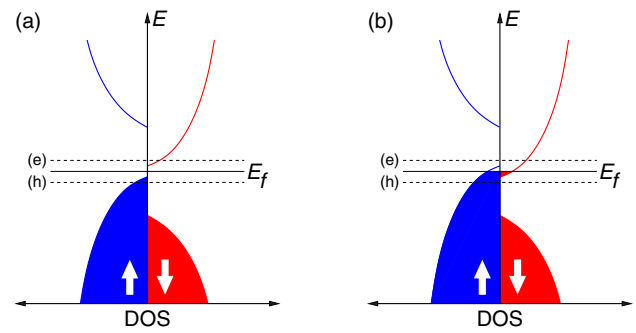


FIG. 4. (a) Schematic representation of the density of states for a type-II SGS with a small gap between the majority- and minority-spin bands at the Fermi energy E_F . (b) The same as (a) with a small overlap of bands of different spin channels. E_F denotes the Fermi level, and the letters (e) and (h) represent electronlike and holelike behavior, respectively.

Fig. 4 and with red bars we indicate the part of the gap which is located in the majority-spin band structure. The Fermi level is within the white region since we should have an integer number of occupied bands in both spin directions. In the case of RuCrHfAl and OsCrHfAl, the Fermi level intersects slightly the blue color and thus the valence majority-spin band structure but this is an artifact of the calculations due to numerical accuracy during the calculation of the density of states and this is easily confirmed if one extracts the band structure itself. If one tunes, as described in the next section, the position of the Fermi level, one can shift the Fermi level either within the majority-spin valence band, creating a hole surplus in the materials (the new position of the Fermi level is denoted with a dashed line and an “h” in the left panel of Fig. 4), or within the minority-spin conduction band, creating a surplus of electrons (dashed line with “e” in the left panel of Fig. 4).

In the rest of the type-II SGS compounds, there is an overlap between the majority-spin VBM and the minority-spin CBM as shown in the right panel of Fig. 4. Now the Fermi level intersects both the majority-spin valence band and the minority-spin conduction band. This is clearly shown in the upper panel of Fig. 5 where the region of overlap for these compounds is denoted by an orange region and the E_F for nearly all these compounds falls within the orange region. Below and above the orange region are the blue and red regions which denote the part of the energy gaps below and above the Fermi level which are located exclusively at the minority-spin and majority-spin band structures, respectively. A small shift of the Fermi level as discussed above can lead to a material with a hole or electron surplus which can be used as carriers in the material. There are materials like FeVTiSi, FeVTaAl, and FeVNbAl which present very large values of gaps both below and above the Fermi level and would be ideal for reconfigurable spintronic devices. Comparing the lattice constants, one observes in Fig. 5 that for realistic devices one has to use type-II SGSs with an overlap of the bands, because the type-II SGSs discussed in the above paragraph, which present a gap between the VBM and CBM, have very large lattice constants with respect to the HMMs.

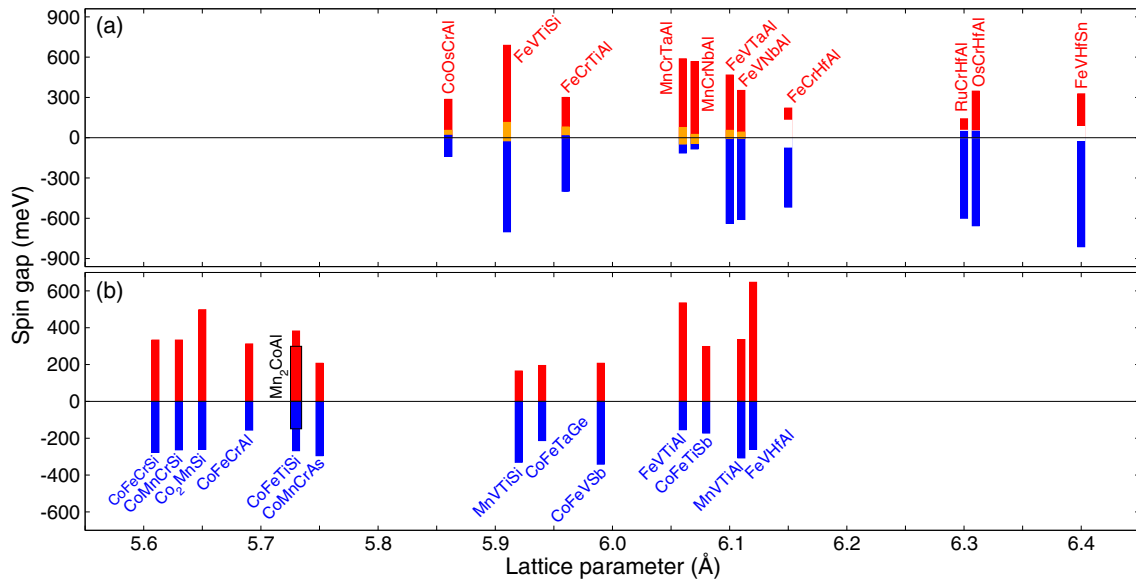


FIG. 5. Comparison of the lattice parameters (a) for type-II SGSs and (b) for HMMs as well as type-I SGSs. The blue (black) and red (dark gray) bars illustrate the size of the gap below and above Fermi level E_F , respectively. The orange (light gray) or white bars represent the value of the overlap or the spin gap, respectively (see discussion in text). The Fermi level is located at 0 meV.

B. Tuning the type-II SGS

To achieve the fabrication of the devices discussed in Sec. II, one needs to use perfect type-II SGS. The maximum of the majority-spin valence band and the minimum of the minority-spin conduction band should be located exactly at the same energy position, which should be also the Fermi level. None of the compounds discussed above and presented in Table I and in Fig. 5 is a perfect type-II SGS. Thus, we should search for a way to tune the properties of these compounds. An obvious way to achieve that should be to start with two parent compounds presenting a spin gap (white region) and an overlap (orange region) in Fig. 5 and mix them. Adding the correct fraction of each compound would lead to the disappearance of the overlap and to a perfect type-II SGS (see Fig. 6).

But one has to be careful in choosing the two candidates for the mixture. These compounds should not differ in more than two elements and both elements have to be located in the same sublayer. So, for example, mixing FeVHfSi with FeVHfGe works (Fig. 6) while mixing FeCrHfAl with FeVTaAl does not. In the last example, the compounds differ only in the X' and Y element, but these two are located in different sublayers (see Fig. 3). In the material FeVHfSi_{0.243}Ge_{0.757} the conduction band and the valence band would touch at E_F (see Fig. 6). But please note that alloying can cause other undesirable side effects. In the case that particular states of different alloy components are close in energy, alloying can lead to a substantial band broadening. The band broadening depends also on the concentration. To avoid this side effect one can use alloy components, the states of which are separated in energy or are located far from the Fermi energy. In the latter case the band broadening affects the state far below the band gap area. Another possible effect of alloying is the change of the compound stoichiometry, which can

also lead to the desired effect without band broadening the band edges. Furthermore, Heusler alloys can be doped with other elements. Hence, shifting the Fermi level to touch the minimum of the conduction band or the maximum of the valence band is possible.

We also checked if it is possible to achieve a band touching by adding strain or hydrostatic pressure. Compressing the samples by 5 GPa changes the lattice constant around 1% but does not affect the electronic properties. Şaşıoğlu *et al.* and Gavriluk *et al.* investigated the dependency of the Curie temperature on the applied pressure. In both cases T_C is increasing with increasing pressure [56,57]. Shigeta *et al.* analyzed the effect of pressure on the magnetic moment in Co₂TiSn and could not identify a change while applying

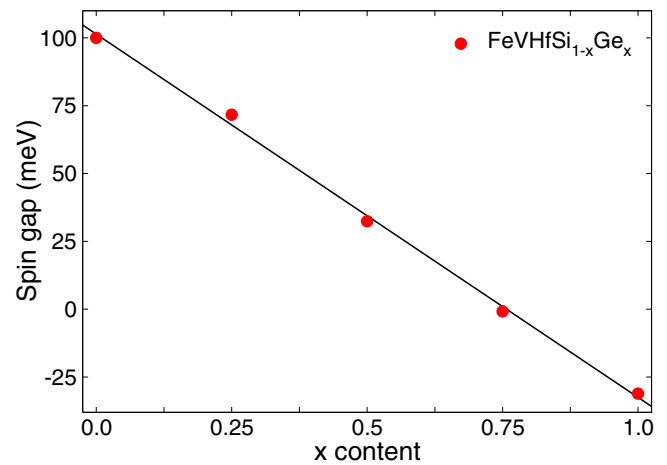


FIG. 6. Indirect spin gap in FeVHfSi_{1-x}Ge_x as a function of Ge concentration. The black line displays the linear fit. For $x = 0.757$ we get a perfect type-II SGS.

pressure up to 1.27 GPa [58]. To investigate the effect of strain we built an eight-atom tetragonal unit cell ($a = b \neq c$; $\alpha = \beta = \gamma = \pi/2$) and calculated the electronic structure when the c axis was contracted or expanded while the volume of the cell stayed constant. So for the a and b axis, we followed the formula

$$a = b = \sqrt{\frac{V}{c(1-x)}}, \quad (4)$$

where x denotes the applied strain and V stands for the volume of the cell. This eventuates in a change of the electronic properties. Some bands are shifted to higher and some to lower energy. Thus, a general rule when the gap is closing could not be identified.

C. Exchange interactions and Curie temperature

For realistic applications of spintronic devices, the Curie temperature T_C of the electrode materials in tunnel junctions is extremely important. Materials with T_C values much above room temperature are required. Most of the experimentally existing half-metallic Heusler compounds fulfill this requirement with T_C values ranging from 300 to 1100 K. Compounds with the highest reported T_C values such as Co_2MnSi (985 K [48]) and Co_2FeSi (1100 K [48]) possess also large sublattice and thus total magnetic moments of $5 \mu_B$ and $6 \mu_B$, respectively. Extensive *ab initio* calculations on multisublattice Heusler alloys have shown that there are several exchange interactions which coexist and are superimposed. Hence, a straightforward separation of the contributions of different mechanisms is not easy since DFT is not based on a model Hamiltonian approach and does not use a perturbative treatment. Exchange coupling in Heusler compounds, in which the total magnetic moment is localized on one sublattice (usually Mn-based compounds), is well understood on the basis of the Anderson $s-d$ mixing model [59–62]. It was shown that due to the large spatial separation of the Mn atoms in Heusler alloys ($d_{\text{Mn-Mn}} > 4 \text{ \AA}$) the Mn $3d$ states belonging to different atoms do not overlap considerably. Thus, an indirect exchange interaction between Mn atoms should play a crucial role in determining the magnetic state of the systems. However, the situation is different for the compounds studied here since the large part of the total magnetic moment is carried by two or three magnetic atoms with spatial separations of 2.5–3 Å. Therefore, the direct exchange coupling between the nearest magnetic atoms can dominate over the indirect one.

In order to simplify the discussion we can write the total magnetic exchange field acting on the sublattice μ as $J_{\text{total}}^\mu \sim J_{\text{direct}}^{\mu\nu} + J_{\text{indirect}}^{\mu\nu} + J_{\text{indirect}}^{\mu\mu}$, where the first two terms represent the direct and indirect exchange couplings between different sublattices. The last term is intrasublattice indirect coupling. In compounds like Co_2MnSi and Mn_2CoAl in which the Y sublattice carries a large magnetic moment the direct coupling provides the leading contribution to the total exchange coupling and determines the character of the magnetic state [63]. In most of the compounds considered, especially in type-II SGSs (see Table I) the X and X' sublattices carry the magnetic moment. These sublattices have an interatomic distance $d_{X-X'} \sim 3 \text{ \AA}$ and thus direct and indirect exchange

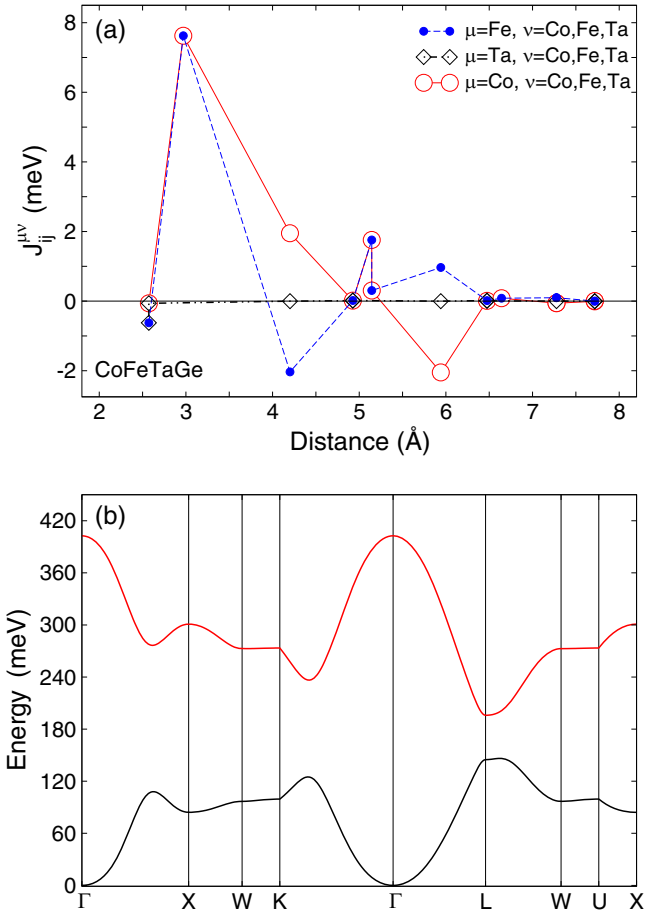


FIG. 7. (a) Intersublattice ($\mu \neq \nu$) and intrasublattice ($\mu = \nu$) Heisenberg exchange parameters as a function of distance for type-I spin-gapless semiconductor CoFeTaGe. (b) Calculated magnon dispersion along the high-symmetry lines in the Brillouin zone for CoFeTaGe. The black curve represents the acoustic mode while red (dark gray) illustrates the optical branch.

coupling becomes important. It should be noted here that, in reality, the situation is not so simple and the exchange field acting on the sublattices should be determined from the solution of a matrix equation.

Due to the presence of a spin gap in both HMMs and SGSs the exchange interactions decay quickly with distance [64,65]. As representative of the type-I and type-II SGSs in Figs. 7 and 8 we present the calculated intrasublattice and intersublattice Heisenberg exchange parameters and corresponding magnon dispersion for CoFeTaGe (type-I SGS) and FeVTiSi (type-II SGS) compounds, respectively. As seen in both materials the intersublattice as well as the intrasublattice exchange parameters quickly decay with distance and for the interatomic separations larger than 8 Å all parameters vanish. In both compounds, the Co and Fe (Fe and V) sublattices form a cubic cell. In the case of CoFeTaGe, the Co and Fe sublattices possess similar magnetic moments of about $1.1 \mu_B$, while the Ta atom has a small induced magnetic moment of $-0.26 \mu_B$, which couples antiferromagnetically to the Co and Fe sublattices. As seen in Fig. 7(a) the intersublattice Fe-Ta as well as Co-Ta interactions are almost negligible despite very short

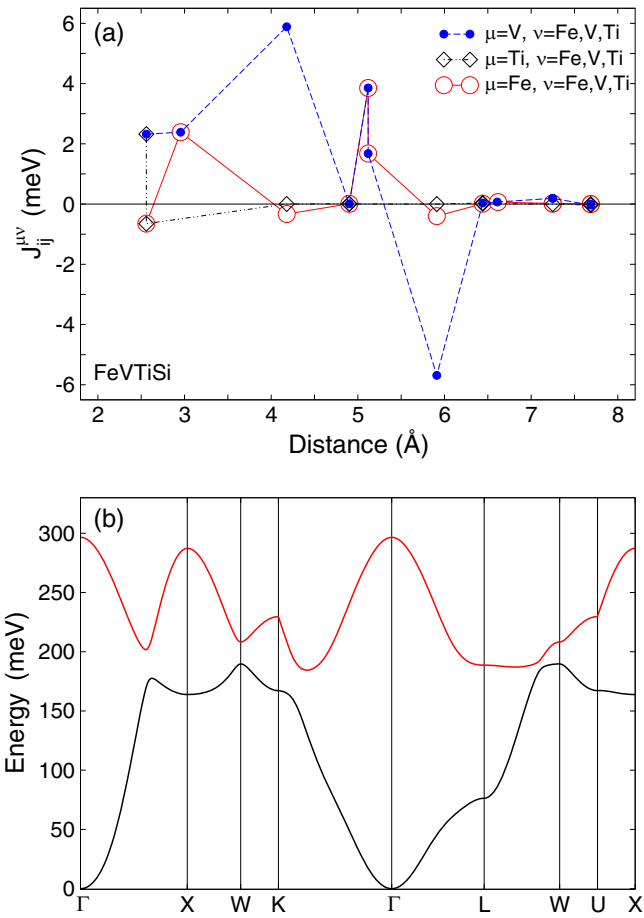


FIG. 8. (a) Intersublattice ($\mu \neq \nu$) and intrasublattice ($\mu = \nu$) Heisenberg exchange parameters as a function of distance for type-II spin-gapless semiconductor FeVTiSi. (b) Calculated magnon dispersion along the high-symmetry lines in the Brillouin zone for FeVTiSi. The black curve represents the acoustic mode while red (dark gray) illustrates the optical branch.

interatomic distance of $d_{Fe-Ta} = 2.57 \text{ \AA}$. This means that the Ta sublattice is more or less decoupled from the rest of the system.

In CoFeTaGe the strongest interaction takes place between the Fe and Co sublattices and it quickly decays with distance, i.e., from $J_1^{Fe-Co} \sim 8 \text{ meV}$ to $J_2^{Fe-Co} \sim 2 \text{ meV}$ and J_3^{Fe-Co} becomes zero. On the other hand, the intrasublattice Fe-Fe and Co-Co exchange interactions behave very differently, i.e., they show Ruderman-Kittel-Kasuya-Yosida-type oscillations with strong damping, however with different sign and more or less with the same amplitude. Thus, their contributions into the total exchange coupling almost cancel each other and only Fe-Co intersublattice exchange interactions play a decisive role in determining ground-state and finite-temperature properties of the type-I SGS compound CoFeTaGe.

The situation is a bit different for the type-II SGS FeVTiSi compound, in which V sublattice carries a large magnetic moment of $2.33 \mu_B$, while Fe and Ti sublattices have relatively small magnetic moments of $0.57 \mu_B$ and $0.1 \mu_B$, respectively. Due to different sublattice magnetic moments the patterns of calculated exchange parameters presented in

Fig. 8(a) are also different than in the CoFeTaGe compound. In FeVTiSi the Ti sublattice couples ferromagnetically to the Fe and V sublattices due to strong ferromagnetic V-Ti intersublattice exchange interaction, while the Fe-Ti interaction is antiferromagnetic but its strength is one-third of the V-Ti interaction and thus the overall contribution turns out to be ferromagnetic. The Fe and V sublattices interact ferromagnetically with $J_1^{Fe-V} > J_2^{Fe-V}$ and J_2^{Fe-V} splits into two due to different exchange paths along the [111] direction [see Fig. 8(a)]. The strongest interaction in FeVTiSi takes place between nearest- and next-nearest-neighbor V atoms, which have opposite sign and similar strength. Note that each V atom has 12 nearest-neighbor and 6 next-nearest neighbor V atoms. Furthermore, the intrasublattice Fe-Fe interactions are antiferromagnetic but negligibly small. Moreover, all exchange parameters quickly decay with distance and become zero after 8 Å. Note also that in all other type-II SGSs, except CoOsCrAl, the X' sublattice (V or Cr atoms) carries a large magnetic moment (see Table I) and, as a result, the calculated patterns of intrasublattice exchange parameters (results not shown) are similar to the FeVTiSi case. In most of the type-II SGSs the Y sublattice couples antiferromagnetically to the X and X' sublattices. However, this coupling is weak due to the small magnetic moment of atoms in the Y sublattice.

As mentioned in the preceding section the ferrimagnetic ground state in most of the considered compounds (20 out of 25) can be qualitatively accounted for on the basis that half-filled shells tend to yield a strong trend toward antiferromagnetism. As seen in Table I, when the Y sublattice is occupied by the Cr (Mn) atom and the X' sublattice is occupied by Mn or Fe (Os) the coupling between these sublattices is antiferromagnetic since both Cr and Mn atoms possess half-filled $3d$ shells and Fe (Os) is close to half filling. Most of the materials satisfy either one or both conditions.

In Figs. 7(b) and 8(b) we present the magnon dispersion along the high-symmetry lines in the Brillouin zone for CoFeTaGe and FeVTiSi, respectively. Note that for both compounds the induced small magnetic moments on Ta and Ti atoms are not treated as independent degrees of freedom in magnon dispersion calculations and thus we have only two branches. The acoustic branches in both materials are typical for magnets with short-range interactions, where nearest-neighbor and next-nearest-neighbor intersublattice and intrasublattice exchange interactions dominate, and do not yield any magnetic instabilities. Magnetic instabilities can occur if the acoustic magnon modes have very low (close to zero) or negative energies in some parts of the Brillouin zone but this is not the case for any of the studied compounds. Around the Γ point the energy-dispersion curves show a quadratic behavior with spin-wave stiffness constants of $D = 224 \text{ meV \AA}^2$ for CoFeTaGe and $D = 314 \text{ meV \AA}^2$ for FeVTiSi. These values are comparable to the typical values of transition-metal ferromagnets which usually range between 300 and 600 meV \AA^2 .

The optical magnon branch, which corresponds to the out-of-phase precession of magnetic moments in X and X' sublattices, has a strong dispersion in both compounds. As the magnetic moments in X and X' sublattices in CoFeTaGe have similar values the optical branch looks like a mirror image of the acoustic branch [see Fig. 7(b)].

Calculated exchange parameters are used to estimate the Curie temperature T_C within the multisublattice mean-field approximation [see Eq. (2)]. The obtained T_C values are presented in Table I. For comparison, available experimental data are also included. As seen for all compounds except CoFeTiSi the estimated T_C values are above room temperature, ranging from 308 to 1123 K. Our mean-field estimation of T_C for Co₂MnSi and CoFeCrAl is in reasonable agreement with available experimental data. However, T_C for Mn₂CoAl is overestimated, which can be attributed to the mean-field approach. As in the mean-field approach spin fluctuations are assumed to be small and the spin-flip Stoner excitations are neglected, it gives the upper bound for T_C values, however in materials with large coordination number (fcc lattice) and with long-range exchange interactions the mean-field T_C values are close to the ones obtained with random-phase approximation and classical Monte Carlo methods. Of course, this is not the case for the Mn₂CoAl compound, which possesses very large nearest-neighbor intersublattice Mn-Mn and Mn-Co exchange interactions and, as a result, mean-field considerably overestimates the T_C by 50%, while the Monte Carlo method results in a T_C value of 770 K [33]. Note that in HMMs and type-I SGSs the presence of spin gap around the Fermi energy prevents spin-flip transitions. Thus, Stoner excitations do not play an important role in the thermodynamics of these materials.

On the other hand, underestimation of T_C by about 35% in the CoFeCrSi compound can be attributed to the long-wavelength approximation in linear response theory, which underestimates exchange parameters in materials with small magnetic moments like fcc Ni, which has been discussed extensively in the literature by several authors [66–71]. In the case of the CoFeCrSi compound, the Fe atom has a small magnetic moment of $0.22 \mu_B$ and thus the long-wavelength approximation in linear response theory is expected to underestimate the intersublattice Fe-Co as well as the Fe-Cr exchange parameters, and as a consequence we obtain a small T_C value of 517 K compared to the experimental value of 790 K. Due to the long-wavelength approximation our estimated T_C values might be smaller than the experimental values when these materials are grown since most of the considered compounds have one or two transition-metal sublattices with small magnetic moments.

Finally, we would like to comment on the semiempirical relation between calculated T_C values and the sum of the absolute values of the sublattice magnetic moments $m_T^{\text{abs}} = \sum_i |m_i|$ which are presented in Table I. The relation between T_C and m_T^{abs} is presented in Fig. 9. As seen the T_C increases almost linearly, $T_C \sim 161m_T^{\text{abs}}$, with increasing m_T^{abs} , and materials with largest m_T^{abs} values like Mn₂CoAl and Co₂MnSi possess also the highest T_C values. Most of the compounds have m_T^{abs} values in between $2.5 \mu_B$ and $5 \mu_B$ and thus moderate Curie temperatures. Deviations from the linear behavior can be traced back to the sublattice magnetic moments and thus the pattern of exchange interactions. In materials like FeVHfAl, 80% of the m_T^{abs} is carried by the V sublattice and thus intrasublattice V-V exchange interactions play a decisive role in the formation of T_C rather than intrasublattice exchange interactions. Of course, no such general rule exists since also compounds like CoFeVSb with similar sublattice magnetic moments show strong deviation.

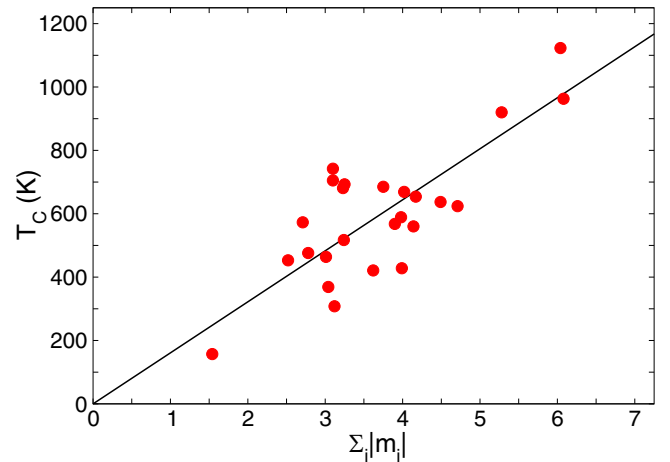


FIG. 9. The dependence of the calculated Curie temperatures on the sum of the absolute values of the sublattice magnetic moments m_T^{abs} ($m_T^{\text{abs}} = \sum_i |m_i|$) presented in Table I. The solid line displays the linear fit $y = 161x$.

V. CONCLUSION

Spintronics is a rapidly developing area of nanoelectronics. The emergence of new concepts like reconfigurable magnetic tunnel diodes and transistors requires the design of materials with novel functionalities. For that purpose, Heusler compounds are a preferential choice to identify such materials. In the present paper, we searched suitable half-metallic magnets and spin-gapless semiconductors among the family of ordered quaternary Heusler compounds with the chemical formula $XX'YZ$ to realize reconfigurable magnetic tunnel diodes and transistors. We managed to identify 25 compounds which combine HMM or SGS properties with negative formation energies and small convex hull energy distances so that they can be grown experimentally.

Following the identification of the compounds of interest, we employed state-of-the-art *ab initio* electronic band-structure calculations to determine their lattice constant, the spin magnetic moments, and their electronic structure. The total spin magnetic moment of all compounds exhibits a Slater-Pauling behavior and the ones being SGS have either 21 or 26 valence electrons per unit cell as expected for SGSs. Among the ones that are SGSs, there are five of the so-called type I which possess a gap in the minority-spin band structure and a zero gap in the majority-spin band structure. The other 11 SGS compounds are of type II, presenting gaps in both spin directions. None of these 11 compounds is a perfect SGS but as we show suitable mixing of two parent compounds leads to the tuning of their electronic properties and the appearance of perfect SGS type-II characteristics (the maximum of the majority-spin valence band and the minimum of the minority-spin conduction band touch exactly at the Fermi level). All compounds present large values of atomic spin magnetic moments and the calculated exchange constants are short-range stabilizing the magnetic state. We calculated the Curie temperatures for all 25 compounds and found them to be well above room temperature.

We expect that our results will pave the way for experimentalists to fabricate magnetic tunnel diodes and transistors by combining suitable HMM and SGS quaternary Heusler compounds.

ACKNOWLEDGMENTS

E.Ş. and I.M. gratefully acknowledge funding provided by the European Union (EFRE) and by Deutsche Forschungsgemeinschaft SFB Grant No. TRR 227.

- [1] I. Žutić, J. Fabian, and S. D. Sarma, *Rev. Mod. Phys.* **76**, 323 (2004).
- [2] K. Sato, L. Bergqvist, J. Kudrnovský, P. H. Dederichs, O. Eriksson, I. Turek, B. Sanyal, G. Bouzerar, H. Katayama-Yoshida, V. A. Dinh, T. Fukushima, H. Kizaki, and R. Zeller, *Rev. Mod. Phys.* **82**, 1633 (2010).
- [3] M. I. Katsnelson, V. Y. Irkhin, L. Chioncel, A. I. Lichtenstein, and R. A. de Groot, *Rev. Mod. Phys.* **80**, 315 (2008).
- [4] A. Hirohata and K. Takanashi, *J. Phys. D* **47**, 193001 (2014).
- [5] J. Ma, V. I. Hegde, K. Munira, Y. Xie, S. Keshavarz, D. T. Mildebrath, C. Wolverton, A. W. Ghosh, and W. H. Butler, *Phys. Rev. B* **95**, 024411 (2017).
- [6] J. Ma, J. He, D. Mazumdar, K. Munira, S. Keshavarz, T. Lovorn, C. Wolverton, A. W. Ghosh, and W. H. Butler, *Phys. Rev. B* **98**, 094410 (2018).
- [7] S. Sanvito, C. Oses, J. Xue, A. Tiwari, M. Zic, T. Archer, P. Tozman, M. Venkatesan, M. Coey, and S. Curtarolo, *Sci. Adv.* **3**, e1602241 (2017).
- [8] S. V. Faleev, Y. Ferrante, J. Jeong, M. G. Samant, B. Jones, and S. S. P. Parkin, *Phys. Rev. B* **95**, 045140 (2017).
- [9] S. V. Faleev, Y. Ferrante, J. Jeong, M. G. Samant, B. Jones, and S. S. P. Parkin, *Phys. Rev. Appl.* **7**, 034022 (2017).
- [10] I. Galanakis, K. Özdoğan, and E. Şaşıoğlu, *AIP Adv.* **6**, 055606 (2019).
- [11] I. Galanakis, K. Özdoğan, and E. Şaşıoğlu, *J. Phys.: Condens. Matter* **26**, 086003 (2014).
- [12] Y. Venkateswara, S. Gupta, S. S. Samatham, M. R. Varma, Enamullah, K. G. Suresh, and A. Alam, *Phys. Rev. B* **97**, 054407 (2018).
- [13] J. Tsidilkovski, *Electron Spectrum of Gapless Semiconductors*, edited by K. von Klitzing, Springer Series in Solid-State Sciences Vol. 116 (Springer-Verlag, Berlin, 1997).
- [14] J. A. Kurzman, M.-S. Miao, and R. Seshadri, *J. Phys.: Condens. Matter* **23**, 465501 (2011).
- [15] S. Chen, S. Huang, G. Guo, J. Lee, S. Chiang, W. Chen, Y. Liang, K. Lu, and J. Chen, *Appl. Phys. Lett.* **99**, 012103 (2011).
- [16] K. S. Novoselov, A. K. Geim, S. V. Morozov, D. Jiang, Y. Zhang, S. V. Dubonos, I. V. Grigorieva, and A. A. Firsov, *Science* **306**, 666 (2004).
- [17] X. Wang, *Phys. Rev. Lett.* **100**, 156404 (2008).
- [18] X. Wang, G. Peleckis, C. Zhang, H. Kimura, and S. Dou, *Adv. Mater.* **21**, 2196 (2009).
- [19] R. A. de Groot, F. M. Mueller, P. G. van Engen, and K. H. J. Buschow, *Phys. Rev. Lett.* **50**, 2024 (1983).
- [20] Y. Pan and Z. Yang, *Chem. Phys. Lett.* **518**, 104 (2011).
- [21] S.-D. Guo and B.-G. Liu, *J. Phys.: Condens. Matter* **24**, 045502 (2012).
- [22] Y. Pan and Z. Yang, *Phys. Rev. B* **82**, 195308 (2010).
- [23] S. Ouardi, G. H. Fecher, C. Felser, and J. Kübler, *Phys. Rev. Lett.* **110**, 100401 (2013).
- [24] K. Özdoğan, E. Şaşıoğlu, and I. Galanakis, *J. Appl. Phys.* **113**, 193903 (2013).
- [25] G. Z. Xu, E. K. Liu, Y. Du, G. J. Li, G. D. Liu, W. H. Wang, and G. H. Wu, *Europhys. Lett.* **102**, 17007 (2013).
- [26] Q. Gao, I. Opahle, and H. Zhang, *Phys. Rev. Mater.* **3**, 024410 (2019).
- [27] S. Kämmerer, A. Thomas, A. Hütten, and G. Reiss, *Appl. Phys. Lett.* **85**, 79 (2004).
- [28] W. Wang, H. Sukegawa, R. Shan, S. Mitani, and K. Inomata, *Appl. Phys. Lett.* **95**, 182502 (2009).
- [29] S. V. Faleev, Y. Ferrante, J. Jeong, M. G. Samant, B. Jones, and S. S. P. Parkin, *Phys. Rev. Mater.* **1**, 024402 (2017).
- [30] E. Şaşıoğlu and S. Blügel, Magnetic tunnel diode and magnetic tunnel transistor, US Patent No. 20180309047A1 (2016).
- [31] A. Zubair, A. Nourbakhsh, J.-Y. Hong, M. Qi, Y. Song, D. Jena, J. Kong, M. Dresselhaus, and T. Palacios, *Nano Lett.* **17**, 3089 (2017).
- [32] E. Şaşıoğlu, S. Blügel, and I. Mertig, *Appl. Electron. Mater.* **1**, 1552 (2019).
- [33] A. Jakobsson, P. Mavropoulos, E. Şaşıoğlu, S. Blügel, M. Ležaić, B. Sanyal, and I. Galanakis, *Phys. Rev. B* **91**, 174439 (2015).
- [34] A. Liechtenstein, M. Katsnelson, V. Antropov, and V. Gubanov, *J. Magn. Magn. Mater.* **67**, 65 (1987).
- [35] P. Klaer, B. Balke, V. Alijani, J. Winterlik, G. H. Fecher, C. Felser, and H. J. Elmers, *Phys. Rev. B* **84**, 144413 (2011).
- [36] X.-P. Wei, Y.-L. Zhang, Y.-D. Chu, X.-W. Sun, T. Sun, P. Guo, and J.-B. Deng, *J. Phys. Chem. Solids* **82**, 28 (2015).
- [37] S. Smidstrup, D. Stradi, J. Wellendorff, P. A. Khomyakov, U. G. Vej-Hansen, M.-E. Lee, T. Ghosh, E. Jónsson, H. Jónsson, and K. Stokbro, *Phys. Rev. B* **96**, 195309 (2017).
- [38] M. Van Setten, M. Giantomassi, E. Bousquet, M. J. Verstraete, D. R. Hamann, X. Gonze, and G.-M. Rignanese, *Comput. Phys. Commun.* **226**, 39 (2018).
- [39] M. Tas, E. Şaşıoğlu, C. Friedrich, and I. Galanakis, *J. Magn. Magn. Mater.* **441**, 333 (2017).
- [40] J. P. Perdew, K. Burke, and M. Ernzerhof, *Phys. Rev. Lett.* **77**, 3865 (1996).
- [41] H. J. Monkhorst and J. D. Pack, *Phys. Rev. B* **13**, 5188 (1976).
- [42] M. Geilhufe, S. Achilles, M. A. Köbis, M. Arnold, I. Mertig, M. Hergert, and A. Ernst, *J. Phys.: Condens. Matter* **27**, 435202 (2015).
- [43] P. W. Anderson, in *Solid State Physics*, edited by F. Seitz and D. Turnbull (Academic, New York, 1963), Vol. 14, pp. 99–214.

- [44] E. Şaşıoğlu, L. M. Sandratskii, and P. Bruno, *Phys. Rev. B* **70**, 024427 (2004).
- [45] S. Yamada, S. Kobayashi, F. Kuroda, K. Kudo, S. Abo, T. Fukushima, T. Oguchi, and K. Hamaya, *Phys. Rev. Mater.* **2**, 124403 (2018).
- [46] J. E. Saal, S. Kirklin, M. Aykol, B. Meredig, and C. Wolverton, *JOM* **65**, 1501 (2013).
- [47] Y. Jin, P. Kharel, P. Lukashev, S. Valloppilly, B. Staten, J. Herran, I. Tutić, M. Mitrakumar, B. Bhusal, A. O’Connell *et al.*, *J. Appl. Phys.* **120**, 053903 (2016).
- [48] J. Kübler, G. H. Fecher, and C. Felser, *Phys. Rev. B* **76**, 024414 (2007).
- [49] P. Kharel, W. Zhang, R. Skomski, S. Valloppilly, Y. Huh, R. Fuglsby, S. Gilbert, and D. J. Sellmyer, *J. Phys. D* **48**, 245002 (2015).
- [50] B. Wang, Q. Lu, Y. Ge, K. Zhang, W. Xie, W.-M. Liu, and Y. Liu, *Phys. Rev. B* **96**, 134116 (2017).
- [51] M. Mizuguchi, H. Akinaga, T. Manago, K. Ono, M. Oshima, and M. Shirai, *J. Magn. Magn. Mater.* **239**, 269 (2002).
- [52] M. Mizuguchi, H. Akinaga, T. Manago, K. Ono, M. Oshima, M. Shirai, M. Yuri, H. Lin, H. Hsieh, and C. Chen, *J. Appl. Phys.* **91**, 7917 (2002).
- [53] H. Akinaga, T. Manago, and M. Shirai, *Jpn. J. Appl. Phys.* **39**, L1118 (2000).
- [54] H. Akinaga and M. Mizuguchi, *J. Phys.: Condens. Matter* **16**, S5549 (2004).
- [55] See Supplemental Material at <http://link.aps.org/supplemental/10.1103/PhysRevMaterials.3.124415> for the DOS pictures of all 25 studied compounds.
- [56] E. Şaşıoğlu, L. M. Sandratskii, and P. Bruno, *Phys. Rev. B* **71**, 214412 (2005).
- [57] A. Gavriluk, G. Stepanov, V. Sidorov, and S. Irkaev, *J. Appl. Phys.* **79**, 2609 (1996).
- [58] I. Shigeta, Y. Fujimoto, R. Ooka, Y. Nishisako, M. Tsujikawa, R. Y. Umetsu, A. Nomura, K. Yubuta, Y. Miura, T. Kanomata *et al.*, *Phys. Rev. B* **97**, 104414 (2018).
- [59] P. W. Anderson, *Phys. Rev.* **124**, 41 (1961).
- [60] C. G. Da Silva and L. Falicov, *J. Phys. C* **5**, 63 (1972).
- [61] Z.-P. Shi, P. M. Levy, and J. L. Fry, *Phys. Rev. B* **49**, 15159 (1994).
- [62] E. Şaşıoğlu, L. M. Sandratskii, and P. Bruno, *Phys. Rev. B* **77**, 064417 (2008).
- [63] E. Şaşıoğlu, L. M. Sandratskii, P. Bruno, and I. Galanakis, *Phys. Rev. B* **72**, 184415 (2005).
- [64] J. Ruz, L. Bergqvist, J. Kudrnovský, and I. Turek, *Phys. Rev. B* **73**, 214412 (2006).
- [65] J. Kudrnovský, V. Drchal, I. Turek, and P. Weinberger, *Phys. Rev. B* **78**, 054441 (2008).
- [66] P. Bruno, *Phys. Rev. Lett.* **90**, 087205 (2003).
- [67] V. Antropov, *J. Magn. Magn. Mater.* **262**, L192 (2003).
- [68] V. Antropov, M. van Schilfhaarde, S. Brink, and J. Xu, *J. Appl. Phys.* **99**, 08F507 (2006).
- [69] M. Katsnelson and A. Lichtenstein, *J. Phys.: Condens. Matter* **16**, 7439 (2004).
- [70] P. H. Dederichs, S. Blügel, R. Zeller, and H. Akai, *Phys. Rev. Lett.* **53**, 2512 (1984).
- [71] A. Jacobsson, G. Johansson, O. Gorbatov, M. Ležaić, B. Sanyal, S. Blügel, and C. Etz, [arXiv:1702.00599](https://arxiv.org/abs/1702.00599).

6.2 Magnetic tunnel junctions based on spin-gapless semiconductors and half-metallic magnets for magnetic memory and logic applications.

Magnetic tunnel junctions (MTJs) based on half-metallic Heusler compounds arouse great interest within the last decades [209–211], especially for non-volatile memory and magnetic logic applications. HMMs have been proposed as ideal electrode materials for MTJs to realize extremely large TMR values. In the previous section, we identified promising SGSs and HMMs within the family of ordered quaternary Heusler compounds for spintronic device application. In the following publication, "Ab initio study of magnetic tunnel junctions based on half-metallic and spin-gapless semiconducting Heusler compounds: Reconfigurable diode and inverse TMR effect for magnetic memory and logic applications" [TA2], we discuss from first principles the current-voltage characteristics, reconfigurable rectification properties as well as the TMR ratio of two different MTJs based on SGSs and HMMs within the family of quaternary Heusler compounds. We stick to the SGSs FeVTaAl and FeVTiSi due to their large energy gaps in opposite spin channels below and above the Fermi level, MgO as tunnel barrier, and for the HMMs, we choose MnVTaAl and CoFeVSb since both Heusler compounds exhibit nearly symmetric spin gaps around the Fermi level and possess similar lattice constants to MgO. These MTJs conduct current either under reverse or forward bias

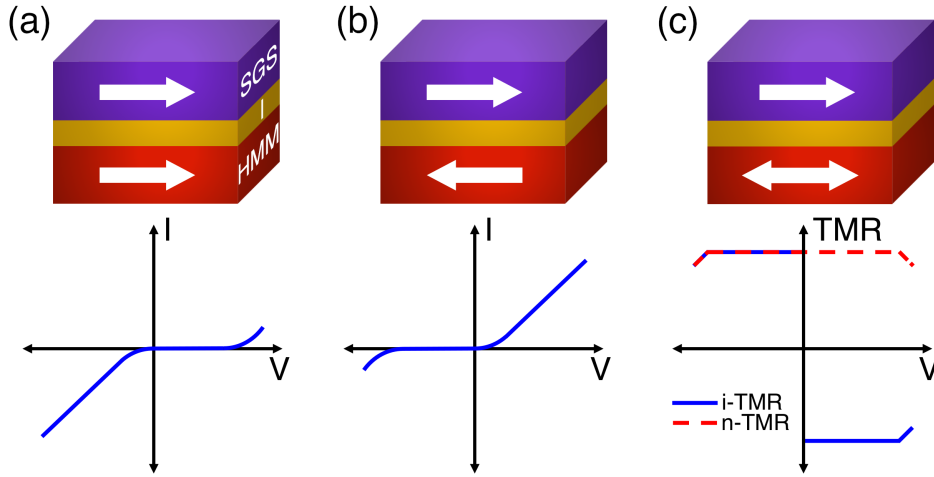


Figure 6.2: Schematic representation of the MTJ based on a HMM and a SGS for the parallel (a) and anti-parallel (b) orientation of the magnetization directions of the electrodes together with the corresponding current-voltage (I - V) characteristics. (c) Dependency of the TMR effect on the bias voltage in MTJs. The inverse (i-)TMR effect is represented by a blue line while the normal (n-)TMR effect is illustrated by a red dashed line. Adapted (figure) from T. Aull *et al.* manuscript submitted for publication, also available at arXiv:2202.06752 (2022); *Ab initio* study of magnetic tunnel junctions based on half-metallic and spin-gapless semiconducting Heusler compounds: Reconfigurable diode and inverse TMR effect for magnetic memory and logic applications, Ref. [TA2].

depending on the relative orientation of the magnetization direction of the electrodes and blocks the current in the opposite direction (see Figs. 6.2 (a) and 6.2 (b)). This reconfigurable diode effect leads to an inverse TMR effect rather than a normal TMR effect as in most of the conventional MTJs (see Fig. 6.2 (c)).

The following publication: Reprinted (submitted manuscript) from (T. Aull *et al.* manuscript submitted for publication, also available at arXiv:2202.06752 (2022); *Ab initio* study of magnetic tunnel junctions based on half-metallic and spin-gapless semiconducting Heusler compounds: Reconfigurable diode and inverse TMR effect for magnetic memory and logic applications, Ref. [TA2]).

***Ab initio* study of magnetic tunnel junctions based on half-metallic and spin-gapless semiconducting Heusler compounds: Reconfigurable diode and inverse TMR effect for magnetic memory and logic applications**

T. Aull,^{*} E. Şaşıoğlu, and I. Mertig

Institute of Physics, Martin Luther University Halle-Wittenberg, D-06120 Halle (Saale), Germany

(Dated: February 15, 2022)

Magnetic tunnel junctions (MTJs) have attracted strong research interest within the last decades due to their potential use as non-volatile memory such as MRAM as well as for magnetic logic applications. Half-metallic magnets (HMMs) have been suggested as ideal electrode materials for MTJs to achieve an extremely large tunnel magnetoresistance (TMR) effect. Despite their high TMR ratios, MTJs based on HMMs do not exhibit current rectification, i.e., a diode effect, which was achieved in a novel MTJ concept [ACS Appl. Electron. Mater. **1**, 1552–1559 (2019)] based on HMMs and type-II spin-gapless semiconductors (SGSs). The proposed concept has been recently experimentally demonstrated using Heusler compounds. In the present work, we investigate from first-principles MTJs based on type-II SGS and HMM quaternary Heusler compounds FeVTaAl, FeVTiSi, MnVTiAl, and CoVTiSb. Our *ab initio* quantum transport calculations based on a non-equilibrium Green's function method have demonstrated that the MTJs under consideration exhibit current rectification with relatively high on/off ratios. We show that, in contrast to conventional semiconductor diodes, the rectification bias voltage window (or breakdown voltage) of the MTJs is limited by the spin gap of the HMM and SGS Heusler compounds, which can be tuned by doping the electrode materials. A unique feature of the present MTJs is that the diode effect can be configured dynamically, i.e., depending on the relative orientation of the magnetization of the electrodes, the MTJ allows the electrical current to pass either in one or the other direction, which leads to an inverse TMR effect. The combination of nonvolatility, reconfigurable diode functionality, tunable rectification voltage window, and high Curie temperature of the electrode materials make the proposed MTJs very promising for room temperature spintronic applications and opens new ways to magnetic memory and logic concepts as well as logic-in-memory computing.

I. INTRODUCTION

The current computing technology is based on the von-Neumann architecture [1], in which the central processing unit and the memory are connected via a shared bus system causing the memory bandwidth bottleneck and high power consumption. It was demonstrated that for many computing tasks, the major amount of energy and time is needed to transfer data between the memory and the CPU, rather than the information processing itself [2, 3]. To tackle the bandwidth bottleneck in today's microprocessors, new information processing concepts such as logic-in-memory computing are receiving substantial interest [4–9]. The logic-in-memory computing architecture requires non-volatile memory elements. Among the emerging non-volatile memory technologies, the magnetoresistive random access memory (MRAM) is the most promising candidate due to its almost infinite endurance. The MRAM combines relatively high access speeds with non-volatility. In particular, spin-transfer torque (STT)-MRAM and spin-orbit torque (SOT)-MRAM emerged as promising candidates to replace the L3- and L2-cache [10, 11] of modern microprocessors.

In conventional magnetic tunnel junctions (MTJs), a non-magnetic insulator of a few nanometer thickness is

sandwiched between two ferromagnetic electrodes [12, 13]. Thus, the electronic transport is spin-dependent and mainly determined by quantum tunneling. For this reason, the tunnel magnetoresistance (TMR) ratio and the conductance are very important quantities of MTJs [14–17]. The resistance of such devices differs in two configurations, when the magnetization of the left and right electrode is parallel oriented and when the orientation is switched to anti-parallel, resulting in the TMR effect. When no bias voltage is applied, the TMR ratio is defined as $\text{TMR} = (G_{\uparrow\uparrow} - G_{\uparrow\downarrow}) / (G_{\uparrow\downarrow} + G_{\uparrow\uparrow})$, where $G_{\uparrow\uparrow}$ ($G_{\uparrow\downarrow}$) denotes the conductance in the parallel (anti-parallel) configuration of the electrodes. For finite biases, the TMR expression becomes $\text{TMR} = (I_{\uparrow\uparrow} - I_{\uparrow\downarrow}) / (I_{\uparrow\downarrow} + I_{\uparrow\uparrow})$, where $I_{\uparrow\uparrow}$ ($I_{\uparrow\downarrow}$) is the tunnel current through the device in the parallel (anti-parallel) orientation of the magnetization of the electrodes. It is worth noting that the tunnel barrier material, as well as the thickness of the tunnel barrier, and the applied bias voltage can influence the TMR effect [13, 18, 19]. Another factor that can affect the sign and the value of the TMR ratio is a structural asymmetry in the junctions. Heiliger *et al.* proposed that independent of the applied bias voltage, in asymmetric junctions the value of $I_{\uparrow\downarrow}$ exceeds the amount of $I_{\uparrow\uparrow}$ and, as a consequence, leads to a negative TMR ratio [20, 21]. The dependency of the TMR ratio on the applied bias voltage for both, the normal and the inverse TMR effect, is schematically illustrated in Fig. 1 (a).

MTJs played a significant role in spintronics develop-

^{*} thorsten.aull@physik.uni-halle.de

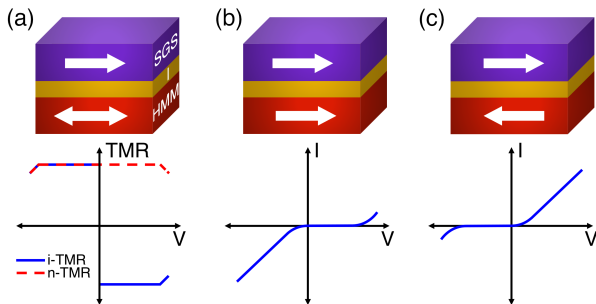


FIG. 1. (a) Top: Schematic representation of the magnetic tunnel junction based on a half-metallic magnet and a spin gapless semiconductor. Bottom: Dependency of the TMR effect on the bias voltage in MTJs. The inverse (i-)TMR effect is illustrated by a blue line while the normal (n-)TMR effect is represented by a red dashed line. (b) and (c) The same as (a) for the parallel and anti-parallel orientation of the magnetization directions of the electrodes as well as the corresponding current-voltage (I - V) characteristics. The white arrows indicate the magnetization direction of the electrodes.

ment as they are suitable for several applications ranging from read-head sensors to non-volatile memory devices such as STT-MRAM and SOT-MRAM and from non-volatile logic concepts to logic-in-memory computing [22–24]. Magnetic logic promises non-volatile, low-power computing and up to now, several different approaches have been proposed such as the quantum cellular automata [25, 26], domain-wall logic [27, 28], MTJ logic [29–31], etc. The latter is of particular interest because it opens the way to logic-in-memory computing, i.e., storing and processing the data within the same chip and thus providing an opportunity to explore novel computing architectures beyond the classical von-Neumann architecture [32, 33]. MTJ-based magnetic logic proposals can be divided into three categories: i) external field-driven MTJ logic, ii) spin Hall effect driven MTJ logic, and iii) logic based on magnetic tunnel diodes and magnetic tunnel transistors.

In the first category, the logic gates are built from MTJs, which are arranged in a bridge-type configuration and the logic inputs are provided by external wires, which creates a magnetic field that switches the magnetization direction of one electrode in MTJ. In this way, all logic gates can be realized with few MTJs [29, 30, 34]. The utilization of an inverse TMR effect can even further reduce the number of MTJs in logic gates [31, 35]. However, the drawback of this approach is that it is not scalable due to input wires and their routing near the MTJs. In the second category, the logic gates are based on a novel four-terminal spin Hall effect driven MTJ with fully electrically-separated write/read paths [36–38]. These four-terminal MTJ devices can overcome the challenges of operation gain and direct cascading in current spintronic logic circuits. Moreover, simulations have indicated that correct logic fan-out operation can be achieved with voltage below 150 mV, which is promising for low

power computing [38]. Note that in both approaches the logic operation gain (i.e., output voltage margin) depends mainly on the TMR ratio of the MTJs. While in the third category, a MTJ possesses, in addition to the TMR effect (memory), a current rectification (diode effect) functionality. Such MTJs also constitute the basic building blocks of the three-terminal magnetic tunnel transistors for logic applications. The TMR effect and current rectification have been observed for single barrier asymmetric MTJs as well as for double barrier MTJs with tunnel barriers of different transparency [39–42]. Although in initial studies of magnetic tunnel transistors low magnetocurrent ratios and transfer rates α are reported [43–47], in recent experiments of fully epitaxial magnetic tunnel transistors a large magnetocurrent ratio and transfer rate α is detected [48]. Besides being the basic building blocks of the three-terminal magnetic tunnel transistors, the MTJs possessing the diode effect is of particular interest for high-density 3D cross-point STT-MRAM applications as it eliminates the need for an additional selection device [42], i.e., a MOSFET transistor or a p-n diode [49–51].

In contrast to MTJ-based logic proposals, in the first and second category as well as other concepts like spin-orbit torque logic [52] not mentioned above (for a detailed discussion the reader is referred to Refs. 53 and 54, which report a benchmarking of beyond-CMOS devices including various spintronic logic concepts), magnetic tunnel diodes and transistors can operate extremely high frequencies, i.e., in THz regime, making them ideal candidates for high speed electronic and spintronic applications. However, despite THz operation frequencies, conventional magnetic tunnel diodes and transistors come with fundamental issues such as low on/off current ratios and less asymmetric current-voltage characteristics in diodes and base-collector leakage currents in transistors, which might lead to high power dissipation. In Ref. 55, we have proposed a magnetic tunnel diode and transistor concept, which overcomes the limitations of conventional magnetic tunnel devices and provides additional unique functionalities like reconfigurability, which was recently experimentally demonstrated [56]. The concept is based on spin-gapless semiconductors (SGSs) [57] and half-metallic magnets (HMMs) [58]. The two-terminal magnetic tunnel diode (or MTJ) is comprised of a SGS electrode and a HMM electrode separated by a thin insulating tunnel barrier. A schematic representation of the structure of the reconfigurable magnetic tunnel diode is shown in Fig. 1(b) and 1(c). Depending on the relative orientation of the magnetization of the electrodes the MTJ allows the electrical current to pass either in one or the other direction.

The aim of the present paper is a computational design of MTJs based on HMM and SGS quaternary Heusler compounds for room temperature device applications. Heusler compounds offer a unique platform to realize MTJs as these materials possess very high Curie temperatures (above room temperature) as well as HMM and

SGS behavior within the same family [59–61]. To this end, the selection of the HMM and SGS electrode materials from the quaternary Heusler family for the design of MTJs is based on our recent study in Ref. 61. We stick to SGS FeVTaAl and FeVTiSi compounds due to their large energy gaps in opposite spin channels around the Fermi level [61], MgO as tunnel barrier due to the lattice matching, and for the HMMs, although we have a large variety of choice, we choose MnVTaAl and CoFeVSb since both materials exhibit nearly symmetric spin gaps above and below E_F and possess similar lattice constants to MgO. *Ab initio* quantum transport calculations based on the non-equilibrium Green's function (NEGF) method have demonstrated that the MTJs based on HMM and SGS Heusler compounds exhibit, in addition to inverse TMR effect, current rectification, i.e., diode effect, which can be dynamically configured. We show that in contrast to semiconductor diodes (p-n diode or Schottky diode), the rectification voltage window (or breakdown voltage) of these MTJs is limited by the spin gap of HMM and SGS Heusler compounds, which can be tuned by doping electrode materials. The calculated zero temperature on/off current ratios vary between 10^2 - 10^7 , being lowest for the FeVTiSi/MgO/CoFeVSb MTJ, which can be attributed to the overlap of the conduction and valence bands of opposite spin channels around the Fermi level. The combination of non-volatility and dynamically reconfigurable diode effect as well as the very high Curie temperature of quaternary Heusler compounds make the proposed MTJs very promising for room temperature spintronic memory and logic applications. The rest of the paper is organized as follows: In Section II, we discuss the I - V characteristics of the MTJ concept by using the spin-dependent energy-band diagrams. In Section III, we present the computational details of our study. Our computational results are presented and discussed in Section IV, and finally, in Section V, we give our summary and outlook.

II. HMM/I/SGS MAGNETIC TUNNEL JUNCTIONS

In Fig. 1(b) and 1(c), we schematically show a MTJ based on a HMM and a SGS in the parallel and anti-parallel configuration of the electrodes, respectively, together with the corresponding I - V curves. HMMs have been used as electrode materials for MTJs to achieve extremely large TMR effects. Despite their large TMR ratios, the MTJs based on HMMs do not present current rectification, i.e., a diode effect. In Ref. 55, it was proposed that replacing one of the HMM electrodes with a SGS material in a MTJ gives rise to additional functionalities, i.e., current rectification, inverse TMR effect, and reconfigurability of the MTJ. Such a MTJ is then called a reconfigurable magnetic tunnel diode (MTD). Besides the HMM, the SGS material is the key component of the MTD. SGSs have been proposed by Wang in 2008 as a theoretical concept [57]. By employing first-principles

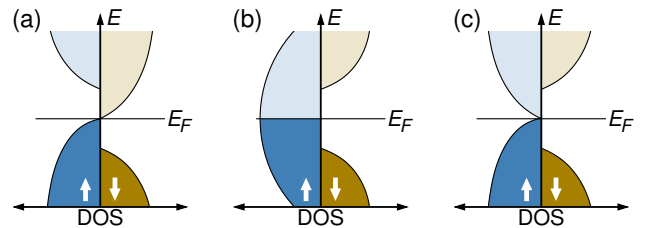


FIG. 2. Schematic representation of the density of states for (a) a type-II spin-gapless semiconductor, (b) a half-metallic magnet, and (c) a type-I spin-gapless semiconductor.

calculations Wang demonstrated that doping PbPdO₂ with Co atoms results in a new class of materials: the SGSs [57, 62]. Since then, different classes of materials have been predicted to present SGS behavior of various types, i.e., from type-I to type-IV SGSs [57, 59–61, 63–65] and some of the predicted SGSs have been experimentally realized [66]. Since type-II SGSs are the key component of the reconfigurable MTD, in Fig. 2 we present the schematic density of states (DOS) of a type-II SGS together with a conventional HMM as well as a type-I SGS, which can be also used as a replacement of the HMM in a MTJ. As seen in Fig. 2(a) the type-II SGS possesses a unique electronic band structure, i.e., it presents a finite gap below and above the Fermi level E_F in different spin channels while the valence- and conduction-bands of different spin channels touch at E_F . On the other hand, in HMMs, the majority-spin channel behaves like in normal metals, but the minority-spin channel exhibits a gap around the Fermi level like in a semiconductor or insulator. The DOS of type-I SGSs is similar to HMMs [see Fig. 2(b) and 2(c)]. The minority-spin channel looks the same while in the majority-spin channel a zero-width gap appears at the Fermi level since the conduction- and valence-band edges touch at E_F .

The operation principle of the reconfigurable MTD is extensively discussed in Ref. 55 and hence here we present a short overview of the concept by using the spin-resolved energy-band diagram shown in Fig. 3. The spin-resolved energy-band diagram is based on the schematic DOSs provided in Fig. 2(a) and 2(b), i.e., the type-II SGS material possesses a gap in the minority-spin (majority-spin) channel below (above) the Fermi level while the HMM exhibits a gap in the minority-spin channel around the Fermi energy. We further assume that the type-II SGS electrode, the tunnel barrier, and the half-metallic material have the same work function and equal Fermi levels and therefore we do not consider charge transfer at the interfaces. However, real materials, as it will be discussed in Section IV, possess different work functions and so there occurs charge transfer between one material and the other at the interface, which might cause a band bending in the SGS electrode. Moreover, due to interactions at the interface, the junction materials might not conserve the SGS or HMM characteristics close to the interface and thus the band diagram will not be as sharp as presented in Fig. 3.

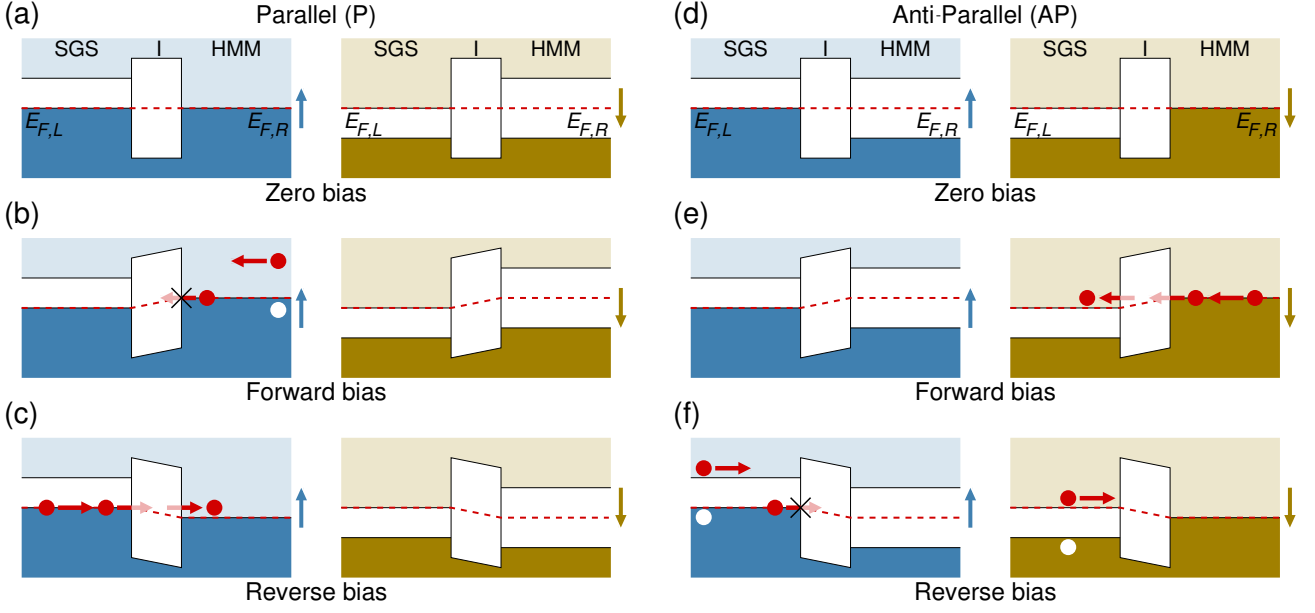


FIG. 3. Schematic representation of the spin-resolved energy-band diagram for the SGS/I/HMM MTJ for parallel (P) orientation of the magnetization directions of the electrodes (a) for zero bias, (b) under forward bias, and (c) under reverse bias. The electrons (holes) and the Fermi energy are denoted by red (white) spheres and a dashed line, respectively, and the tunneling process is illustrated by partly shaded red arrows. (d), (e), and (f) represent the same as (a), (b), and (c) for the anti-parallel (AP) orientation of the magnetization directions of the electrodes [see Figure 1 (b) and 1 (c)].

The I - V characteristics of the SGS/MgO/HMM junction illustrated in Fig. 1 (b) and 1 (c) can be qualitatively explained by Bardeen's approach for tunneling [67, 68]. For a simple tunnel barrier, the tunnel current $I(V)$ is given by the expression $I(V) \sim \sum_{\sigma} \int_{-\infty}^{+\infty} \rho_{\text{HMM}}^{\sigma}(E+eV) \rho_{\text{SGS}}^{\sigma}(E) |T(V)|^2 f(E) [1-f(E+eV)] dE$, where $\rho_{\text{SGS}}^{\sigma}(E)$ and $\rho_{\text{HMM}}^{\sigma}(E+eV)$ denote the DOS of the SGS and HMM electrodes with spin σ and $f(E)$ being the Fermi distribution function. $T(V)$ is the transmission probability, which is proportional to $e^{-d\sqrt{\phi-V}}$, where d is the thickness of the tunnel barrier and ϕ is the barrier height. As shown in Fig. 3 (b), when the magnetization directions of the electrodes are aligned parallel and a positive bias voltage (forward bias) is applied to the SGS electrode, electrons in the occupied majority-spin valence band of the HMM electrode cannot tunnel through the insulating barrier into the SGS electrode because there are no available states above the Fermi energy in the majority-spin channel of the SGS electrode unless a certain bias voltage is reached. For minority-spin electrons, the HMM electrode behaves like an insulator and thus no electron transport takes place. For a negative bias voltage (reverse bias), electrons in the majority-spin channel in the SGS material can tunnel into the unoccupied states of the HMM as shown in Fig. 3 (c). In the minority-spin channel, neither in the SGS electrode nor in the HMM electrode states are available that can contribute to a current. Thus, the tunneling current through the MTJ is 100% spin-polarized. A similar discussion holds for the anti-parallel orientation

of the magnetization direction of the SGS and HMM electrodes, for which the corresponding energy-band diagram is presented in Figs. 3 (d)-(f). Note that in the schematic representation of the I - V characteristics of the MTJ [see Fig. 1 (b) and 1 (c)], we use the standard definition of current for semiconductor devices, i.e., the current direction is opposite to the electron motion direction, while in Ref. 55, the same direction is taken for the current and electron motion. This is why the I - V characteristics are different in Ref. 55.

The presence of the reconfigurable diode effect in MTJs based on SGSs and HMMS leads to an inverse TMR effect rather than a normal TMR effect as in most of the conventional MTJs. The voltage dependence of the TMR presented in Fig. 1 (a) can be explained on the basis of the I - V characteristics discussed above. For a positive (forward) bias voltage, I_{\downarrow} will take a finite value while I_{\uparrow} is equal to zero. While for a negative (reverse) bias voltage, the situation is exactly the opposite. Thus, for forward bias, the TMR ratio will take the value -100% in a bias voltage window, which is set by the bandgap of the SGS and HMM electrodes. Similarly, under a reverse bias, the TMR ratio will be normalized to $+100\%$. Note that we use here a different definition of the TMR ratio compared to the Jullière model [69].

Up to now, the discussion of the I - V curves and voltage dependence of the TMR effect in SGS/I/HMM MTJs was based on the schematic energy-band diagram at zero temperature and perfect SGS behavior of the electrode material. However, at finite temperatures, thermally ex-

TABLE I. Material composition of the considered MTJs, lattice constants a_0 , c/a ratio, sublattice and total magnetic moments, work function (Φ), Curie temperatures T_C of the cubic phase, and the electronic ground state. All T_C values are taken from Ref. 61.

| SGS/MgO/HMM junction | MgO-interface | Compound | a_0 (Å) | c/a | m_X (μ_B) | $m_{X'}$ (μ_B) | m_Y (μ_B) | m_{total} (μ_B) | Φ (eV) | T_C (K) | Ground state |
|----------------------|---------------|----------|--------------|-------|----------------------|-------------------------|----------------------|-----------------------------------|----------------|--------------|--------------|
| FeVTaAl/MgO/MnVTiAl | FeV-MnV | FeVTaAl | 6.10 | 1.00 | 0.85 | 2.38 | -0.19 | 3.00 | 3.75 | 681 | SGS |
| | | MgO | 6.10 | 0.98 | - | - | - | - | 4.53 | - | I |
| | | MnVTiAl | 6.10 | 1.01 | -2.42 | 2.61 | 0.86 | 1.00 | 3.59 | 963 | HMM |
| FeVTiSi/MgO/CoFeVSb | FeV-CoFe | FeVTiSi | 5.91 | 1.00 | 0.57 | 2.33 | 0.10 | 3.00 | 3.52 | 464 | SGS |
| | | MgO | 5.91 | 1.04 | - | - | - | - | 4.55 | - | I |
| | | CoFeVSb | 5.91 | 1.12 | 1.08 | 1.20 | 0.78 | 3.00 | 4.10 | 308 | HMM |

cited electrons (non-spin-flip processes) can be transmitted from one electrode to the other in the off-state and thus cause a leakage current [see Figs. 3(b) and 3(f)]. This reduces the on/off and TMR ratios. Nevertheless, such processes can be significantly reduced by increasing the bandgap of the SGS and HMM materials as the Fermi-Dirac distribution function decays exponentially with increasing energy. Besides thermally excited non-spin-flip electrons, spin-flip processes stemming from spin-orbit coupling and electron-magnon interaction can also reduce the on/off ratio as well as the TMR effect [70–72].

III. COMPUTATIONAL DETAILS

Our *ab initio* study of the SGS/MgO/HMM MTJs is based on spin-polarized density functional theory (DFT) using the QUANTUMATK software package (version S-2021.06) [73, 74]. We used linear combinations of atomic orbitals (LCAO) as basis-set together with norm-conserving PseudoDojo pseudopotentials [75] with the Perdew-Burke-Ernzerhof (PBE) parametrization of the exchange-correlation functional [76]. For the determination of the ground-state properties, we use a $15 \times 15 \times 15$ Monkhorst-Pack \mathbf{k} -point grid and as density mesh cutoff for the separation of core and valence electrons 145 Hartree. Since the PBE-GGA is well-known to underestimate band gaps [77–79], we use the DFT-1/2 method [80, 81] as implemented in the QUANTUMATK package to correct the bandgap in the calculations of the transmission spectra. The changes in the SGS and HMM band structure by applying the DFT-1/2 method are negligible. For the structural optimization, all forces converge to at least $0.01 \text{ eV}/\text{Å}$ and self-consistency was achieved when the energies between two steps of the SCF cycle differ less than 10^{-4} eV . For the transport calculations, we employ the non-equilibrium Green’s function (NEGF) approach combined with the DFT method using an $11 \times 11 \times 115$ \mathbf{k} -point mesh. To calculate the I - V characteristics, QUANTUMATK applies the Landauer-Büttiker approach [82], where $I(V) = e/h \sum_{\sigma} \int T^{\sigma}(E, V) [f_L(E, V) - f_R(E, V)] dE$,

where $f_L(E, V)$ and $f_R(E, V)$ represent the Fermi-Dirac distribution of the left and right electrode, respectively. Furthermore, the transmission coefficient $T^{\sigma}(E, V)$ depends on the spin σ of the electrons, the applied bias voltage V , and the energy E . For the calculation of $T^{\sigma}(E, V)$, we chose a dense 100×100 \mathbf{k} -mesh. Moreover, the self-consistent I - V calculations are compared with a zero-bias linear response approach.

IV. RESULTS AND DISCUSSION

In Section II, we qualitatively discussed the I - V characteristics of the MTJs based on SGSs and HMMs using the spin-dependent energy-band diagram and a simple tunnel barrier model. However, quantum tunneling is a very sophisticated process in real materials as it depends on the symmetry of the wave functions in the electrodes, their decay rate, and their matching at the interface. The decay rate is determined by the thickness and barrier height as well as the complex energy bands of the insulating material [83, 84]. Therefore, fully *ab initio* quantum transport calculations are needed to determine the I - V characteristics of the MTJs based on SGSs and HMMs. We choose FeVTaAl and FeVTiSi quaternary Heusler compounds as SGS electrode together with MnVTiAl and CoFeVSb as HMM electrode and construct two different types of MTJs. All four electrode materials possess Curie temperatures above room temperature as presented in Table I. To construct the MTJs, we take the type-II SGS electrode material in the cubic structure and relax the tunnel barrier MgO as well as the HMM electrode material with respect to the in-plane lattice parameter of the first electrode. For this reason, we include the c/a ratios for the HMM electrodes and MgO, respectively, which take the tetragonal structure in Table I. The atomic structure of one MTJ is illustrated in Fig. 4(a). The left electrode FeVTaAl is a SGS, the right electrode MnVTiAl is a HMM, and MgO acts as a tunnel barrier. The FeVTaAl (MnVTiAl) has two types of interface terminations with MgO: FeV and TaAl (MnV and TiAl). Our total energy calculations have shown that the FeV-MgO (MnV-MgO) ter-

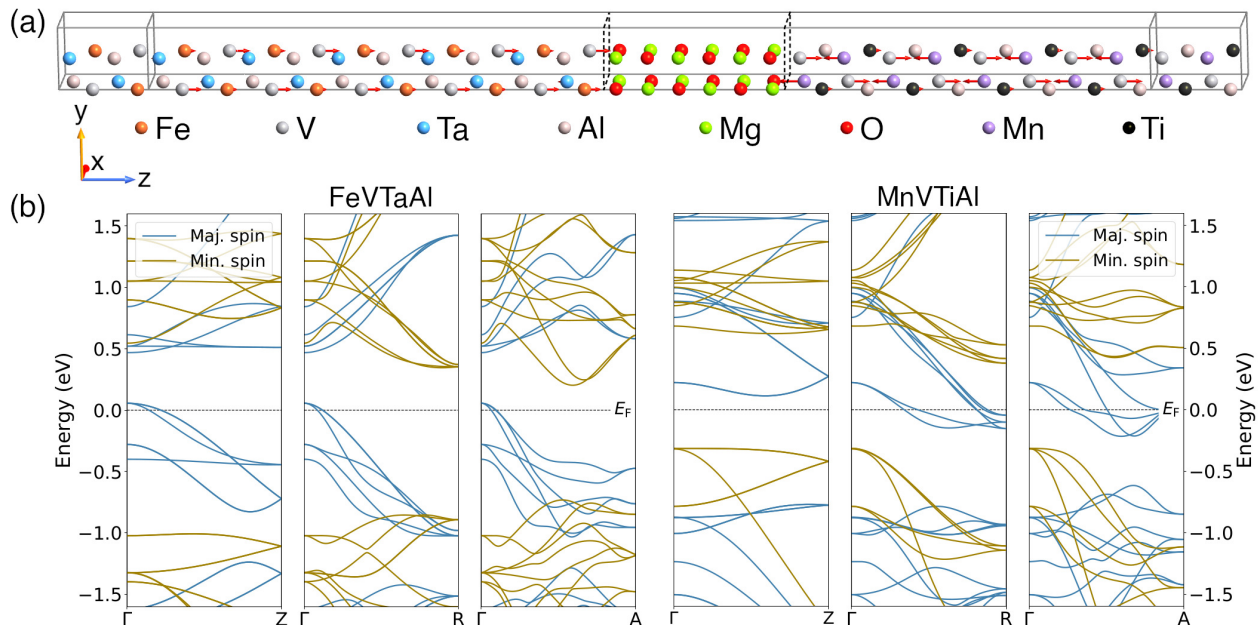


FIG. 4. (a) The atomic structure of the FeVTaAl/MgO/MnVTiAl tunnel junction. The system is periodic in xy -plane orthogonal to the z -axis, which is the transport direction. The red arrows mark the direction and the size of the magnetic moments within the scattering region. The small induced magnetic moments are overlaid by the atomic radii. The black dashed boxes illustrate the interface. (b) The calculated spin-resolved bulk band structure along the device stack direction, [001], for FeVTaAl (left panel) and MnVTiAl (right panel). The dashed black line denotes the Fermi level which is set to zero.

mination possesses lower energy. Similarly, as for the second MTJ FeVTiSi/MgO/CoFeVSb (see Table I), the FeV-MgO (CoFe-MgO) termination has lower energy.

For both MTJs, the thickness of the MgO tunnel barrier varies between three and six monolayers (0.6-1.4 nm) and the SGS and HMM electrodes are constructed by repeating the minimal tetragonal unit cell five times along the [001] direction. Depending on the number of MgO layers, the length of the device (screening region) lies between 60 Å and 66 Å. The device is periodic in the xy -plane and the z -direction is the transport direction. We adjusted the alignment of the magnetic moments to the z -axis. The direction and magnitude of the atomic magnetic moments of the electrode materials in the MTJ are represented by the red arrows and their size in Fig. 4 (a). At both interfaces, the magnetic moments deviate from their bulk values (see Table I). At the FeVTaAl-MgO interface, the largest difference is obtained for the Fe atom whose magnetic moment increases from $0.85 \mu_B$ to $1.82 \mu_B$ while the moment of the Ta atom decreases from $\sim 0.2 \mu_B$ to $-0.4 \mu_B$. The changes at the remaining atoms are negligible. Similar behavior is observed for the MnVTiAl-MgO interface, where the largest deviation occurs in the magnetic moment of the Mn atom, whose value decreases from $-2.42 \mu_B$ to $-3.30 \mu_B$ while the magnetic moments of the other atoms remain more or less unchanged.

Next, we will discuss the electronic properties of the FeVTaAl/MgO/MnVTiAl junction at zero bias, i.e., in

equilibrium. Thus, we present the bulk band structure along the transport direction of both junction materials in Fig. 4 (b). The MnVTiAl compound exhibits a nearly symmetric bandgap of 330 meV above and 310 meV below the Fermi level in the minority-spin channel, while FeVTaAl exhibits a type-II SGS behavior. Note that in the chosen direction, the SGS properties are not well displayed, and thus for a full band structure the reader is referred to Refs. 60 and 61. As we discussed above, the strong variation of the magnetic moments at the interface implies that the HMM and SGS properties are also lost. The loss of the HMM and SGS properties stems from two factors: i) electronic structure, i.e., the Fe and V (Mn and V) atoms at the interface possess different local atomic environments, and thus non-bonding states can emerge close to the Fermi level. Such states significantly reduce the spin-polarization at the interface [85, 86]. ii) Charge transfer across the tunnel junction due to the work function difference of the electrodes (see Table I). Since MnVTiAl exhibits the lower work function, electrons flow from the majority-spin (minority-spin) channel of MnVTiAl to the majority-spin (minority-spin) channel of FeVTaAl for parallel (anti-parallel) alignment of the magnetization directions of the electrodes. When this charge redistribution reaches equilibrium, MnVTiAl is positively charged near the interface region, whereas FeVTaAl is negatively charged and, as a result, an electric dipole is induced, which affects the electronic as well as the magnetic properties of both electrode materials

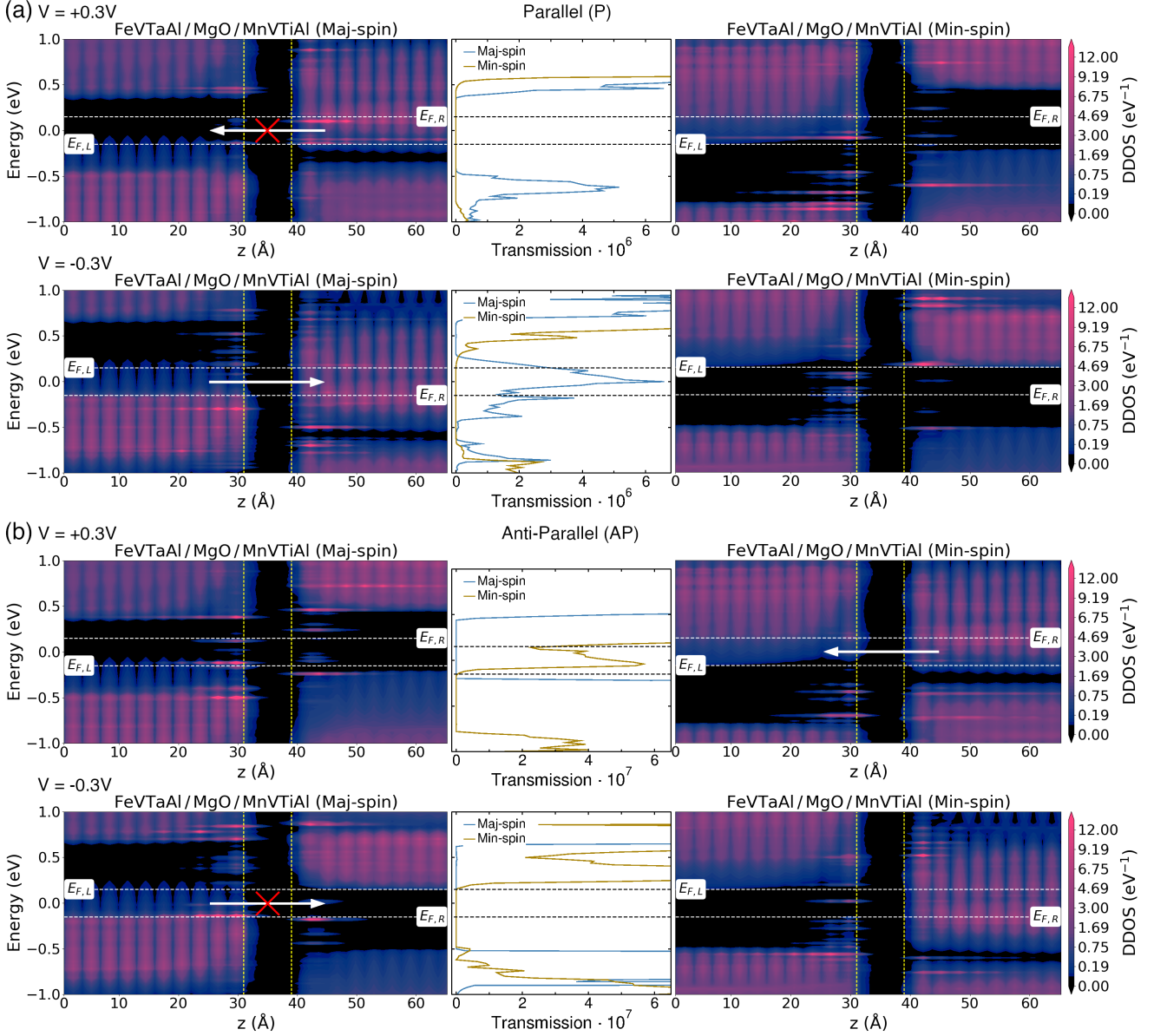


FIG. 5. (a) Projected device density of states (DDOS) for the majority (left panels) and minority (right panels) spin channel of the FeVTaAl/MgO/MnVTiAl junction for parallel orientation of the magnetization directions of the electrodes under an applied bias of $+0.3$ V and -0.3 V (the corresponding atomic structure is presented in 4 (a)). In the middle panels we show the calculated transmission spectrum for both spin channels. The dashed lines display the Fermi level of the left and right electrodes while the vertical yellow dashed lines denote the interfaces between the electrodes and MgO. The MgO tunnel barrier thickness is taken to be 1.1 nm, i.e., five monolayers. (b) The same as (a) for anti-parallel orientation of the magnetization directions of the electrodes. The majority and minority spin-channel are illustrated with respect to the magnetic orientation of the left electrode.

around the interface region. The loss of HMM and SGS properties at the interface region can be seen in the device density of states (DDOS) presented in Fig. 5 (see also Fig. 2 in the supplemental material [87]).

The I - V characteristics of the MTJs under consideration are calculated by using two different approaches: i) finite-bias NEGF method and ii) a linear response approach. The latter is computationally much cheaper,

while, however, significant differences may appear in the calculated I - V curves when compared to the self-consistent NEGF calculations as will be discussed below. In the middle panels of Fig. 5 (a) and 5 (b), we present the calculated transmission spectrum for the FeVTaAl/MgO/MnVTiAl MTJ for the applied bias voltage of $+0.3$ V and -0.3 V for the parallel and anti-parallel configuration of the magnetization direction of the elec-

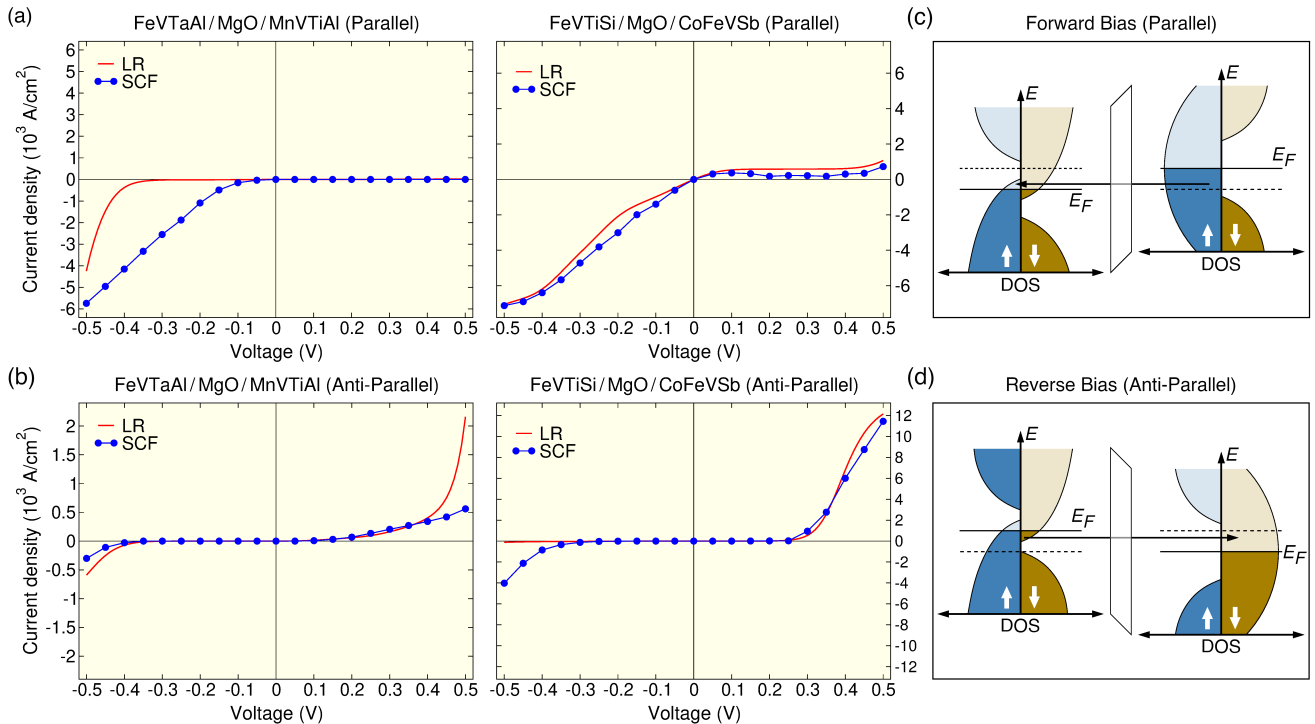


FIG. 6. (a) The current-voltage characteristics for the FeVTaAl/MgO/MnVTiAl (left panel) and FeVTiSi/MgO/CoFeVSb junction (right panel) for five monolayers of MgO barrier thickness in the parallel configuration. The I - V curves are calculated using both SCF and LR methods. (b) The same as (a) for the anti-parallel alignment of the magnetization directions of the electrodes. (c) and (d) illustrate the origin of the leakage current under forward and reverse bias for parallel and anti-parallel orientation of the magnetization direction of the electrodes, respectively.

trodes, respectively. The transmission spectrum and consequently the I - V curves of the FeVTaAl/MgO/MnVTiAl MTJ displayed in Fig. 6 can be explained on the basis of the DDOS [Fig. 5 (a) and 5 (b)]. For parallel orientation of the magnetization directions of the electrodes, under forward bias ($V = +0.3$ V), the transmission coefficient for majority-spin electrons is zero due to the gap in the type-II SGS material above the Fermi level. Since MnVTiAl exhibits a gap in the minority-spin channel around the Fermi energy, the transmission coefficient is also zero for minority-spin electrons and thus the MTJ is in off-state, i.e., no current flows through it under forward bias. Under reverse bias ($V = -0.3$ V), majority-spin electrons of occupied states in the SGS electrode FeVTaAl can tunnel into unoccupied states of the HMM electrode MnVTiAl through the MgO tunneling barrier and, as a consequence, the transmission coefficient takes a finite value. In the minority-spin channel, FeVTaAl possesses a gap below E_F and MnVTiAl below and above the Fermi level, and hence, in both materials, no states are available which could contribute to a current within the applied voltage window. Thus, the on-current of the MTJ in parallel configuration is 100 % spin-polarized.

Switching the magnetization direction of the electrodes from the parallel to the anti-parallel configuration results in switching the I - V characteristics of the MTJ (see

Fig. 1 (b) and 1 (c)), i.e, the MTJ is in on-state under forward bias, while it is in off-state under reverse bias. In this case, the HMM electrode MnVTiAl possesses a gap in the majority-spin channel and thus this channel does not contribute to the current. However, in the minority-spin channel, electrons from the occupied states above the Fermi energy in MnVTiAl can tunnel through the MgO tunnel barrier into unoccupied states in FeVTaAl, and thus the transmission coefficient takes a finite value under forward bias, which leads again to a 100 % spin-polarization of the current. While for a reverse bias, no current flows through the MTJ since in the majority-spin channel the HMM electrode MnVTiAl possesses a gap around the Fermi energy, while in the minority-spin channel the SGS electrode FeVTaAl presents a gap below E_F , and hence for both spin channels the transmission coefficient is zero.

In Fig. 6 (a) and 6 (b), we present the I - V characteristics of both MTJs within the finite-bias NEGF method, which will be called self-consistent field (SCF) and the linear response approach (LR) for a MgO thickness of five monolayers (1.1 nm). As seen for the parallel orientation of the magnetization direction of the electrodes, both MTJs are in off-state under forward bias and in on-state under reverse bias. However, this might be seen as contradicting to the conventional p-n diodes, in which

the diode is in on-state under forward bias. In our case this is a matter of the construction of the MTJ, i.e., by exchanging the electrode materials, one obtains the I - V characteristics of conventional diodes. In the SCF calculations, we obtain a monotonic increase of the current I with bias voltage V for both MTJs with zero turn-on voltages V_T for both FeVTaAl/MgO/MnVTiAl and FeVTiSi/MgO/CoFeVSb junctions in the parallel configuration, respectively. Switching the magnetization direction of the HMM electrode from parallel to anti-parallel results in switching the I - V characteristics of the MTJs as shown in Fig. 6(b). Both MTJs are now in on-state under forward bias, while they are in off-state under reverse bias. In contrast to the parallel alignment of the magnetization directions, in this case, the turn-on voltage V_T for the FeVTiSi/MgO/CoFeVSb is large, i.e., 0.25 V, which can be understood on the basis of the DDOS presented in supplemental material [87]. The large work function difference of the electrode materials (FeVTiSi and CoFeVSb) gives rise to a band bending in the energy-band diagram of this MTJ and as a consequence one obtains an effectively thick tunnel barrier for small bias voltages, which leads to a large turn on voltage under forward bias. Furthermore, the on-state currents for parallel and anti-parallel configurations of the same MTJ is also quite different. For instance, in the FeVTaAl/MgO/MnVTiAl junction for the parallel configuration the on-state current is one order of magnitude larger than the corresponding current in the anti-parallel configuration, while in the FeVTiSi/MgO/CoFeVSb junction the situation is different, here the on-state current is by a factor of two smaller in the parallel configuration. For comparison, the I - V curves obtained from the linear-response approach have been included in Fig. 6(a) and 6(b). As seen, qualitatively the linear response current follows the SCF results with some differences such as the turn-on voltage in the case of the FeVTaAl/MgO/MnVTiAl junction in the parallel configuration and the overestimated leakage current in the case of the FeVTiSi/MgO/CoFeVSb junction also for the parallel configuration. We do not expect a quantitative agreement between these approaches because for the linear response method one assumes a bias-independent transmission spectrum and thus this method is not capable of an accurate description of the I - V characteristics. The zero-bias transmission spectrum for the linear response calculations of both MTJs can be found in the supplemental material [87].

We now would like to comment on the off-state leakage currents of both MTJs. In principle, at zero temperature, one would obtain a zero off-state current for a perfect SGS electrode. However, in our MTJs both SGS electrodes, FeVTaAl and FeVTiSi, possess a sizeable band overlap between the valence and conduction bands of opposite spin channels around E_F as schematically illustrated in Figs. 6(c) and 6(d) (see also the supplemental material of Ref. 61 for the DOS). For parallel (anti-parallel) aligned magnetization directions of the

electrodes, band overlaps allow majority-spin (minority-spin) electrons to tunnel from the occupied states of the HMM (type-II SGS) electrode through the insulating region into unoccupied states of the type-II SGS (HMM) material. Since FeVTiSi possesses an overlap of 150 meV whereas the overlap in FeVTaAl amounts to just 60 meV, a larger leakage current arises in the FeVTiSi/MgO/CoFeVSb junction. At zero temperature, the obtained on/off current ratios of both MTJs at ± 0.3 V vary between 10^2 and 10^7 .

In contrast to conventional semiconductor diodes (p-n diode, Schottky diode, Zener diode), in which the rectification bias voltage window (or reverse bias breakdown voltage of the diode) varies between 3-200 V, in the present MTJs, this voltage window is limited by the spin gap of the HMM and SGS Heusler compounds. In analogy to conventional semiconductor diodes, we can express the breakdown voltage for the parallel and anti-parallel configurations as $V_B^P = \min\{(SG_{SGS}, E_F^A), (SG_{HMM}, E_F^B)\}$ and $V_B^{AP} = \min[(SG_{SGS}, E_F^B), (SG_{HMM}, E_F^A)]$, where (SG_{SGS}, E_F^A) and (SG_{HMM}, E_F^B) stand for the spin gap of the SGS and HMM electrodes above and below the Fermi energy, respectively. Using the spin gap values of the SGSs and HMMs from Ref. 61, one gets breakdown voltages V_B^P (V_B^{AP}) of 0.31 V and -0.34 V (0.33 V and -0.30 V) for the parallel (anti-parallel) configurations of the FeVTaAl/MgO/MnVTiAl and FeVTiSi/MgO/CoFeVSb MTJ, respectively. Since the estimation of the breakdown voltage is based on the DOS picture of the materials, the calculated V_B^P (V_B^{AP}) values can differ substantially since, as mentioned before, in tunneling processes the bands along the transport direction, their symmetry character, and their matching across the interface play a decisive role. Indeed, the actual calculated V_B^P values in Fig. 6 are larger than the simple estimated ones for the parallel configuration, while for the anti-parallel configuration the calculated V_B^{AP} values are more close to the estimated ones. However, the simple estimated values set the lower limit of the breakdown voltages V_B^P and V_B^{AP} .

Recently Maji and Nath reported the fabrication of a MTJ composed of HMM Co_2MnSi , SGS Ti_2CoSi , and 3 nm MgO tunnel barrier [56]. The authors demonstrated a reconfigurable diode effect with a relatively high on/off ratio of 10^3 and a very high TMR ratio of 892% at 5 K which decreases with increasing the temperature. Moreover, the breakdown voltage of the MTJ under reverse bias was reported to be around -0.5 V, which is basically the spin gap of the Co_2MnSi compound. Indeed, this is the first experimental demonstration of the concept that we proposed in 2019 [55]. Note that the authors in Ref. 56 used Ti_2CoSi as a SGS electrode, however, this material exhibits a type-III SGS behavior in simple DOS picture [64], whereas in tunneling experiments it behaves like a type-II SGS due to reasons that we discussed above. A detailed discussion of the experiments of Maji and Nath is beyond the scope of the present paper since we were aware of this work after the completion of

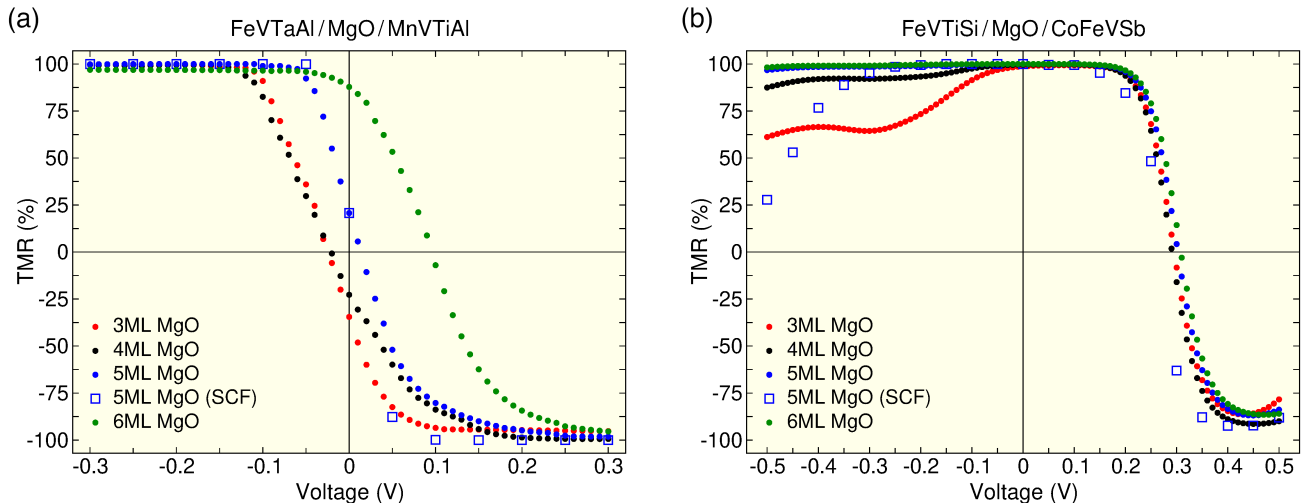


FIG. 7. (a) Voltage dependence of the TMR ratio of the FeVTaAl/MgO/MnVTiAl MTJ for different MgO thicknesses calculated within the linear response approach. For the case of five monolayers of MgO thickness, the results are compared with SCF calculations. (b) The same as (a) of the FeVTiSi/MgO/CoFeVSb MTJ.

the present paper. However, we are planning to consider the MTJ of Ref. 56 in a separate future study.

The I - V characteristics discussed above as well as the TMR ratio, which will be discussed below, in our MTJs are calculated for zero temperature. The temperature effects (non-spin-flip thermal excitations, see Fig. 3) are usually included in NEGF transport calculations of semiconductor devices via the Fermi-Dirac distribution function. However, due to the technical limitation of the QUANTUMATK package as discussed in detail in Ref. 88 for spintronic materials, we neglected these thermal excitations in transport calculations. Moreover, besides high energy non-spin-flip thermal excitations, temperature affects the magnetic and electronic structure of the SGSs and HMMs via Stoner excitations and magnons or collective spin waves. In type-II SGSs, electrons around the Fermi energy can be excited via spin-flip with a nearly vanishing amount of energy [see Fig. 2 (a)]. Such excitations are known as single-particle Stoner excitations and occupy, in our case, the unoccupied minority-spin states above E_F . As a consequence, these electrons contribute to a leakage current in the anti-parallel orientation of the magnetization direction of the type-II SGS and HMM electrode. On the other hand, due to the existence of a gap in HMMs, Stoner excitations are not allowed in these materials. Nevertheless, at finite temperatures, electron-magnon interactions might give rise to the appearance of non-quasiparticle states in the spin gap above the Fermi level of HMMs [89]. As a consequence, these states reduce the spin-polarization of the HMM material and thus influence its transport properties. Furthermore, defects at the interface might also affect the characteristics of the SGSs and HMMs and contribute to a leakage current and reduce the on/off ratio and TMR effect.

Finally, we would like to discuss the TMR effect in the MTJs under study. As mentioned above, the reconfig-

urable diode effect gives rise to an inverse TMR effect in this type of MTJs. The voltage dependence of the TMR ratio for both MTJs is presented in Fig. 7 (a) and 7 (b) for four different MgO tunnel barrier thicknesses. Due to the computational efficiency, we stick here to the linear response approach, however, for five monolayers of MgO tunnel barrier thickness, we compare the obtained results with the SCF method. For negative bias voltages (reverse bias), both MTJs present a positive TMR effect while at a certain applied bias voltage, due to unique band structure of the SGS electrode, the TMR changes its sign to a negative value, and thus the MTJs exhibits an inverse TMR effect. In principle, for a perfect SGS electrode material, one expects a sharp transition from positive to negative TMR values at zero bias voltage as displayed in Fig. 1 (a), however, in the present MTJs, this transition takes place in a finite voltage window and the transition point is shifted to finite voltages especially in the FeVTiSi/MgO/CoFeVSb tunnel junction. Two parameters are mainly responsible for the behavior of the TMR curves. These are the on/off current ratio, which reduces the TMR ratio, and the threshold voltage V_T , which causes a voltage shift of the transition point. Like in I - V curves, the spin gap of the electrode materials plays an essential role for the TMR ratio and its sign. For instance, in FeVTiSi/MgO/CoFeVSb tunnel junction the high TMR is obtained in a very small voltage window, especially for negative voltages and the TMR ratio is significantly reduced for voltages beyond the -0.3 V, which is more or less the spin gap of the HMM CoFeVSb material.

V. SUMMARY AND OUTLOOK

MTJs based on Fe, Co, and CoFeB, as well as HMM Heusler compounds, have been extensively studied in spintronics for magnetic memory and magnetic logic applications. Despite their high TMR ratios, especially the MTJs based on HMMs, conventional MTJs do not exhibit current rectification, i.e., a diode effect. A novel MTJ concept has been proposed in Ref. 55, which exhibits reconfigurable current rectification together with an inverse TMR effect. This MTJ concept was based on HMMs and SGSs and it has been recently demonstrated experimentally using Heusler compounds [56]. In the present work, by employing the state-of-the-art DFT and NEGF methods, we designed two different MTJs based on the type-II SGS and HMM quaternary Heusler compounds FeVTaAl, FeVTiSi, MnVTiAl, and CoVTiSb. We have shown that both MTJs [FeVTaAl(001)/MgO/MnVTiAl(001) and FeVTiSi(001)/MgO/CoFeVSb(001)] exhibit a current rectification with a relatively high on/off ratio of up to 10^7 . We showed that in contrast to conventional semiconductor diodes such as p-n junction diode or Schottky diode, the rectification bias voltage window (or breakdown voltage) of these MTJs is limited by the spin gap of the HMM and SGS Heusler electrode material in agreement with recent experiments. A unique feature of the present MTJs is that they can be configured dynamically, i.e., depending on the relative orientation of the magnetization direction of the electrodes, the MTJ allows electrical current to pass either in one or the other direction. This feature gives rise to an inverse TMR effect in such devices. The inverse TMR effect has been investigated as a function of the MgO tunnel barrier thickness. We find that the sign change of the TMR from a positive to a negative value takes place not at zero bias voltage, but small finite voltages, which can be explained by the on/off ratio (leakage current) and threshold voltage V_T

of the MTJs. Moreover, like in I - V curves, the spin gap of the electrode materials plays an essential role in TMR ratio and its sign.

The current non-volatile magnetic memory technology (STT-MRAM and beyond) and several magnetic logic proposals utilize conventional MTJs that have limited functionality. The MTJs based on HMMs and SGSs studied in the present paper provide major advantages over conventional MTJs and open new ways to magnetic memory and logic concepts. For instance, these MTJs might be of particular interest for high-density 3D cross-point STT-MRAM applications as they eliminate the need for an additional selection device such as a MOSFET transistor or a p-n diode. Apart from memory applications, the MTJs constitute the basic building blocks of the three-terminal magnetic tunnel transistors with unique properties as discussed in Ref. 55. Moreover, the present MTJs also open the way to logic-in-memory computing, i.e., storing and processing the data within the same chip and thus providing an opportunity to explore novel computing architectures beyond the classical von-Neumann architecture.

We expect that the present results will pave the way for experimentalists to fabricate MTJs based on the suggested Heusler compounds. Although in the present work we consider only a few materials, Heusler compounds represent a remarkable class of materials with more than 1000 members and offer a unique platform to grow within the same family of compounds HMMs and SGSs with similar lattice constants. Moreover, their HMM and SGS properties can be tuned by chemical doping and thus making them very promising for future spintronic devices with unique functionalities.

ACKNOWLEDGMENTS

This work was supported by SFB CRC/TRR 227 of Deutsche Forschungsgemeinschaft (DFG) and by the European Union (EFRE) via Grant No: ZS/2016/06/79307.

-
- [1] J. von Neumann, First Draft of a Report on the EDVAC, *IEEE Ann. Hist. Comput.* **15**, 27 (1993).
 - [2] M. Horowitz, 1.1 Computing's energy problem (and what we can do about it), in *Solid-State Circuits Conference Digest of Technical Papers (ISSCC)* (IEEE International, 2014) pp. 10–14.
 - [3] H. Li, B. Gao, Z. Chen, Y. Zhao, P. Huang, H. Ye, L. Liu, X. Liu, and J. Kang, A learnable parallel processing architecture towards unity of memory and computing, *Sci. Rep.* **5**, 13330 (2015).
 - [4] E. Linn, R. Rosezin, S. Tappertzhofen, U. Böttger, and R. Waser, Beyond von Neumann—logic operations in passive crossbar arrays alongside memory operations, *Nanotechnology* **23**, 305205 (2012).
 - [5] T. You, Y. Shuai, W. Luo, N. Du, D. Bürger, I. Skorupa, R. Hübner, S. Henker, C. Mayr, R. Schüffny, *et al.*, Exploiting memristive BiFeO₃ bilayer structures for compact sequential logics, *Adv. Funct. Mater.* **24**, 3357 (2014).
 - [6] S. Gao, F. Zeng, M. Wang, G. Wang, C. Song, and F. Pan, Implementation of Complete Boolean Logic Functions in Single Complementary Resistive Switch, *Sci. Rep.* **5**, 1 (2015).
 - [7] Y. Zhou, Y. Li, L. Xu, S. Zhong, H. Sun, and X. Miao, 16 Boolean logics in three steps with two anti-serially connected memristors, *Appl. Phys. Lett.* **106**, 233502 (2015).
 - [8] Z.-R. Wang, Y.-T. Su, Y. Li, Y.-X. Zhou, T.-J. Chu, K.-C. Chang, T.-C. Chang, T.-M. Tsai, S. M. Sze, and X.-S. Miao, Functionally Complete Boolean Logic in 1T1R Resistive Random Access Memory, *IEEE Electron Device Lett.* **38**, 179 (2017).

- [9] K. M. Kim, N. Xu, X. Shao, K. J. Yoon, H. J. Kim, R. S. Williams, and C. S. Hwang, Single-Cell Stateful Logic Using a Dual-Bit Memristor, *Phys. Status Solidi Rapid Res. Lett.* **13**, 1800629 (2019).
- [10] W. Xu, H. Sun, X. Wang, Y. Chen, and T. Zhang, Design of Last-Level On-Chip Cache Using Spin-Torque Transfer RAM (STT RAM), *IEEE Trans. Very Large Scale Integr. (VLSI) Syst.* **19**, 483 (2011).
- [11] G. Prenat, K. Jabeur, P. Vanhauwaert, G. D. Pendina, F. Oboril, R. Bishnoi, M. Ebrahimi, N. Lamard, O. Bouille, K. Garelo, J. Langer, B. Ocker, M.-C. Cyrille, P. Gambardella, M. Tahoori, and G. Gaudin, Ultra-Fast and High-Reliability SOT-MRAM: From Cache Replacement to Normally-Off Computing, *IEEE Trans. Multi-Scale Comput. Syst.* **2**, 49 (2016).
- [12] S. Yuasa, T. Nagahama, A. Fukushima, Y. Suzuki, and K. Ando, Giant room-temperature magnetoresistance in single-crystal Fe/MgO/Fe magnetic tunnel junctions, *Nat. Mater.* **3**, 868 (2004).
- [13] S. S. P. Parkin, C. Kaiser, A. Panchula, P. M. Rice, B. Hughes, M. Samant, and S.-H. Yang, Giant tunnelling magnetoresistance at room temperature with MgO (100) tunnel barriers, *Nat. Mater.* **3**, 862 (2004).
- [14] D. Ebke, J. Schmalhorst, N.-N. Liu, A. Thomas, G. Reiss, and A. Hütten, Large tunnel magnetoresistance in tunnel junctions with $\text{Co}_2\text{MnSi}/\text{Co}_2\text{FeSi}$ multilayer electrode, *Appl. Phys. Lett.* **89**, 162506 (2006).
- [15] X. Kou, J. Schmalhorst, A. Thomas, and G. Reiss, Temperature dependence of the resistance of magnetic tunnel junctions with MgO barrier, *Appl. Phys. Lett.* **88**, 212115 (2006).
- [16] G. Reiss, A. Hütten, S. Kämmerer, and J. Schmalhorst, Co_2MnSi as full Heusler alloy ferromagnetic electrode in magnetic tunneling junctions, *Phys. Status Solidi C* **3**, 1322 (2006).
- [17] P. Krzysteczko, X. Kou, K. Rott, A. Thomas, and G. Reiss, Current induced resistance change of magnetic tunnel junctions with ultra-thin MgO tunnel barriers, *J. Magn. Magn. Mater.* **321**, 144 (2009).
- [18] J. Mathon and A. Umerski, Theory of tunneling magnetoresistance of an epitaxial Fe/MgO/Fe(001) junction, *Phys. Rev. B* **63**, 220403 (2001).
- [19] S. Ikeda, J. Hayakawa, Y. Ashizawa, Y. M. Lee, K. Miura, H. Hasegawa, M. Tsunoda, F. Matsukura, and H. Ohno, Tunnel magnetoresistance of 604% at 300K by suppression of Ta diffusion in CoFeB/MgO/CoFeB pseudo-spin-valves annealed at high temperature, *Appl. Phys. Lett.* **93**, 082508 (2008).
- [20] C. Heiliger, P. Zahn, B. Y. Yavorsky, and I. Mertig, Influence of the interface structure on the bias dependence of tunneling magnetoresistance, *Phys. Rev. B* **72**, 180406 (2005).
- [21] C. Heiliger, P. Zahn, B. Y. Yavorsky, and I. Mertig, Interface structure and bias dependence of Fe/MgO/Fe tunnel junctions: Ab initio calculations, *Phys. Rev. B* **73**, 214441 (2006).
- [22] S. Jain, A. Ranjan, K. Roy, and A. Raghunathan, Computing in Memory With Spin-Transfer Torque Magnetic RAM, *IEEE Trans. Very Large Scale Integr. (VLSI) Syst.* **26**, 470 (2017).
- [23] S. K. Kingra, V. Parmar, C.-C. Chang, B. Hudec, T.-H. Hou, and M. Suri, SLIM: Simultaneous Logic-in-Memory Computing Exploiting Bilayer Analog OxRAM Devices, *Sci. Rep.* **10**, 1 (2020).
- [24] R. De Rose, T. Zanotti, F. M. Puglisi, F. Crupi, P. Pavan, and M. Lanuzza, STT-MTJ Based Smart Implication for Energy-Efficient Logic-in-Memory Computing, *Solid State Electron.* **184**, 108065 (2021).
- [25] R. P. Cowburn and M. E. Welland, Room Temperature Magnetic Quantum Cellular Automata, *Science* **287**, 1466 (2000).
- [26] I. Amlani, A. O. Orlov, G. Toth, G. H. Bernstein, C. S. Lent, and G. L. Snider, Digital Logic Gate Using Quantum-Dot Cellular Automata, *Science* **284**, 289 (1999).
- [27] D. A. Allwood, G. Xiong, C. C. Faulkner, D. Atkinson, D. Petit, and R. P. Cowburn, Magnetic Domain-Wall Logic, *Science* **309**, 1688 (2005).
- [28] M. Tsoi, R. E. Fontana, and S. S. P. Parkin, Magnetic domain wall motion triggered by an electric current, *Appl. Phys. Lett.* **83**, 2617 (2003).
- [29] R. Richter, L. Bär, J. Wecker, and G. Reiss, Nonvolatile field programmable spin-logic for reconfigurable computing, *Appl. Phys. Lett.* **80**, 1291 (2002).
- [30] A. Ney, C. Pampuch, R. Koch, and K. Ploog, Programmable computing with a single magnetoresistive element, *Nature* **425**, 485 (2003).
- [31] A. Thomas, D. Meyners, D. Ebke, N.-N. Liu, M. D. Sacher, J. Schmalhorst, G. Reiss, H. Ebert, and A. Hütten, Inverted spin polarization of Heusler alloys for spintronic devices, *Appl. Phys. Lett.* **89**, 012502 (2006).
- [32] H. Dery, P. Dalal, L. Cywiński, and L. J. Sham, Spin-based logic in semiconductors for reconfigurable large-scale circuits, *Nature* **447**, 573 (2007).
- [33] B. Behin-Aein, D. Datta, S. Salahuddin, and S. Datta, Proposal for an all-spin logic device with built-in memory, *Nat. Nanotechnol.* **5**, 266 (2010).
- [34] J. S. Friedman and A. V. Sahakian, Complementary Magnetic Tunnel Junction Logic, *IEEE Trans. Electron Devices* **61**, 1207 (2014).
- [35] S. Isogami and T. Owada, Electronic circuit using magnetic tunnel junctions with normal and inverse magnetoresistive effects, *IEEJ Trans. Electr. Electron. Eng.* **9**, S73 (2014).
- [36] D. M. Bromberg, D. H. Morris, L. Pileggi, and J.-G. Zhu, Novel STT-MTJ device enabling all-metallic logic circuits, *IEEE Trans. Magn.* **48**, 3215 (2012).
- [37] S. Fukami, T. Suzuki, K. Nagahara, N. Ohshima, Y. Ozaki, S. Saito, R. Nebashi, N. Sakimura, H. Honjo, K. Mori, *et al.*, Low-current perpendicular domain wall motion cell for scalable high-speed MRAM, in *2009 Symposium on VLSI Technology* (IEEE, 2009) pp. 230–231.
- [38] W. Kang, C. Zheng, Y. Zhang, D. Ravelosona, W. Lv, and W. Zhao, Complementary Spintronic Logic With Spin Hall Effect-Driven Magnetic Tunnel Junction, *IEEE Trans. Magn.* **51**, 1 (2015).
- [39] C. de Buttet, M. Hehn, F. Montaigne, C. Tiusan, G. Malinowski, A. Schuhl, E. Snoeck, and S. Zoll, Low-resistance magnetic tunnel junctions with an MgO–Al₂O₃ composite tunnel barrier: Asymmetric transport characteristics and free electron modeling of a self-limited oxidation bilayer, *Phys. Rev. B* **73**, 104439 (2006).
- [40] M. Chshiev, D. Stoeffler, A. Vedyayev, and K. Ounadjela, Magnetic diode effect in double-barrier tunnel junctions, *EPL* **58**, 257 (2002).
- [41] C. Tiusan, M. Chshiev, A. Iovan, V. Da Costa, D. Stoeffler, T. Dimopoulos, and K. Ounadjela, Quantum coherent

- ent transport versus diode-like effect in semiconductor-free metal/insulator structure, *Appl. Phys. Lett.* **79**, 4231 (2001).
- [42] A. Iovan, S. Andersson, Y. G. Naidyuk, A. Vedyayev, B. Dieny, and V. Korenivski, Spin Diode Based on Fe/MgO Double Tunnel Junction, *Nano Lett.* **8**, 805 (2008).
- [43] S. van Dijken, X. Jiang, and S. S. P. Parkin, Spin-dependent hot electron transport in Ni₈₁Fe₁₉ and Co₈₄Fe₁₆ films on GaAs(001), *Phys. Rev. B* **66**, 094417 (2002).
- [44] R. Sato and K. Mizushima, Spin-valve transistor with an Fe/Au/Fe(001) base, *Appl. Phys. Lett.* **79**, 1157 (2001).
- [45] G. Rodary, M. Hehn, T. Dimopoulos, D. Lacour, J. Bangert, H. Jaffrès, F. Montaigne, F. N. Van Dau, F. Petroff, A. Schuhl, *et al.*, Development of a magnetic tunnel transistor based on a double tunnel junction, *J. Magn. Magn. Mater* **290**, 1097 (2005).
- [46] M. Gobbi, A. Bedoya-Pinto, F. Golmar, R. Llopis, F. Casanova, and L. Hueso, C₆₀-based hot-electron magnetic tunnel transistor, *Appl. Phys. Lett.* **101**, 102404 (2012).
- [47] J. H. Lee, K.-I. Jun, K.-H. Shin, S. Y. Park, J. K. Hong, K. Rhie, and B. C. Lee, Large magnetocurrents in double-barrier tunneling transistors, *J. Magn. Magn. Mater.* **286**, 138 (2005).
- [48] T. Nagahama, H. Saito, and S. Yuasa, Hot electron transport in magnetic tunnel transistors with an epitaxial MgO tunnel barrier, *Appl. Phys. Lett.* **96**, 112509 (2010).
- [49] R. Aluguri and T.-Y. Tseng, Notice of Violation of IEEE Publication Principles: Overview of Selector Devices for 3-D Stackable Cross Point RRAM Arrays, *IEEE J. Electron Devices Soc.* **4**, 294 (2016).
- [50] G. W. Burr, R. S. Shenoy, K. Virwani, P. Narayanan, A. Padilla, B. Kurdi, and H. Hwang, Access devices for 3D crosspoint memory, *J. Vac. Sci. Technol. B Nanotechnol. Microelectron.* **32**, 040802 (2014).
- [51] X. Peng, R. Madler, P.-Y. Chen, and S. Yu, Cross-point memory design challenges and survey of selector device characteristics, *J. Comput. Electron.* **16**, 1167 (2017).
- [52] D. E. Nikonov, G. I. Bourianoff, and T. Ghani, Proposal of a Spin Torque Majority Gate Logic, *IEEE Electron Device Lett.* **32**, 1128 (2011).
- [53] D. E. Nikonov and I. A. Young, Benchmarking of Beyond-CMOS Exploratory Devices for Logic Integrated Circuits, *IEEE J. Explor. Solid-State Comput. Devices Circuits* **1**, 3 (2015).
- [54] C. Pan and A. Naeemi, An Expanded Benchmarking of Beyond-CMOS Devices Based on Boolean and Neuro-morphic Representative Circuits, *IEEE J. Explor. Solid-State Comput. Devices Circuits* **3**, 101 (2017).
- [55] E. Şaşıoğlu, S. Blügel, and I. Mertig, Proposal for Reconfigurable Magnetic Tunnel Diode and Transistor, *ACS Appl. Electron. Mater.* **1**, 1552 (2019).
- [56] N. Maji and T. K. Nath, Demonstration of reconfigurable magnetic tunnel diode and giant tunnel magnetoresistance in magnetic tunnel junctions made with spin gapless semiconductor and half-metallic Heusler alloy, *Appl. Phys. Lett.* **120**, 072401 (2022).
- [57] X. L. Wang, Proposal for a New Class of Materials: Spin Gapless Semiconductors, *Phys. Rev. Lett.* **100**, 156404 (2008).
- [58] R. A. de Groot, F. M. Mueller, P. G. v. Engen, and K. H. J. Buschow, New Class of Materials: Half-Metallic Ferromagnets, *Phys. Rev. Lett.* **50**, 2024 (1983).
- [59] K. Özdoğan, E. Şaşıoğlu, and I. Galanakis, Slater-Pauling behavior in LiMgPdSn-type multifunctional quaternary Heusler materials: Half-metallicity, spin-gapless and magnetic semiconductors, *J. Appl. Phys.* **113**, 193903 (2013).
- [60] Q. Gao, I. Opahle, and H. Zhang, High-throughput screening for spin-gapless semiconductors in quaternary Heusler compounds, *Phys. Rev. Mater.* **3**, 024410 (2019).
- [61] T. Aull, E. Şaşıoğlu, I. V. Maznichenko, S. Ostanin, A. Ernst, I. Mertig, and I. Galanakis, Ab initio design of quaternary Heusler compounds for reconfigurable magnetic tunnel diodes and transistors, *Phys. Rev. Materials* **3**, 124415 (2019).
- [62] X. Wang, G. Peleckis, C. Zhang, H. Kimura, and S. Dou, Colossal electroresistance and giant magnetoresistance in doped PbPdO₂ thin films, *Adv. Mater.* **21**, 2196 (2009).
- [63] G. Z. Xu, E. K. Liu, Y. Du, G. J. Li, G. D. Liu, W. H. Wang, and G. H. Wu, A new spin gapless semiconductors family: Quaternary Heusler compounds, *EPL* **102**, 17007 (2013).
- [64] S. Skaftouros, K. Özdoğan, E. Şaşıoğlu, and I. Galanakis, Search for spin gapless semiconductors: The case of inverse Heusler compounds, *Appl. Phys. Lett.* **102**, 022402 (2013).
- [65] I. Galanakis, K. Özdoğan, and E. Şaşıoğlu, Spin-filter and spin-gapless semiconductors: The case of Heusler compounds, *AIP Adv.* **6**, 055606 (2016).
- [66] S. Ouardi, G. H. Fecher, C. Felser, and J. Kübler, Realization of spin gapless semiconductors: The Heusler compound Mn₂CoAl, *Phys. Rev. Lett.* **110**, 100401 (2013).
- [67] J. Bardeen, Tunnelling from a Many-Particle Point of View, *Phys. Rev. Lett.* **6**, 57 (1961).
- [68] R. Meservey and P. M. Tedrow, Spin-polarized electron tunneling, *Phys. Rep.* **238**, 173 (1994).
- [69] M. Julliere, Tunneling between ferromagnetic films, *Phys. Lett. A* **54**, 225 (1975).
- [70] A. M. Bratkovsky, Assisted tunneling in ferromagnetic junctions and half-metallic oxides, *Appl. Phys. Lett.* **72**, 2334 (1998).
- [71] J. Inoue and S. Maekawa, Effects of spin-flip and magnon-inelastic scattering on tunnel magnetoresistance, *J. Magn. Magn. Mater.* **198**, 167 (1999).
- [72] J. Schmalhorst, S. Kämmerer, G. Reiss, and A. Hütten, Inelastic electron tunneling spectroscopy and bias voltage dependence of magnetic tunnel junctions with polycrystalline Co₂MnSi electrode, *Appl. Phys. Lett.* **86**, 052501 (2005).
- [73] S. Smidstrup, D. Stradi, J. Wellendorff, P. A. Khomyakov, U. G. Vej-Hansen, M.-E. Lee, T. Ghosh, E. Jónsson, H. Jónsson, and K. Stokbro, First-principles Green's-function method for surface calculations: A pseudopotential localized basis set approach, *Phys. Rev. B* **96**, 195309 (2017).
- [74] S. Smidstrup, T. Markussen, P. Vancaeyveld, J. Wellendorff, J. Schneider, T. Gunst, B. Verstichel, D. Stradi, P. A. Khomyakov, U. G. Vej-Hansen, M.-E. Lee, S. T. Chill, F. Rasmussen, G. Penazzi, F. Corsetti, A. Ojanperä, K. Jensen, M. L. N. Palsgaard, U. Martinez, A. Blom, M. Brandbyge, and K. Stokbro, QuantumATK: an integrated platform of electronic and atomic-scale modelling tools, *J. Phys. Condens. Matter* **32**, 015901 (2020).

- [75] M. J. Van Setten, M. Giantomassi, E. Bousquet, M. J. Verstraete, D. R. Hamann, X. Gonze, and G.-M. Rignanese, The PseudoDojo: Training and grading a 85 element optimized norm-conserving pseudopotential table, *Comput. Phys. Commun.* **226**, 39 (2018).
- [76] J. P. Perdew, K. Burke, and M. Ernzerhof, Generalized gradient approximation made simple, *Phys. Rev. Lett.* **77**, 3865 (1996).
- [77] J. P. Perdew, S. Kurth, A. Zupan, and P. Blaha, Accurate Density Functional with Correct Formal Properties: A Step Beyond the Generalized Gradient Approximation, *Phys. Rev. Lett.* **82**, 2544 (1999).
- [78] J. P. Perdew, W. Yang, K. Burke, Z. Yang, E. K. U. Gross, M. Scheffler, G. E. Scuseria, T. M. Henderson, I. Y. Zhang, A. Ruzsinszky, H. Peng, J. Sun, E. Trushin, and A. Görling, Understanding band gaps of solids in generalized Kohn–Sham theory, *Proc. Natl. Acad. Sci.* **114**, 2801 (2017).
- [79] P. Borlido, T. Aull, A. W. Huran, F. Tran, M. A. Marques, and S. Botti, Large-scale benchmark of exchange–correlation functionals for the determination of electronic band gaps of solids, *J. Chem. Theory Comput.* **15**, 5069 (2019).
- [80] L. G. Ferreira, M. Marques, and L. K. Teles, Approximation to density functional theory for the calculation of band gaps of semiconductors, *Phys. Rev. B* **78**, 125116 (2008).
- [81] L. G. Ferreira, M. Marques, and L. K. Teles, Slater half-occupation technique revisited: the LDA-1/2 and GGA-1/2 approaches for atomic ionization energies and band gaps in semiconductors, *AIP Adv.* **1**, 032119 (2011).
- [82] M. Büttiker, Y. Imry, R. Landauer, and S. Pinhas, Generalized many-channel conductance formula with application to small rings, *Phys. Rev. B* **31**, 6207 (1985).
- [83] W. H. Butler, X.-G. Zhang, T. C. Schulthess, and J. M. MacLaren, Spin-dependent tunneling conductance of Fe|MgO|Fe sandwiches, *Phys. Rev. B* **63**, 054416 (2001).
- [84] S. V. Faleev, Y. Ferrante, J. Jeong, M. G. Samant, B. Jones, and S. S. P. Parkin, Heusler compounds with perpendicular magnetic anisotropy and large tunneling magnetoresistance, *Phys. Rev. Materials* **1**, 024402 (2017).
- [85] Y. Miura, H. Uchida, Y. Oba, K. Nagao, and M. Shi-rai, Coherent tunnelling conductance in magnetic tunnel junctions of half-metallic full Heusler alloys with MgO barriers, *J. Phys.: Condens. Matter* **19**, 365228 (2007).
- [86] Y. Miura, H. Uchida, Y. Oba, K. Abe, and M. Shi-rai, Half-metallic interface and coherent tunneling in $\text{Co}_2YZ/\text{MgO}/\text{Co}_2YZ$ ($YZ = \text{MnSi}, \text{CrAl}$) magnetic tunnel junctions: A first-principles study, *Phys. Rev. B* **78**, 064416 (2008).
- [87] See Supplemental Material at arxiv.org for the zero-bias transmission spectrum of both magnetic tunnel junctions under study for a tunnel barrier thickness of five monolayers of MgO and for the DDOS of the FeVTiSi/MgO/CoFeVSb junction for five monolayers of MgO in anti-parallel configuration at equilibrium (zero bias) and for an applied bias of +0.2 V.
- [88] E. Şaşıoğlu, T. Aull, D. Kutschabsky, S. Blügel, and I. Mertig, Half-Metal–Spin-Gapless-Semiconductor Junctions as a Route to the Ideal Diode, *Phys. Rev. Applied* **14**, 014082 (2020).
- [89] M. I. Katsnelson, V. Y. Irkhin, L. Chioncel, A. I. Lichtenstein, and R. A. de Groot, Half-metallic ferromagnets: From band structure to many-body effects, *Rev. Mod. Phys.* **80**, 315 (2008).

6.3 Half-metal–spin-gapless semiconductor junctions (Ohmic spin diodes)

Conventional diodes possess a junction barrier that electrons need to overcome to turn the diode on, and thus these devices exhibit a threshold voltage. Such threshold voltages give rise to the power dissipation in form of heat and thus are undesirable features. Similar to conventional metal-semiconductor Schottky-barrier diodes, the OSD is constituted of a HMM and a SGS electrode. Since both electrodes are magnetic, depending on the relative magnetization orientation of the electrodes, the HMM-SGS junction conducts current either under forward or reverse bias (see Fig. 6.3). In contrast to conventional Schottky diodes, due to the electronic bandstructure of the SGS electrode, no energy barrier is formed at the interface between the HMM and SGS. Hence, the resistance of the OSD is much lower compared to $p-n$ diodes and therefore leads to a higher current drive capability.

In the following publication, "Half-Metal–Spin-Gapless-Semiconductor Junctions as a Route to the Ideal Diode" [TA3], we introduce the new concept of Ohmic spin diodes whose operation principle relies on the unique spin-dependent transport properties of HMMs and SGSs. Similar to conventional metal-semiconductor junction diodes (Schottky-barrier diodes), HMM-SGS junctions also act as diodes.

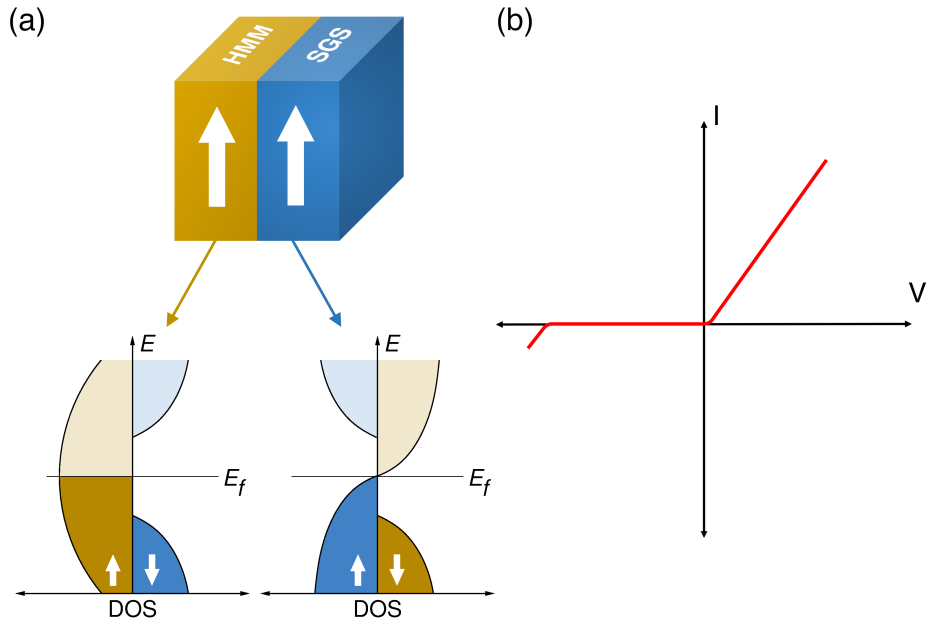


Figure 6.3: (a) Schematic representation of the Ohmic spin diode for parallel oriented electrode magnetization and schematic DOS of the HMM as well as the SGS material. The white arrows indicate the magnetization direction of each electrode. (b) The corresponding $I - V$ characteristics.

We demonstrate the linear current-voltage characteristics of the proposed diode based on HMM Fe/MoS₂ and SGS VS₂ planar heterojunctions.

The following publication: Reprinted (whole article) with permission from (E. Şaşıoğlu*, T. Aull* *et al.* Physical Review Applied **14**, 014082 (2020); Half-Metal–Spin-Gapless-Semiconductor Junctions as a Route to the Ideal Diode., Ref. [TA3]). Copyright (2020) by the American Physical Society (APS).

Half-Metal–Spin-Gapless-Semiconductor Junctions as a Route to the Ideal DiodeErsoy Şaşıoğlu^{1,*}, Thorsten Aull^{1,†}, Dorothea Kutschabsky¹, Stefan Blügel², and Ingrid Mertig^{1,3}¹*Institute of Physics, Martin Luther University Halle-Wittenberg, D-06120 Halle (Saale), Germany*²*Peter Grünberg Institut and Institute for Advanced Simulation, Forschungszentrum Jülich and JARA, D-52425 Jülich, Germany*³*Max Planck Institute of Microstructure Physics, Weinberg 2, D-06120 Halle (Saale), Germany*

(Received 20 February 2020; accepted 9 June 2020; published 27 July 2020)

The ideal diode is a theoretical concept that completely conducts the electric current under forward bias without any loss and that behaves like a perfect insulator under reverse bias. However, real diodes have a junction barrier that electrons have to overcome and thus they have a threshold voltage V_T , which must be supplied to the diode to turn it on. This threshold voltage gives rise to power dissipation in the form of heat and hence is an undesirable feature. In this work, based on half-metallic magnets (HMMs) and spin-gapless semiconductors (SGSs) we propose a diode concept that does not have a junction barrier and the operation principle of which relies on the spin-dependent transport properties of the HMM and SGS materials. We show that the HMM and SGS materials form an Ohmic contact under any finite forward bias, while for a reverse bias the current is blocked due to spin-dependent filtering of the electrons. Thus, the HMM-SGS junctions act as a diode with zero threshold voltage V_T and linear current-voltage (I - V) characteristics as well as an infinite on:off ratio at zero temperature. However, at finite temperatures, non-spin-flip thermally excited high-energy electrons as well as low-energy spin-flip excitations can give rise to a leakage current and thus reduce the on:off ratio under a reverse bias. Furthermore, a zero threshold voltage allows one to detect extremely weak signals and due to the Ohmic HMM-SGS contact, the proposed diode has a much higher current drive capability and low resistance, which is advantageous compared to conventional semiconductor diodes. We employ the nonequilibrium Green's function method combined with density-functional theory to demonstrate the linear I - V characteristics of the proposed diode based on two-dimensional half-metallic Fe/MoS₂ and spin-gapless semiconducting VS₂ planar heterojunctions.

DOI: [10.1103/PhysRevApplied.14.014082](https://doi.org/10.1103/PhysRevApplied.14.014082)**I. INTRODUCTION**

A diode is a two-terminal device that conducts electric current in only one direction but restricts current from flowing in the opposite direction, i.e., it acts as a one-way switch for current. Diodes are also known as rectifiers because they change alternating current into direct current. Diodes are of several types, with different properties depending on the materials that they consist of [1–3]. For instance, p - n -junction diodes are formed by joining a p -type semiconductor to an n -type semiconductor and they are the elementary building blocks of three-terminal transistors. The Esaki diode (or tunnel diode) [4] is a heavily doped p - n -junction diode, in which the electron transport in the contact region is via quantum-mechanical tunneling under forward bias and it shows the negative-differential-resistance (NDR) effect (see Fig. 1), which allows it to function as an oscillator and amplifier.

In connection with the Esaki diode, when the doping concentration on the p side or the n side is nearly or not quite degenerate, the current in the reverse direction is much larger than in the forward direction and hence such a device is called a backward diode [1,5,6]. In contrast to semiconductor-semiconductor diodes, a Schottky-barrier diode [1] is formed by joining a metal to an n -type semiconductor. Compared to typical p - n junctions, Schottky diodes have very fast switching times and a higher current drive capability.

Diodes are used for various applications, ranging from power conversion to overvoltage protection and from signal detection and mixing to switches. Due to the junction barrier, diodes have a threshold (or turn-on) voltage V_T , which must be supplied to the diode for it to conduct any considerable forward current. In Fig. 1, we show schematically the current-voltage (I - V) characteristics of the different types of diodes and compare them with the concepts of the ideal diode and the Ohmic junction. For p - n -junction (silicon) diodes, the threshold voltage V_T is around 0.7 V, while for Schottky diodes V_T is between 0.2

*ersoy.sasioglu@physik.uni-halle.de

†thorsten.aull@physik.uni-halle.de

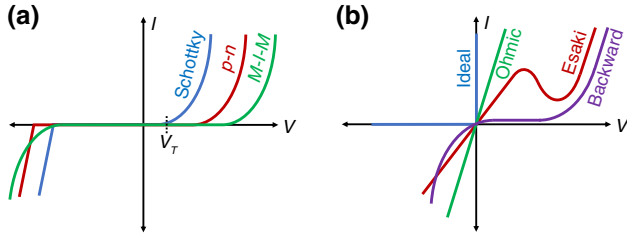


FIG. 1. (a) A schematic representation of the current-voltage (I - V) characteristics of the conventional three types of diodes [Schottky, p - n , and metal-insulator-metal (M - I - M) diodes]. (b) The I - V curves of an ideal diode, an Ohmic junction, an Esaki (tunnel diode), and a backward diode.

V and 0.3 V. Backward diodes have zero threshold voltage but their on:off current ratios as well as their voltage-operation windows are rather small. The threshold voltage V_T gives rise to power dissipation ($P = V_T \times I$) in the diode in the form of heat and hence is an undesirable feature. The larger the value of V_T , the higher is the power dissipation.

Although the ideal diode is a theoretical concept, it has been suggested that superconductor-semiconductor junctions possess I - V characteristics that are similar to the ideal one under a forward bias [7]. Initial experiments by McColl *et al.* on a superconductor-semiconductor junction diode based on lead and p -type GaAs have shown ideal-diode behavior for forward applied voltages less than the superconducting-energy-gap parameter Δ . In this voltage window (a few millielectronvolts), the diode exhibits a high degree of nonlinearity in its I - V characteristics [7]. Superconductor-semiconductor junctions have subsequently been studied as the most sensitive detectors and mixers of microwaves [8–12]. However, in contrast to the Schottky-diode behavior, superconductor-semiconductor junctions possess symmetric I - V curves with $I(-V) = -I(V)$, close to zero bias, giving rise to a relatively small on:off current ratio [12]. Furthermore, the operation temperature of such diodes is limited by the phase-transition temperature of superconductors, which is far below room temperature. Another type of diode that has a zero threshold voltage V_T is the so-called geometric diode, the operation principle of which relies on the geometric asymmetry of a conducting thin film [13–16]. Geometric diodes are ultrafast ballistic transport devices, where the critical dimension of the device is comparable to the mean-free path length of the electrons. It has, however, been shown that the geometric asymmetry of the diode alone cannot induce a current rectification and thus in addition to geometry, nonlinearity (high-order many-body interactions) is required to realize the geometric diode [17]. This also explains why the experimentally measured current rectification in graphene-related geometric diodes is very

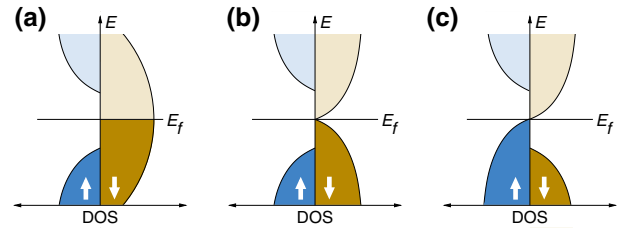


FIG. 2. A schematic representation of the density of states for (a) a half-metallic magnet, (b) a type-I spin-gapless semiconductor, and (c) a type-II spin-gapless semiconductor.

low [13,14], as the nonlinearity, i.e., the electron-phonon interactions, is rather weak in these systems.

For device applications, a special class of materials, the so-called spin-gapless semiconductors (SGSs), are receiving substantial attention. The concept of SGSs was proposed by Wang in 2008 [18,19]. By employing first-principles calculations, the author predicted SGS behavior in the Co-doped dilute magnetic semiconductor PbPdO₂. Subsequently, different classes of materials ranging from two dimensional (2D) to three dimensional (3D) have been predicted to possess SGS behavior and some of them have been confirmed experimentally. The SGSs lie on the border between magnetic semiconductors and half-metallic magnets (HMMs) [20]. A schematic density of states (DOS) of HMMs and SGSs is shown in Fig. 2. In SGSs, the mobility of charge carriers is essentially higher than in normal semiconductors, making them promising materials for nanoelectronic applications. Moreover, the spin-dependent transport properties of SGSs and HMMs lead to the emergence of device concepts in spintronics. Recently, a reconfigurable magnetic tunnel diode and transistor concept based on SGSs and HMMs has been proposed [21,22]. The magnetic tunnel diode allows electric current to pass either in one or the other direction, depending on the relative orientation of the magnetization of the HMM and SGS electrodes. Moreover, the proposed devices present the tunnel magnetoresistance effect, allowing the combination of nonvolatility and reconfigurability on the diode (transistor) level, which is not achievable in semiconductor nanoelectronics.

In this paper, we propose a diode concept, based on a HMM and a SGS electrode, that we call the Ohmic spin diode (OSD) and demonstrate proof of the principle by *ab initio* quantum transport calculations. Analogous to the metal-semiconductor junction diode (the Schottky-barrier diode), HMM-SGS junctions act as a diode, the operation principle of which relies on the spin-dependent transport properties of the HMM and SGS materials. We show that HMM and SGS materials form an Ohmic contact under any finite forward bias, giving rise to linear current-voltage (I - V) characteristics, while for a reverse

bias the current is blocked due to the filtering of the electrons. In contrast to the Schottky diode, the proposed diode does not require the doping of the SGS and also does not have a junction barrier and thus it has a zero threshold voltage V_T and an infinite on:off current ratio at zero temperature. However, at finite temperatures, non-spin-flip thermally excited high-energy electrons as well as low-energy spin-flip excitations can give rise to leakage current and thus reduce the on:off ratio under a reverse bias. Moreover, due to the Ohmic HMM-SGS contact, the proposed diode has a much higher current drive capability and low resistance, which is advantageous compared to conventional semiconductor diodes. To demonstrate the linear I - V characteristics of the concept, we construct a planar HMM-SGS junction based on 2D half-metallic Fe/MoS₂ and spin-gapless semiconducting VS₂ and employ the nonequilibrium Green's function method combined with density-functional theory (DFT). We find that at zero bias the VS₂ and Fe/MoS₂ electrodes couple ferromagnetically; however, this coupling changes sign from ferro to antiferromagnetic for a critical forward bias voltage of $V = 180$ mV. The VS₂-Fe/MoS₂ junction diode possesses linear I - V characteristics for forward bias voltages up to $V = 180$ mV and a very small threshold voltage of $V_T = 30$ meV, which can be attributed to the minority-electron conduction-band minimum of the spin-gapless semiconducting VS₂ material. Moreover, we obtain a very high current density ($J = 2350 \mu\text{A}/\mu\text{m}$ for $V = 180$ mV), which makes the VS₂-Fe/MoS₂ OSD highly promising for low-temperature nanoelectronic applications.

II. HMM-SGS JUNCTIONS

The structure of the proposed OSD and its I - V characteristics are shown schematically in Fig. 3. Analogous to the metal-semiconductor Schottky-barrier diode, the OSD is composed of a HMM electrode and a type-II SGS electrode. Depending on the magnetization direction of the electrodes, the diode conducts current either under forward bias [Fig. 3(a), parallel orientation (ferromagnetic interelectrode coupling)] or under reverse bias [Fig. 3(a), antiparallel orientation (antiferromagnetic interelectrode coupling)], similar to the case of the backward diode mentioned in Sec. I. In the presentation of the schematic I - V characteristics of the OSD in Fig. 3, we assume that HMM material possesses a gap in the spin-up channel around the Fermi level, while type-II SGS material has a gap in the spin-up (spin-down) channel above (below) the Fermi level, as shown schematically in Fig. 2. In type-II SGSs, the conduction- and valence-band edges of the different spin channels touch at the Fermi energy, while in type-I SGSs the spin-up (majority-spin) band looks like the one in HMMs but the difference is in the spin-down (minority-spin) band. The valence- and conduction-band edges are touching at the Fermi energy, so that a zero-width gap

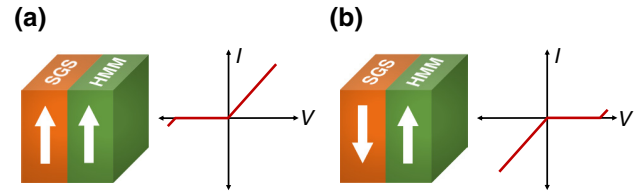


FIG. 3. (a) A schematic representation of the HMM-SGS junction for parallel orientation of the magnetization directions of the electrodes and the corresponding current-voltage (I - V) curves. (b) The same as (a) for the antiparallel orientation of the magnetization directions of the electrodes. The white arrows indicate the direction of the magnetization of the electrodes.

exists. One of the important advantages of type-I SGSs is that no energy is required for the excitation of the electrons from the valence to the conduction band and excited electrons or holes can be 100% spin-polarized as in HMMs. In construction of the OSD, the use of a type-I SGS instead of the HMM is also possible.

The linear I - V characteristics of the OSD presented in Fig. 3(a) can be qualitatively explained on the basis of the schematic energy-band diagram shown in Fig. 4. If we assume that both HMM and SGS electrodes have the same work function and equal Fermi levels, then no charge transfer takes place between the electrodes. However, in real materials, due to different work functions there might be a charge transfer from one material to another at the interface, which might give rise to band bending for the SGS. Besides this, due to interactions, junction materials might not retain their half-metallic and spin-gapless semiconducting properties near the interface and hence the band diagram will not be as sharp as in Fig. 4. For the device configuration shown in Fig. 3(a), the relevant channel for the transport is the minority-spin (spin-down) channel, whereas the majority-spin (spin-up) channel is insulating due to the spin gap of the HMM material on the right-hand side of the junction. In the spin-down channel, the HMM behaves like a normal metal, with states below and above the Fermi energy, while the SGS electrode on the left-hand side behaves like a semiconductor (or insulator) but with a Fermi level touching the conduction-band minimum. Due to this electronic band structure of the SGS, in contrast to the Schottky diode, no energy barrier is formed at the interface between a HMM and a SGS material. Such a junction acts as an Ohmic contact under forward bias, as shown in Fig. 4(b). In this case, the spin-down electrons from the occupied valence band of the HMM electrode can flow into the unoccupied conduction band of the SGS electrode without experiencing a potential barrier, while for a reverse bias the current is blocked due to the spin gap of the HMM material [see Fig. 4(c)]. Note that under a forward bias, the current flowing through the OSD is 100% spin polarized. Note also that

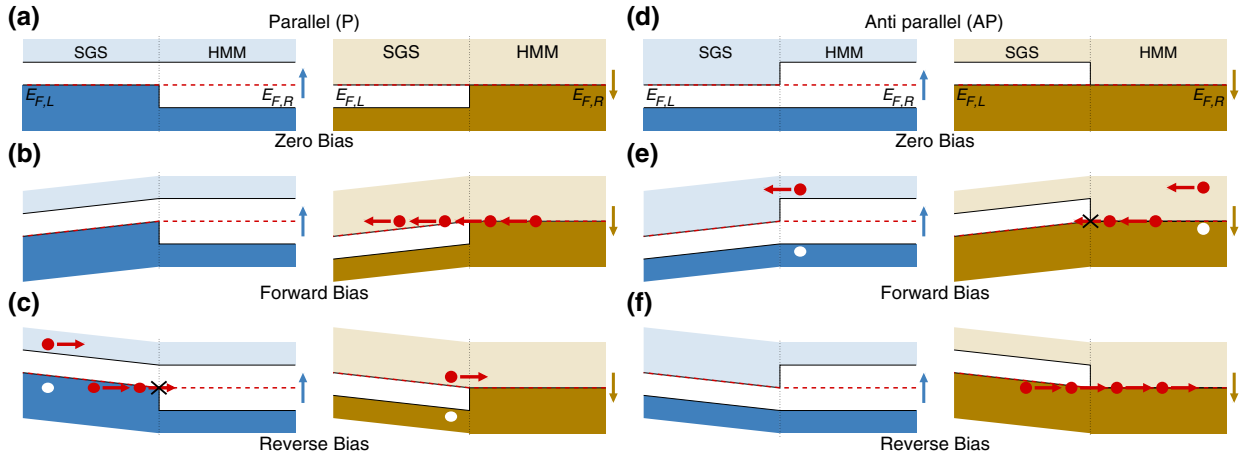


FIG. 4. A schematic representation of the band diagram and thermal (non-spin-flip) electron-hole excitations for spin-up and spin-down electrons for the SGS-HMM contact for parallel (P) orientation of the magnetization directions of the electrodes: (a) for zero bias, (b) for forward bias, and (c) for reverse bias. The Fermi level is denoted by red dashed line. (d)–(f) The same as (a)–(c) for the antiparallel (AP) orientations of the magnetization directions of the electrodes [see Figs. 3(a) and 3(b)].

the same discussion applies in the case of antiparallel orientations of the magnetization directions of the electrodes [see Figs. 4(d), 4(e), and 4(f)].

As the HMM-SGS contact is Ohmic under a forward bias, the current I through the diode varies linearly with the applied voltage V and the ratio V/I gives the combination of the interface (R_I) and series resistance (R_S) of the HMM and SGS materials ($V/I = R_I + R_S$). The resistance of SGS materials is usually much lower than that of conventional n - or p -type semiconductors [23] and thus the combination of low resistance with the Ohmic nature of the interface allows a much higher current drive capability of the proposed OSD. It is worth noting that diodes with low resistance are critical for the performance of high-speed electronic devices. Besides the higher current drive capability of the OSD, the threshold voltage V_T can be tuned by a proper choice of the SGS material. The value of V_T is set by the energy difference between the minority-spin conduction-band minimum and the Fermi level. In an ideal SGS, this difference is zero and thus $V_T = 0$. Note, however, that in type-II SGSs, the spin-gapless semiconducting properties are not protected by any symmetry and thus ideal SGS behavior can only arise if a free parameter—e.g., pressure, strain, or doping—is tuned to a specific value. A zero V_T allows one to detect extremely weak signals, even when no external bias circuit is used. Similar to the Schottky diode, the OSD is also a majority-carrier diode but it does not require doping and it will possess all the advantages of the Schottky diode, such as high operation frequencies, low resistance and capacitance, etc. Note also that, in principle, a Schottky diode can be turned into an Ohmic contact by heavily doping the semiconductor electrode; however, in this case it loses its diode functionality.

Up to now, the discussion of the I - V characteristics of the OSD is based on the schematic band diagram at zero temperature and thus an infinite on:off current ratio can be achieved. However, at finite temperatures, thermally excited electrons and holes can significantly reduce the on:off ratio. At this point, it is important to note that in conventional metal-semiconductor Schottky diodes, electrons flow from the semiconductor to the metal electrode under a forward bias, whereas in the OSD shown in Fig. 3(a), the process is just the opposite, i.e., from the half-metal to the spin-gapless semiconductor. In the former case, the on-state current stems from the combination of thermionic emission over the Schottky barrier and tunneling through the barrier [24–26]. A very detailed analysis of these processes and their relative contributions to the total forward (on-state) current in Schottky diodes can be found in Ref. [24]. Similarly, under a reverse bias, both processes contribute to the leakage current in Schottky diodes, with a significant weight coming from the tunneling (or thermionic field emission), since in this case the height of the Schottky barrier is fixed and only a very small fraction of the thermally excited high-energy electrons, which are at the tail of the Fermi-Dirac distribution function, can pass over the barrier. By increasing the height of the Schottky barrier, the contribution of thermionic emission can be significantly reduced, as the Fermi-Dirac distribution function decays exponentially at high energies [see Fig. 3(a)]; however, the contribution of the tunneling through the barrier cannot be prevented and at the same time the threshold voltage V_T increases. In the OSD, the leakage current due to tunneling does not exist; however, thermally excited high-energy electrons contribute to the reverse current, similar to the case of the Schottky diode. In Figs. 5(b) and 5(c), we show schematically the population of unoccupied

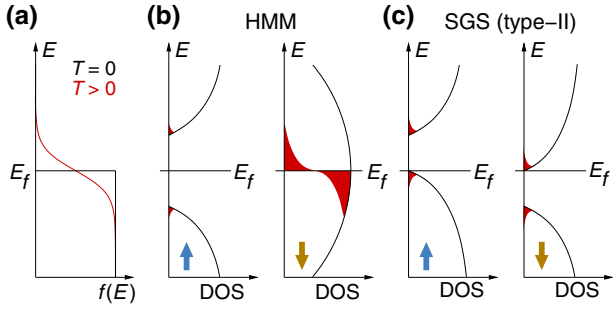


FIG. 5. (a) The Fermi-Dirac distribution for $T = 0$ K (black) and $T > 0$ K (red) and a thermal population of states around the Fermi level for (b) a HMM and (c) type-II SGS. The occupied and unoccupied states above and below the Fermi level, respectively, are marked with a shaded red color.

states around the Fermi energy for a HMM and a type-II SGS. In a HMM, thermal population of the states obeys the Fermi-Dirac distribution, i.e., more states in the metallic spin-channel and very few states for the insulating spin-channel, as they are far from the Fermi level. However, the situation turns out to be slightly different in type-II SGSs, due to their band structure, i.e., only a small fraction of the electrons can be thermally excited due to the gap in both spin channels, somewhat similar to the case of intrinsic semiconductors. Consequently, the reverse-bias current (or the leakage current) is mainly determined by the size of the band gaps in SGS and HMM electrodes and by a proper choice of the large band-gap materials, the on:off current ratio can be significantly increased in OSDs. In addition to thermal excitation, spin-flip processes can reduce the on:off current ratio and this will be discussed later.

In contrast to the Schottky diode, the spin degree of freedom provides a rich configuration space for the I - V curves of the OSD, which are determined by two parameters: (i) the magnetic coupling between electrodes, which allows the dynamical configuration of the diode in the case of antiferromagnetic interelectrode coupling via an external magnetic field; and (ii) the spin character of the gap in HMMs and SGSs. Depending on the magnetic coupling between electrodes, the OSD is in the on state either under forward bias (ferromagnetic interelectrode coupling or parallel orientation) or under reverse bias (antiferromagnetic interelectrode coupling or antiparallel orientation), as shown in Fig. 3. The second parameter, which plays a decisive role in determining the I - V characteristics of the OSD, is the spin-channel dependence of the gap in HMM and SGS electrodes. For instance, as mentioned above in the presentation of the schematic I - V characteristics of the OSD in Fig. 3, we assume that the HMM material has a gap in the spin-up channel and that the SGS material has gaps in the spin-down (below E_F) and spin-up channels (above E_F). Although all known type-II SGSs possess an electronic band structure similar to that in Fig. 2(c), there

TABLE I. The I - V characteristics of the OSD for parallel (P) and antiparallel (AP) orientations of the magnetization directions of the electrodes and all possible combinations of the spin character of the gaps in HMMs and SGSs. SGS ($\downarrow\uparrow$) indicates the spin channel, where the gap exists below and above the Fermi level.

| Spin gap | Orientation | Forward bias | Reverse bias |
|---|-------------|--------------|--------------|
| SGS ($\downarrow\uparrow$)/HMM ($\uparrow\uparrow$) | P | On | Off |
| SGS ($\downarrow\uparrow$)/HMM ($\uparrow\uparrow$) | AP | Off | On |
| SGS ($\downarrow\uparrow$)/HMM ($\downarrow\downarrow$) | P | Off | On |
| SGS ($\downarrow\uparrow$)/HMM ($\downarrow\downarrow$) | AP | On | Off |
| SGS ($\uparrow\downarrow$)/HMM ($\uparrow\uparrow$) | P | Off | On |
| SGS ($\uparrow\downarrow$)/HMM ($\uparrow\uparrow$) | AP | On | Off |
| SGS ($\uparrow\downarrow$)/HMM ($\downarrow\downarrow$) | P | On | Off |
| SGS ($\uparrow\downarrow$)/HMM ($\downarrow\downarrow$) | AP | Off | On |

are many HMMs, such as Heusler alloys, with a gap in the spin-down channel and OSD diodes constructed from such materials might have a different current direction than the present case. For completeness, in Table I we present the I - V characteristics of the OSD by taking into account both magnetic configurations of the electrodes and all possible combinations of the spin character of the gaps in HMMs and SGSs.

As the OSD is comprised of magnetic materials, its operation temperature is limited by the Curie temperature T_C of the constituent materials and thus for realization of the OSD, HMMs and SGSs with high T_C values are required. Two-dimensional transition-metal dichalcogenides [27–30] and 3D quaternary Heusler compounds [31–36] offer a unique platform to design, within the same family of compounds, HMMs and SGSs with high T_C values and similar lattice parameters and compositions, which allow coherent growth of these materials on top of each other. Besides high T_C values, large spin gaps in HMMs and SGSs are crucial in order to achieve a high on:off current ratio in the OSD. In recent years, 2D transition-metal dichalcogenides have received significant experimental and theoretical interest, as they present unique electronic, optical, mechanical, and magnetic properties, thus holding great promise for a wide range of device applications. Devices ranging from vertical tunnel diodes to vertical and lateral tunnel field-effect transistors (TFETs) have been experimentally demonstrated [37–44]. In particular, 2D lateral heterojunctions have opened up a direction in materials science and device applications [45]. TFETs based on 2D material heterojunctions (WTe_2 - MoS_2 , MoTe_2 - MoS_2) have been reported to exhibit a subthreshold slope below 5 mV per decade and high $I_{\text{on}}/I_{\text{off}}$ ratios (approximately 10^8) at a low drain bias of 0.3 V, making them ideal candidates for ultralow-power computing [46].

Among the 2D transition-metal dichalcogenides, V -based compounds (VS_2 , VSe_2 , VTe_2) have attracted

particular interest due to their intrinsic ferromagnetism. These compounds can crystallize into two different structures: the $1H$ phase and the $1T$ phase. The former phase is energetically more stable and possesses a SGS ground state [47,48]. Although, theoretically, both $1H$ and $1T$ phases of V -based 2D compounds have been predicted to show ferromagnetism [49], experimentally the ferromagnetism has, however, only been observed in the $1T$ phase of VS_2 [50] and VSe_2 [51]. Note that the $1T$ phase of VSe_2 does not present SGS behavior; it is a normal ferromagnetic metal. However, in the one-monolayer limit, several 2D transition-metal dichalcogenides can adopt either a $1T$ or a $1H$ structure depending on the growth conditions [52]. It is very likely that VS_2 can also be grown in a $1H$ structure.

III. COMPUTATIONAL METHOD

Ground-state electronic structure calculations are carried out using DFT, implemented in the QuantumATK P-2019.03 package [53]. We use the generalized-gradient-approximation (GGA)–Perdew–Burke–Ernzerhof (PBE) exchange–correlation functional [54] together with PseudoDojo pseudopotentials [55] and LCAO basis sets. A dense $24 \times 24 \times 1$ \mathbf{k} -point grid and a density mesh cutoff of 120 hartree are used. To prevent interactions between the periodically repeated images, 20 Å of vacuum are added and Dirichlet and Neumann boundary conditions are employed. The electron temperature is set to 10 K. The total energy and forces converge to at least 10^{-4} eV and 0.01 eV/Å, respectively. In order to estimate the magnetic anisotropy energy, we employ the magnetic force theorem, including spin-orbit coupling [56].

The transport calculations are performed using DFT combined with the nonequilibrium Green’s function method (NEGF). We use a $24 \times 1 \times 172$ \mathbf{k} -point grid in self-consistent DFT-NEGF calculations. The I - V characteristics are calculated within a Landauer approach [57], where $I(V) = (2e/h) \sum_{\sigma} \int T^{\sigma}(E, V) [f_L(E, V) - f_R(E, V)] dE$. Here, V denotes the bias voltage, $T^{\sigma}(E, V)$ is the spin-dependent transmission coefficient for an electron with spin σ , and $f_L(E, V)$ and $f_R(E, V)$ are the Fermi-Dirac distributions of the left and right electrodes, respectively. The transmission coefficient $T^{\sigma}(E, V)$ is calculated using a 300×1 \mathbf{k} -point grid.

IV. RESULTS AND DISCUSSION

The OSD concept introduced in Sec. II can be realized either by using 3D Heusler compounds or 2D transition-metal dichalcogenides. In the following, due to their structural simplicity, we focus on the 2D materials and demonstrate the proof of principle by *ab initio* quantum transport calculations. As the electrode materials of the OSD, we choose VS_2 and Fe/MoS_2 . The former is an intrinsic ferromagnet with spin-gapless semiconducting

behavior in the monolayer $1H$ phase, while the half-metallic ferromagnetism in the latter Fe/MoS_2 material is achieved by functionalization of the $1H$ semiconducting MoS_2 . Based on first-principles calculations, Jiang *et al.* [58] have shown that deposition of the Fe atoms on MoS_2 gives rise to the 2D half-metallic ferromagnetism with a relatively high T_C value of 465 K and a large spin gap, which makes the Fe/MoS_2 a promising material for spintronic and nanoelectronic applications.

Since the electronic and magnetic as well as the structural properties of both electrode materials have been extensively discussed in the literature, in the following we will briefly overview their basic properties, which will be necessary in order to understand the transport characteristics of the OSD. In Table II, we present the optimized lattice constants and the total magnetic moments as well as the magnetic anisotropy energies for the $1H$ phase of VS_2 and Fe/MoS_2 . Our ground-state calculations for both materials are in good agreement with previously published data. In particular, similar lattice parameters and compositions, as well as the same $1H$ phase, of the two materials are crucial for realization of the planar VS_2 - Fe/MoS_2 heterojunctions. VS_2 has a relatively simple band structure, shown in Fig. 6(b), where the exchange splitting of the V - $3d$ (predominantly d_{z^2}) bands around the Fermi energy is responsible for its spin-gapless semiconducting nature and thus it has a magnetic moment of $1 \mu_B$, carried by the V atom. Furthermore, VS_2 is not a perfect SGS; it has a very small indirect band gap of 50 meV, i.e., the valence-band maximum and the conduction-band minimum are at around 20 meV and 30 meV, respectively. The former plays a decisive role in determining the threshold voltage V_T of the OSD in the case of ferromagnetic coupling of the VS_2 and Fe/MoS_2 electrodes, while the latter plays the same role in the case of antiferromagnetic coupling. Note that in the present OSD based on a planar VS_2 - Fe/MoS_2 heterostructure, the coupling between the electrodes is ferromagnetic, as is discussed later. On the other hand, the Fe-deposited MoS_2 turns into a half-metallic magnet with a gap of about 1 eV in the spin-up channel and with a total magnetic moment of $2 \mu_B$, which is localized on the Fe atom. Note that PBE is well known to underestimate the band gap of semiconductors compared to the more accurate GW approach. However, the situation is different for 2D SGSs, since the application of the GW method for the similar material VSe_2 reduces the band gap from 250 meV (PBE) to 170 meV [29]. We expect a similar behavior for the VS_2 compound when the GW method is employed. Also, spin-orbit coupling has a negligible effect on the spin polarization of both materials and thus it is not taken into account in our device calculations.

In Fig. 6(a), we show the atomic structure of the OSD, which is formed by joining one monolayer of VS_2 (left electrode) and one monolayer of Fe/MoS_2 (right electrode) laterally in a single plane. Due to the almost

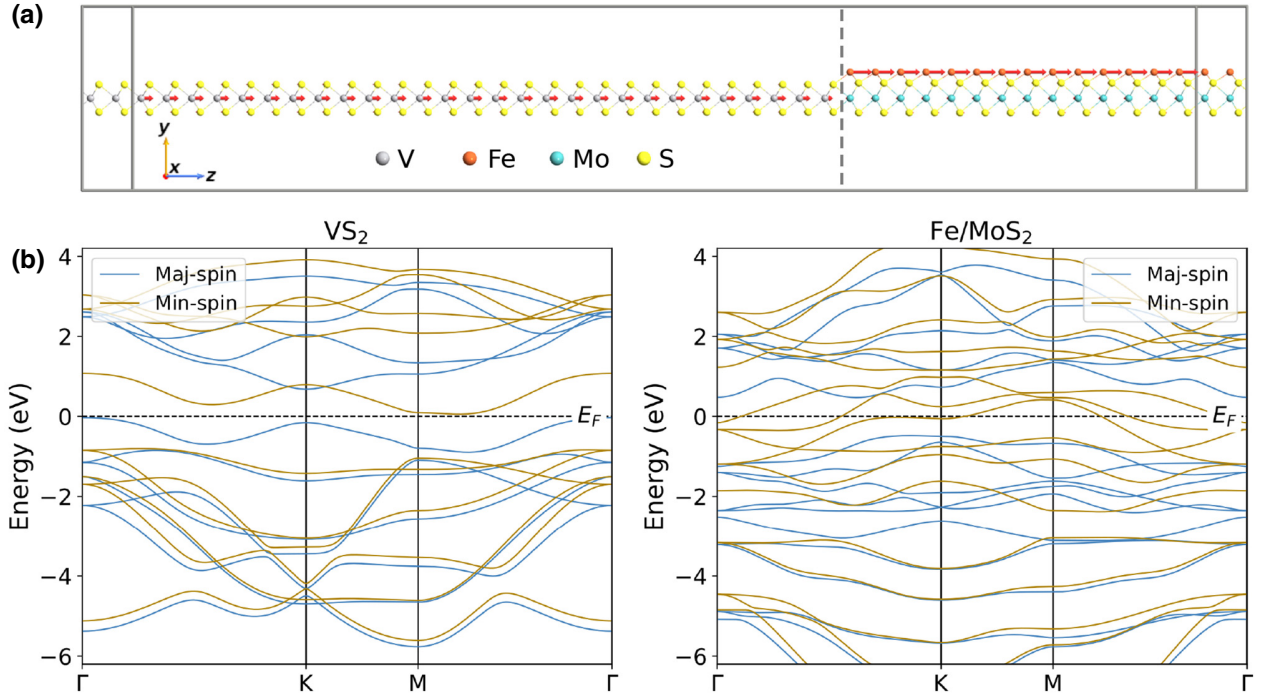


FIG. 6. (a) The atomic structure of the VS_2 - Fe/MoS_2 Ohmic spin diode. The arrows show the magnetic moments of V and Fe atoms in the SGS and HMM electrodes within the scattering region. The size of the arrows is proportional to the magnitude of the magnetic moments. The system is periodic in the x direction in the plane orthogonal to the magnetization direction, which is also the transport direction. The vertical dashed lines denote the interface. (b) The calculated spin-resolved bulk electronic band structure along the high-symmetry lines in the Brillouin zone for VS_2 (left-hand panel) and Fe/MoS_2 (right-hand panel). For both compounds, the dashed lines denote the Fermi energy, which is set to zero.

identical lattice parameters of both materials, as well as their similar compositions, they form a perfect interface. We assume periodicity of the device in the x direction. The z direction is chosen as the transport direction. The total length of the scattering region is about 115.5 \AA , which consists of 77 \AA VS_2 and 38.5 \AA Fe/MoS_2 . The length of the former electrode is chosen to be larger because of the longer screening length in SGSs.

When the half-metallic Fe/MoS_2 makes contact with VS_2 , free electrons will flow from the half-metallic Fe/MoS_2 side to the spin-gapless semiconducting VS_2 side, because the work function of the Fe/MoS_2 is smaller than that of VS_2 (see Table II). Note that the work function of the SGS VS_2 is defined in the same way as in metals, i.e., the energy difference between the vacuum level and the

TABLE II. The calculated lattice parameter a , the total magnetic moment m_T , the magnetic anisotropy energy K (per formula unit), and the work function ϕ for VS_2 and Fe/MoS_2 . The values of the Curie temperature T_c are taken from the literature.

| Compound | a (\AA) | m_T (μ_B) | K (meV) | ϕ (eV) | T_c (K) |
|--------------------------|-------------------------|----------------------|--------------|----------------|--------------|
| VS_2 | 3.174 | 1.00 | 0.20 | 5.71 | 138 [49] |
| Fe/MoS_2 | 3.175 | 2.00 | 0.42 | 4.72 | 465 [58] |

Fermi energy E_F . When the charge redistribution reaches equilibrium, near the interface region the Fe/MoS_2 will be positively charged, whereas the VS_2 will be negatively charged. Thus, an electric dipole will be induced at the interface region. Such a charge redistribution influences the electronic and magnetic properties of the materials near the interface, as seen in the zero-bias projected device density of states (DDOS) shown in Fig. 7. Near the interface, charge transfer takes place within the spin-down channel and thus the magnetic moment of the Fe atoms increases toward the interface, i.e., $2.15 \mu_B \rightarrow 2.17 \mu_B \rightarrow 2.56 \mu_B$, as shown by the arrows in Fig. 6(a), where the size of the arrows is proportional to the magnitude of the magnetic moments. The transferred charge occupies the spin-down channel on the VS_2 side by creating interface states, which can be clearly seen on the projected DDOS shown in Fig. 7 and as a consequence the magnetic moment of the V atoms at the interface and subinterface lines is reduced from its bulk value of $1.13 \mu_B$ to $0.53 \mu_B$ and $0.95 \mu_B$, respectively. As can be seen, the influenced region is rather small, being within four atomic lines and restricted to the spin-down channel. The change in the spin-up channel is more or less negligible.

Long-range magnetic order is prohibited in 2D magnets at finite temperatures due to the Mermin-Wagner

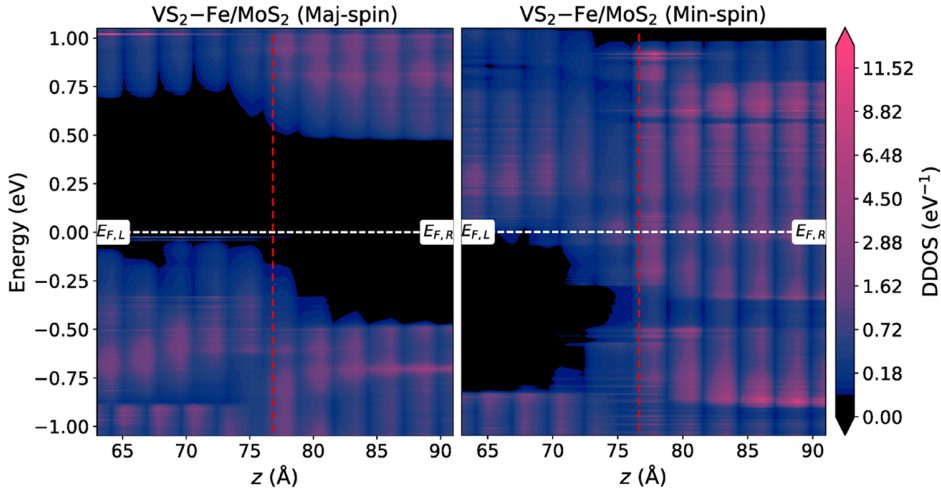


FIG. 7. (a) The zero-bias projected device density of states (DDOS) for the majority (left-hand panel) and minority (right-hand panel) electrons for the Ohmic spin diode around the interface (see Fig. 6 for the atomic structure of the OSD). The horizontal white dashed lines indicate the Fermi level. The vertical red dashed lines denote the interface.

theorem [59]. However, this restriction can be removed by magnetic anisotropy and it enables the occurrence of 2D magnetic order at finite temperatures. For both materials, we calculate the magnetic anisotropy energies K , which are presented in Table II. Both materials have an in-plane magnetization with K values of 0.2 meV (VS_2) and 0.42 meV (Fe/MoS_2). However, the magnetic anisotropy within the plane for VS_2 is negligibly small (a few nano-electronvolts), while for Fe/MoS_2 it is around 5 μeV , which is large enough for a finite-temperature magnetic order. The negligible value of K for VS_2 implies the lack of finite-temperature magnetic order by virtue of the Mermin-Wagner theorem. However, room-temperature ferromagnetism has been experimentally detected in similar materials such as VSe_2 [51], which has also negligible in-plane magnetic anisotropy, and the origin of the long-range ferromagnetic order is attributed to the finite-size effects [60,61]. However, in the VS_2 - Fe/MoS_2 junction, the Fe/MoS_2 acts as a pinning electrode, which introduces a preferred in-plane magnetic orientation in the VS_2 electrode via the ferromagnetic interelectrode coupling. Our calculations show that ferromagnetic interelectrode coupling is preferable compared to antiferromagnetic interelectrode coupling and that the energy difference between the two configurations is about 22 meV.

Besides the magnetic anisotropy energy K and the interelectrode coupling, another important parameter for the realization of the OSD is the Curie temperature T_C of the constituent materials. The T_C values for both materials have been estimated from first principles in Refs. [49] and [58] (see Table II). The T_C value of Fe/MoS_2 is higher than room temperature, while for VS_2 ($T_C = 139$ K) it is below room temperature. Nevertheless, such a value is high enough for an experimental demonstration of the device.

Next, we discuss the electronic and transport properties of the OSD under a finite bias voltage. As mentioned above, although at zero bias the coupling between the

SGS and HMM electrodes is ferromagnetic, we find that this coupling changes sign from ferromagnetic to antiferromagnetic under a forward bias of about 180 mV. Note that electric field or voltage control of magnetism on the nanoscale is highly appealing for the development of nanoelectronic devices with low power consumption [62–64]. A voltage-induced interlayer exchange coupling in magnetic tunnel junctions has been discussed theoretically via high-voltage tunneling [65–67] and has been experimentally demonstrated via mobile oxygen vacancies [68]. A sign change in magnetic coupling with the bias voltage allows the realization of devices with unique functionalities, which will be considered in a separate paper. In Figs. 8(a) and 8(b), we show the spin-resolved projected DDOS for bias voltages of 0.3 V (forward bias) and -0.3 V (reverse bias), respectively. Note that for the purpose of the demonstration of the OSD concept, we constrain the magnetic coupling between electrodes to the ferromagnetic state (parallel orientation) in the VS_2 - Fe/MoS_2 junction for bias voltages higher than 180 mV. As can be seen, for a forward bias, the spin-gapless and the half-metallic behavior is more or less preserved at the interface for both spin channels. Just a few new states arise at the interface in the spin-up channel, this being due to antiferromagnetic coupling of the single V atom at the interface. The interface V atom possesses a magnetic moment of $-0.55 \mu_B$ and variation of the magnetic moments in Fe and other V atoms near the interface is also negligible.

On the other hand, for a reverse bias, the coupling between electrodes remains ferromagnetic and thus the electronic and magnetic structure near the interface is similar to the zero-bias case with the exception of the band bending in the VS_2 electrode, which takes place near the interface region, within 40 Å. Note that the band bending is not linear due to charge transfer as well as the complex metallic screening of the Fe/MoS_2 electrode. Indeed, we observe a flat region of about 15 Å on the

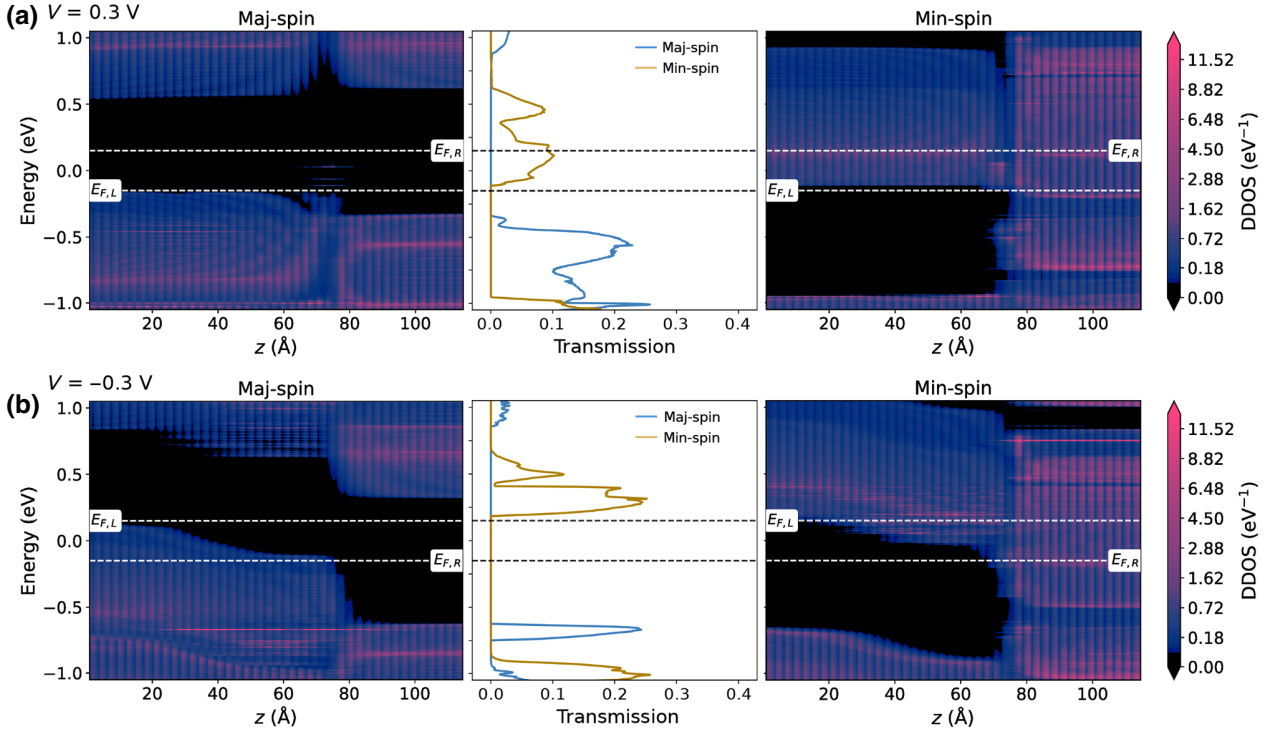


FIG. 8. (a) The projected device density of states (DDOS) for the majority (left-hand panel) and minority (right-hand panel) electrons for the $\text{VS}_2\text{-Fe/MoS}_2$ Ohmic spin diode (see Fig. 6 for the atomic structure of the Ohmic spin diode) under a positive voltage of $V = 0.3$ V. The middle panel shows the calculated transmission spectrum for the majority and minority electrons for the same applied voltage of $V = 0.3$ V. The upper and lower white (black) dashed lines indicate the Fermi level of the SGS and HMM electrodes. (b) The same as (a) for a negative voltage of $V = -0.3$ V.

projected DDOS [see Fig. 8(b)] of the junction on the VS_2 side and then the potential drops more or less linearly with distance.

The I - V characteristics of the $\text{VS}_2\text{-Fe/MoS}_2$ OSD can be qualitatively explained on the basis of the projected DDOS shown in Fig. 8. For a forward bias, the OSD is in the on state, i.e., minority-spin electrons from the occupied states of the Fe/MoS_2 electrode can flow into the unoccupied states of the VS_2 electrode due to the Ohmic contact and thus the transmission coefficient takes finite values within the bias window, as shown in the middle panel of Fig. 8(a). Meanwhile, for majority-spin electrons the transmission coefficient is zero because both Fe/MoS_2 and VS_2 have no states within the voltage window. Thus the on-state current of the OSD is 100% spin polarized. On the other hand, for a reverse bias voltage, no current flows through the OSD, since the energy gap in the majority spin channel of the Fe/MoS_2 electrode prevents the flow of the spin-up electrons from the VS_2 electrode into the Fe/MoS_2 [see Fig. 8(b) left-hand panel], giving rise to a zero transmission coefficient. Similarly, the transmission coefficient for the spin-down channel is also zero due to the energy gap in the VS_2 electrode below the Fermi level.

Figure 9 shows the calculated I - V characteristics of the $\text{VS}_2\text{-Fe/MoS}_2$ OSD at zero temperature. In the on state, the current increases linearly with the applied bias and reaches $2350 \mu\text{A}/\mu\text{m}$ for a bias voltage of 180 mV, which is the maximum bias voltage at which ferromagnetic coupling between electrodes is retained. The $\text{VS}_2\text{-Fe/MoS}_2$ diode possesses a very small threshold voltage of about 30 mV, stemming from the indirect band gap of the SGS VS_2 electrode, which has a conduction-band minimum of 30 meV [see Fig. 6(b)] as discussed before. For bias voltages larger than 180 mV, the I - V curve of the OSD takes a plateau shape, i.e., the current first monotonically increases up to 250 mV and then it starts to decrease. Such behavior can be attributed to the antiferromagnetic coupling of a single V atom at the interface, which now has a gap in the spin-down channel above the Fermi energy, in contrast to the rest of the atoms in the junction. This energy gap acts as a small potential barrier, giving rise to more reflection of the electrons, and thus it reduces the transmission. Furthermore, in the bias-voltage range from 180 mV to 300 mV, the magnetic moment of the V atom at the interface increases from $-0.2 \mu_B$ to $-0.55 \mu_B$, which also explains the plateaulike shape of the I - V curve at higher voltages.

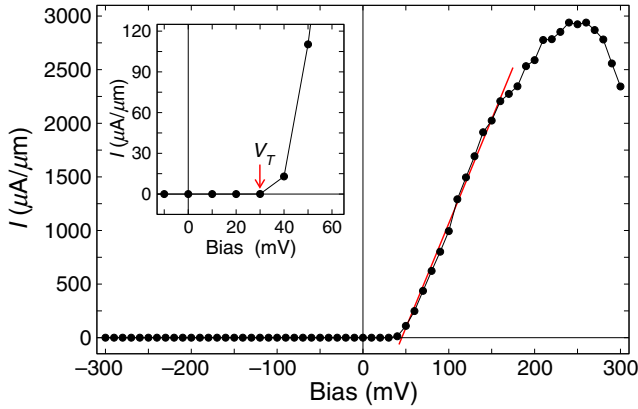


FIG. 9. The calculated current-voltage (I - V) characteristics of the VS_2 -Fe/MoS₂ Ohmic spin diode. The red line shows the Ohmic behavior in the voltage range between 40 mV and 180 mV. The inset shows an enlargement of the range between -10 mV to 60 mV, to specify the threshold voltage V_T .

A feature of the proposed VS_2 -Fe/MoS₂ OSD is that it has a much higher current-drive capability, i.e., in the on state, for a bias voltage of $V = 180$ meV the calculated current density turns out to be around $I = 2350 \mu\text{A}/\mu\text{m}$. This value is much higher than the on-state current density of devices based on 2D semiconducting materials [69] and lies far above the International Roadmap for Devices and Systems (IRDS) [69,70] requirement ($1350 \mu\text{A}/\mu\text{m}$). A negligible turn-on voltage of $V_T = 30$ mV allows us to detect extremely weak signals and thus the OSD might find potential applications in antenna-coupled diode solar cells [71–73]. Besides this, the VS_2 -Fe/MoS₂ OSD possesses an infinite on:off current ratio at zero temperature. However, as discussed in Sec. II, thermally excited high-energy electrons would reduce the on:off current ratio to finite values. In the Landauer formalism of electronic current, the temperature effects can be taken into account via the Fermi-Dirac distribution function of the left [$f_L(E, V, T)$] and right [$f_R(E, V, T)$] electrodes (see Ref. [24]) and thus the on:off current ratio can be calculated for a given temperature T . However, this standard treatment should be modified for SGS materials due to their electronic band structure, which is discussed in Sec. II. Specifically, each spin channel of the SGS material with a proper population of the states above and below the Fermi energy should be taken into account. Since this modification has not been implemented in the current version of the QuantumATK package, we present the I - V characteristics only for zero temperature in Fig. 9.

As mentioned in Sec. II, the spin degree of freedom brings a certain functionality to the OSD, which can be dynamically configured by an external magnetic field; thus the OSD can be used as a switch. However, this is possible only for OSDs having electrodes that couple antiferromagnetically (the AP orientation). So in this case,

in reversing the magnetization direction of one electrode from the antiparallel to the parallel orientation, the OSD switches from the on state to the off state like a transistor. This switching can be easily understood with the help of the schematic band diagram shown in Fig. 4 and will not be discussed here. The situation is even more interesting in the case of VS_2 -Fe/MoS₂ OSD, i.e., in addition to the voltage-induced switching from the on state to the off state at around $V = 180$ mV, the OSD can again be switched back to the on state by a weak external magnetic field, making the VS_2 -Fe/MoS₂ OSD highly appealing for nanoelectronic applications.

Finally, we would like to comment on the effect of low-energy spin excitations on the I - V characteristics of the VS_2 -Fe/MoS₂ OSD. Apart from the high-energy thermal (non-spin-flip) excitations that we discuss in Sec. II, the temperature affects the electronic and magnetic structure of the VS_2 and Fe/MoS₂ via spin-dependent excitations, i.e., Stoner excitation and collective spin waves or magnons. In type-II SGSs such as VS_2 , electrons can be excited from the majority-spin channel to the minority-spin channel via spin flip with almost vanishing energy [see Fig. 2(c)]. These excitations are known as single-particle Stoner excitations. They can populate the unoccupied minority-spin channel of VS_2 just above the Fermi energy. However, in VS_2 , Stoner excitations require a large momentum transfer, since the valance-band maximum and the conduction-band minimum are at different \mathbf{k} points in the Brillouin zone. The former is at the Γ point, while the latter is close to the M point [for the band structure of VS_2 , see Fig. 6(b)] and thus single-particle spin-flip excitation requires a large momentum transfer and takes place at high temperatures close to the Curie temperature T_C . Nevertheless, they can populate the unoccupied minority channel above the Fermi energy and give rise to a leakage current under a reverse bias [see Fig. 4(c)]. Moreover, the on:off current ratio will be further reduced. On the other hand, in half-metallic Fe/MoS₂, Stoner excitations are not allowed due to the existence of the spin gap; however, at finite temperatures, electron-magnon interaction can give rise to the appearance of nonquasiparticle states within the half-metallic gap just above the Fermi energy [74]. Thus, such states can reduce the spin polarization of the half-metallic Fe/MoS₂ and affect its transport properties. Lastly, in addition to non-spin-flip as well as spin-flip excitations, defects at the interface, which destroy the SGS or HMM behavior, can also reduce the on:off current ratio of the OSD.

V. CONCLUSIONS

In conclusion, we propose a diode concept that we call the OSD, based on SGS and HMM materials. Analogous to the metal-semiconductor junction diode (the Schottky-barrier diode), HMM-SGS junctions act as a diode the operation principle of which relies on the

spin-dependent transport properties of the constituent HMM and SGS materials. We show that the HMM and SGS materials form an Ohmic contact under any finite forward bias voltage, giving rise to linear I - V characteristics, while for a reverse bias the current is blocked due to spin-dependent filtering of the electrons. In contrast to the Schottky diode, the proposed OSD does not require doping of the SGS electrode and it also does not have a junction barrier; thus it has a zero threshold voltage V_T and an infinite on:off current ratio at zero temperature. However, at finite temperatures, non-spin-flip thermally excited high-energy electrons as well as low-energy spin-flip excitations can give rise to a leakage current and thus reduce the on:off ratio under a reverse bias. As the leakage current is mainly determined by the size of the band gaps in SGS and HMM electrodes and by a proper choice of large band-gap materials, the on:off current ratio can be significantly increased in OSDs. Moreover, the spin degree of freedom provides a rich configuration space for the I - V characteristics of the OSD, which are determined by two parameters: (i) the spin character of the gap in HMM and SGS; and (ii) the magnetic coupling between electrodes, which allows the dynamical configuration of the diode in the case of antiferromagnetic coupling (antiparallel orientation) via an external magnetic field. We show that depending on the magnetic coupling between electrodes, the OSD is in the on state either under forward bias (parallel orientation) or under reverse bias (antiparallel orientation).

By employing the NEGF method combined with DFT, we demonstrate the rectification characteristics of the proposed OSD based on 2D half-metallic Fe/MoS₂ and spin-gapless semiconducting VS₂ planar heterojunctions. We find that the VS₂-Fe/MoS₂ junction diode possesses linear I - V characteristics for forward bias voltages up to 180 mV and that a bias voltage-induced ferromagnetic to antiferromagnetic interelectrode coupling then takes place. Such a sign change in magnetic coupling with bias voltage allows the realization of devices with unique functionalities, which will be considered in a separate paper. Moreover, the VS₂-Fe/MoS₂ OSD has a much higher current-drive capability ($I = 2350 \mu\text{A}/\mu\text{m}$) and a very small threshold voltage of $V_T = 30$ mV, which allows us to detect extremely weak signals; thus it might find potential applications in antenna-coupled diode solar cells. We expect that our results will pave the way for experimentalists to fabricate the OSD based on 2D materials.

ACKNOWLEDGMENTS

E.Ş. and I.M. acknowledge support from *Sonderforschungsbereich* TRR 227 of the Deutsche Forschungsgemeinschaft (DFG) and funding provided by the European Union (EFRE), Grant No. ZS/2016/06/79307.

E.Ş. and T.A. contributed equally to this work.

- [1] Simon M. Sze and Kwok K. Ng, *Physics of Semiconductor Devices* (John Wiley & Sons, Hoboken, 2007), 3rd ed.
- [2] Umesh K. Mishra and Jasprit Singh, *Semiconductor Device Physics and Design* (Springer Science & Business Media, Dordrecht, 2008).
- [3] J.-P. Colinge and Cynthia A. Colinge, *Physics of Semiconductor Devices* (Springer Science & Business Media, New York, 2006).
- [4] Leo Esaki, New phenomenon in narrow germanium p - n junctions, *Phys. Rev.* **109**, 603 (1958).
- [5] Xiaochi Liu, Deshun Qu, Hua-Min Li, Inyong Moon, Faisal Ahmed, Changsik Kim, Myeongjin Lee, Yongsuk Choi, Jeong Ho Cho, James C. Hone *et al.*, Modulation of quantum tunneling via a vertical two-dimensional black phosphorus and molybdenum disulfide p - n junction, *ACS Nano* **11**, 9143 (2017).
- [6] Krishna Murali, Medha Dandu, Sarthak Das, and Kausik Majumdar, Gate-tunable WSe₂/SnSe₂ backward diode with ultrahigh-reverse rectification ratio, *ACS Appl. Mater. Interfaces* **10**, 5657 (2018).
- [7] M. McColl, M. F. Millea, and A. H. Silver, The superconductor-semiconductor Schottky barrier diode detector, *Appl. Phys. Lett.* **23**, 263 (1973).
- [8] M. McColl, R. J. Pedersen, M. F. Bottjer, M. F. Millea, A. H. Silver, and F. L. Vernon, Jr., The super-Schottky diode microwave mixer, *Appl. Phys. Lett.* **28**, 159 (1976).
- [9] A. W. Kleinsasser, T. N. Jackson, D. McInturff, F. Rammo, G. D. Pettit, and J. M. Woodall, Crossover from tunneling to metallic behavior in superconductor-semiconductor contacts, *Appl. Phys. Lett.* **57**, 1811 (1990).
- [10] A. W. Kleinsasser and A. Kastalsky, Excess voltage and resistance in superconductor-semiconductor junctions, *Phys. Rev. B* **47**, 8361 (1993).
- [11] Shun-Tsung Lo, Kuang Yao Chen, Sheng-Di Lin, J.-Y. Wu, T. L. Lin, M. R. Yeh, T.-M. Chen, and C.-T. Liang, Controllable disorder in a hybrid nanoelectronic system: Realization of a superconducting diode, *Sci. Rep.* **3**, 2274 (2013).
- [12] Dimtry Panna, Krishna Balasubramanian, Shlomi Bouscher, Yujia Wang, Pu Yu, Xi Chen, and Alex Hayat, Nanoscale high- T_c YBCO/GaN super-Schottky diode, *Sci. Rep.* **8**, 5597 (2018).
- [13] Zixu Zhu, Saumil Joshi, Sachit Grover, and Garret Moddel, Graphene geometric diodes for terahertz rectennas, *J. Phys. D: Appl. Phys.* **46**, 185101 (2013).
- [14] Zixu Zhu, Saumil Joshi, and Garret Moddel, High performance room temperature rectenna IR detectors using graphene geometric diodes, *IEEE J. Sel. Top. Quantum Electron.* **20**, 70 (2014).
- [15] Gregory Auton, Dmytro B. But, Jiawei Zhang, Ernie Hill, Dominique Coquillat, Christophe Consejo, Philippe Nouvel, Wojciech Knap, Luca Varani, Frederic Teppe, Jeremie Torres, and Aimin Song, Terahertz detection and imaging using graphene ballistic rectifiers, *Nano Lett.* **17**, 7015 (2017).
- [16] Taehee Kang, R. H. Joon-Yeon Kim, Geunchang Choi, Jaiu Lee, Hyunwoo Park, Hyeongtag Jeon, Cheol-Hwan Park, and Dai-Sik Kim, Terahertz rectification in ring-shaped quantum barriers, *Nat. Commun.* **9**, 4914 (2018).

- [17] Nianbei Li and Jie Ren, Non-reciprocal geometric wave diode by engineering asymmetric shapes of nonlinear materials, *Sci. Rep.* **4**, 6228 (2014).
- [18] X. L. Wang, Proposal for a New Class of Materials: Spin Gapless Semiconductors, *Phys. Rev. Lett.* **100**, 156404 (2008).
- [19] Xiaolin Wang, Germanas Peleckis, Chao Zhang, Hideo Kimura, and Shixue Dou, Colossal electroresistance and giant magnetoresistance in doped PbPdO₂ thin films, *Adv. Mater.* **21**, 2196 (2009).
- [20] R. A. De Groot, F. M. Mueller, P. G. Van Engen, and K. H. J. Buschow, New Class of Materials: Half-Metallic Ferromagnets, *Phys. Rev. Lett.* **50**, 020401 (1983).
- [21] E. Şaşıoğlu and S. Blügel, Magnetic tunnel diode and magnetic tunnel transistor, U.S. Patent No. US20180309047A1 (2016).
- [22] Ersoy Şaşıoğlu, Stefan Blügel, and Ingrid Mertig, Proposal for reconfigurable magnetic tunnel diode and transistor, *Appl. Electron. Mater.* **1**, 1552 (2019).
- [23] Siham Ouardi, Gerhard H. Fecher, Claudia Felser, and Jürgen Kübler, Realization of Spin Gapless Semiconductors: The Heusler Compound Mn₂CoAl, *Phys. Rev. Lett.* **110**, 100401 (2013).
- [24] Daniele Stradi, Umberto Martinez, Anders Blom, Mads Brandbyge, and Kurt Stokbro, General atomistic approach for modeling metal-semiconductor interfaces using density functional theory and nonequilibrium Green's function, *Phys. Rev. B* **93**, 155302 (2016).
- [25] H. Zhang, E. J. Miller, and E. T. Yu, Analysis of leakage current mechanisms in Schottky contacts to GaN and Al_{0.25}Ga_{0.75}N/GaN grown by molecular-beam epitaxy, *J. Appl. Phys.* **99**, 023703 (2006).
- [26] A. Latreche, Combined thermionic emission and tunneling mechanisms for the analysis of the leakage current for Ga₂O₃ Schottky barrier diodes, *SN Appl. Sci.* **1**, 188 (2019).
- [27] Mingsheng Xu, Tao Liang, Minmin Shi, and Hongzheng Chen, Graphene-like two-dimensional materials, *Chem. Rev.* **113**, 3766 (2013).
- [28] Nicolas Mounet, Marco Gibertini, Philippe Schwaller, Davide Campi, Andrius Merkys, Antimo Marrazzo, Thibault Sohier, Ivano Eligio Castelli, Andrea Cepellotti, Giovanni Pizzi, and Nicola Marzari, Two-dimensional materials from high-throughput computational exfoliation of experimentally known compounds, *Nat. Nanotechnol.* **13**, 246 (2018).
- [29] Sten Hastrup, Mikkel Strange, Mohnish Pandey, Thorsten Deilmann, Per S. Schmidt, Nicki F. Hinsche, Morten N. Gjerding, Daniele Torelli, Peter M. Larsen, Anders C. Riis-Jensen, Jakob Gath, Karsten W. Jacobsen, Jens J. Mortensen, Thomas Olsen, and Kristian S. Thygesen, The computational 2D materials database: High-throughput modeling and discovery of atomically thin crystals, *2D Mater.* **5**, 042002 (2018).
- [30] M. Gibertini, M. Koperski, A. F. Morpurgo, and K. S. Novoselov, Magnetic 2D materials and heterostructures, *Nat. Nanotechnol.* **14**, 408 (2019).
- [31] K. Özdoğan, E. Şaşıoğlu, and I. Galanakis, Slater-Pauling behavior in LiMgPdSn-type multifunctional quaternary Heusler materials: Half-metallicity, spin-gapless and magnetic semiconductors, *J. Appl. Phys.* **113**, 193903 (2013).
- [32] Sergey V. Faleev, Yari Ferrante, Jaewoo Jeong, Mahesh G. Samant, Barbara Jones, and Stuart S. P. Parkin, Heusler compounds with perpendicular magnetic anisotropy and large tunneling magnetoresistance, *Phys. Rev. Mater.* **1**, 024402 (2017).
- [33] Tanja Graf, Claudia Felser, and Stuart S. P. Parkin, Simple rules for the understanding of Heusler compounds, *Prog. Solid State Chem.* **39**, 1 (2011).
- [34] Qiang Gao, Ingo Opahle, and Hongbin Zhang, High-throughput screening for spin-gapless semiconductors in quaternary Heusler compounds, *Phys. Rev. Mater.* **3**, 024410 (2019).
- [35] Thorsten Aull, Ersoy Şaşıoğlu, Igor V. Maznichenko, Sergey Ostanin, Arthur Ernst, Ingrid Mertig, and Iosif Galanakis, *Ab initio* design of quaternary Heusler compounds for reconfigurable magnetic tunnel diode and transistor, *Phys. Rev. Mater.* **3**, 124415 (2019).
- [36] Worasak Rotjanapittayakul, Jariyane Prasoongkit, Ivan Rungger, Stefano Sanvito, Wanchai Pijitrojana, and Thomas Archer, Search for alternative magnetic tunnel junctions based on all-Heusler stacks, *Phys. Rev. B* **98**, 054425 (2018).
- [37] Branimir Radisavljevic, Aleksandra Radenovic, Jacopo Brivio, Valentina Giacometti, and Andras Kis, Single-layer MoS₂ transistors, *Nat. Nanotechnol.* **6**, 147 (2011).
- [38] Likai Li, Yijun Yu, Guo Jun Ye, Qingqin Ge, Xuedong Ou, Hua Wu, Donglai Feng, Xian Hui Chen, and Yuanbo Zhang, Black phosphorus field-effect transistors, *Nat. Nanotechnol.* **9**, 372 (2014).
- [39] Deep Jariwala, Vinod K. Sangwan, Lincoln J. Lauhon, Tobin J. Marks, and Mark C. Hersam, Emerging device applications for semiconducting two-dimensional transition metal dichalcogenides, *ACS Nano* **8**, 1102 (2014).
- [40] Gianluca Fiori, Francesco Bonaccorso, Giuseppe Iannaccone, Tomás Palacios, Daniel Neumaier, Alan Seabaugh, Sanjay K. Banerjee, and Luigi Colombo, Electronics based on two-dimensional materials, *Nat. Nanotechnol.* **9**, 768 (2014).
- [41] Tania Roy, Mahmut Tosun, Xi Cao, Hui Fang, Der-Hsien Lien, Peida Zhao, Yu-Ze Chen, Yu-Lun Chueh, Jing Guo, and Ali Javey, Dual-gated MoS₂/WSe₂ van der Waals tunnel diodes and transistors, *ACS Nano* **9**, 2071 (2015).
- [42] Yuan Liu, Nathan O. Weiss, Xidong Duan, Hung-Chieh Cheng, Yu Huang, and Xiangfeng Duan, Van der Waals heterostructures and devices, *Nat. Rev. Mater.* **1**, 16042 (2016).
- [43] Rusen Yan, Sara Fathipour, Yimo Han, Bo Song, Shudong Xiao, Mingda Li, Nan Ma, Vladimir Protasenko, David A. Muller, Debdeep Jena, and Huili G. Xing, Esaki diodes in van der Waals heterojunctions with broken-gap energy band alignment, *Nano Lett.* **15**, 5791 (2015).
- [44] Filippo Giannazzo, Giuseppe Greco, Fabrizio Roccaforte, and Sushant S. Sonde, Vertical transistors based on 2D materials: Status and prospects, *Crystals* **8**, 70 (2018).
- [45] Ming-Yang Li, Chang-Hsiao Chen, Yumeng Shi, and Lain-Jong Li, Heterostructures based on two-dimensional layered materials and their potential applications, *Mater. Today* **19**, 322 (2016).

- [46] Jean Choukroun, Marco Pala, Shiang Fang, Efthimios Kaxiras, and Philippe Dollfus, High performance tunnel field effect transistors based on in-plane transition metal dichalcogenide heterojunctions, *Nanotechnology* **30**, 025201 (2018).
- [47] Houlong L. Zhuang and Richard G. Hennig, Stability and magnetism of strongly correlated single-layer VS₂, *Phys. Rev. B* **93**, 054429 (2016).
- [48] Nannan Luo, Chen Si, and Wenhui Duan, Structural and electronic phase transitions in ferromagnetic monolayer VS₂ induced by charge doping, *Phys. Rev. B* **95**, 205432 (2017).
- [49] Huei-Ru Fuh, Ching-Ray Chang, Yin-Kuo Wang, Richard F. L. Evans, Roy W Chantrell, and Horng-Tay Jeng, New-type single-layer magnetic semiconductor in transition-metal dichalcogenides VX₂ (X = S, Se and Te), *Sci. Rep.* **6**, 32625 (2016).
- [50] Daqiang Gao, Qixin Xue, Xingze Mao, Weixiao Wang, Qiang Xu, and Desheng Xue, Ferromagnetism in ultrathin VS₂ nanosheets, *J. Mater. Chem. C* **1**, 5909 (2013).
- [51] Manuel Bonilla, Sadhu Kolekar, Yujing Ma, Horacio Coy Diaz, Vijaysankar Kalappattil, Raja Das, Tatiana Eggers, Humberto R. Gutierrez, Manh-Huong Phan, and Matthias Batzill, Strong room-temperature ferromagnetism in VSe₂ monolayers on van der Waals substrates, *Nat. Nanotechnol.* **13**, 289 (2018).
- [52] Gang Hee Han, Dinh Loc Duong, Dong Hoon Keum, Seok Joon Yun, and Young Hee Lee, Van der Waals metallic transition metal dichalcogenides, *Chem. Rev.* **118**, 6297 (2018).
- [53] Søren Smidstrup, Daniele Stradi, Jess Wellendorff, Petr A. Khomyakov, Ulrik G. Vej-Hansen, Maeng-Eun Lee, Tushar Ghosh, Elvar Jónsson, Hannes Jónsson, and Kurt Stokbro, First-principles Green's-function method for surface calculations: A pseudopotential localized basis set approach, *Phys. Rev. B* **96**, 195309 (2017).
- [54] John P. Perdew, Kieron Burke, and Matthias Ernzerhof, Generalized Gradient Approximation Made Simple, *Phys. Rev. Lett.* **77**, 3865 (1996).
- [55] M. J. Van Setten, Matteo Giantomassi, Eric Bousquet, Matthieu J. Verstraete, Don R. Hamann, Xavier Gonze, and G.-M. Rignanese, The PseudoDojo: Training and grading a 85 element optimized norm-conserving pseudopotential table, *Comput. Phys. Commun.* **226**, 39 (2018).
- [56] Søren Smidstrup *et al.*, QuantumATK: An integrated platform of electronic and atomic-scale modelling tools, *J. Phys. Condens. Matter* **32**, 015901 (2019).
- [57] M. Büttiker, Y. Imry, R. Landauer, and S. Pinhas, Generalized many-channel conductance formula with application to small rings, *Phys. Rev. B* **31**, 6207 (1985).
- [58] Chenghuan Jiang, Yitian Wang, Yehui Zhang, Haowei Wang, Qian Chen, and Jianguo Wan, Robust half-metallic magnetism in two-dimensional Fe/MoS₂, *J. Phys. Chem. C* **122**, 21617 (2018).
- [59] N. David Mermin and Herbert Wagner, Absence of Ferromagnetism or Antiferromagnetism in One- or Two-Dimensional Isotropic Heisenberg Models, *Phys. Rev. Lett.* **17**, 1133 (1966).
- [60] S. T. Bramwell and P. C. W. Holdsworth, Magnetization: A characteristic of the Kosterlitz-Thouless-Berezinskii transition, *Phys. Rev. B* **49**, 8811 (1994).
- [61] Daniele Torelli, Kristian Sommer Thygesen, and Thomas Olsen, High throughput computational screening for 2D ferromagnetic materials: The critical role of anisotropy and local correlations, *2D Mater.* **6**, 045018 (2019).
- [62] Fumihiro Matsukura, Yoshinori Tokura, and Hideo Ohno, Control of magnetism by electric fields, *Nat. Nanotechnol.* **10**, 209 (2015).
- [63] R. O. Cherifi, V. Ivanovskaya, L. C. Phillips, A. Zobelli, I. C. Infante, E. Jacquet, V. Garcia, S. Fusil, P. R. Briddon, N. Guiblin, A. Mougín, A. A. Únal, F. Kronast, S. Valencia, B. Dkhil, A. Barthélémy, and M. Bibes, Electric-field control of magnetic order above room temperature, *Nat. Mater.* **13**, 345 (2014).
- [64] V. L. Korenev, I. V. Kalitukha, I. A. Akimov, V. F. Sapega, E. A. Zhukov, E. Kirstein, O. S. Ken, D. Kudlacik, G. Karzewski, M. Wiater, N. D. Ilyinskaya, N. M. Lebedeva, T. A. Komissarova, Yu. G. Kusrayev, D. R. Yakovlev, and M. Bayer, Low voltage control of exchange coupling in a ferromagnet-semiconductor quantum well hybrid structure, *Nat. Commun.* **10**, 2899 (2019).
- [65] Chun-Yeol You and S. D. Bader, Prediction of switching/rotation of the magnetization direction with applied voltage in a controllable interlayer exchange coupled system, *J. Magn. Magn. Mater.* **195**, 488 (1999).
- [66] Y.-H. Tang, Nicholas Kiuoussis, Alan Kalitsov, W. H. Butler, and Roberto Car, Controlling the Nonequilibrium Interlayer Exchange Coupling in Asymmetric Magnetic Tunnel Junctions, *Phys. Rev. Lett.* **103**, 057206 (2009).
- [67] Shehrin Sayed, Cheng-Hsiang Hsu, Niklas Roschewsky, See-Hun Yang, and Sayeef Salahuddin, Electric-field control of the interlayer exchange coupling for magnetization switching, arXiv:1911.00183 (2019).
- [68] T. Newhouse-Illige, Yaohua Liu, M. Xu, D. Reifsnnyder Hickey, A. Kundu, H. Almasi, Chong Bi, Xiao Wang, J. W. Freeland, D. J. Keavney, C. J. Sun, Y. H. Xu, M. Rosales, X. M. Cheng, Shufeng Zhang, K. A. Mkhoyan, and W. G. Wang, Voltage-controlled interlayer coupling in perpendicularly magnetized magnetic tunnel junctions, *Nat. Commun.* **8**, 15232 (2017).
- [69] Zhi-Qiang Fan, Xiang-Wei Jiang, Jun-Wei Luo, Li-Ying Jiao, Ru Huang, Shu-Shen Li, and Lin-Wang Wang, In-plane Schottky-barrier field-effect transistors based on 1T/2H heterojunctions of transition-metal dichalcogenides, *Phys. Rev. B* **96**, 165402 (2017).
- [70] International Roadmap for Devices and Systems (IRDS) (2017), available at <https://irds.ieee.org>.
- [71] Mazen Shanawani, Diego Masotti, and Alessandra Costanzo, THz rectennas and their design rules, *Electronics* **6**, 99 (2017).
- [72] Saumil Joshi and Garret Moddel, Simple figure of merit for diodes in optical rectennas, *IEEE J. Photovolt.* **6**, 668 (2016).
- [73] Sachit Grover, Saumil Joshi, and Garret Moddel, Quantum theory of operation for rectenna solar cells, *J. Phys. D: Appl. Phys.* **46**, 135106 (2013).
- [74] M. I. Katsnelson, V. Yu. Irkhin, Liviu Chioncel, A. I. Lichtenstein, and Robert A. de Groot, Half-metallic ferromagnets: From band structure to many-body effects, *Rev. Mod. Phys.* **80**, 315 (2008).

6.4 Design of Ohmic spin diodes based on quaternary Heusler compounds

In the previous section, we introduced the concept of the OSD using HMMs and SGSs. Due to their SGS and HMM properties as well as very high Curie temperatures, quaternary Heusler compounds offer a platform to design OSDs for room temperature applications.

In the last paper, "First principles design of Ohmic spin diodes based on quaternary Heusler compounds" [TA4], we computationally design four different OSDs using the SGSs FeVNbAl, FeVTaAl, and FeVTiSi and HMMs Co₂MnSi, MnVTiAl, and FeVHfAl. Our calculations indicate that all four OSDs exhibit linear $I - V$ characteristics in the on-state and possess zero threshold voltages (see Fig. 6.4). The obtained on/off current ratios vary between 30 and 10⁵. The small values can be attributed to the leakage current in the off-state. We demonstrate that the leakage current mainly stems from the small overlaps between the valance and conduction band edges of opposite spin channels at the Fermi level in the SGS materials.

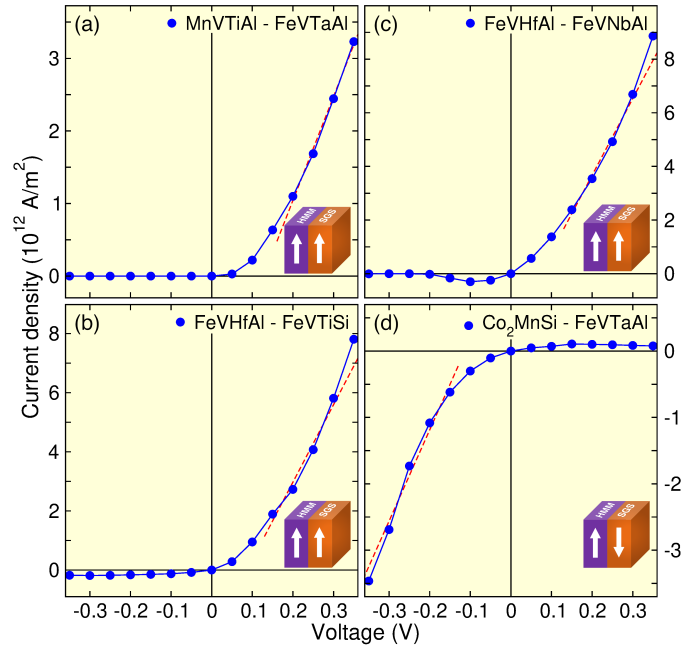


Figure 6.4: (a)-(d) Calculated $I - V$ curves for the four suggested OSDs based on quaternary Heusler compounds. The red dashed lines illustrate a linear fit and the coupling of the electrodes is represented by a small graphic in the lower right corner. Adapted (figure) from (T. Aull *et al.* Appl. Phys. Lett. **118**, 052405 (2021); First principles design of Ohmic spin diodes based on quaternary Heusler compounds., Ref. [TA4]), with the permission of AIP Publishing.

The following publication: Reprinted (whole article) from (T. Aull *et al.* Applied Physics Letters **118**, 052405 (2021); First principles design of Ohmic spin diodes based on quaternary Heusler compounds., Ref. [TA4]), with the permission of AIP Publishing.

First principles design of Ohmic spin diodes based on quaternary Heusler compounds

Cite as: Appl. Phys. Lett. **118**, 052405 (2021); doi: 10.1063/5.0037085

Submitted: 10 November 2020 · Accepted: 17 January 2021 ·

Published Online: 2 February 2021



View Online



Export Citation



CrossMark

T. Aull,^{1,a)} E. Şaşıoğlu,¹ and I. Mertig^{1,2}

AFFILIATIONS

¹Institute of Physics, Martin Luther University Halle-Wittenberg, D-06120 Halle (Saale), Germany

²Max Planck Institute of Microstructure Physics, Weinberg 2, D-06120 Halle (Saale), Germany

^{a)}Author to whom correspondence should be addressed: thorsten.aull@physik.uni-halle.de

ABSTRACT

The Ohmic spin diode (OSD) is a recent concept in spintronics, which is based on half-metallic magnets and spin-gapless semiconductors (SGSs). Quaternary Heusler compounds offer a unique platform to realize the OSD for room temperature applications as these materials possess very high Curie temperatures as well as half-metallic and spin-gapless semiconducting behavior within the same family. Using state-of-the-art first-principles calculations combined with the nonequilibrium Green's function method, we design four different OSDs based on half-metallic and spin-gapless semiconducting quaternary Heusler compounds. All four OSDs exhibit linear current–voltage (I – V) characteristics with zero threshold voltage V_T . We show that these OSDs possess a small leakage current, which stems from the overlap of the conduction and valence band edges of opposite spin channels around the Fermi level in the SGS electrodes. The obtained on/off current ratios vary between 30 and 10^5 . Our results can pave the way for the experimental fabrication of the OSDs within the family of ordered quaternary Heusler compounds.

Published under license by AIP Publishing. <https://doi.org/10.1063/5.0037085>

Spintronics is a rapidly emerging field in current nanoelectronics. Due to their diverse and tunable electronic and magnetic properties, Heusler compounds received great interest for potential applications in spintronics. In particular, within the last two decades, half metallic Heusler compounds with 100% spin polarization of the conduction electrons at the Fermi energy¹ have been extensively studied both, theoretically and experimentally, for memory and sensor applications. In addition to half metallicity in ordinary X_2YZ -type Heusler compounds, several quaternary Heuslers with chemical formula $XX'YZ$, with X , X' , and Y being transition-metal atoms and Z being an sp element, have been theoretically predicted to exhibit spin-gapless semiconducting behavior and some of them have been experimentally synthesized.^{2–5} Spin-gapless semiconductors (SGSs) possess a unique electronic structure, in which conduction- and valence-band edges of opposite spins touch at the Fermi level⁶ and thus SGS behavior leads to unique functionalities and device concepts.

Half-metallic Heusler compounds have been considered as ideal electrode materials in magnetic tunnel junctions for spin-transfer torque magnetic memory applications due to their very high Curie temperatures. The use of Co-based Heusler compounds in magnetic tunnel junctions made the experimental observation of high tunnel magnetoresistance (TMR) effects possible.^{8–12} However, magnetic

tunnel junctions constructed with half metals do not present any rectification (or diode effect) for logic operations. Lately, logic functionality in magnetic tunnel junctions is achieved by replacing one of the electrodes by a SGS material. In Ref. 13, based on half-metallic magnets (HMMs) and SGSs, a reconfigurable magnetic tunnel diode and transistor have been proposed. This concept combines logic and memory on the diode and transistor level. Moreover, in a recent publication, the present authors proposed another device concept based on HMMs and SGSs, which is the so-called Ohmic spin diode (OSD).¹⁴ It has been computationally demonstrated that the OSD comprising two-dimensional half-metallic Fe/MoS₂ and spin-gapless semiconducting VS₂ exhibits linear current–voltage (I – V) characteristics with zero threshold voltage V_T . OSDs have a much higher current drive capability and low resistance, which is advantageous compared to conventional semiconductor p – n junction diodes and metal–semiconductor Schottky diodes.

The aim of the present Letter is a computational design of OSDs based on quaternary Heusler compounds for room temperature applications. Heusler compounds offer a unique platform to realize the OSD as these materials possess very high Curie temperatures (much above room temperature) as well as half-metallic and spin-gapless semiconducting behavior within the same family. To this end, the

selection of the SGS and HMM electrode materials from the Heusler family for the design of OSDs is based on our recent study in Ref. 7, where we focus on Curie temperatures, spin-gaps, formation energy, and Hull distance for a large number of quaternary Heusler compounds. Among the considered materials, three SGSs (FeVNbAl, FeVTaAl, and FeVTiSi) turn out to be promising for device applications. As for the half-metallic Heusler compounds, we have a large variety of choice, but we stick to the quaternary ones (MnVTiAl, FeVHfAl) with similar lattice constants to the SGSs in order to ensure a coherent growth on top of each other. Additionally, we also consider the well-known half-metallic Co₂MnSi system among the ordinary full Heusler compounds as an electrode material.

Our first-principles design of the OSDs is based on the density functional theory (DFT) using the QUANTUMATK package (version P-2019.12).^{15,16} As the exchange-correlation functional, we chose the Perdew-Burke-Ernzerhof (PBE) parametrization¹⁷ combined with norm-conserving PseudoDojo pseudopotentials¹⁸ and linear combinations of atomic orbitals (LCAO) as the basis set. As a **k**-point grid for the ground state properties, we use a 15 × 15 × 15 Monkhorst-Pack grid and a density mesh cutoff of 120 Hartree. For the transport calculations, we combined DFT with the nonequilibrium Green's function method (NEGF). We use a 15 × 15 × 160 **k**-point mesh in self-consistent DFT-NEGF calculations. The *I*-*V* characteristics were calculated within the Landauer approach,¹⁹ where $I(V) = e/h \sum_{\sigma} \int T^{\sigma}(E, V) [f_L(E, V) - f_R(E, V)] dE$. *V* stands for the bias voltage and the transmission coefficient $T^{\sigma}(E, V)$ depends additionally on spin σ of an electron and energy *E*. Furthermore, $f_L(E, V)$ and $f_R(E, V)$ denote the Fermi-Dirac distribution of the left and right electrodes, respectively. For the calculation of $T^{\sigma}(E, V)$, we chose a 25 × 25 **k**-point grid.

In Fig. 1, we present schematically the structure of the OSD and the corresponding *I*-*V* characteristics. The concept of the OSD has been extensively discussed in Ref. 14 and thus here we will only give a short overview of the device. The OSD consists of HMM and SGS materials and possesses linear *I*-*V* characteristics. The schematic density of states (DOS) of these materials is also shown in Fig. 1. Depending on the choice of the junction materials, the HMM and SGS electrodes can couple ferromagnetically (ferromagnetic OSD) or antiferromagnetically (antiferromagnetic OSD) at the interface giving rise

to corresponding *I*-*V* curves shown in Fig. 1. The operation principle of the OSD relies on the unique spin-dependent transport properties of HMMs and SGSs as discussed in Ref. 14 in detail.

In the proposal of the OSD,¹⁴ the proof of principle was demonstrated by using two-dimensional transition-metal dichalcogenides VS₂ (SGS) and Fe/MoS₂ (HMM) as electrode materials. Since VS₂ possesses an estimated Curie temperature of 138 K,²⁰ it is not suitable for room temperature applications. For more realistic devices, we now consider six Heusler compounds as mentioned before and construct four different OSDs: (i) FeVHfAl-FeVTiSi, (ii) FeVHfAl-FeVNbAl, (iii) MnVTiAl-FeVTaAl, and (iv) Co₂MnSi-FeVTaAl. All six Heusler compounds possess extremely high Curie temperatures as presented in Table I. For the construction of the OSD, we assume the situation where one material needs to be grown on top of the other one. Thus, in our simulations, we take one electrode (SGS) in the cubic structure and relax the second electrode material (HMM) with respect to the in-plane lattice parameter of the first one. Therefore, in Table I, we include the *c/a* ratios for the half metallic electrode materials, which take the tetragonal structure. In Table I, we present also the obtained magnetic moments, magnetic anisotropy energies (MAEs), and work functions. As expected, tetragonal distortion results in a significant change in the magnetic anisotropy energy of HMMs, which is at least two orders of magnitude larger than the SGSs, being in good agreement with the literature.²¹

We now focus on the first OSD and discuss its structural, electronic, and magnetic properties. Figure 2(a) illustrates the atomic structure of the OSD based on half-metallic MnVTiAl (left electrode) and spin-gapless semiconducting FeVTaAl (right electrode) quaternary Heusler compounds. We use a minimal tetragonal unit cell along the [001] direction containing eight atoms. For each electrode, this cells was repeated five times and defines the screening region. The length (screening region) of the device is around 62 Å. In the other three OSDs, the considered screening region lies in between 61 Å and 63 Å, depending on the materials. As the strength of the spin-orbit coupling (SOC) is very weak in these materials, we neglect the SOC in transport calculations and thus we chose the *z*-direction as the transport direction and also adjusted the alignment of the magnetic moments to the *z*-axis. The red arrows and their size in Fig. 2(a) represent the direction and magnitude of the atomic magnetic moments in the junction materials. In this OSD, the HMM and SGS electrodes couple ferromagnetically at the interface, i.e., the energy difference between ferromagnetic and antiferromagnetic coupling is about 400 meV.

Looking at the magnetic moments at the interface region in Fig. 2, we notice that the size of the arrows deviates from their bulk behavior, i.e., far from the interface. In particular, the magnetic moment of the Mn atom in MnVTiAl at the interface decreases from 2.42 μ_B to 0.07 μ_B . This is due to the fact that in the interface region, MnVTaAl is formed, which also presents HMM behavior with bulk magnetic moments of $m_{Mn} = 0.08 \mu_B$, $m_V = 1.97 \mu_B$, $m_{Ta} = -0.04 \mu_B$, and $m_{Al} = -0.01 \mu_B$. Therefore, the half metallic character of the MnVTiAl compound is retained at the interface. However, the FeVTaAl compound loses its spin-gapless semiconducting nature near the interface region as it will be discussed later in detail.

Next, we would like to discuss the electronic properties of the MnVTiAl-FeVTaAl junction at equilibrium, i.e., at zero bias. The bulk band structure along the transport direction of the junction materials

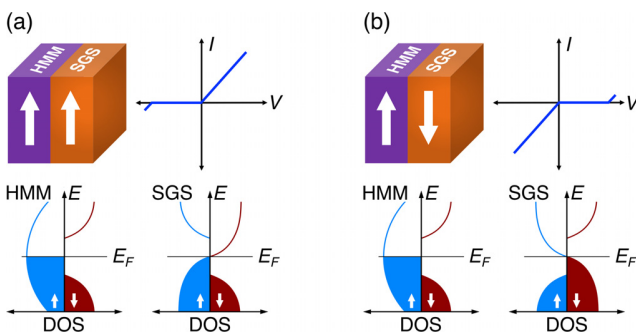


FIG. 1. (a) Upper part: schematic representation of the Ohmic spin diode and corresponding current-voltage (*I*-*V*) characteristics. Arrows show the magnetization direction of the HMM and SGS electrodes (ferromagnetic OSD). Lower part: schematic representation of the density of states for a HMM and SGS. (b) The same as (a) for antiferromagnetic coupling of the HMM and SGS electrodes (antiferromagnetic OSD).

TABLE I. Material composition of the considered OSDs, coupling of the electrodes, lattice constants a , c/a ratio, sublattice and total magnetic moments, work function (Φ), the magnetic anisotropy energy (MAE), Curie temperatures T_C of the cubic phase and the electronic ground state. The T_C values are taken from Ref. 7.

| HMM-SGS junction | Coupling | Compound | a_0 (Å) | c/a | m_X (μ_B) | $m_{X'}$ (μ_B) | m_Y (μ_B) | m total (μ_B) | Φ (eV) | MAE ^a ($\mu\text{eV/at.}$) | T_C (K) | Ground state |
|------------------------------|----------------------|----------|--------------|-------|----------------------|-------------------------|----------------------|------------------------|----------------|--|--------------|--------------|
| MnVTiAl-FeVTaAl | $\uparrow\uparrow$ | FeVTaAl | 6.10 | 1.00 | 0.85 | 2.38 | -0.19 | 3.00 | 3.75 | 0.63 | 681 | SGS |
| | | MnVTiAl | 6.10 | 1.01 | -2.42 | 2.61 | 0.86 | 1.00 | 3.59 | 11.94 | 963 | HMM |
| FeVHfAl-FeVTiSi | $\uparrow\uparrow$ | FeVTiSi | 5.91 | 1.00 | 0.57 | 2.33 | 0.10 | 3.00 | 3.52 | -0.94 | 464 | SGS |
| | | FeVHfAl | 5.91 | 1.12 | -0.15 | 2.06 | 0.10 | 2.00 | 4.10 | 117.44 | 742 | HMM |
| FeVHfAl-FeVNbAl | $\uparrow\uparrow$ | FeVNbAl | 6.11 | 1.00 | 0.81 | 2.32 | -0.11 | 3.00 | 3.72 | 0.25 | 693 | SGS |
| | | FeVHfAl | 6.11 | 1.04 | -0.68 | 2.41 | 0.29 | 2.00 | 3.45 | 62.44 | 742 | HMM |
| Co ₂ MnSi-FeVTaAl | $\uparrow\downarrow$ | FeVTaAl | 6.10 | 1.00 | 0.79 | 2.32 | -0.11 | 3.00 | 3.75 | 0.63 | 681 | SGS |
| | | CoCoMnSi | 6.10 | 0.86 | 1.01 | 1.01 | 3.18 | 5.00 | 3.83 | 57.50 | 920 | HMM |

^aOut-of-plane magnetization is marked as negative MAE.

is shown in Fig. 2(b). MnVTiAl is a HMM with a bandgap of around 650 meV in the minority-spin channel, while FeVTaAl shows SGS properties. Note that the spin-gapless semiconducting behavior along the chosen directions is not well seen, and for a detailed discussion, the reader is referred to Refs. 4 and 7. Nikolaev *et al.*²² and Bai *et al.*²³ provided a detailed discussion about the importance of band matching for the transport properties of giant magnetoresistance (GMR) spintronic devices. In our case, as seen in Fig. 2(b), there is a good band matching for the majority spin states near the Fermi level close to the Γ -point between the electrode materials, especially along the Γ -R and

Γ -A directions. Note that a good band matching suppresses the electron back scattering at the interface and ensures a smooth propagation of majority spin electrons from the FeVTaAl electrode to the MnVTiAl electrode. In Fig. 3, we present the device density of states (DDOS) of the MnVTiAl-FeVTaAl junction. As mentioned above, the half metallicity of MnVTiAl is preserved at the interface, which can be seen in the majority-spin and minority-spin channel DDOS presented in Fig. 3. However, the SGS character of FeVTaAl is lost near the interface region due to the charge transfer from the half-metallic electrode to the SGS (see the left panel of Fig. 3). This charge

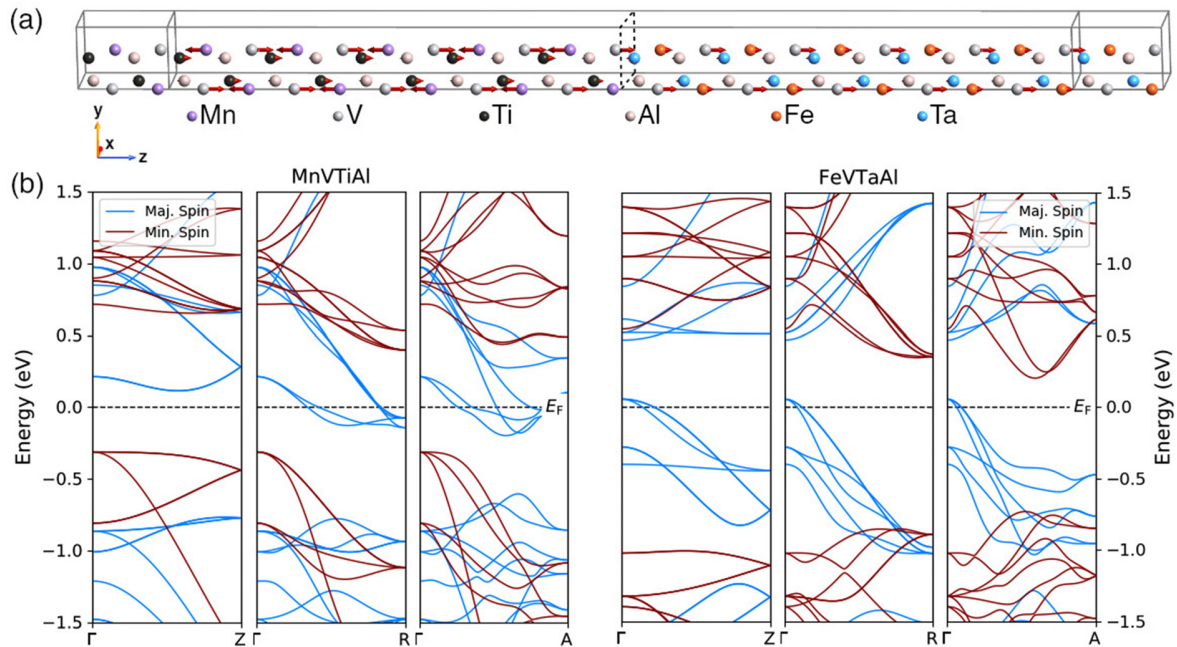


FIG. 2. (a) The atomic structure of the MnVTiAl-FeVTaAl Ohmic spin diode. The system is periodic in x - and y -direction in the plane orthogonal to the z -direction, which is the transport direction. The red arrows illustrate the direction as well as the magnitude of the magnetic moments within the scattering region. Small magnetic moments are overlaid by the atomic radii. The black dashed box denotes the interface. (b) The calculated spin-resolved bulk electronic band structure along the device stack direction, [001], for MnVTiAl (left panel) and FeVTaAl (right panel). For both compounds, the Fermi level is set to zero (dashed black line).

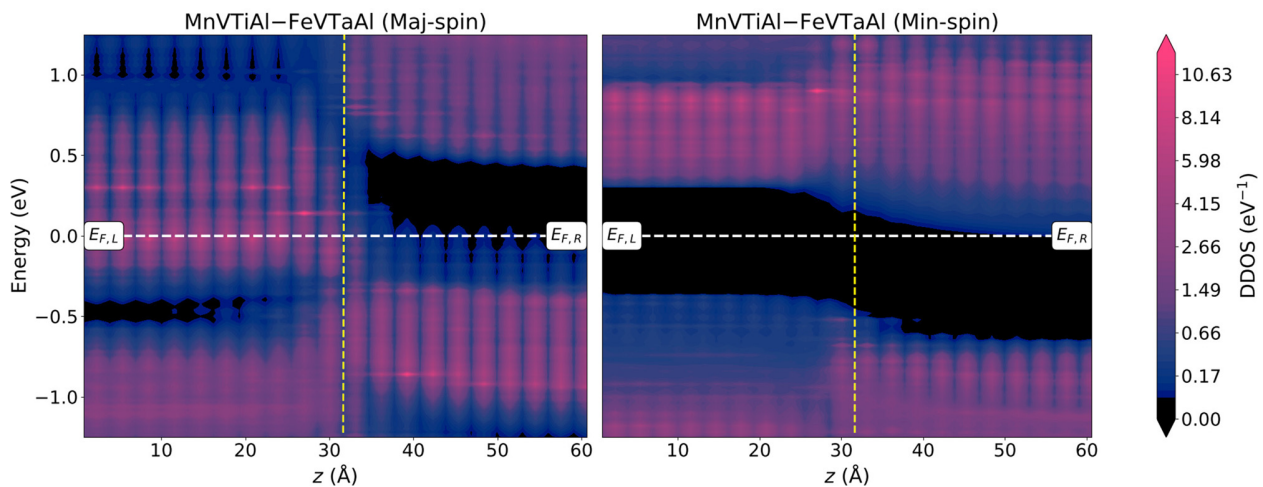


FIG. 3. Projected device density of states (DDOS) at zero bias (equilibrium) for the majority (left panel) and minority spin channel (right panel) of the MnVTiAl–FeVTaAl OSD (the atomic structure is given in Fig. 2). The white dashed lines display the Fermi level while the vertical yellow dashed lines denote the interface.

transfer stems from the work function difference of 160 meV between the two electrode materials. As MnVTiAl has the lower work function, electrons flow from the majority-spin channel of MnVTiAl to the majority spin-channel of FeVTaAl. Once the charge redistribution reaches equilibrium, MnVTiAl will be positively charged near the interface region, whereas FeVTaAl will be negatively charged and hence an electric dipole will be induced. This dipole influences the electronic and magnetic properties of both materials. Since the magnetic moment of the Mn atom in the MnVTiAl electrode has already been discussed above, we will briefly comment on the magnetic moment of the V atoms near the interface region. The magnetic moment of the V atoms in MnVTiAl is reduced to $2.25\mu_B$ close to the interface and recovers to the bulk value within two unit cells. On the other hand, the variation of magnetic moments in the FeVTaAl electrode near the interface region is around $0.1\mu_B$. Thus, the affected region by the charge transfer is restricted to five atomic layers for the majority-spin channel. The minority-spin channel is not substantially affected for both junction materials.

Until now, we discussed the properties of the OSD for zero bias and will now focus on the current–voltage (I – V) characteristics when a bias voltage is applied. Therefore, Figs. 4(a) and 4(b) illustrate the DDOS for both spin channels for the MnVTiAl–FeVTaAl junction under a bias voltage of +0.3 V and –0.3 V, respectively. Also, the corresponding transmission spectra are presented there. For both forward and reverse bias, the electronic and magnetic properties of both materials are not influenced by the bias voltage. The I – V characteristics of the MnVTiAl–FeVHfAl junction presented in Fig. 5(a) can be explained on the basis of the DDOS. Under a forward bias voltage, majority spin electrons from the occupied states below the Fermi level in FeVTaAl can be transmitted to unoccupied states above the Fermi level in MnVTiAl. Thus, the transmission coefficient has a finite value in this case. However, for the minority spin electrons, the transmission coefficient is zero because both materials have no states that could contribute to transport in the given voltage window. Thus, the forward current (on-current) is 100% spin polarized. Also, under an applied

reverse bias voltage, the transmission coefficient for minority-spin electrons is zero due to the energy gap in both materials. On the other hand, the overlap of conduction and valence bands of opposite spin channels around the Fermi energy in FeVTaAl gives rise to a nonzero transmission coefficient for majority-spin electrons, which leads to a leakage current that will be discussed in detail in the following paragraph.

Before we discuss the origin of the leakage current, we will briefly comment on the I – V characteristics of the other three OSDs, which are also presented in Fig. 5. As seen there, for all OSDs we obtain a linear behavior starting from around +0.15 V for the ferromagnetic OSDs (MnVTiAl–FeVTaAl, FeVHfAl–FeVTiSi, and FeVHfAl–FeVNbAl junctions) and around –0.15 V in the case of the antiferromagnetic OSD Co₂MnSi–FeVTaAl. For the three ferromagnetic OSDs, the I – V curves are more or less similar to each other, while the Co₂MnSi–FeVTaAl junction is in the off state for a forward bias and in the on state for a reverse bias, which is somewhat similar to the backward diode.^{24–26} An interesting feature of this latter OSD would be its dynamical configuration since the magnetic coupling strength of the electrodes at the interface is rather weak (~ 17 meV). Thus, by applying an external magnetic field, the I – V curves of the diode can be reversed similar to the case of reconfigurable magnetic tunnel diode concept in Ref. 13. Returning back to the discussion of the I – V characteristics, all four OSDs exhibit exactly zero threshold voltage V_T under forward bias. It is worth noting that all semiconductor diodes have sizeable threshold voltages V_T ($V_T \sim 0.7$ V for silicon p – n diodes), which gives rise to the power dissipation ($P = V_T \cdot I$) in form of heat and thus this is an undesirable effect. The larger the value of the threshold voltage V_T , the higher is the power dissipation in a diode. Furthermore, for all OSDs, the leakage currents are small compared to the on-currents. The leakage current can be traced back to the small overlap of conduction and valence band edges of opposite spin channels around the Fermi level in the SGS electrode as schematically shown in Figs. 5(e) and 5(f) (see Refs. 4 and 7 for the band structure and DOS of the SGS materials). Band overlaps allow in the

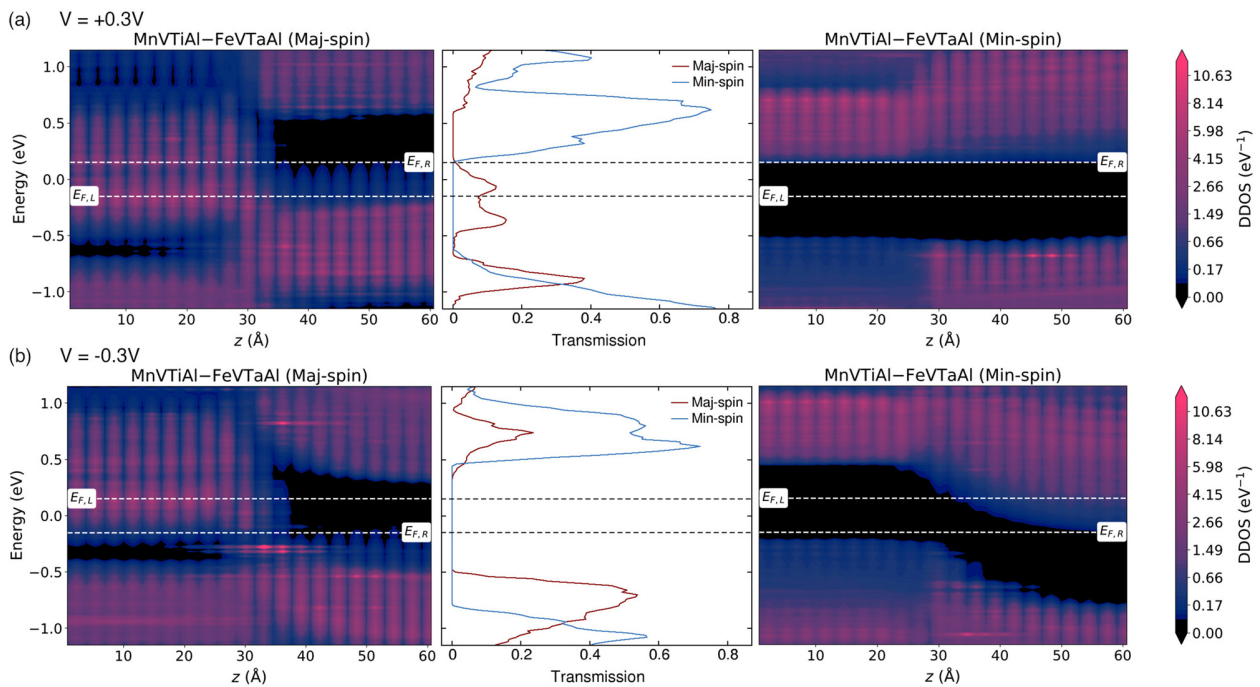


FIG. 4. (a) Projected local device density of states (DDOS) for the majority (left panel) and minority (right panel) spin channel in MnVTiAl–FeVTaAl OSD (the atomic structure of an OSD is provided in Fig. 2) for a bias voltage of $V = 0.3$ V. In the middle panel, we present the calculated transmission spectrum for both spin channels. The dashed lines indicate the Fermi energy of the left and right electrode. (b) displays the same as (a) for a bias voltage $V = -0.3$ V.

ferromagnetic (antiferromagnetic) OSD the flow of majority spin electrons from the occupied states of the HMM (SGS) material into the unoccupied states of the SGS (HMM) electrode. Thus, this process gives rise to a small leakage current. However, the leakage current is absent in the minority-spin channel in both cases due to the energy gaps in the electrode materials. Therefore, leakage currents can be prevented by using ideal SGS materials, i.e., without an overlap in conduction and valence band edges of opposite spin channels around the Fermi energy. Since FeVTiSi exhibits an overlap of 150 meV while FeVNbAl and FeVTaAl possess overlaps of 45 meV and 60 meV, respectively, the FeVHfAl–FeVTiSi junction shows the largest leakage current.

Finally, we would like to comment on the on/off ratios and current densities of the OSDs. The I_{ON}/I_{OFF} ratios at ± 0.3 V vary between 30 (FeVHfAl–FeVTiSi) and 10^5 (MnVTiAl–FeVTaAl) at zero temperature. Since FeVTiSi possesses the largest overlap between the conduction and valence band edges of opposite spin channels around E_F , the FeVHfAl–FeVTiSi junction shows the largest leakage current as discussed above and thus the lowest on/off ratio. From that point of view, also the on/off current ratios can be increased by using materials with ideal spin-gapless semiconducting behavior. Here, the MnVTiAl–FeVTaAl junction seems to be the best candidate for realizing the OSD. Another aspect that influences the on/off ratios is temperature, which is neglected in our transport calculations due to the technical limitation of the QUANTUMATK package for spintronic materials as discussed in Ref. 14. Temperature effects as well as the spin-flip

excitations can further reduce the on/off current ratio in OSDs (see Ref. 14 for a detailed discussion). As for the current densities, the calculated values are comparable to the elementary metals and much higher than conventional p - n or p - i - n diodes.^{27–30} It is worth noting that in transport calculations within the QUANTUMATK package, all inelastic scattering processes stemming from phonons as well as electrons and magnons are neglected. All these neglected processes can substantially reduce the current density of the OSDs.

In conclusion, the OSD is a recently proposed concept in spintronics and requires materials with unique electronic properties, in particular, half-metallic and spin-gapless semiconducting behavior. Since both properties have already been identified in the family of ordered quaternary Heusler compounds, this family is a preferable choice for the realization of such devices. Moreover, most of the compounds within this family possess very high Curie temperatures, making them potential candidates for spintronic applications at room temperature. By using first-principles DFT calculations combined with the NEGF method, we proposed four different HMM–SGS junctions (or OSDs) within the family of quaternary Heusler compounds. All four OSDs show linear I - V characteristics with zero threshold voltage V_T in the on state and small leakage currents in the off state, which can be attributed to the small overlap of conduction and valence band edges of opposite spin channels around the Fermi level in the SGS electrode. In three of the designed OSDs, the HMM and SGS electrodes couple ferromagnetically, while in the Co_2MnSi –FeVTaAl junction, this coupling is antiferromagnetic and thus this diode can be

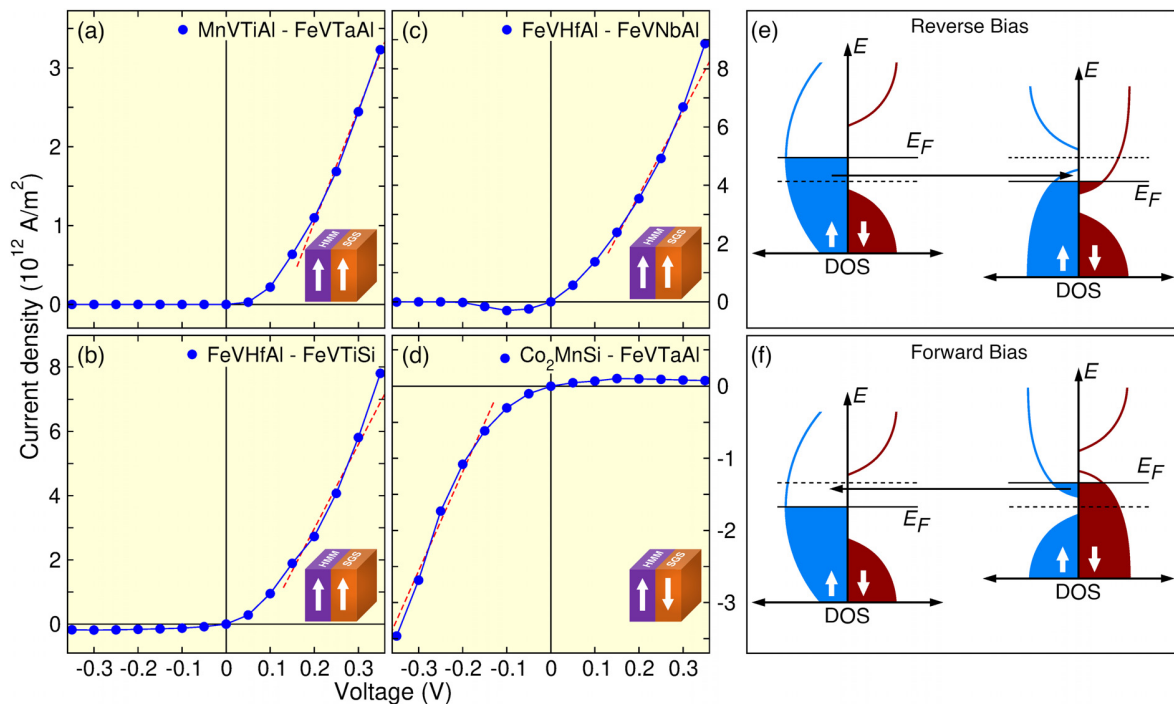


FIG. 5. Calculated current–voltage (I – V) characteristics for all HMM–SGS junctions (a)–(d). The red lines display a linear fit. The coupling of the electrodes is displayed by a small image in the lower right corner. (e) and (f) show the origin of the leakage current under reverse and forward bias for ferromagnetically and antiferromagnetically coupled HMM and SGS electrodes, respectively.

configured dynamically via an external magnetic field. Furthermore, the zero threshold voltage V_T is important for reducing the power consumption in a diode as it scales linearly with V_T . We hope that our results pave the way for the experimental fabrication of OSDs based on quaternary Heusler compounds.

This work was supported by the European Union (EFRE), Grant No. ZS/2016/06/79307 and by Deutsche Forschungsgemeinschaft (DFG) SFB CRC/TRR 227.

DATA AVAILABILITY

The data that support the findings of this study are available from the corresponding author upon reasonable request.

REFERENCES

- R. A. De Groot, F. M. Mueller, P. G. Van Engen, and K. H. J. Buschow, *Phys. Rev. Lett.* **50**, 2024 (1983).
- K. Özdoğan, E. Şaşioğlu, and I. Galanakis, *J. Appl. Phys.* **113**, 193903 (2013).
- I. Galanakis, K. Özdoğan, and E. Şaşioğlu, *AIP Adv.* **6**, 055606 (2016).
- Q. Gao, I. Opahle, and H. Zhang, *Phys. Rev. Mater.* **3**, 024410 (2019).
- S. Ouardi, G. H. Fecher, C. Felser, and J. Kübler, *Phys. Rev. Lett.* **110**, 100401 (2013).
- X. L. Wang, *Phys. Rev. Lett.* **100**, 156404 (2008).
- T. Aull, E. Şaşioğlu, I. V. Maznichenko, S. Ostanin, A. Ernst, I. Mertig, and I. Galanakis, *Phys. Rev. Mater.* **3**, 124415 (2019).
- S. Kämmerer, A. Thomas, A. Hütten, and G. Reiss, *Appl. Phys. Lett.* **85**, 79 (2004).
- Y. Sakuraba, A. M. Hattori, M. Oogane, Y. Ando, H. Kato, A. Sakuma, T. Miyazaki, and H. Kubota, *Appl. Phys. Lett.* **88**, 192508 (2006).
- W. Wang, H. Sukegawa, R. Shan, S. Mitani, and K. Inomata, *Appl. Phys. Lett.* **95**, 182502 (2009).
- G. Z. Xu, E. K. Liu, Y. Du, G. J. Li, G. D. Liu, W. H. Wang, and G. H. Wu, *Europhys. Lett.* **102**, 17007 (2013).
- S. V. Faleev, Y. Ferrante, J. Jeong, M. G. Samant, B. Jones, and S. S. P. Parkin, *Phys. Rev. Mater.* **1**, 024402 (2017).
- E. Şaşioğlu, S. Blügel, and I. Mertig, *ACS Appl. Electron. Mater.* **1**, 1552 (2019).
- E. Şaşioğlu, T. Aull, D. Kutschabsky, S. Blügel, and I. Mertig, *Phys. Rev. Appl.* **14**, 014082 (2020).
- S. Smidstrup, D. Stradi, J. Wellendorff, P. A. Khomyakov, U. G. Vej-Hansen, M.-E. Lee, T. Ghosh, E. Jónsson, H. Jónsson, and K. Stokbro, *Phys. Rev. B* **96**, 195309 (2017).
- S. Smidstrup, T. Markussen, P. Vancaerfeld, J. Wellendorff, J. Schneider, T. Gunst, B. Verstichel, D. Stradi, P. A. Khomyakov, U. G. Vej-Hansen, M.-E. Lee, S. T. Chill, F. Rasmussen, G. Penazzi, F. Corsetti, A. Ojanperä, K. Jensen, M. L. N. Palsgaard, U. Martinez, A. Blom, M. Brandbyge, and K. Stokbro, *J. Phys.* **32**, 015901 (2020).
- J. P. Perdew, K. Burke, and M. Ernzerhof, *Phys. Rev. Lett.* **77**, 3865 (1996).
- M. J. Van Setten, M. Giantomassi, E. Bousquet, M. J. Verstraete, D. R. Hamann, X. Gonze, and G.-M. Rignanese, *Comput. Phys. Commun.* **226**, 39 (2018).
- M. Büttiker, Y. Imry, R. Landauer, and S. Pinhas, *Phys. Rev. B* **31**, 6207 (1985).
- H.-R. Fuh, C.-R. Chang, Y.-K. Wang, R. F. Evans, R. W. Chantrell, and H.-T. Jeng, *Sci. Rep.* **6**, 32625 (2016).
- F. Kuroda, T. Fukushima, and T. Oguchi, *J. Appl. Phys.* **127**, 193904 (2020).
- K. Nikolaev, P. Kolbo, T. Pokhil, X. Peng, Y. Chen, T. Ambrose, and O. Mryasov, *Appl. Phys. Lett.* **94**, 222501 (2009).
- Z. Bai, Y. Cai, L. Shen, G. Han, and Y. Feng, *Appl. Phys. Lett.* **102**, 152403 (2013).
- S. M. Sze and K. K. Ng, *Physics of Semiconductor Devices*, 3rd ed. (John Wiley & Sons, Hoboken, 2007).

- ²⁵K. Murali, M. Dandu, S. Das, and K. Majumdar, *ACS Appl. Mater. Interfaces* **10**, 5657 (2018).
- ²⁶T. Roy, M. Tosun, X. Cao, H. Fang, D.-H. Lien, P. Zhao, Y.-Z. Chen, Y.-L. Chueh, J. Guo, and A. Javey, *ACS Nano* **9**, 2071 (2015).
- ²⁷A. J. Harris, R. S. Walker, and R. Sneddon, *J. Appl. Phys.* **51**, 4287 (1980).
- ²⁸R. A. Gibson, W. E. Spear, P. G. Le Comber, and A. J. Snell, *J. Non-Cryst. Solids* **35-36**, 725 (1980).
- ²⁹N. Szydlo, E. Chartier, N. Proust, J. Magarino, and D. Kaplan, *Appl. Phys. Lett.* **40**, 988 (1982).
- ³⁰J. Deng, J. M. Pearce, R. J. Koval, V. Vlahos, R. W. Collins, and C. R. Wronski, *Appl. Phys. Lett.* **82**, 3023 (2003).

7 Summary and Outlook

Summary The current non-volatile magnetic memory technology (STT-MRAM, SOT-MRAM, and beyond), as well as several magnetic logic concepts, utilize conventional magnetic tunnel junctions (MTJs) with limited functionalities. Despite large tunnel magnetoresistance (TMR) values, conventional tunnel junctions do not present current rectification, i.e., a diode effect. Using spin-gapless semiconductors (SGSs) and half-metallic magnets (HMMs) as electrode materials in MTJs leads to new functionalities, i.e., current rectification, reconfigurability, and inverse TMR effect. Thus, in the present thesis, we investigated novel spintronic device concepts based on SGSs and HMMs. Quaternary Heusler compounds allow designing within the same family HMMs and SGSs with similar lattice constants, large energy gaps below and above the Fermi level, and high Curie temperatures for room temperature applications. By employing state-of-the-art DFT calculations, we identified 25 materials within the family of quaternary Heusler compounds for possible application in spintronic devices. Next, based on the screening of SGSs and HMMs within the family of ordered quaternary Heusler compounds, we computationally designed two different MTJs using SGSs and HMMs as electrode materials separated by different thicknesses of MgO layers as a tunnel barrier. We discussed their current-voltage characteristics and the TMR ratio for magnetic logic and memory application. Finally, we introduced a new device concept based on SGSs and HMMs called Ohmic spin diode (OSD), which is to some extent similar to conventional metal-semiconductor diodes (Schottky-barrier diodes). The OSDs show linear $I - V$ curves under any finite forward bias voltage, possess zero threshold voltage, and block the current under reverse bias due to spin-dependent filtering of the electrons. By employing the NEGF method combined with DFT, we proposed four different HMM-SGS junctions within the family of quaternary Heusler compounds.

Outlook The current computing technology is based on the von-Neumann architecture. There, the memory and the central processing unit (CPU) are connected via a shared bus system which causes high power consumption and the well-known memory bandwidth bottleneck. Thus, for many computing tasks, a large amount of energy and time is needed to transfer data between the memory and the CPU, rather than the information processing itself. Spintronics is a research field that aims to solve the major problems in the existing conventional microelectronics. MTJs played a crucial role in spintronics development since they are suitable for several applications ranging from non-volatile memory devices to read-head sensors as well as from logic-in-memory computing to non-volatile logic concepts. The transfer from conventional electronics to spintronics paves the way for realizing devices with low power consumption, high storage capacity, as well as fast operation. In fact, conventional tunnel junctions are used as non-volatile memory elements, e.g., in STT- or SOT-MRAM devices, and new magnetic logic concepts based on MTJs have been proposed and demonstrated. Nevertheless, several magnetic logic concepts and the current non-volatile magnetic

memory technology employ MTJs with limited functionality. The unique characteristics of devices based on HMMs and SGSs offer new ways for magnetic logic concepts and memory elements as they combine an inverse TMR effect and a dynamically reconfigurable diode effect in a single device. Especially magnetic tunnel junction logic is of particular interest as it opens the way to logic-in-memory computing, i.e., processing and storing information within a single device and hence providing a possibility to explore computing architectures beyond the von-Neumann architecture. Besides this, tunnel junctions that exhibit a current rectification effect are of particular interest for cross-point STT-MRAM applications since they eliminate the necessity of selection devices. Moreover, the MTJs under study are the basis of the three-terminal reconfigurable magnetic tunnel transistors with exceptional properties.

List of publications

- [TA1] T. Aull, E. Şaşıoğlu, I. V. Maznichenko, S. Ostanin, A. Ernst, I. Mertig, and I. Galanakis
Ab initio design of quaternary Heusler compounds for reconfigurable magnetic tunnel diodes and transistors
Phys. Rev. Mater. **3**, 124415 (2019)
- [TA2] T. Aull, E. Şaşıoğlu, and I. Mertig
Ab initio study of magnetic tunnel junctions based on half-metallic and spin-gapless semiconducting Heusler compounds: Reconfigurable diode and inverse TMR effect for magnetic memory and logic applications
Manuscript submitted for publication, also available at arXiv:2202.06752 (2022)
- [TA3] E. Şaşıoğlu*, T. Aull*, D. Kutschabsky, S. Blügel, and I. Mertig
Half-Metal–Spin-Gapless-Semiconductor Junctions as a Route to the Ideal Diode
Phys. Rev. Appl. **14**, 014082 (2020)
- [TA4] T. Aull, E. Şaşıoğlu, and I. Mertig
First principles design of Ohmic spin diodes based on quaternary Heusler compounds
Appl. Phys. Lett. **118**, 052405 (2021)
- [TA5] P. Borlido, T. Aull, A. Huran, F. Tran, M. A. L. Marques, and S. Botti
Large-Scale Benchmark of Exchange–Correlation Functionals for the Determination of Electronic Band Gaps of Solids
J. Chem. Theory Comput. **9**, 5069 (2019)
- [TA6] T. Aull, I. V. Maznichenko, S. Ostanin, E. Şaşıoğlu, and I. Mertig
Externally controlled and switchable 2D electron gas at the Rashba interface between ferroelectrics and heavy *d* metals
Phys. Rev. Research **3**, 043110 (2021)

* These authors contributed equally

Copyrights

Publication [TA1]: Reprinted (whole article) with permission from (T. Aull *et al.* Physical Review Materials **3**, 124415 (2019); *Ab initio* design of quaternary Heusler compounds for reconfigurable magnetic tunnel diodes and transistors). Copyright (2019) by the American Physical Society (APS).

Publication [TA3]: Reprinted (whole article) with permission from (E. Şaşıoğlu *et al.* Physical Review Applied **14**, 014082 (2020); Half-Metal–Spin-Gapless-Semiconductor Junctions as a Route to the Ideal Diode). Copyright (2020) by the American Physical Society (APS).

Publication [TA4]: Reprinted (whole article) from (T. Aull *et al.* Applied Physics Letters **118**, 052405 (2021); First principles design of Ohmic spin diodes based on quaternary Heusler compounds), with the permission of AIP Publishing.

Bibliography

- ¹G. E. Moore, “Cramming more Components onto Integrated Circuits”, *Electronics* **38**, 114–117.
- ²M. Hilbert and P. López, “The World’s Technological Capacity to Store, Communicate, and Compute Information”, *Science* **332**, 60–65 (2011).
- ³H. J. Sommer III, Professor of Mechanical Engineering, Penn State University, *Magnetic-core memory*, 02.11.2006, visited on 15.02.2022, <https://www.britannica.com/technology/magnetic-core-storage>.
- ⁴G. Binasch, P. Grünberg, F. Saurenbach, and W. Zinn, “Enhanced magnetoresistance in layered magnetic structures with antiferromagnetic interlayer exchange”, *Phys. Rev. B* **39**, 4828 (1989).
- ⁵M. N. Baibich, J. M. Broto, A. Fert, F. N. Van Dau, F. Petroff, P. Etienne, G. Creuzet, A. Friederich, and J. Chazelas, “Giant Magnetoresistance of (001)Fe/(001)Cr Magnetic Superlattices”, *Phys. Rev. Lett.* **61**, 2472 (1988).
- ⁶M. Julliere, “Tunneling between ferromagnetic films”, *Phys. Lett. A* **54**, 225–226 (1975).
- ⁷S. S. P. Parkin, C. Kaiser, A. Panchula, P. M. Rice, B. Hughes, M. Samant, and S.-H. Yang, “Giant tunnelling magnetoresistance at room temperature with MgO (100) tunnel barriers”, *Nat. Mater.* **3**, 862–867 (2004).
- ⁸R. Richter, L. Bär, J. Wecker, and G. Reiss, “Nonvolatile field programmable spin-logic for reconfigurable computing”, *Appl. Phys. Lett.* **80**, 1291–1293 (2002).
- ⁹A. Ney, C. Pampuch, R. Koch, and K. Ploog, “Programmable computing with a single magnetoresistive element”, *Nature* **425**, 485–487 (2003).
- ¹⁰A. Thomas, D. Meyners, D. Ebke, N.-N. Liu, M. D. Sacher, J. Schmalhorst, G. Reiss, H. Ebert, and A. Hütten, “Inverted spin polarization of Heusler alloys for spintronic devices”, *Appl. Phys. Lett.* **89**, 012502 (2006).
- ¹¹E. Şaşıoğlu, S. Blügel, and I. Mertig, “Proposal for Reconfigurable Magnetic Tunnel Diode and Transistor”, *ACS Appl. Electron. Mater.* **1**, 1552–1559 (2019).
- ¹²M. Born and R. Oppenheimer, “Zur Quantentheorie der Molekeln”, *Ann. d. Phys.* **389**, 457–484 (1927).
- ¹³M. A. L. Marques, N. T. Maitra, F. M. Nogueira, E. K. U. Gross, and A. Rubio, “Fundamentals of Time-Dependent Density Functional Theory”, in *Lecture Notes in Physics*, Vol. 837 (Springer, Berlin, 2012), p. 54.
- ¹⁴L. H. Thomas, “The calculation of atomic fields”, *Math. Proc. Camb. Phil. Soc.* **23**, 542–548 (1927).
- ¹⁵E. Fermi, “Un Metodo Statistico per la Determinazione di alcune Proprietà dell’Atomo”, *Rend. Accad. Naz. Lincei* **6**, 32 (1927).
- ¹⁶E. Fermi, “Eine statistische Methode zur Bestimmung einiger Eigenschaften des Atoms und ihre Anwendung auf die Theorie des periodischen Systems der Elemente”, *Zeit. für Phys.* **48**, 73–79 (1928).
- ¹⁷P. A. M. Dirac, “Note on Exchange Phenomena in the Thomas Atom”, *Math. Proc. Camb. Phil. Soc.* **26**, 376–385 (1930).
- ¹⁸P. Hohenberg and W. Kohn, “Inhomogeneous Electron Gas”, *Phys. Rev.* **136**, B864 (1964).

-
- ¹⁹R. M. Martin, *Electronic Structure: Basic Theory and Practical Methods* (Cambridge University Press, 2004).
- ²⁰A. Szabo and N. S. Ostlund, *Modern Quantum Chemistry: Introduction to Advanced Electronic Structure Theory*, Dover Books on Chemistry (Dover Publications, New York, 1996).
- ²¹A. A. Abrikosov, I. P. Gorkov, and I. E. Dzyaloshinski, *Methods of Quantum Field Theory in Statistical Physics* (Dover Publications, 1976).
- ²²M. Peskin and D. Schroeder, *An Introduction to Quantum Field Theory*, Advanced book classics (Avalon Publishing, 1995).
- ²³A. Fetter and J. Walecka, *Quantum Theory of Many-Particle Systems*, Dover Books on Physics (Dover Publications, 2012).
- ²⁴G. Stefanucci and R. Van Leeuwen, *Nonequilibrium Many-Body Theory of Quantum Systems: A Modern Introduction* (Cambridge University Press, 2015).
- ²⁵E. E. Salpeter and H. A. Bethe, “A Relativistic Equation for Bound-State Problems”, *Phys. Rev.* **84**, 1232 (1951).
- ²⁶L. Hedin, “New Method for Calculating the One-Particle Green’s Function with Application to the Electron-Gas Problem”, *Phys. Rev.* **139**, A796 (1965).
- ²⁷R. M. Dreizler and E. K. U. Gross, *Density Functional Theory: An Approach to the Quantum Many-Body Problem* (Springer, Berlin, 2012).
- ²⁸K. Capelle, “A bird’s-eye view of density-functional theory”, *Braz. J. Phys.* **36**, 1318–1343 (2006).
- ²⁹W. Kohn, “Nobel Lecture: Electronic structure of matter – wave functions and density functionals”, *Rev. Mod. Phys.* **71**, 1253–1266 (1999).
- ³⁰R. G. Parr and Y. Weitao, *Density-Functional Theory of Atoms and Molecules*, International Series of Monographs on Chemistry (Oxford University Press, 1989).
- ³¹“A primer in Density Functional Theory”, in *Lecture Notes in Physics*, Vol. 620, edited by C. Fiolhais, F. Nogueira, and M. A. L. Marques (Springer, Berlin, 2003).
- ³²M. Levy, “Universal variational functionals of electron densities, first-order density matrices, and natural spin-orbitals and solution of the v -representability problem”, *Proc. Natl. Acad. Sci. U.S.A.* **76**, 6062–6065 (1979).
- ³³M. Levy, “Electron densities in search of Hamiltonians”, *Phys. Rev. A* **26**, 1200–1208 (1982).
- ³⁴R. M. Dreizler and J. da Providência, *Density Functional Methods In Physics*, Vol. 123 (Springer, Boston, 1985).
- ³⁵A. Shimony and H. Feshbach, *Physics as natural philosophy: Essays in honor of Laszlo Tisza on his seventy-fifth birthday* (MIT press, Cambridge, 1982).
- ³⁶E. H. Lieb, “Density functionals for coulomb systems”, *Int. J. Quantum Chem.* **24**, 243–277 (1983).
- ³⁷J. P. Perdew and A. Zunger, “Self-interaction correction to density-functional approximations for many-electron systems”, *Phys. Rev. B* **23**, 5048–5079 (1981).

- ³⁸W. Kohn and L. J. Sham, “Self-Consistent Equations Including Exchange and Correlation Effects”, *Phys. Rev.* **140**, A1133–A1138 (1965).
- ³⁹F. A. Hamprecht, A. J. Cohen, D. J. Tozer, and N. C. Handy, “Development and assessment of new exchange-correlation functionals”, *J. Chem. Phys.* **109**, 6264–6271 (1998).
- ⁴⁰G. E. Scuseria and V. N. Staroverov, “Chapter 24 - Progress in the development of exchange-correlation functionals”, in *Theory and Applications of Computational Chemistry*, edited by C. E. Dykstra, G. Frenking, K. S. Kim, and G. E. Scuseria (Elsevier, Amsterdam, 2005), pp. 669–724.
- ⁴¹R. van Leeuwen, “Density Functional Approach to the Many-Body Problem: Key Concepts and Exact Functionals”, in *Advances in Quantum Chemistry*, Vol. 43 (Academic Press, 2003), pp. 25–94.
- ⁴²M. A. L. Marques, M. J. Oliveira, and T. Burnus, “Libxc: A library of exchange and correlation functionals for density functional theory”, *Comput. Phys. Commun.* **183**, 2272–2281 (2012).
- ⁴³A. D. Becke, “Perspective: Fifty years of density-functional theory in chemical physics”, *J. Chem. Phys.* **140**, 18A301 (2014).
- ⁴⁴N. Mardirossian and M. Head-Gordon, “Thirty years of density functional theory in computational chemistry: an overview and extensive assessment of 200 density functionals”, *Mol. Phys.* **115**, 2315–2372 (2017).
- ⁴⁵S. Lehtola, C. Steigemann, M. J. Oliveira, and M. A. Marques, “Recent developments in libxc — A comprehensive library of functionals for density functional theory”, *SoftwareX* **7**, 1–5 (2018).
- ⁴⁶J. P. Perdew and K. Schmidt, “Jacob’s ladder of density functional approximations for the exchange-correlation energy”, *AIP Conference Proceedings* **577**, 1–20 (2001).
- ⁴⁷J. P. Perdew, “Density functional theory and the band gap problem”, *Int. J. Quantum Chem.* **28**, 497–523 (1985).
- ⁴⁸V. I. Anisimov, F. Aryasetiawan, and A. Lichtenstein, “First-principles calculations of the electronic structure and spectra of strongly correlated systems: the *LDA + U* method”, *J. Phys.: Cond. Matter* **9**, 767 (1997).
- ⁴⁹M. Lüders, A. Ernst, M. Däne, Z. Szotek, A. Svane, D. Ködderitzsch, W. Hergert, B. L. Györfy, and W. M. Temmerman, “Self-interaction correction in multiple scattering theory”, *Phys. Rev. B* **71**, 205109 (2005).
- ⁵⁰F. Tran and P. Blaha, “Accurate Band Gaps of Semiconductors and Insulators with a Semilocal Exchange-Correlation Potential”, *Phys. Rev. Lett.* **102**, 226401 (2009).
- ⁵¹F. Aryasetiawan and O. Gunnarsson, “The *GW* method”, *Rep. Prog. Phys.* **61**, 237 (1998).
- ⁵²J. Tao, J. P. Perdew, V. N. Staroverov, and G. E. Scuseria, “Climbing the Density Functional Ladder: Nonempirical Meta-Generalized Gradient Approximation Designed for Molecules and Solids”, *Phys. Rev. Lett.* **91**, 146401 (2003).
- ⁵³J. P. Perdew, K. Burke, and M. Ernzerhof, “Generalized Gradient Approximation Made Simple”, *Phys. Rev. Lett.* **77**, 3865–3868 (1996).

- ⁵⁴U. von Barth and L. Hedin, “A local exchange-correlation potential for the spin polarized case: I”, *J. Phys. C: Solid State Phys.* **5**, 1629 (1972).
- ⁵⁵B. N. Finkelstein and G. E. Horowitz, “Über die Energie des He-atoms und des positiven H₂-Ions im Normalzustande”, *Z. Physik* **48**, 118–122 (1928).
- ⁵⁶J. E. Lennard-Jones, “The electronic structure of some diatomic molecules”, *Trans. Faraday Soc.* **25**, 668–686 (1929).
- ⁵⁷C. C. J. Roothaan, “New Developments in Molecular Orbital Theory”, *Rev. Mod. Phys.* **23**, 69–89 (1951).
- ⁵⁸J. C. Slater, “Atomic Shielding Constants”, *Phys. Rev.* **36**, 57–64 (1930).
- ⁵⁹S. F. Boys, “Electronic wave functions - I. A general method of calculation for the stationary states of any molecular system”, *Proc. R. Soc. Lond. A* **200**, 542–554 (1950).
- ⁶⁰H. Hellmann, “A New Approximation Method in the Problem of Many Electrons”, *J. Chem. Phys.* **3**, 61–61 (1935).
- ⁶¹D. R. Hamann, M. Schlüter, and C. Chiang, “Norm-Conserving Pseudopotentials”, *Phys. Rev. Lett.* **43**, 1494–1497 (1979).
- ⁶²U. von Barth and C. D. Gelatt, “Validity of the frozen-core approximation and pseudopotential theory for cohesive energy calculations”, *Phys. Rev. B* **21**, 2222–2228 (1980).
- ⁶³C. Herring, “A New Method for Calculating Wave Functions in Crystals”, *Phys. Rev.* **57**, 1169–1177 (1940).
- ⁶⁴W. E. Pickett, “Pseudopotential methods in condensed matter applications”, *Comput. Phys. Rep.* **9**, 115–197 (1989).
- ⁶⁵J. C. Phillips and L. Kleinman, “New Method for Calculating Wave Functions in Crystals and Molecules”, *Phys. Rev.* **116**, 287–294 (1959).
- ⁶⁶L. Kleinman and D. M. Bylander, “Efficacious Form for Model Pseudopotentials”, *Phys. Rev. Lett.* **48**, 1425–1428 (1982).
- ⁶⁷M. Fuchs and M. Scheffler, “Ab initio pseudopotentials for electronic structure calculations of poly-atomic systems using density-functional theory”, *Comput. Phys. Commun.* **119**, 67–98 (1999).
- ⁶⁸D. J. Singh and L. Nordstrom, *Planewaves, Pseudopotentials, and the LAPW Method* (Springer, Boston, 2006).
- ⁶⁹G. B. Bachelet, D. R. Hamann, and M. Schlüter, “Pseudopotentials that work: From H to Pu”, *Phys. Rev. B* **26**, 4199–4228 (1982).
- ⁷⁰D. Vanderbilt, “Soft self-consistent pseudopotentials in a generalized eigenvalue formalism”, *Phys. Rev. B* **41**, 7892–7895 (1990).
- ⁷¹O. F. Sankey and D. J. Niklewski, “*Ab initio* multicenter tight-binding model for molecular-dynamics simulations and other applications in covalent systems”, *Phys. Rev. B* **40**, 3979–3995 (1989).
- ⁷²D. Sánchez-Portal, E. Artacho, and J. M. Soler, “Analysis of atomic orbital basis sets from the projection of plane-wave results”, *J. Phys.: Condens. Matter* **8**, 3859 (1996).

- ⁷³E. Artacho, D. Sánchez-Portal, P. Ordejón, A. García, and J. M. Soler, “Linear-Scaling ab-initio Calculations for Large and Complex Systems”, *Phys. Status Solidi B* **215**, 809–817 (1999).
- ⁷⁴C. Kittel, *Introduction to Solid State Physics* (John Wiley & Sons, New York, 1967).
- ⁷⁵M. G. Burt, “The justification for applying the effective-mass approximation to microstructures”, *J. Phys.: Condens. Matter* **4**, 6651–6690 (1992).
- ⁷⁶R. Kubo, “Statistical-Mechanical Theory of Irreversible Processes. I. General Theory and Simple Applications to Magnetic and Conduction Problems”, *J. Phys. Soc. Jpn.* **12**, 570–586 (1957).
- ⁷⁷D. A. Greenwood, “The Boltzmann Equation in the Theory of Electrical Conduction in Metals”, *Proc. Phys. Soc.* **71**, 585–596 (1958).
- ⁷⁸J. M. Zillman, *Electrons and Phonons: The Theory of Transport Phenomena in Solids* (Clarendon Press, Oxford, 1960).
- ⁷⁹I. Mertig, “Transport properties of dilute alloys”, *Rep. Prog. Phys.* **62**, 237–276 (1999).
- ⁸⁰S. Datta, *Electronic Transport in Mesoscopic Systems*, edited by H. Ahmed, M. Pepper, and A. Broers, Cambridge Studies in Semiconductor Physics and Microelectronic Engineering (Cambridge University Press, Cambridge, 1995).
- ⁸¹R. Landauer, “Spatial Variation of Currents and Fields Due to Localized Scatterers in Metallic Conduction”, *IBM J. Res. Dev.* **1**, 223–231 (1957).
- ⁸²M. Büttiker, “Absence of backscattering in the quantum Hall effect in multiprobe conductors”, *Phys. Rev. B* **38**, 9375–9389 (1988).
- ⁸³L. V. Keldysh et al., “Diagram Technique for Nonequilibrium Processes”, *Sov. Phys. JETP* **20**, 1018–1026 (1965).
- ⁸⁴R. Landauer, “Conductance from transmission: common sense points”, *Phys. Scr.* **1992**, 110 (1992).
- ⁸⁵Y. V. Nazarov and Y. M. Blanter, *Quantum transport: Introduction to Nanoscience* (Cambridge University Press, 2009).
- ⁸⁶M. Paulsson, F. Zahid, and S. Datta, in *Nanoscience, Engineering, and Technology Handbook*, edited by G. Goddard, D. Brenner, S. Lyshevski, and G. Iafrate (CRC press, Boca Raton, 2002) Chap. Resistance of a Molecule.
- ⁸⁷P. S. Damle, A. W. Ghosh, and S. Datta, “Nanoscale Device Modeling”, in *Molecular Nanoelectronics*, edited by M. A. Reed and T. Lee (American Scientific Publishers, Valencia, 2003).
- ⁸⁸M. Brandbyge, J.-L. Mozos, P. Ordejón, J. Taylor, and K. Stokbro, “Density-functional method for nonequilibrium electron transport”, *Phys. Rev. B* **65**, 165401 (2002).
- ⁸⁹M. Paulsson, “Non Equilibrium Green’s Functions for Dummies: Introduction to the One Particle NEGF equations”, arXiv e-prints, arXiv:cond-mat/0210519 (2002).
- ⁹⁰L. Ballentine, “Scattering”, in *Quantum Mechanics: A Modern Development* (World Scientific Publishing, Singapore, 2014), pp. 421–470.

- ⁹¹W. Nolting, “Green’s Functions”, in *Theoretical Physics 9: Fundamentals of Many-body Physics*, 2nd ed. (Springer, Cham, 2018), pp. 109–204.
- ⁹²K. Wildberger, P. Lang, R. Zeller, and P. H. Dederichs, “Fermi-Dirac distribution in ab initio Green’s-function calculations”, *Phys. Rev. B* **52**, 11502–11508 (1995).
- ⁹³W. H. Press, B. P. Flannery, S. A. Teukolsky, and W. T. Vetterling, *Numerical Recipes*, 3rd ed. (Cambridge University Press, Cambridge, 2007).
- ⁹⁴T. N. Todorov, “Spatial distribution of the electric current and field in atomic-scale conductors”, *Philos. Mag. B* **79**, 1577–1590 (1999).
- ⁹⁵M. Brandbyge, N. Kobayashi, and M. Tsukada, “Conduction channels at finite bias in single-atom gold contacts”, *Phys. Rev. B* **60**, 17064–17070 (1999).
- ⁹⁶R. A. de Groot, F. M. Mueller, P. G. v. Engen, and K. H. J. Buschow, “New Class of Materials: Half-Metallic Ferromagnets”, *Phys. Rev. Lett.* **50**, 2024–2027 (1983).
- ⁹⁷X. L. Wang, “Proposal for a New Class of Materials: Spin Gapless Semiconductors”, *Phys. Rev. Lett.* **100**, 156404 (2008).
- ⁹⁸X. Wang, Z. Cheng, G. Zhang, H. Yuan, H. Chen, and X.-L. Wang, “Spin-gapless semiconductors for future spintronics and electronics”, *Phys. Rep.* **888**, 1–57 (2020).
- ⁹⁹D. Rani, L. Bainsla, A. Alam, and K. G. Suresh, “Spin-gapless semiconductors: Fundamental and applied aspects”, *J. Appl. Phys.* **128**, 220902 (2020).
- ¹⁰⁰E. Şaşıoğlu, T. Aull, D. Kutschabsky, S. Blügel, and I. Mertig, “Half-Metal–Spin-Gapless-Semiconductor Junctions as a Route to the Ideal Diode”, *Phys. Rev. Applied* **14**, 014082 (2020).
- ¹⁰¹B. Zhang, G. Song, J. Sun, J. Leng, C. Zhang, and J. Wang, “Two-dimensional stable Mn based half metal and antiferromagnets promising for spintronics”, *Nanoscale* **12**, 12490–12496 (2020).
- ¹⁰²F. Heusler, “Über magnetische Manganlegierungen”, *Verh. Dtsch. Phys. Ges.* **5**, 219 (1903).
- ¹⁰³K. Özdoğan and I. Galanakis, “First-principles electronic and magnetic properties of the half-metallic antiferromagnet Cr_2MnSb ”, *J. Magn. Magn. Mater.* **321**, L34–L36 (2009).
- ¹⁰⁴C. Jiang, M. Venkatesan, and J. Coey, “Transport and magnetic properties of Mn_2VAl : Search for half-metallicity”, *Solid State Commun.* **118**, 513–516 (2001).
- ¹⁰⁵K. Ramesh Kumar, N. Harish Kumar, G. Markandeyulu, J. Arout Chelvane, V. Neu, and P. Babu, “Structural, magnetic and transport properties of half-metallic ferrimagnet Mn_2VGa ”, *J. Magn. Magn. Mater.* **320**, 2737–2740 (2008).
- ¹⁰⁶S. Ouardi, G. H. Fecher, C. Felser, and J. Kübler, “Realization of Spin Gapless Semiconductors: The Heusler Compound Mn_2CoAl ”, *Phys. Rev. Lett.* **110**, 100401 (2013).
- ¹⁰⁷G. Kreiner, A. Kalache, S. Hausdorf, V. Alijani, J.-F. Qian, G. Shan, U. Burkhardt, S. Ouardi, and C. Felser, “New Mn_2 -based Heusler Compounds”, *Z. anorg. allg. Chem.* **640**, 738–752 (2014).
- ¹⁰⁸K. Ullakko, J. Huang, V. Kokorin, and R. O’Handley, “Magnetically controlled shape memory effect in Ni_2MnGa intermetallics”, *Scr. Mater.* **36**, 1133–1138 (1997).

- ¹⁰⁹P. J. Webster and K. R. A. Ziebeck, in *Alloys and Compounds of d-Elements with Main Group Elements. Part 2*, edited by H. P. J. Wijn, Landolt-Börnstein - Group III, Vol. 19C (Springer, Berlin, 1988), pp. 75–184.
- ¹¹⁰J. Pierre, R. V. Skolozdra, J. Toboła, S. Kaprzyk, C. Hordequin, M. A. Kouacou, I. Karla, R. Currat, and E. Lelièvre-Berna, “Properties on request in semi-Heusler phases”, *J. Alloys Comp.* **262-263**, 101–107 (1997).
- ¹¹¹P. J. Webster, K. R. A. Ziebeck, and K.-U. Neumann, in *Magnetic Properties of Metals*, edited by H. P. J. Wijn, Landolt-Börnstein - Group III, Vol. 32C (Springer, Berlin, 2001), pp. 64–414.
- ¹¹²J. Toboła, J. Pierre, S. Kaprzyk, R. V. Skolozdra, and M. A. Kouacou, “Crossover from semiconductor to magnetic metal in semi-Heusler phases as a function of valence electron concentration”, *J. Phys.: Condens. Matter* **10**, 1013–1032 (1998).
- ¹¹³J. Toboła and J. Pierre, “Electronic phase diagram of the XTZ (X=Fe, Co, Ni; T=Ti, V, Zr, Nb, Mn; Z=Sn, Sb) semi-Heusler compounds”, *J. Alloys Comp.* **296**, 243–252 (2000).
- ¹¹⁴J. Toboła, S. Kaprzyk, and P. Pecheur, “Theoretical search for magnetic half-Heusler semiconductors”, *Phys. Stat. Sol. B* **236**, 531–535 (2003).
- ¹¹⁵R. Dhakal, S. Nepal, I. Galanakis, R. Adhikari, and G. Kaphle, “Prediction of half-metallicity and spin-gapless semiconducting behavior in the new series of FeCr-based quaternary Heusler alloys: an ab initio study”, *J. Alloys Compd.*, 160500 (2021).
- ¹¹⁶S. Ishida, S. Akazawa, Y. Kubo, and J. Ishida, “Band theory of Co₂MnSn, Co₂TiSn and Co₂TiAl”, *J. Phys. F: Met. Phys.* **12**, 1111 (1982).
- ¹¹⁷S. Ishida, S. Fujii, S. Kashiwagi, and S. Asano, “Search for Half-Metallic Compounds in Co₂MnZ (Z=IIIb, IVb, Vb Element)”, *J. Phys. Soc. Jpn.* **64**, 2152–2157 (1995).
- ¹¹⁸H. Akai, “Ferromagnetism and Its Stability in the Diluted Magnetic Semiconductor (In, Mn)As”, *Phys. Rev. Lett.* **81**, 3002–3005 (1998).
- ¹¹⁹H. Akinaga, T. Manago, and M. Shirai, “Material Design of Half-Metallic Zinc-Blende CrAs and the Synthesis by Molecular-Beam Epitaxy”, *Jpn. J. Appl. Phys.* **39**, L1118 (2000).
- ¹²⁰A. Stroppa, S. Picozzi, A. Continenza, and A. J. Freeman, “Electronic structure and ferromagnetism of Mn-doped group-IV semiconductors”, *Phys. Rev. B* **68**, 155203 (2003).
- ¹²¹R. J. Soulen, J. M. Byers, M. S. Osofsky, B. Nadgorny, T. Ambrose, S. F. Cheng, P. R. Broussard, C. T. Tanaka, J. Nowak, J. S. Moodera, A. Barry, and J. M. D. Coey, “Measuring the Spin Polarization of a Metal with a Superconducting Point Contact”, *Science* **282**, 85–88 (1998).
- ¹²²I. Galanakis, P. H. Dederichs, and N. Papanikolaou, “Origin and properties of the gap in the half-ferromagnetic Heusler alloys”, *Phys. Rev. B* **66**, 134428 (2002).
- ¹²³I. Galanakis, P. H. Dederichs, and N. Papanikolaou, “Slater-Pauling behavior and origin of the half-metallicity of the full-Heusler alloys”, *Phys. Rev. B* **66**, 174429 (2002).
- ¹²⁴S. Skaftouros, K. Özdoğan, E. Şaşıoğlu, and I. Galanakis, “Search for spin gapless semiconductors: The case of inverse Heusler compounds”, *Appl. Phys. Lett.* **102**, 022402 (2013).

- ¹²⁵K. Özdoğan, E. Şaşıoğlu, and I. Galanakis, “Slater-Pauling behavior in LiMgPdSn-type multifunctional quaternary Heusler materials: Half-metallicity, spin-gapless and magnetic semiconductors”, *J. Appl. Phys.* **113**, 193903 (2013).
- ¹²⁶Y. Pan and Z. Yang, “Exploration of magnetism in armchair graphene nanoribbons with radical groups”, *Chem. Phys. Lett.* **518**, 104–108 (2011).
- ¹²⁷S.-D. Guo and B.-G. Liu, “Density-functional-theory investigation of pressure induced semiconductor–metal transitions in the ferromagnetic semiconductor HgCr_2Se_4 ”, *J. Phys.: Condens. Matter.* **24**, 045502 (2012).
- ¹²⁸Y. Pan and Z. Yang, “Electronic structures and spin gapless semiconductors in BN nanoribbons with vacancies”, *Phys. Rev. B* **82**, 195308 (2010).
- ¹²⁹G. Z. Xu, E. K. Liu, Y. Du, G. J. Li, G. D. Liu, W. H. Wang, and G. H. Wu, “A new spin gapless semiconductors family: Quaternary Heusler compounds”, *EPL* **102**, 17007 (2013).
- ¹³⁰Q. Gao, I. Opahle, and H. Zhang, “High-throughput screening for spin-gapless semiconductors in quaternary Heusler compounds”, *Phys. Rev. Materials* **3**, 024410 (2019).
- ¹³¹L. Li, Y. Yu, G. J. Ye, Q. Ge, X. Ou, H. Wu, D. Feng, X. H. Chen, and Y. Zhang, “Black phosphorus field-effect transistors”, *Nat. Nanotechnol.* **9**, 372 (2014).
- ¹³²B. Radisavljevic, A. Radenovic, J. Brivio, V. Giacometti, and A. Kis, “Single-layer MoS_2 transistors”, *Nat. Nanotechnol.* **6**, 147–150 (2011).
- ¹³³D. Jariwala, V. K. Sangwan, L. J. Lauhon, T. J. Marks, and M. C. Hersam, “Emerging device applications for semiconducting two-dimensional transition metal dichalcogenides”, *ACS Nano* **8**, 1102–1120 (2014).
- ¹³⁴T. Roy, M. Tosun, X. Cao, H. Fang, D.-H. Lien, P. Zhao, Y.-Z. Chen, Y.-L. Chueh, J. Guo, and A. Javey, “Dual-Gated $\text{MoS}_2/\text{WSe}_2$ van der Waals Tunnel Diodes and Transistors”, *ACS Nano* **9**, 2071–2079 (2015).
- ¹³⁵Y. Liu, N. O. Weiss, X. Duan, H.-C. Cheng, Y. Huang, and X. Duan, “Van der Waals heterostructures and devices”, *Nat. Rev. Mater.* **1**, 16042 (2016).
- ¹³⁶F. Giannazzo, G. Greco, F. Roccaforte, and S. S. Sonde, “Vertical Transistors Based on 2D Materials: Status and Prospects”, *Crystals* **8**, 70 (2018).
- ¹³⁷M.-Y. Li, C.-H. Chen, Y. Shi, and L.-J. Li, “Heterostructures based on two-dimensional layered materials and their potential applications”, *Mater. Today* **19**, 322–335 (2016).
- ¹³⁸B. Huang, G. Clark, E. Navarro-Moratalla, D. R. Klein, R. Cheng, K. L. Seyler, D. Zhong, E. Schmidgall, M. A. McGuire, D. H. Cobden, et al., “Layer-dependent ferromagnetism in a van der Waals crystal down to the monolayer limit”, *Nature* **546**, 270–273 (2017).
- ¹³⁹M. Bonilla, S. Kolekar, Y. Ma, H. C. Diaz, V. Kalappattil, R. Das, T. Eggers, H. R. Gutierrez, M.-H. Phan, and M. Batzill, “Strong room-temperature ferromagnetism in VSe_2 monolayers on van der Waals substrates”, *Nat. Nanotechnol.* **13**, 289–293 (2018).
- ¹⁴⁰Q. Chen, Y. Ouyang, S. Yuan, R. Li, and J. Wang, “Uniformly Wetting Deposition of Co Atoms on MoS_2 Monolayer: A Promising Two-Dimensional Robust Half-Metallic Ferromagnet”, *ACS Appl. Mater. Interfaces* **6**, 16835–16840 (2014).
- ¹⁴¹C. Jiang, Y. Wang, Y. Zhang, H. Wang, Q. Chen, and J. Wan, “Robust half-metallic magnetism in two-dimensional Fe/MoS_2 ”, *J. Phys. Chem. C* **122**, 21617–21622 (2018).

- ¹⁴²S. Haastrup, M. Strange, M. Pandey, T. Deilmann, P. S. Schmidt, N. F. Hinsche, M. N. Gjerding, D. Torelli, P. M. Larsen, A. C. Riis-Jensen, J. Gath, K. W. Jacobsen, J. J. Mortensen, T. Olsen, and K. S. Thygesen, “The Computational 2D Materials Database: high-throughput modeling and discovery of atomically thin crystals”, *2D Mater.* **5**, 042002 (2018).
- ¹⁴³M. N. Gjerding, A. Taghizadeh, A. Rasmussen, S. Ali, F. Bertoldo, T. Deilmann, U. P. Holguin, N. R. Knøsgaard, M. Kruse, S. Manti, T. G. Pedersen, T. Skovhus, M. K. Svendsen, J. J. Mortensen, T. Olsen, and K. S. Thygesen, “Recent progress of the computational 2D materials database (C2DB)”, *2D Mater.* **8**, 044002 (2021).
- ¹⁴⁴S. Tomar, B. Ghosh, S. Mardanya, P. Rastogi, B. S. Bhadoria, Y. S. Chauhan, A. Agarwal, and S. Bhowmick, “Intrinsic magnetism in monolayer transition metal trihalides: A comparative study”, *J. Magn. Mag. Mater.* **489**, 165384 (2019).
- ¹⁴⁵X. Li and J. Yang, “CrXTe₃ (X = Si, Ge) nanosheets: two dimensional intrinsic ferromagnetic semiconductors”, *J. Mater. Chem. C* **2**, 7071–7076 (2014).
- ¹⁴⁶H. L. Zhuang and R. G. Hennig, “Stability and magnetism of strongly correlated single-layer VS₂”, *Phys. Rev. B* **93**, 054429 (2016).
- ¹⁴⁷H.-R. Fuh, C.-R. Chang, Y.-K. Wang, R. F. Evans, R. W. Chantrell, and H.-T. Jeng, “Newtype single-layer magnetic semiconductor in transition-metal dichalcogenides VX₂ (X = S, Se and Te)”, *Sci. Rep.* **6**, 32625 (2016).
- ¹⁴⁸D. Gao, Q. Xue, X. Mao, W. Wang, Q. Xu, and D. Xue, “Ferromagnetism in ultrathin VS₂ nanosheets”, *J. Mater. Chem. C* **1**, 5909–5916 (2013).
- ¹⁴⁹N. Luo, C. Si, and W. Duan, “Structural and electronic phase transitions in ferromagnetic monolayer VS₂ induced by charge doping”, *Phys. Rev. B* **95**, 205432 (2017).
- ¹⁵⁰G. H. Han, D. L. Duong, D. H. Keum, S. J. Yun, and Y. H. Lee, “van der Waals Metallic Transition Metal Dichalcogenides”, *Chem. Rev.* **118**, 6297–6336 (2018).
- ¹⁵¹IEEE IRDS, “International Roadmap for Devices and Systems”, Available at irds.ieee.org. (2017).
- ¹⁵²J. von Neumann, “First Draft of a Report on the EDVAC”, *IEEE Ann. Hist. Comput.* **15**, 27–75 (1993).
- ¹⁵³N. R. Mahapatra and B. Venkatrao, “The Processor-Memory Bottleneck: Problems and Solutions”, *XRDS: Crossroads* **5**, 2–es (1999).
- ¹⁵⁴M. Horowitz, “1.1 Computing’s energy problem (and what we can do about it)”, in *Solid-State Circuits Conference Digest of Technical Papers (ISSCC)* (IEEE International, 2014), pp. 10–14.
- ¹⁵⁵J. Åkerman, “Toward a Universal Memory”, *Science* **308**, 508–510 (2005).
- ¹⁵⁶A. Hirohata, K. Yamada, Y. Nakatani, I.-L. Prejbeanu, B. Diény, P. Pirro, and B. Hillebrands, “Review on spintronics: Principles and device applications”, *J. Magn. Magn. Mater.* **509**, 166711 (2020).
- ¹⁵⁷D. E. Nikonov and I. A. Young, “Overview of Beyond-CMOS Devices and a Uniform Methodology for Their Benchmarking”, *Proc. IEEE* **101**, 2498–2533 (2013).

-
- ¹⁵⁸S. K. Banerjee, L. F. Register, E. Tutuc, D. Reddy, and A. H. MacDonald, “Bilayer pseudospin field-effect transistor (BiSFET): A proposed new logic device”, *IEEE Electron. Device Lett.* **30**, 158–160 (2009).
- ¹⁵⁹J. A. Currivan, Y. Jang, M. D. Mascaró, M. A. Baldo, and C. A. Ross, “Low energy magnetic domain wall logic in short, narrow, ferromagnetic wires”, *IEEE Magn. Lett.* **3**, 3000104 (2012).
- ¹⁶⁰S. S. P. Parkin, M. Hayashi, and L. Thomas, “Magnetic Domain-Wall Racetrack Memory”, *Science* **320**, 190–194 (2008).
- ¹⁶¹A. Fert, V. Cros, and J. Sampaio, “Skyrmions on the track”, *Nat. Nanotechnol.* **8**, 152–156 (2013).
- ¹⁶²T. Shinjo, *Nanomagnetism and Spintronics* (Elsevier, Amsterdam, 2009).
- ¹⁶³T. Miyazaki and N. Tezuka, “Giant magnetic tunneling effect in Fe/Al₂O₃/Fe junction”, *J. Magn. Magn. Mater.* **139**, L231–L234 (1995).
- ¹⁶⁴J. S. Moodera, L. R. Kinder, T. M. Wong, and R. Meservey, “Large Magnetoresistance at Room Temperature in Ferromagnetic Thin Film Tunnel Junctions”, *Phys. Rev. Lett.* **74**, 3273–3276 (1995).
- ¹⁶⁵J. Mathon and A. Umerski, “Theory of tunneling magnetoresistance of an epitaxial Fe/MgO/Fe(001) junction”, *Phys. Rev. B* **63**, 220403 (2001).
- ¹⁶⁶W. H. Butler, X.-G. Zhang, T. C. Schulthess, and J. M. MacLaren, “Spin-dependent tunneling conductance of Fe|MgO|Fe sandwiches”, *Phys. Rev. B* **63**, 054416 (2001).
- ¹⁶⁷M. Bowen, V. Cros, F. Petroff, A. Fert, C. Martinez Boubeta, J. L. Costa-Krämer, J. V. Anguita, A. Cebollada, F. Briones, J. De Teresa, et al., “Large magnetoresistance in Fe/MgO/FeCo(001) epitaxial tunnel junctions on GaAs(001)”, *Appl. Phys. Lett.* **79**, 1655–1657 (2001).
- ¹⁶⁸S. Yuasa, T. Nagahama, A. Fukushima, Y. Suzuki, and K. Ando, “Giant room-temperature magnetoresistance in single-crystal Fe/MgO/Fe magnetic tunnel junctions”, *Nat. Mater.* **3**, 868–871 (2004).
- ¹⁶⁹J. M. Daughton and J. S. T. Huang, *Magnetoresistive memory including thin film storage cells having tapered ends*, Patent US4731757A, 1986.
- ¹⁷⁰D. M. Bromberg, D. H. Morris, L. Pileggi, and J.-G. Zhu, “Novel STT-MTJ device enabling all-metallic logic circuits”, *IEEE Trans. Magn.* **48**, 3215–3218 (2012).
- ¹⁷¹B. Behin-Aein, D. Datta, S. Salahuddin, and S. Datta, “Proposal for an all-spin logic device with built-in memory”, *Nat. Nanotechnol.* **5**, 266–270 (2010).
- ¹⁷²C. Heiliger, P. Zahn, B. Y. Yavorsky, and I. Mertig, “Influence of the interface structure on the bias dependence of tunneling magnetoresistance”, *Phys. Rev. B* **72**, 180406 (2005).
- ¹⁷³C. Heiliger, P. Zahn, B. Y. Yavorsky, and I. Mertig, “Interface structure and bias dependence of Fe/MgO/Fe tunnel junctions: *Ab initio* calculations”, *Phys. Rev. B* **73**, 214441 (2006).
- ¹⁷⁴G. Finocchio, R. Tomasello, B. Fang, A. Giordano, V. Puliafito, M. Carpentieri, and Z. Zeng, “Perspectives on spintronic diodes”, *Appl. Phys. Lett.* **118**, 160502 (2021).

- ¹⁷⁵J. Cai, L. Zhang, B. Fang, W. Lv, B. Zhang, G. Finocchio, R. Xiong, S. Liang, and Z. Zeng, “Sparse neuromorphic computing based on spin-torque diodes”, *Appl. Phys. Lett.* **114**, 192402 (2019).
- ¹⁷⁶N. Leroux, A. Mizrahi, D. Markovic, D. Sanz-Hernandez, J. Trastoy, P. Bortolotti, L. Martins, A. Jenkins, R. Ferreira, and J. Grollier, “Hardware realization of the multiply and accumulate operation on radio-frequency signals with magnetic tunnel junctions”, *Neuromorph. Comput. Eng.* **1**, 011001 (2021).
- ¹⁷⁷A. Tulapurkar, Y. Suzuki, A. Fukushima, H. Kubota, H. Maehara, K. Tsunekawa, D. Djayaprawira, N. Watanabe, and S. Yuasa, “Spin-torque diode effect in magnetic tunnel junctions”, *Nature* **438**, 339–342 (2005).
- ¹⁷⁸R. Urcuyo, D. L. Duong, H. Y. Jeong, M. Burghard, and K. Kern, “High Performance Graphene–Oxide–Metal Diode through Bias-Induced Barrier Height Modulation”, *Adv. Electron. Mater.* **2**, 1600223 (2016).
- ¹⁷⁹C. de Buttet, M. Hehn, F. Montaigne, C. Tiusan, G. Malinowski, A. Schuhl, E. Snoeck, and S. Zoll, “Low-resistance magnetic tunnel junctions with an MgO–Al₂O₃ composite tunnel barrier: Asymmetric transport characteristics and free electron modeling of a self-limited oxidation bilayer”, *Phys. Rev. B* **73**, 104439 (2006).
- ¹⁸⁰J. G. Simmons, “Potential Barriers and Emission-Limited Current Flow Between Closely Spaced Parallel Metal Electrodes”, *J. Appl. Phys.* **35**, 2472–2481 (1964).
- ¹⁸¹A. Iovan, S. Andersson, Y. G. Naidyuk, A. Vedyayev, B. Dieny, and V. Korenivski, “Spin Diode Based on Fe/MgO Double Tunnel Junction”, *Nano Lett.* **8**, 805–809 (2008).
- ¹⁸²S. S. P. Parkin, K. P. Roche, M. G. Samant, P. M. Rice, R. B. Beyers, R. E. Scheuerlein, E. J. O’Sullivan, S. L. Brown, J. Bucchigano, D. W. Abraham, Y. Lu, M. Rooks, P. L. Trouilloud, R. A. Wanner, and W. J. Gallagher, “Exchange-biased magnetic tunnel junctions and application to nonvolatile magnetic random access memory”, *J. Appl. Phys.* **85**, 5828–5833 (1999).
- ¹⁸³S. Tehrani, E. Chen, M. Durlam, M. DeHerrera, J. M. Slaughter, J. Shi, and G. Kerzyski, “High density submicron magnetoresistive random access memory”, *J. Appl. Phys.* **85**, 5822–5827 (1999).
- ¹⁸⁴M. Chshiev, D. Stoeffler, A. Vedyayev, and K. Ounadjela, “Magnetic diode effect in double-barrier tunnel junctions”, *EPL* **58**, 257 (2002).
- ¹⁸⁵C. Tiusan, M. Chshiev, A. Iovan, V. Da Costa, D. Stoeffler, T. Dimopoulos, and K. Ounadjela, “Quantum coherent transport versus diode-like effect in semiconductor-free metal/insulator structure”, *Appl. Phys. Lett.* **79**, 4231–4233 (2001).
- ¹⁸⁶T. Nozaki, N. Tezuka, and K. Inomata, “Quantum Oscillation of the Tunneling Conductance in Fully Epitaxial Double Barrier Magnetic Tunnel Junctions”, *Phys. Rev. Lett.* **96**, 027208 (2006).
- ¹⁸⁷A. Iovan, D. B. Haviland, and V. Korenivski, “Diode effect in asymmetric double-tunnel barriers with single-metal nanoclusters”, *Appl. Phys. Lett.* **88**, 163503 (2006).
- ¹⁸⁸E. Şaşıoğlu and S. Blügel, *Magnetic tunnel diode and magnetic tunnel transistor*, Patent US20180309047A1, 2016.

-
- ¹⁸⁹N. Maji and T. K. Nath, “Demonstration of reconfigurable magnetic tunnel diode and giant tunnel magnetoresistance in magnetic tunnel junctions made with spin gapless semiconductor and half-metallic Heusler alloy”, *Appl. Phys. Lett.* **120**, 072401 (2022).
- ¹⁹⁰V. V. Zhirnov, R. K. Cavin, J. A. Hutchby, and G. I. Bourianoff, “Limits to binary logic switch scaling - a gedanken model”, *Proc. IEEE* **91**, 1934–1939 (2003).
- ¹⁹¹S. Datta and B. Das, “Electronic analog of the electro-optic modulator”, *Appl. Phys. Lett.* **56**, 665–667 (1990).
- ¹⁹²S. Datta, “How we proposed the spin transistor”, *Nat. Electron.* **1**, 604–604 (2018).
- ¹⁹³H. C. Koo, J. H. Kwon, J. Eom, J. Chang, S. H. Han, and M. Johnson, “Control of Spin Precession in a Spin-Injected Field Effect Transistor”, *Science* **325**, 1515–1518 (2009).
- ¹⁹⁴W. Y. Choi, H.-J. Kim, J. Chang, S. H. Han, H. C. Koo, and M. Johnson, “Electrical detection of coherent spin precession using the ballistic intrinsic spin Hall effect”, *Nat. Nanotechnol.* **10**, 666–670 (2015).
- ¹⁹⁵S. Sugahara and M. Tanaka, “A spin metal–oxide–semiconductor field-effect transistor using half-metallic-ferromagnet contacts for the source and drain”, *Appl. Phys. Lett.* **84**, 2307–2309 (2004).
- ¹⁹⁶T. Marukame, T. Inokuchi, M. Ishikawa, H. Sugiyama, and Y. Saito, “Read/write operation of spin-based MOSFET using highly spin-polarized ferromagnet/MgO tunnel barrier for reconfigurable logic devices”, in *IEDM* (2009), pp. 1–4.
- ¹⁹⁷Y. Saito, T. Marukame, T. Inokuchi, M. Ishikawa, H. Sugiyama, and T. Tanamoto, “Spin injection, transport, and read/write operation in spin-based MOSFET”, *Thin Solid Films* **519**, 8266–8273 (2011).
- ¹⁹⁸Y. Saito, “Spin-based MOSFET and its applications”, *ECS Trans.* **37**, 217–228 (2011).
- ¹⁹⁹D. J. Monsma, J. C. Lodder, T. J. A. Popma, and B. Dieny, “Perpendicular Hot Electron Spin-Valve Effect in a New Magnetic Field Sensor: The Spin-Valve Transistor”, *Phys. Rev. Lett.* **74**, 5260–5263 (1995).
- ²⁰⁰S. van Dijken, X. Jiang, and S. S. P. Parkin, “Spin-dependent hot electron transport in $\text{Ni}_{81}\text{Fe}_{19}$ and $\text{Co}_{84}\text{Fe}_{16}$ films on GaAs(001)”, *Phys. Rev. B* **66**, 094417 (2002).
- ²⁰¹R. Jansen, “The spin-valve transistor: a review and outlook”, *J. Phys. D: Appl. Phys.* **36**, R289 (2003).
- ²⁰²S. M. Sze and K. K. Ng, *Physics of Semiconductor Devices*, 3rd ed. (John Wiley & Sons, Hoboken, 2007).
- ²⁰³S. Van Dijken, X. Jiang, and S. S. Parkin, “Room temperature operation of a high output current magnetic tunnel transistor”, *Appl. Phys. Lett.* **80**, 3364–3366 (2002).
- ²⁰⁴T. Nagahama, H. Saito, and S. Yuasa, “Hot electron transport in magnetic tunnel transistors with an epitaxial MgO tunnel barrier”, *Appl. Phys. Lett.* **96**, 112509 (2010).
- ²⁰⁵M. I. Katsnelson, V. Y. Irkhin, L. Chioncel, A. I. Lichtenstein, and R. A. de Groot, “Half-metallic ferromagnets: From band structure to many-body effects”, *Rev. Mod. Phys.* **80**, 315–378 (2008).

- ²⁰⁶C. Zeng, E. B. Song, M. Wang, S. Lee, C. M. Torres, Jr., J. Tang, B. H. Weiller, and K. L. Wang, “Vertical Graphene-Base Hot-Electron Transistor”, *Nano Lett.* **13**, 2370–2375 (2013).
- ²⁰⁷S. Vaziri, G. Lupina, C. Henkel, A. D. Smith, M. Östling, J. Dabrowski, G. Lippert, W. Mehr, and M. C. Lemme, “A Graphene-Based Hot Electron Transistor”, *Nano Lett.* **13**, 1435–1439 (2013).
- ²⁰⁸A. Zubair, A. Nourbakhsh, J.-Y. Hong, M. Qi, Y. Song, D. Jena, J. Kong, M. Dresselhaus, and T. Palacios, “Hot Electron Transistor with van der Waals Base-Collector Heterojunction and High-Performance GaN Emitter”, *Nano Lett.* **17**, 3089–3096 (2017).
- ²⁰⁹T. Daibou, M. Shinano, M. Hattori, Y. Sakuraba, M. Oogane, Y. Ando, and T. Miyazaki, “Tunnel Magnetoresistance Effect in CoFeB/MgO/Co₂FeSi and Co₂MnSi Tunnel Junctions”, *IEEE Trans. Magn.* **42**, 2655–2657 (2006).
- ²¹⁰P. J. Chen, G. Feng, and R. D. Shull, “Use of Half Metallic Heusler Alloys in CoFeB/MgO/Heusler Alloy Tunnel Junctions”, *IEEE Trans. Magn.* **49**, 4379–4382 (2013).
- ²¹¹C. J. Palmstrøm, “Heusler compounds and spintronics”, *Prog. Cryst. Growth Charact. Mater.* **62**, 371–397 (2016).

Acknowledgement

Without many people who accompanied and supported me within the last three years, writing and, in particular, finishing this thesis would not have been possible.

First of all, I would like to express my gratitude to my supervisor Prof. Ingrid Mertig for the fantastic opportunity to work in her group. Nothing of this would be possible if not for her. She was sharing her knowledge with me and I found great support not only on the scientific but also on the personal level.

Next, I would like to thank Dr. Ersoy Şaşıoğlu. Without him, this thesis would not have been possible. He was motivating me for the topic and always found time and patience for all questions that came to my mind.

Furthermore, I would like to thank both my office-mates, Franziska and Albert, with whom I had serious discussions about physical and other commonplace problems.

In addition, I would like to thank all other members of the group of Prof. Ingrid Mertig here in Halle: Michael, Igor, Sergey, Annika, Christian, Jürgen, Borge, Oliver, Till, Franz, Robin, Nicki, Sergio, Ismael, Kathrin, Alina, Frau Jurate Claus, and Frau Dr. Angelika Chassé. We had a fantastic, friendly working atmosphere and many discussions about different topics. I felt very welcome from the first day.

Finally, I would like to thank my friends, my parents and my sister. Without their support and encouragement, I would not have been able to finish my PhD.

Curriculum vitae

Education

- since Dec. 2018* PhD studies at the Martin Luther University, Halle (Saale), Germany
Supervisor: Prof. Dr. Ingrid Mertig
- Oct. 2016 - Nov. 2018* Master of Science in Physics at the Martin Luther University,
Halle (Saale), Germany
Master thesis: "Hybrid functional with selfconsistent density-dependent mixing"
- Oct. 2013 - Sep. 2016* Bachelor of Science in Medical Physics at the Martin Luther University,
Halle (Saale), Germany
Bachelor thesis: "Röntgenabsorption und zirkularer Dichroismus an K-Kanten in Übergangsmetalloxiden"
- 2005 - 2013* Gymnasium (grammar school) Franz-Miltenberger-Gymnasium,
Bad Brückenau, Germany
- 2001 - 2005* Grundschule (elementary school) Bad Brückenau, Bad Brückenau,
Germany

Academic work experience

- 2015 - 2018* Student assistant, Martin Luther University, Halle (Saale), Germany

Halle (Saale), den 17. Februar 2022

Thorsten Udo Aull

Eidstattliche Erklärung

Hiermit erkläre ich, Thorsten Udo Aull, gemäß §5 der Promotionsordnung der Naturwissenschaftlichen Fakultäten I, II und III der Martin-Luther-Universität Halle-Wittenberg vom 13.07.2016, dass ich die vorliegende Arbeit

Novel spintronic device concepts based on spin-gapless semiconductors and half-metallic magnets

selbstständig und ohne fremde Hilfe verfasst, andere als die von mir angegebenen Quellen und Hilfsmittel nicht benutzt und die den benutzten Werken wörtlich oder inhaltlich entnommenen Stellen als solche kenntlich gemacht habe. Ich erkläre die Angaben wahrheitsgemäß gemacht, keine vergeblichen Promotionsversuche unternommen und keine Dissertation an einer anderen wissenschaftlichen Einrichtung zur Erlangung eines akademischen Grades eingereicht zu haben. Ich bin weder vorbestraft noch sind gegen mich Ermittlungsverfahren anhängig.

Halle (Saale), den 17. Februar 2022

Thorsten Udo Aull